TU Delft

Delft University of Technology

Electron wave front modulation with patterned mirrors

Krielaart, M.A.R.

DOI
10.4233/uuid:285e9079-e12c-4cd4-9a34-555bf66237c7

Publication date
2021

Document Version
Final published version

Citation (APA)
Krielaart, M. A. R. (2021). *Electron wave front modulation with patterned mirrors*. [Dissertation (TU Delft), Delft University of Technology]. https://doi.org/10.4233/uuid:285e9079-e12c-4cd4-9a34-555bf66237c7

Important note
To cite this publication, please use the final published version (if applicable).
Please check the document version above.

Copyright
Other than for strictly personal use, it is not permitted to download, forward or distribute the text or part of it, without the consent of the author(s) and/or copyright holder(s), unless the work is under an open content license such as Creative Commons.

Takedown policy
Please contact us and provide details if you believe this document breaches copyrights.
We will remove access to the work immediately and investigate your claim.

This work is downloaded from Delft University of Technology.
For technical reasons the number of authors shown on this cover page is limited to a maximum of 10.

Electron wave front modulation with patterned mirrors

Electron wave front modulation with patterned mirrors

Proefschrift

ter verkrijging van de graad van doctor
aan de Technische Universiteit Delft,
op gezag van de Rector Magnificus prof. dr. ir. T. H. J. J. van der Hagen,
voorzitter van het College voor Promoties,
in het openbaar te verdedigen op maandag 15 maart 2021 om 15:00 uur.

door

Markus Adriaan Rudolf KRIELAART

Master of Science in Applied Physics,
Universiteit Twente, Enschede, Nederland,
geboren te Kampen, Nederland.

Dit proefschrift is goedgekeurd door de

promotor: prof. dr. ir. P. Kruit

Samenstelling promotiecommissie:

Rector Magnificus,	voorzitter
Prof. dr. ir. P. Kruit,	Technische Universiteit Delft, promotor

Onafhankelijke leden:

Prof. dr. K. K. Berggren	Massachusetts Institute of Technology
Prof. dr. P. Hommelhoff	Friedrich-Alexander Universität Erlangen-Nürnberg
Prof. dr. R. M. Tromp	Universiteit Leiden
Prof. dr. ir. L. J. van Vliet	Technische Universiteit Delft
Prof. dr. ir. J. Thijssen	Technische Universiteit Delft

Keywords: Electron microscopy, wave front modulation, electron mirror, aberration correction, electron beam separator.

Printed by: Gildeprint B.V.

Copyright © 2021 by M. A. R. Krielaart

ISBN 978-94-6384-202-0

An electronic version of this dissertation is available at
http://repository.tudelft.nl/.

Contents

Summary ix

Samenvatting xiii

1 Introduction 1
1.1 Introduction . . . 2
1.2 Quantum electron microscopy . . . 2
1.3 Designing a prototype QEM . . . 4
References . . . 4

2 Grating mirror for diffraction of electrons 7
2.1 Introduction . . . 8
2.1.1 Grating parameters . . . 8
2.2 Methods . . . 9
2.3 Results . . . 11
2.4 Discussion . . . 14
References . . . 16

3 Principles of Electron Wave Front Modulation with Two Miniature Electron Mirrors 17
3.1 Introduction . . . 18
3.1.1 Electron wave front shaping . . . 18
3.2 Phase modulation with an electron mirror . . . 19
3.2.1 Electron phase as a function of electric potential . . . 20
3.2.2 Electric field as a function of mirror pattern . . . 27
3.2.3 Phase modulation as a function of pattern pitch and bias voltage . . . 32
3.2.4 Mirror pattern as a function of target phase distribution . . . 33
3.2.5 Chromatic effects as a function of pattern parameters . . . 35
3.3 Amplitude and phase modulation with electron mirrors . . . 35
3.3.1 Virtual phase plate based on two electron mirrors . . . 37
3.4 Numerical methods . . . 39
3.4.1 WKB approximation solver . . . 39
3.4.2 WKB lookup table generator . . . 40
3.4.3 Fresnel propagator . . . 41
3.4.4 Target phase and pattern solver . . . 41
3.4.5 Scalar potential constructor . . . 42
3.5 Application examples for electron mirrors . . . 43
3.5.1 Zernike phase mirror . . . 43
3.5.2 Tuning diffraction efficiency . . . 44
3.5.3 Beam mode conversion . . . 49
3.5.4 Arbitrary phase and amplitude modulation . . . 50
3.6 Discussion and conclusion . . . 52
References . . . 55

4 Design of a miniature double mirror setup for electron wave front shaping 59
4.1 Introduction . . . 60
4.1.1 Electron microscopy with two mirrors . . . 60
4.1.2 Experimental modalities . . . 63
4.2 Optical design . . . 63
4.2.1 Miniature electron mirrors . . . 64
4.2.2 Electron ray trajectory . . . 64
4.2.3 Round trip dispersion . . . 65
4.3 Optical components . . . 67
4.3.1 Miniature electron optics . . . 68
4.3.2 Miniature liner tubes . . . 70
4.3.3 Slit deflector (‘Barn door’) . . . 71
4.3.4 Quadrupole deflector . . . 72
4.4 Mechanical design . . . 72
4.4.1 Dimensional constraints . . . 72
4.4.2 Deflector manufacturing . . . 75
4.4.3 Beam separator . . . 76
4.4.4 Integrated design . . . 77
4.4.5 Layer alignment tolerance . . . 77
4.5 Integration of parts . . . 80
4.5.1 Top and bottom layer . . . 80
4.5.2 Middle layer . . . 81
4.5.3 Combination of layers . . . 82
4.6 Discussion and conclusion . . . 82
References . . . 84

5 Miniature electron beam separator based on three stacked dipoles 87
5.1 Introduction . . . 88
5.2 EBE Electron optics . . . 90
5.2.1 Beam separator . . . 90
5.2.2 Beam separator for two parallel axes . . . 92
5.2.3 Energy filter . . . 92
5.2.4 Higher order effects . . . 93
5.3 Electromechanical design . . . 94
5.3.1 Machining tolerances . . . 95
5.3.2 Electrodes and enclosure . . . 96
5.3.3 Electromechanical integration . . . 97
5.4 Experimental methods . . . 98
5.4.1 Experimental setup . . . 98
5.4.2 Deflection and distortion fields . . . 99
5.4.3 Detection limit and errors . . . 100

5.5 Results and discussion 100
5.5.1 Dipole strength 100
5.5.2 Multipole strength 102
5.5.3 Overview of obtained fields. 105
5.6 Conclusions 105
References. 106

6 Flat electron mirror **109**
6.1 Introduction. 110
6.2 Basic concepts 112
6.3 Numerical methods 113
6.3.1 Computationally updating the EOD input file 114
6.3.2 Aberration coefficients and spot size calculation 115
6.4 Design of the tetrode mirror 118
6.4.1 Coarse parameter sweep 118
6.4.2 Fine parameter sweep 119
6.4.3 Dependence of aberration coefficients on design parameters 121
6.5 Discussion and conclusion 122
References. 123

7 Conclusion **125**

Appendices **129**

A Numerical solutions of the Schrödinger equation **131**
A.1 Introduction. 131
A.2 Solutions for a linear sloped potential 131
A.3 Coupling the linear and modulated potential region 133
A.4 Numerical implementation 134
A.5 Obtaining a solution 135
A.6 Stability and convergence 137
A.7 Linear sloped potential solution for two dimensional wave $\psi(x, y)$ 137
A.8 Phase angle of an electron reflected from a sloped potential with a bump 140
References. 141

B Turning point coordinates through the Lambert-W function **143**
References. 143

C Quantitative effects of miniature liner tubes on field distortions **145**
References. 147

D Spot size as a function of defocus, in the presence of both third and fifth order spherical aberration coefficients. **149**
D.1 Introduction. 149
D.2 Numerical methods 151
D.2.1 Obtaining the FW100 152
D.2.2 Obtaining the Fraction of Current (FC). 152
D.2.3 Defocus leading to minimum FW50 153

D.3 Applications . . . 154
D.3.1 Minimize C_{s3} effects through defocus of C_1 . . . 154
D.3.2 Minimize C_{s5} and C_{s3} effects through defocus of C_1 . . . 154
References . . . 156
Acknowledgements **157**
Curriculum Vitæ **159**
List of Publications **161**

Summary

We propose a microscopy scheme for the controlled modulation of the electron wave front that utilizes patterned electron mirrors. The ability to control the wave front of the electron finds many applications in electron microscopy, for instance in contrast enhancement techniques, beam mode conversion, low-dose imaging techniques such as quantum electron microscopy (QEM) and multi-pass transmission electron microscopy (MP-TEM), or structural hypothesis testing.

Wave front modulation is a technique that enables one to locally alter the wave front of an electron that is spread out in space. We have studied the possibilities of using electron mirrors for that. The electron mirror is an optical element that decelerates and thereafter reflects an incident electron beam, by means of an electrostatic potential that is more negative than that of the field-free energy of the electron. Electron mirrors are most commonly used for aberration correction in electron microscopy.

When a topographic pattern is applied onto the mirror electrode, the nearby electric field in front of the mirror electrode becomes modulated in space, and adheres to the shape of the applied pattern. We studied the effect that a diffraction line grating pattern has on the phase of the reflected wave front. For this, we have developed a numerical method that solves the time independent Schrödinger equation for the modulated potential in front of the mirror. This is a computationally expensive task. The process can be sped up by making use of the WKB approximation method, however the use of this method close to the turning point of the electron in front of the mirror is not valid in general. We have compared the exact numerical solutions to those obtained with the WKB approximation method, and found empirically that a quantitative agreement is obtained when the obtained results of both methods are expressed as a function of the thickness of the (modulated) classical turning point. The obtained results indicate that when a single spatial frequency (or pitch) is used at the mirror pattern, this results in a far field diffraction pattern with the intensities of the various order diffraction spots given by the square of Bessel functions of the same order, as a function of the thickness of the turning point. We refer to a mirror that diffracts the reflected wave front as an 'electron grating mirror'.

The electron mirror fully reflects the incident wave front, and thus no absorption processes can take place. For this reason, the mirror can only be used to modulate the phase, and not the amplitude, during the reflection near the mirror electrode. The resulting phase modulation can be expressed as an amplitude contrast when the reflected wave front is defocused on a plane conjugate to the plane of reflection. We suggest that a second electron mirror can be placed here, that can be used to modulate again the phase of the incident wave front that is already amplitude modulated now. Alternative to that, the second mirror can also be placed in the Fourier plane of the first mirror. That way, the second mirror can be used to modulate the phase of the diffraction spots that are formed due to the phase modulation at mirror 1. In both cases, the use of two electron mirrors can in principle provide full control

over the wave front of the electron.

The proposed scheme avoids any interaction between the electron beam and optical elements. Therefore, we expect to avoid the typical disadvantages such as built up of charge at phase plates, and reduced life time and transmissivity, that are usually associated to conventional transmission based methods for wave front shaping that relies on phase plates or amplitude masks. For this reason, we coin the term *virtual phase plate* for the technique that we introduce here.

To study the feasibility of the technique, we have constructed numerical methods that enable to relate the effect that an arbitrary mirror topography has on the phase of the reflected wave front. For the inverse problem, we have constructed a numerical model that provides the pattern topography that is required to obtain a target wave front distribution. For this, we make use of the WKB approximation method and apply it either on each spatial frequency that is part of the mirror topography, or the targeted phase distribution after reflection. We recognize that in general it is not allowed to linearly add the resulting pattern height components, but we reason that for small phase modulation amplitudes, below $\pi/6$ radian per spatial frequency, linear addition only results in small ($\leq 1\%$) errors in the reconstructed phase. This result may be referenced to as the electron mirror analog of the weak phase approximation that is used in transmission techniques. We have applied the reconstruction model to several optical problems, and demonstrated that the use of two electron mirrors can for instance realize beam mode conversion of plane waves into vortex beams that carry orbital angular momentum, or for instance to sculpt a wave front that shows resemblance to the institute logo of the Delft University of Technology.

We further analyzed the deteriorating effects of mechanical tolerances on the reflected beam. The effect of a tilt error between the mirror electrode and the optical axis is found to be small and results in a beam deflection angle of $\leq 10\%$ of the tilt error. Modern manufacturing techniques allow for tilt errors below 1 mrad, and thus we do not expect problems with that. We are more concerned about the possible curvature of the mirror electrode that exceeds the spread of the beam as a result of mechanical stress. For instance, astigmatism may form when the mirror electrode contains a non-flatness of order single digit nanometers or less in height, that spans across the beam width.

A practical design for a prototype setup must not only contain the two electron mirrors, but in addition to that also the necessary lenses to focus the beam. The combination of a mirror electrode with a three aperture lens is commonly referred to as a tetrode mirror, and we use this as a basis for the two mirror elements. Such a setup is however usually characterized by high values of spherical and chromatic aberrations, that deteriorate the resolution that can be obtained with a microscope. We have analyzed how the shape of the tetrode mirror can help to reduce these aberration coefficients, by means of electron ray trace calculations. From these calculations, we found that it is important to choose the spacing between the mirror electrode and the field limiting aperture that is positioned above the mirror electrode to be small, with respect to the radius of this aperture. This way, the third order coefficient of spherical aberration can be made negative, and the resulting tetrode

mirror becomes limited only by the fifth order coefficient of spherical aberration, allowing for a broader beam spread in front of the mirror.

We suggest to position the two tetrode mirrors on a common optical axis, such that the mirror electrodes terminate both sides of this axis. This axis can run in parallel to that of an existing microscope system in which the mirror system becomes integrated. A series of deflectors can then be used to first deflect the beam away from the microscope axis towards the mirror axis, and subsequently to coordinate the electron trajectory in between the mirrors and back towards the point of origin at the microscope axis. The electron beam is thus effectively removed from the optical axis, and reinserted at the same position after a double mirror reflection. This requires a deflection in front of both mirrors that is dependent on the direction of incidence of the beam, which may be realized by making use of crossed electric and magnetic fields, that are in turn oriented perpendicular to the optical axis of the mirror system. This is commonly referred to as the Wien configuration, and the optical element associated to this configuration is generically referred to as a Wien filter.

By keeping the deflection angles between the two axes small, to within 100 mrad, it can be shown that the deteriorating effects of beam deflection dispersion can be kept small. For this reason, we suggest to make use of miniature optics that can be fabricated by means of lithographic techniques. However, conventional Wien filters are rather large devices. In addition, they usually do not accommodate for two axes that are in close proximity to each other. For these reasons, we have developed a new type of Wien filter, that we refer to as EBE beam separator. The acronym EBE refers to the separation of the perpendicular electric (E) and magnetic (B) fields inside the device, which is in contrast to most Wien filters, in which these fields are found to overlap. By separating the fields, we can create an electrostatic deflection field in the top and bottom layers of the device that is oriented in opposite direction on both axes and points towards each other, and a common magnetic field at the middle layer that is oriented perpendicular to the electric fields.

We have built and experimentally tested an EBE beam separator that has two optical axes that are separated by only one millimeter. In the characterization experiment, we propagate the beam of a scanning electron microscope (SEM) through the EBE beam separator, and focus the beam onto the unpolished side of a silicon wafer. At steps of increasing deflection field strength, we record micrographs of the silicon wafer. Displacements between consecutive micrographs as a result of the beam deflection are obtained numerically through Speeded-Up Robust Features (SURF) image registration. From the obtained displacement maps, we extracted the deflection (dipole) and higher order quadrupole and hexapole field coefficients of the EBE separator. From this, we obtained an electric dipole strength of 1.98 mrad/V and a magnetic strength of 0.275 mrad/mA, valid at a 2 keV beam energy. The higher order distortion fields currently limit the resolution at the image plane that is in between the two tetrode mirrors to approximately 500 nm due to astigmatism, and 150 nm due to the hexapole distortion. We expect that more accurate machining of the electrode poles can help to eliminate at least the astigmatism, as this distortion most likely originates from the non-parallelism of the electrode plates.

We are currently integrating two patterned tetrode electron mirrors, combined with the EBE beam separator and additional required deflection optics into the specimen chamber of a scanning electron microscope. Initial progress has been made on deflection and reflection of the beam towards and at the first electron mirror. We have however not yet managed to obtain a double reflection with the beam. This will be our first next attempt. After that, the feasibility of using patterned mirrors for arbitrary wave front modulation may initially be demonstrated by imaging the diffraction pattern of the wave front reflected from the grating mirror onto a scintillator detection screen. When two electron grating mirrors are used for this, the experiment may serve as an experimental demonstration of Mach-Zehnder interferometry with electrons. At a more advanced stage, the deflector at the microscope axis may be replaced with a temporally controlled fast deflector, as this may allow to trap the electron in a loop and reflect the electron multiple times at each mirror before reaching the detector screen. That way, the setup that we propose here can also be used as a proof of concept for QEM and MP-TEM.

Samenvatting

Wij stellen een microscopietechniek ter wille van elektron golffrontmodulatie voor, welke gebruik maakt van elektronenspiegels. De mogelijkheid om het golffront van een elektron te kunnen controleren kent vele toepassingen in de elektronenmicroscopie, zoals bijvoorbeeld voor contrastverbetering, bundel coördinaattransformatie, microscopie met lage stralingsdosis zoals kwantum elektronen microscopie en meervoudige transmissie elektron microscopie, of voor het testen van een structuurhypothese van het preparaat.

Golffrontmodulatie is een techniek die de gebruiker in staat stelt om lokale wijzigingen aan het golffront van een over de ruimte uitgespreid elektron aan te brengen. We hebben gekeken naar de mogelijkheid om dit met behulp van elektronenspiegels uit te voeren. De elektronenspiegel is een optisch element welke een inkomend elektron vertraagd alvorens het in zijn geheel te reflecteren, en maakt hiervoor gebruik van een elektrostatisch potentiaal dat negatiever is dan dat van de veld-vrije energie van het elektron. Elektronenspiegels vinden tegenwoordig al veelal een toepassing in aberratiecorrectie voor elektronenmicroscopen.

Wanneer een elektronenspiegel topografisch van een patroon wordt voorzien, dan zal het nabije elektrische veld een soortgelijke vorm aannemen. Wij hebben bestudeerd wat het effect van een lijndiffractiepatroon op de fase van het gereflecteerde golffront is. Hiertoe hebben wij een numerieke methode ontwikkeld, welke de Schrödinger vergelijking voor het gemoduleerde elektrisch veld in de nabijheid van de spiegel oplost. Dit is numeriek een kostbare taak. Het proces kan versneld worden door gebruik te maken van de WKB benaderingsmethode, alhoewel het gebruik hiervan juist in de nabijheid van het spiegelvlak niet in het algemeen toegestaan is. Wij hebben de exacte numerieke oplossing en oplossingen verkregen via de WKB benaderingsmethode met elkaar vergeleken, en empirisch bevonden dat een kwantitatieve overeenkomst tussen de uitkomsten verkregen wordt, indien de resultaten worden uitgedrukt als functie van de dikte van het gemoduleerde spiegelvlak. Uit de verkregen resultaten kan worden afgeleid dat bij gebruik van een enkele spatiele frequentie (of herhaalafstand) in het spiegelpatroon, dat dit resulteert in een diffractiepatroon in het optische verre veld. De intensiteit van de verscheidene diffractiepunten is dan gegeven door Besselfuncties van de orde gelijk aan die van het diffractiepunt, als functie van de dikte van het spiegelvlak. Wij verwijzen vanaf nu naar een spiegel welke een dergelijke karakteristiek vertoond als een 'diffractiespiegel voor elektronen'.

Aangezien een elektronenspiegel de inkomende bundel in zijn geheel reflecteert, vinden er geen absorptieprocessen plaats bij de elektrode. Om deze reden kan een elektronenspiegel alleen gebruikt worden om de fase, en dus niet de amplitude, van het golffront te beïnvloeden in de directe nabijheid van de spiegel. Deze nabije fasemodulatie kan echter tot amplitudemodulatie ter expressie worden gebracht, wanneer deze gedefocusseerd word afgebeeld op een optisch vlak dat geconjugeerd is aan dat van de spiegel. Wij suggereren om in dit geconjugeerde vlak een tweede spiegel te plaatsen, waar nogmaals fasemodulatie op het invallende golffront toegepast kan

worden. Als alternatief op deze methode zou het ook mogelijk zijn om de tweede spiegel in een Fouriervlak van de eerste spiegel te plaatsen. Beide methodes zouden bij een combinatie van twee spiegels de mogelijkheid kunnen bieden tot volledige controle over de amplitude en fase van het elektronengolffront.

De door ons voorgestelde techniek voorkomt enige vorm van interactie tussen de elektronenbundel en de optische elementen. Om deze reden verwachten wij geen gevoeligheid te ondervinden voor typische nadelen als ladingsopbouw, verminderde levensduur, en verminderde doorlaatbaarheid welke normaal gesproken geassocieerd worden met tegenhangende technieken uit in transmissie elektronen microscopie. Om deze reden spreken wij in referentie naar onze techniek ook wel over een 'virtuele faseplaat' voor elektronen.

Om de haalbaarheid van de techniek te onderzoeken, hebben wij numerieke modellen opgesteld waarmee we het verband tussen een willekeurig gekozen spiegelpatroon en de resulterende fase in het golffront kunnen bepalen. Ook voor het omgekeerde probleem, waarin een spiegelpatroon moet worden gevonden welke een gewenste fasemodulatie ten gevolge heeft, hebben wij een model opgesteld. Hiertoe maken wij gebruik van de WKB benaderingsmethode en passen dit toe op iedere spatiele frequentie van dan wel het spiegelpatroon, of anders de gewenste fasemodulatie. Wij erkennen dat het in het algemeen niet toegestaan is om de op deze wijze verkregen patrooncomponenten lineair bij elkaar op te tellen, maar maken aannemelijk dat dit voor fasemodulaties kleiner dan $\pi/6$ radialen slechts leid tot beperkte fouten ($< 1\%$) in de gereconstrueerde fase. Dit resultaat kan vergeleken worden met dat wat bekend is als de zwakke fasebenadering voor transmissietechnieken. Wij hebben onze reconstructietechniek toegepast op verscheidene optische vraagstukken, en hiermee laten zien dat het gebruik van twee elektronenspiegels bijvoorbeeld het omzetten van vlakke golven in spiraalvormige golven kan realiseren, alsook het omzetten van een vlakke golf in een golffront dat gelijkenis vertoond met het beeldmerk van de Technische Universiteit Delft.

Wij hebben ook gekeken naar de effecten van mechanische toleranties op de gereflecteerde bundel. Het effect van een hoekfout tussen de spiegelelektrode en de optische as is klein bevonden, namelijk met een afbuighoek voor de bundel welke $\leq 10\%$ is aan de mechanische hoekfout. Moderne fabricagemethoden leveren een hoekfout van minder dan 1 mrad, en hier verwachten wij dan ook geen problemen. Wij zijn meer bezorgt over de mogelijk kromming van de spiegelelektrode over een afstand welke groter is dan de spreiding van de elektronenbundel. Dit kan veroorzaakt worden door mechanische spanning in de spiegelelektrode en kan astigmatisme ten gevolge hebben, wanneer de niet-vlakheid over de breedte van de bundel in de orde van (sub)nanometers schaalt.

Een praktisch ontwerp voor een prototype opstelling omhelst meer dan alleen de plaatsing van twee elektronenspiegels, en vereist ook de plaatsing van onder andere elektronenlenzen om de bundel te focusseren. De combinatie van een spiegelelektrode met een lens bestaande uit drie elektrodes met daarin op elkaar uitgelijnde openingen staat ook wel bekend als een tetrodespiegel. Wij gebruiken deze gangbare opbouw als basis voor onze twee spiegelelementen. Een dergelijke samenstelling is echter doorgaans gekenmerkt door hoge waardes van sferische en chromatisch aber-

raties, welke de resolutie van de techniek sterk kunnen benadelen. Wij hebben geanalyseerd hoe de vorm van de lens elektrodes kan helpen om de aberraties te beperken, door middel van elektronenstraalsimulaties. Uit deze berekeningen is gebleken dat het met name van belang is om de afstand tussen de spiegelelektrode en de eerste bovenliggende electrode klein te houden, ten opzichte van de straal van de opening in deze elektrode. Op deze manier kan de derde orde sferische lensfout negatief gemaakt worden, waardoor de haalbare resolutie van de tetrodespiegel slechts beperkt wordt door de vijfde orde sferische fout, wat een verdere uitspreiding van het golffront op het spiegelvlak mogelijk maakt.

We stellen voor om de twee tetrodespiegels op een gemeenschappelijke optische as te plaatsen, zodanig dat de beide spiegels elk een kant van de as afsluiten. Deze spiegel as kan parallel aan de optische as van een bestaand microscoopsysteem geplaatst worden. Er is dan een aantal deflecterende elementen nodig, welke opeenvolgend de bundel afbuigen van de microscoop as richting de spiegel as, en vervolgens ook de stralengang tussen de spiegels en terug naar de microscoop as coördineren. Effectief gezien wordt de elektronenbundel op deze manier tijdelijk van de microscoop as afgehaald, om na een dubbele reflectie weer op hetzelfde punt terug te keren. Dit vereist een afbuiging van de bundel vlak voor de spiegels, welke afhankelijk is van de invalsrichting. Een manier om dit mogelijk te maken is door de combinatie van gekruiste elektrische en magnetische velden, welke op hun beurt weer loodrecht op de spiegel as zijn georiënteerd. Dit wordt ook wel een Wien configuratie genoemd, en wordt toegepast in zogenaamde Wien filters.

Door de afbuighoeken klein te houden, namelijk binnen 100 mrad, kunnen effecten als afbuigdispersie welke een nadelig effect op de bundel hebben binnen de perken gehouden worden. Om deze reden stellen we voor om gebruik te maken van miniatuuroptiek, welke door middel van moderne lithografische processen gefabriceerd kunnen worden. Conventionele Wien filters zijn echter behoorlijk omvangrijk. Daarnaast bevatten ze doorgaans niet de ruimte om twee assen vlak naast elkaar te omvatten. Om deze redenen hebben wij een nieuwe type Wien filter ontwikkeld, naar welke wij refereren als een EBE bundelscheider. Het acroniem EBE verwijst hier naar de ruimtelijke scheiding van de loodrecht op elkaar georiënteerde elektrische (E) en magnetische (B) velden in de bundelscheider, wat afwijkt van de gangbare configuratie in Wien filters waarin deze velden met elkaar overlappen. Door de velden ruimtelijk van elkaar te scheiden, kunnen we in de boven- en onderlaag van de EBE bundelscheider op beide assen een elektrisch veld aanleggen, welke naar elkaar toe wijst, en op de middelste laag een gedeeld magnetisch veld aanleggen.

We hebben een EBE bundelscheider gebouwd en getest, waarin de twee parallelle assen slecht een millimeter uit elkaar liggen. Tijdens het karakteriseren propageren we een bundel uit de rasterscan elektronenmicroscoop door de EBE bundelscheider, en focusseren deze bundel op de ongepolijste zijde van een silicium substraat. Terwijl de afbuigvelden stapsgewijs worden verhoogd, worden tussentijds afbeeldingen van het substraat opgeslagen. De verplaatsing tussen twee opeenvolgende afbeeldingen wordt vervolgens numeriek bepaald met behulp van een beeldregistratietechnieken. Uit de hiertoe verkregen data kunnen we de afbuigsterkte (tweepolig) en hogere orde vierpolige en zespolige stoorvelden afleiden. We hebben een elektrische afbuig-

sterkte van 1.98 mrad/V, en een magnetische afbuigsterkte van 0.275 mrad/mA gevonden, geldig voor een bundelenergie van 2 keV. Door de aanwezigheid van hogere orde storingsvelden is de huidige resolutie op het afbeeldingsvlak tussen de twee tetrodespiegels in momenteel beperkt tot 500 nm vanwege astigmatisme, en 150 nm vanwege de zespolige verstoring. Wij verwachten echter dat met name de beperking vanwege de astigmatisme verminderd kan worden door een meer zorgvuldiger fabricageproces van de polen, aangezien een hoekfout tussen twee polen direct leid tot astigmatisme.

Momenteel zijn we in de fase aanbeland waarin twee tetrodespiegels, voorzien van een patroon, gecombineerd met een EBE bundelscheider en de overige vereiste afbuigelementen worden samengebracht in een experimentele testopstelling, welke in de preparaatkamer van een rasterscan elektronenmicroscoop past. We hebben het echter nog niet voor elkaar gekregen om een dubbele reflectie te bewerkstelligen. Dat zou nu het eerst volgende doel moeten zijn. Daarna zou de haalbaarheid van het gebruik van spiegelpatronen voor gecontroleerde fasemodulatie aangetoond kunnen worden, door het diffractiepatroon van een gereflecteerde bundel af te beelden op een scintillatiescherm. Wanneer twee diffractiespiegels voor elektronen worden toegepast, zou dit kunnen dienen als een experimentele demonstratie van Mach-Zehnder interferentie voor elektronen. In een later stadium van ontwikkeling zou het afbuigelement welke op de microscoop as staat vervangen kunnen worden door een variant welke snel in de tijd geschakeld kan worden, zodanig dat een elektron tussen de twee spiegels opgesloten kan worden en er meerdere reflecties per spiegel plaats kunnen vinden, alvorens het elektron op het scintillatiescherm bekeken gaat worden. Met een dergelijke aanpak, kan de door ons beschreven opstelling ook gebruikt worden als demonstratiemodel voor bijvoorbeeld QEM en MP-TEM.

1

Introduction

1.1. Introduction

When the electron wave front is spread out in space due to the uncertainty principle, local variations in its phase may occur when the electron wave front is send through an object. This suggests that a single electron may contain a lot of information about an object that it interacted with. However, when this principle is applied in practice, what is done routinely nowadays in transmission electron microscopy, the information that the electron has about the object becomes visible as only a single point on the detector, due to the wave function collapse. For this reason, many electrons must be send through the object under investigation (the 'sample', or 'specimen') before a sufficient contrast that reveals the nature of the specimen at the detector is obtained.

The use of high energy electrons in all forms of transmission based electron microscopy is well known to cause radiation damage to the specimen under inspection, in the form of knock-on displacement damage, or ionization damage [1]. Because of that, the resulting detector image may very well not be representative of the unaffected specimen that was inserted into the microscope, and the attainable resolution is said to have become electron dose-limited. A naïve solution to this limitation would be to reduce the electron dose, but this is at the expanse of the signal to noise ratio or measurement error and thus the information that can be extracted from the formed micrograph.

Another way to improve the measurement error is realized by making use of correlated probe particles. The measurement error can then be improved from $1/\sqrt{N}$ (shot-noise, for uncorrelated probe particles) to $1/N$ (Heisenberg limit, for correlated probe particles), with N the number of probe-specimen interactions [2]. However, such correlated states are difficult to obtain in electron microscopy, and instead it is suggested to make use of a single probe particle that interacts with the specimen multiple times [3].

1.2. Quantum electron microscopy

Ideally, one should avoid exposure of the specimen by the electron beam and still obtain information about the specimen. While this may sound contradictory, this may very well be possible by making use of the quantum nature of matter. In 1993, Elitzur and Vaidman suggested that the absence or presence of a specimen could be detected, without directly interacting with it, by positioning the object in one of the arms of a Mach-Zehnder interferometer [4], such as shown in [Fig. 1.1]. The interferometer could be aligned such that detection of the probing particle in the dark field detector (D2) would only result in the presence of the specimen inside the interferometer, while detection of the particle in the bright field detector (D1) would yield an inconclusive outcome about the presence or absence of the specimen. The detection of the specimen in the absence of interaction of the specimen with the probe particle is referred to as an interaction-free measurement. It can be shown that up to 25% of the cases in which the object was present in the interferometer leads to a dark field detection event and thus not the absorption, or interaction, of the probe particle with the specimen.

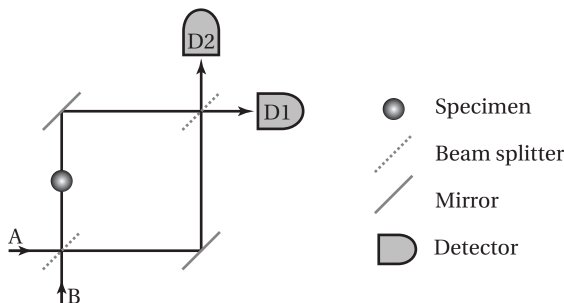

Figure 1.1: Mach-Zehnder interferometer with a specimen in one of the beam paths. The detection of the specimen is performed interaction-free when the probing particle enters the interferometer at port A, and is detected by detector D2. The probability of interaction-free detections can be brought arbitrarily close to 1 by circulating the interferometer output channels in front of the detectors back to ports A and B multiple times, before performing the detection.

The percentage of interaction-free detections can in principle be increased up to 100%, when the output at the ports of the interferometer in front of the detectors are circulated back to the input ports [5]. The presence of the object in the interferometer then prohibits the coherent built-up of signal in the respective arm of the interferometer, that would have otherwise occurred in the absence of the object. For this to work, it is required that the beam splitting ratio is adjusted such that after the chosen number of circulations the full intensity of the probe particle exits the interferometer towards detector D1 in the absence of a specimen.

The first design for an interaction-free measurement method that uses electrons was proposed in 2009, and relies on the transition of probability amplitude in a two-level quantum system that consists of a double well potential [6]. It was suggested that a practical realization of the required double well potential could be realized by bending a linear Paul trap into a circle, therewith confining the single electron to a circular trajectory that intersects with the specimen plane.

Interaction-free measurement schemes for electrons are nowadays referred to as quantum electron microscopy (QEM). More recent work has identified the developments that are still required to realize a practical implementation of the imaging scheme into a microscope [7]. These developments include a coherent beam splitter and combiner for electrons, that serve the role of the adjustable beam splitters in the Mach-Zehnder interferometer from [Fig. 1.1], an electron resonator that enables the repeated imaging of the specimen with a single electron, and a temporally gated 'barn door' that regulates the entry and exit of the electron into and from this resonator.

Close to the development of QEM stands the development of multi-pass transmission electron microscopy (MP-TEM). Here, instead of splitting the electron wave front, the electron wave is spread out over the sample plane and this spread out wave is repeatedly transmitted through the sample in order to increase the phase contrast at the resulting micrograph [3] at lower dose compared to obtaining an equal num-

ber of direct images with multiple electrons. In contrast to QEM, the realization of MP-TEM is not depending on the development of a coherent beam splitter for electrons, but does share the need for an electron resonator and barn door device.

1.3. Designing a prototype QEM

Only in the very recent past practical prototype designs that implement QEM [8] and MP-TEM [9] imaging schemes into existing electron microscopes have been reported, with parts of that progress based on work that is presented in this thesis. In this thesis, the ground work for using electron mirrors as adjustable coherent beam splitters is presented in chapter 2. For this to work, it is required to pattern the mirror electrode with a grating structure and apply an electric potential that is more negative than the energy of the incident electron.

Later, we realized that the use of not one but instead two electron mirrors could enable a more general approach to electron wave front shaping. In chapter 3 we lay out the theoretical and numerical framework for a double mirror setup that could enable amplitude and phase shaping of the electron wave front, and a practical design for what we now refer to as a *virtual phase plate* for electron beams is presented in chapter 4. The setup enables one in principle to demonstrate QEM, MP-TEM, as well as arbitrary amplitude and phase shaping of the electron wave front in general, all in one setup. A prototype for this setup is designed such that it can be tested inside the specimen chamber of a scanning electron microscope.

From the experimental design it will become apparent that additional electron optics components must be developed to realize the electron trajectories in the prototype setup. A miniature electron beam separator is designed and tested and the results of this work are presented in chapter 5. In addition to this development, we found that the application of electron mirrors is severely limited by optical aberrations that form during mirror reflections. A numerical study is presented in chapter 6 that treats this problem, and a geometrical design for a flat electron mirror with only small aberrations that results from this study is presented.

References

[1] R. Egerton, *Radiation damage to organic and inorganic specimens in the TEM,* Micron **119**, 72 (2019).

[2] V. Giovannetti, S. Lloyd, and L. Maccone, *Advances in quantum metrology,* Nature Photonics **5**, 222 (2011).

[3] T. Juffmann, S. A. Koppell, B. B. Klopfer, C. Ophus, R. M. Glaeser, and M. A. Kasevich, *Multi-pass transmission electron microscopy,* Scientific Reports **7** (2017), 10.1038/s41598-017-01841-x.

[4] A. C. Elitzur and L. Vaidman, *Quantum mechanical interaction-free measurements,* Foundations of Physics **23**, 987 (1993).

[5] P. Kwiat, H. Weinfurter, T. Herzog, A. Zeilinger, and M. A. Kasevich, *Interaction-free measurement,* Physical Review Letters **74**, 4763 (1995).

[6] W. P. Putnam and M. F. Yanik, *Noninvasive electron microscopy with interaction-free quantum measurements,* Physical Review A **80** (2009), 10.1103/physreva.80.040902.

[7] P. Kruit, R. Hobbs, C.-S. Kim, Y. Yang, V. Manfrinato, J. Hammer, S. Thomas,

P. Weber, B. Klopfer, C. Kohstall, T. Juffmann, M. Kasevich, P. Hommelhoff, and K. Berggren, *Designs for a quantum electron microscope,* Ultramicroscopy **164**, 31 (2016).

[8] M. Turchetti, C.-S. Kim, R. Hobbs, Y. Yang, P. Kruit, and K. K. Berggren, *Design and simulation of a linear electron cavity for quantum electron microscopy,* Ultramicroscopy **199**, 50 (2019).

[9] S. A. Koppell, M. Mankos, A. J. Bowman, Y. Israel, T. Juffmann, B. B. Klopfer, and M. A. Kasevich, *Design for a 10 keV multi-pass transmission electron microscope,* Ultramicroscopy **207**, 112834 (2019).

2

Grating mirror for diffraction of electrons

Abstract.

The ability to imprint a phase pattern onto a coherent electron wave would find many applications in electron optics, in analogy to what is already possible with photons in light optics. Spatially dependent phase manipulation is achieved in transmission electron microscopy by passing the beam through a phase plate. However, in transmission mode this technique suffers from crystal imperfections and electron-matter interaction. If instead the electron wave is reflected of a spatially modulated potential, these difficulties can be circumvented.

To demonstrate this principle, we consider here a periodic topological mirror structure that results in a sinusoidal plane of reflection for the incident electron. The reflection of the electron then takes place just above the physical mirror surface. Such 'electron grating mirror' is expected to diffract the incident wave upon reflection by the introduced path length difference. The mirror can then be used as an electron beam splitter and coupler, analogous to semi-transparent mirrors used in light optics. This enables for instance a loss-less Mach-Zehnder interferometer for electrons.

A numerical model that solves the Schrödinger equation for this system is obtained to enable a quantitative description of the grating mirror. The results show that the obtained diffraction order intensities behave like squared Bessel function of their respective order, and thus for instance the results show how an increase in grating pitch reduces the sensitivity to energy spread in the incident electron beam. Additionally, we show how the use of the WKB approximation enables faster calculations in the case of general patterns.

This chapter has been published as M. A. R. Krielaart, and P. Kruit, *Grating mirror for diffraction of electrons*, Physical Review A **98** (2018), 10.1103/physreva.98.063806.

2.1. Introduction

Quantum electron microscopy (QEM) aims at the interaction free imaging of beam sensitive materials [1]. To realize this technique, new electron optical devices are required. One of these new devices is a grating mirror for electrons. The physics of an electron grating mirror is not described before and we will introduce it here. We show how a grating mirror can be used to reflect an incident coherent electron beam and subsequently re-arrange the amplitude of the several created sub-beams.

The grating mirror consists of a topological pattern of rectangular bars that is kept at a potential just above the beam energy, thus effectively creating a periodically modulated mirror potential in space. Alternatively, a grating mirror can be realized by a pattern of lines kept at varying voltage levels but this is not treated here. In QEM, a grating mirror fulfills the role of coherent beam splitter and coupler: it enables the transfer of the beam intensity from a reference beam into a sample beam and vice versa, analogous to an optical beam splitter found in interference experiments.

2.1.1. Grating parameters

The geometry of the grating mirror [Fig. 2.1(a, b)] is described by a pattern pitch (p) and amplitude (δ). To obtain an order of magnitude estimate for these parameters, we draw an analogy with a multiple slit experiment. Here, the angles of the k-vectors with the optical axis are related via the pitch and wave length (λ) by approximately $\theta \approx \lambda/p$. The resulting diffraction pattern can then be imaged onto a screen via a (system of) lens(es). The diffraction spot separation is then approximately given by $d_{\text{spot}} \approx \theta f$, where f is the focal length of the lens system.

For initial experiments, we will use low beam energies ($1-4$ keV) and MEMS fabricated lenses. Plugging in these energies and the small ($10-30$ mm) focal lengths of the lenses, typical values for pitch are in the range of $p = 100-500$ nm. This should then result in spot separations on our detector screen in the order of micrometers. When the pattern amplitude δ is then in the same order of magnitude as the pitch, the resulting equipotentials that form above the physical mirror structure exhibit the required sinusoidal shape. Grating mirrors with pitch and amplitude in the range mentioned can be fabricated from a flat silicon waver using lithography processes. An electrostatic potential is applied to the pattern and the resulting field is confined in space by a (grounded) field-limiting aperture, placed at a distance d above the pattern.

For $\{p, \delta\} \ll d$, the electric field in the confined region can be approximated analytical by solving the Laplace equation. To do so, we describe the potential applied to the pattern on a straight line by

$$U(0, y) = U_p \left[1 + \frac{\delta}{d}\cos\left(\frac{2\pi}{p}y\right)\right]. \tag{2.1}$$

Here, U_p is the pattern bias potential (a constant) and the second term modulates the potential to mimic the presence of the pattern. By using separation of variables, the potential inside the confined region can then be shown to satisfy

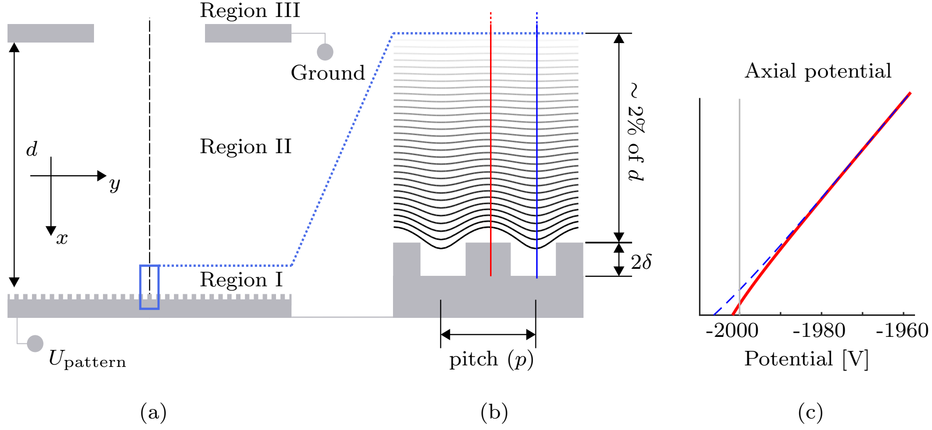

Figure 2.1: (a) Parameters describing the grating mirror and coordinate system. (b) Details of region I, defining the pitch and amplitude of the pattern. Equipotential lines are shown schematically. (c) Axial and side potential corresponding to the details of region I.

$$U(x, y) = U_p \left[1 + d^{-1} \left(\delta \sin(k_p y) \exp(k_p x) - x\right)\right]. \tag{2.2}$$

This result is valid for $x < 0, \forall y$. The wave number k_p is directly related to the pitch of the pattern, $k_p = 2\pi/p$. From [Eq. 2.2] it is observed that the modulation of the potential attenuates exponentially fast away from the mirror surface (region I in [Fig. 2.1]). For a distance $\sim 5/k_p \ll d$ above the pattern (region II) the equipotential surfaces are virtually flat again.

An electron incident to the mirror decelerates first on the linear potential ramp inside region II. By spreading out the electron beam over the pattern, path length differences occur within the electron wave as it is being reflected inside region I. It is expected that this leads to a modulation of the phase of the wave function of the electron with corresponding diffraction effects in the far field. As the mirror is an amplitude splitter, consecutive illumination is expected to result in a coherent build-up of phase modulation, leading to increased probability amplitudes in the diffracted beams.

In this paper, we describe quantitatively how the pattern parameters (pitch, amplitude, applied potential and field strength) dictate the physics of the electron grating mirror.

2.2. Methods

Approximation methods, such as WKB [2] or convolution methods [3], allow for first order estimation of the pattern effects. When applied along one spatial dimension parallel to the optical axis of the system (see [Fig. 2.2(a)]), the WKB method yields an integral over the selected electron trajectory that calculates the accumulated

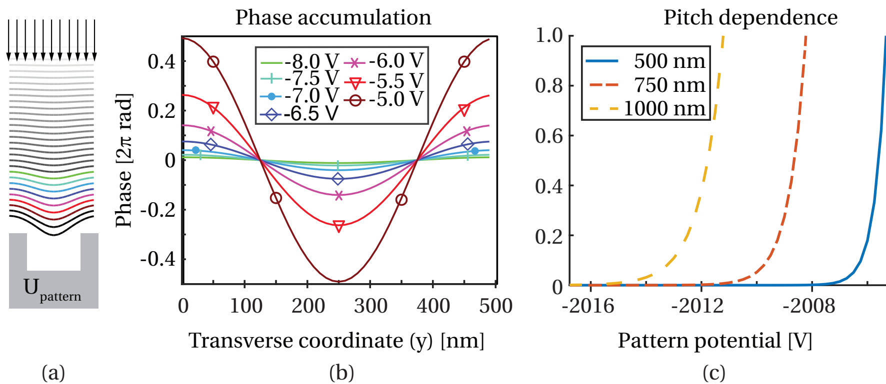

Figure 2.2: (a) WKB approximation with integral paths parallel to the optical axis of the system. The arrows indicate (schematically) the starting point for the integration. (b) Obtained phase accumulation as a function of pattern potential (legend items with respect to −2000 V beam energy) and transverse coordinate. The offset is subtracted such that only the modulated part of the phase is shown. (c) The effect of grating pitch on the relative phase accumulation.

phase of an electron with given momentum $p(x) = \sqrt{2m_e K}$ and K the kinetic energy of the electron, related by,

$$\phi(x, y) = \hbar^{-1} \int p(x, y) \mathrm{d}x. \tag{2.3}$$

Here, the transverse coordinate y is treated as a parameter, that allows to select different paths parallel to the optical axis. The phase modulation in the presence of the grating mirror can now be calculated by integration along various parallel paths starting and ending at the interface of regions I and II. This reveals an increase in phase modulation as the spread out electron reflects closer to the physical grating structure [Fig. 2.2(b, c)] as may physically be expected.

When the incident electron is described as a plane wave, $\psi_{\text{in}} = a \exp(ik_{\text{in}} x_0)$, where k_{in} is the appropriate wave number, then the obtained spatial phase modulation $\phi(x, y)$ from [Eq. 2.3] enables us to write the reflected wave at the interface of Regions I and II (x_0) as $\psi_{\text{out}} = a \exp(i\phi(x_0, y))$. A Fourier transform of the reflected wave with imprinted phase pattern $\phi(x, y)$ then yields the spectrum of all k-vectors and their intensities.

However, the WKB approximation is generally not valid in the vicinity of the classical turning point of the electron just in front of the pattern [2]. This follows from the WKB *ansatz*, resulting in an inverse proportionality of the amplitude of the wave function and momentum p. Since the momentum $p(x, y) \to 0$ at the turning point, the wave function diverges here. It is just at this location, where the influence of the mirror pattern is dominant. Because of this, we do not trust *a priori* results obtained by using the WKB method. For this reason, we also calculate the effect of the mirror potential by numerically solving the Schrödinger equation inside region I,

by coupling it to known analytical solutions of region II. Details of this more time consuming calculation are included in [App. A]. Afterward, we compare the results of the WKB and numerical method in order to validate the use of the WKB method.

2.3. Results

In the full numerical solution of the Schrödinger equation, we describe the interface between region I and region II of respectively unknown and known solution by the wave function $\psi_b(x_b, y)$ as

$$\begin{aligned}\psi_b(x_b, y) &= \sum_n A_n \mathrm{Ai}^-(u_n(x_b)) \exp(ik_{y,n}y) \\ &+ \sum_n B_n \mathrm{Ai}^+(u_n(x_b)) \exp(ik_{y,n}y). \end{aligned} \tag{2.4}$$

Here, the coefficients A_n represent probability amplitudes of incident waves with wave vector $\vec{k}$ determined by the angle with respect to the optical axis. Coefficients B_n are obtained from the calculation and yield directly the probability amplitudes of the respective k-vectors of reflected waves.

When we consider an incident plane wave that travels parallel to the optical axis, all coefficients $A_n = 0$ are set to zero, except for $A_0 = 1$. In the following, a field free electron energy of $\mathcal{E} = 2$ keV is assumed. This requires a pattern potential of $U_p \leq -2$ kV. When we assume a field strength of 10 kV/mm, the field limiting aperture is positioned at a distance $d = 200$ μm above the grating mirror.

The effect of a 500 nm pitch grating pattern is studied for various pattern potentials in order to show the effect of field modulation on the reflected electron. The intensities $I_n = \mathrm{conj}(B_n) \times B_n$ of the most dominant diffraction orders ($n = 0, \pm 1, \pm 2$) are plotted as a function of the pattern potential [Fig. 2.3(a)]. From this, it is observed that a maximum intensity of 34% is obtained in the first order diffracted beam. This compares to transmission studies of diffractive gratings [4] and motivates the term 'electron grating mirror' for the studied device.

To study the effect of a tilt angle between the incident beam and the normal of the mirror surface, two options are considered. First, we set all but one of the A_n coefficients to zero. This simulates the effect entering the mirror field at exactly one allowed angle. The results of this simulation (not shown) indicate no sensitivity to angle of incidence but rather shift the entire spectrum of coefficients B_n such that it is centered around the selected incidence coefficient A_n. Next, the effect of a tilt angle between the incident beam and the normal of the mirror that is smaller than the first order angle is studied. This is possible by adding multiple pitches to the numerical domain. Again, it is found that the resulting spectrum of B_n is centered around the incidence coefficient.

The diffractive properties of the mirror invite to treat the system in a way similar to a diffractive crystal. One then studies the intensity of the various orders of diffraction as function of the crystal thickness. Here, we consider the amplitude of classical mirror plane equipotential (given by $U_{\text{class.}} = \mathcal{E}/e$) as effective 'crystal'

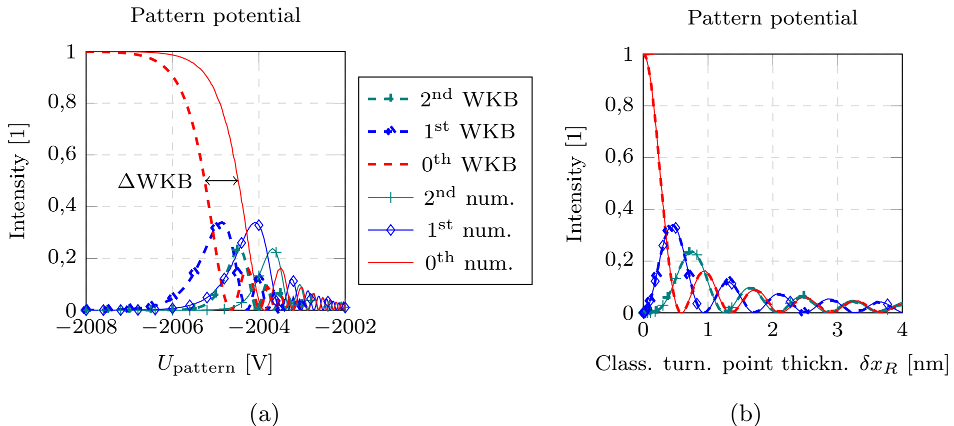

Figure 2.3: (a) The intensity of the four most dominant orders as function of pattern potential. Solid lines (direct solution) and dashed lines (WKB approximation) of the Schrödinger equation are shown. (b) The amplitude (δx_R) of the classical mirror plane $U_{\text{class.}} = \mathcal{E}/e$ [V] and corresponding diffraction order intensities are shown.

thickness. The thickness δx_R of the crystal can then be tuned by changing the pattern potential.

In [Fig. 2.3(b)] the diffraction intensities are plotted as a function of this effective thickness δx_R. As it can be seen from the figure, the intensity in the first order diffracted beam increases linear as function of effective thickness for amplitudes close to zero. This linear increase is at the expense of intensity of the zeroth-order (central) beam and can be interpreted as an exchange of intensity between the two modes. In this range of effective thickness, the grating mirror can be applied as a non-symmetrical beam splitter, meaning that a non-50/50 splitting ratio is achieved. It should be noted though that both the positive and negative orders are generated equally.

Earlier, we derived the exponential attenuation of the field modulation as function of pitch. As a result, it should be expected that the pitch influences the bias potential interval, over which the central beam becomes fully attenuated. In [Fig. 2.4] we show the intensity of the first orders of diffraction for a grating mirror with pitch of 500 nm and 1000 nm. Indeed, it is evident from the plots shown that an increase in pitch stretches the interval over which the first order diffracted beam is generated, from approximately 2.3 V to 5.0 V.

The implications of this last result for an experiment are evident when one considers the energy spread inherent to an electron beam. By increasing the pitch, the sensitivity for energy spread is reduced, leading to better spatially defined diffraction spots. However, by increasing the pitch, one also has to increase the width of the beam that is spread out over the mirror surface, in order to illuminate an equal number of pitches when compared to the smaller pitch. As an alternative to increasing the pitch, one can also increase the field strength between the mirror and field-limiting aperture, by reducing the distance between the two or applying a

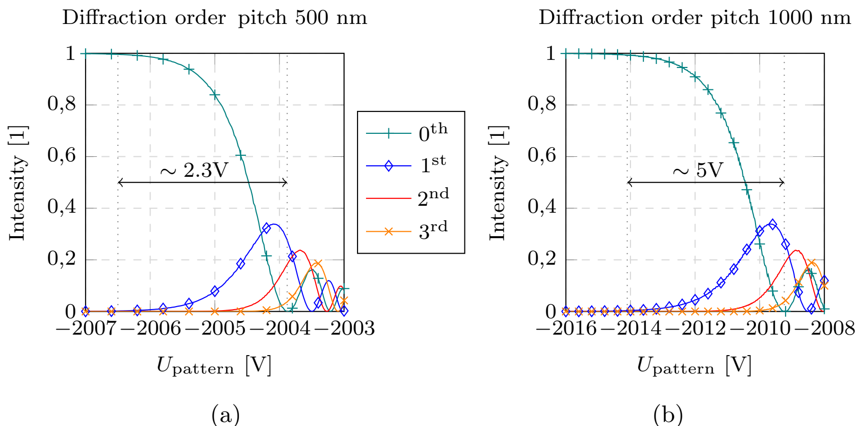

Figure 2.4: Diffraction order intensities for a fixed pitch of (a) 500 nm and (b) 1000 nm. An increase in pitch results in a wider bias potential window for complete attenuation of the central order beam.

positive bias to the field limiting aperture.

The above results are all obtained from the numerical solution of the Schrödinger equation, which is a computationally demanding procedure. We now compare the obtained results to the outcome of the WKB method in order to assert the validity of the latter. For this, we consider again a single pitch of the grating mirror. We use our analytical expression for the equipotential above the grating mirror [Eq. 2.2] and integrate the momentum along paths running parallel to the optical axis, in order to obtain the spatial phase modulation. The obtained phase profile is then decomposed in the various spectral components using Fourier analysis and this yield the intensity of the diffracted beams.

In [Fig. 2.3(a)], the intensity of the central, first and second order beams (dashed lines) are plotted as a function of applied pattern potential. Comparison to the exact solution (solid lines) shows good qualitative agreement. Quantitatively however, the WKB result is shifted approximately 1 volt with respect to the exact solution. It thus appears that the electron approaches the mirror more closely in the WKB approximation as compared to the exact case. Indeed, this is the case when one considers the Airy function solution of the exact case. The maximum of the probability $|\psi|^2$ for finding the electron is positioned not at, but just before the classical turning point (also see [Fig. A.1(a)]) and thus the electron spends more time at this point then at the classical turning point itself.

From the above, it appears to be evident that the WKB approximation does not yield useful quantitative results when the beam intensities are expressed as a function of applied pattern potential. However, we found that by expressing the beam intensities as function of *classical turning point thickness* (δx_R) instead, a perfect agreement between the WKB and exact method is obtained, as shown in [Fig. 2.3(b)]. One can then calculate the potential necessary for this thickness in hind sight.

2.4. Discussion

The physics of a constant pitch grating mirror is studied via two different methods. We observe a physical correspondence of the studied grating mirror with that of a diffractive crystal. Different pattern parameters are studied as well and these show similar results.

It should be noted that the diffraction order intensities as function of effective crystal thickness [Fig. 2.3(b)] are remarkably similar to the square of Bessel functions of corresponding orders. This may suggest that an analytical solution for the studied system exists. This would enable a general description of diffraction order intensities for any periodic grating mirror.

We demonstrated in the previous section that the WKB and exact method show remarkable quantitative agreement, when the beam intensities are expressed as a function of classical turning point thickness instead of applied bias potential. This observation allows speeding up of future calculations, since the calculation of the WKB integral takes only a few seconds. This is an improvement over the use of exact solutions, the calculation of which takes up to 30 minutes on the PC used for the shown calculations. Additionally, the WKB method allows more flexibility for studying non-periodic patterns.

Finally, we discuss several effects which might prevent us from obtaining the coherent diffraction as we described. The most obvious disturbing effect is a possible low-frequency distortion of the mirror topography, for instance the effect of curvature of the surface due to stress inside the material. We can approximate the maximum allowable curvature by assuming illumination of the mirror with a beam of 20 μm diameter. Then, for the generation of the first order diffracted beam, a field modulation of the classical turning point of 0.5 nm is required[1]. From [Eq. 2.2], we can then estimate a maximum thickness variation of 1 nm is tolerated within this region. A further increase in curvature will ultimately lead to blurring of the diffracted beams in the image plane of the mirror system. Similarly, the potential on the surface of the mirror is assumed to be very uniform. At 10 kV/mm, a topography change of 1 nm, as just discussed, is equivalent to a potential change of 10 mV. This sets requirements for the surface treatment of the mirror surface. Also, contamination should be avoided because this could lead to local charging. In principle, the electron beam does not need to touch the mirror surface ever, but during the alignment procedures it will be hard to really avoid electrons reaching the surface.

A more subtle effect is that of the induced mirror charges inside the mirror. At the sub-nA current that will be used, electrons can be treated as arriving individually. The proximity of an electron near a wall induces an image charge (distribution) inside this wall [5]. At the point of nearest approach to the mirror surface (approximately 500 nm when only the first order diffracted beam is induced) this yields an increase of the potential at the classical turning point. A simple calculation shows that this is in the order of millivolts. The force from the mirror charge on the electron is always perpendicular to the surface, so we do not expect any effect

[1] Assuming 2 keV beam, 500 nm pitch and mirror potential of −2004 V. Numbers are approximations.

from this. However, as the electron moves towards and away from the mirror, the induced surface charges on the mirror surface are dragged along, possibly causing dissipation [6, 7]. In the which-way setup of [7], this dissipation due to Joule heating is recognized as the mechanism that leads to dephasing of the state of the wave function associated with the respective path. As a result, decoherence is observed as the electron propagates alongside the wall.

A similar effect is observed for intensity splitting in nanofabricated gratings [8]. Here, the dissipative effect of the image charge can be related to the side walls of the slits that the electron passes through. The question is if this effect could cause decoherence in our proposed set-up. The effect would be that a localized excitation in the mirror surface would cause the electron to lose energy, in the process collapsing the wave function to a smaller area than the original 20 μm. This would affect the diffraction. We do not have a full theory from which we can derive the probability of this effect. However, we point out that in all of the cases in the literature, the dephasing of the wave function is the result of splitting the wave function and successive dissipation in one of the resulting trajectories as it travels for some distance parallel and very close to a surface. As this is not the case for the reflective grating mirror that we present here, we expect that the probability of decoherence will be smaller than in those cases. Also, earlier experimental work involving electron holography [3] with reflected electrons did not indicate any effects of decoherence.

A final effect to be considered is bremsstrahlung, the emission of a photon while decelerating and accelerating the electron. Potentially this could cause energy spread or local collapse and thus loss of coherence. However, a non-relativistic estimate of the average energy that is lost per electron to bremsstrahlung for an initial electron energy of 2 keV reflected in a 10 kV/mm field gives 1×10^{-9} eV, which can safely be neglected.

Further requirements on experimental set-ups for demonstration of the grating mirror for electrons would require stable power supplies, with an accuracy that is well below the energy spread of the electron beam. This criterion is easily satisfied with modern supplies and the optional use of an additional low-pass filter on the output.

This all said, we must admit that we have tried to observe the diffraction experimentally and so far have not obtained convincing results.

Future work requires experimental verification of the grating mirror. This demands the micro fabrication of the grating mirror and (lens) apertures. The spatial coherence of the electron beam should then extend across a distance of multiple pitches. From our simulations it is obtained that a small pitch requires the electron to approach the mirror to such proximity that higher order diffracted beams may not be generated. On the other hand, a too large pitch places a more demanding condition on spatial beam coherence.

The realization of a quantum electron microscope can benefit from the presented work, as we describe accurately the intensity of the diffracted beams for given operation parameters. One should however take into account the coherent built-up of signal in the higher order diffracted beams [9].

Acknowledgments. Author M. A. R. K. would like to thank J. M. Thijssen of the Theoretical Physics group at Delft University of Technology for helpful discussions on the initial model design. This work is funded by the Netherlands Organisation for Scientific Research (NWO).

References

[1] P. Kruit, R. G. Hobbs, C.-S. Kim, Y. Yang, V. R. Manfrinato, J. Hammer, S. Thomas, P. Weber, B. Klopfer, C. Kohstall, T. Juffmann, M. A. Kasevich, P. Hommelhoff, and K. K. Berggren, *Designs for a quantum electron microscope,* Ultramicroscopy **164**, 31 (2016).

[2] P.W. Hawkes and E. Kasper, *Principles of electron optics*, Vol. 3 (Academic press, New York, 1994).

[3] H. Lichte and G. Möllenstedt, *Measurement of the roughness of supersmooth surfaces using an electron mirror interference microscope,* Journal of Physics E: Scientific Instruments **12**, 941 (1979).

[4] T. R. Harvey, J. S. Pierce, A. K. Agrawal, P. Ercius, M. Linck, and B. J. McMorran, *Efficient diffractive phase optics for electrons,* New Journal of Physics **16**, 093039 (2014).

[5] P. Machnikowski, *Theory ofwhich pathdephasing in single electron interference due to trace in conductive environment,* Physical Review B **73** (2006), 10.1103/physrevb.73.155109.

[6] J. R. Anglin, J. P. Paz, and W. H. Zurek, *Deconstructing decoherence,* Physical Review A **55**, 4041 (1997).

[7] P. Sonnentag and F. Hasselbach, *Measurement of decoherence of electron waves and visualization of the quantum-classical transition,* Physical Review Letters **98** (2007), 10.1103/physrevlett.98.200402.

[8] B. Barwick, G. Gronniger, L. Yuan, S.-H. Liou, and H. Batelaan, *A measurement of electron-wall interactions using transmission diffraction from nanofabricated gratings,* Journal of Applied Physics **100**, 074322 (2006).

[9] Y. Yang, C.-S. Kim, R. G. Hobbs, P. Kruit, and K. K. Berggren, *Efficient two-port electron beam splitter via a quantum interaction-free measurement,* Physical Review A **98** (2018), 10.1103/physreva.98.043621.

3

Principles of Electron Wave Front Modulation with Two Miniature Electron Mirrors

Abstract.

We have analyzed the possibilities of wave front shaping with miniature patterned electron mirrors through the WKB approximation. Based on this, we propose a microscopy scheme that uses two miniature electron mirrors on an auxiliary optical axis that is in parallel with the microscope axis. A design for this microscopy scheme is presented for which the two axes can be spatially separated by as little as 1 mm. We first provide a mathematical relationship between the electric potential and the accumulated phase modulation of the reflected electron wave front using the WKB approximation. Next, we derive the electric field in front of the mirror, as a function of a topographic or pixel wise excited mirror pattern. With this, we can relate the effect of a mirror pattern onto the near-field phase, or far field intensity distribution and use this to provide a first optical insight into the functioning of the patterned mirror. The equations can only be applied numerically, for which we provide a description of the relevant numerical methods. Finally, these methods are applied to find mirror patterns for controlled beam diffraction efficiency, beam mode conversion, and an arbitrary phase and amplitude distribution. The successful realization of the proposed methods would enable arbitrary shaping of the wave front without electron-matter interaction, and hence we coin the term virtual phase plate for this design. The design may also enable the experimental realization of a Mach-Zehnder interferometer for electrons, as well as interaction-free measurements of radiation sensitive specimen.

3.1. Introduction

The use of spatial light modulators [1] and digital micromirror devices [2, 3] in light optics has enabled the controlled and dynamic shaping of photon beams. Methods for the shaping of charged particle beams are unfortunately not as versatile yet. To the electron microscopy community its development would provide many opportunities, such as beam mode conversion [4], or low-dose imaging of unstained biological specimen [5, 6]. Recent experimental work indicates promising progress towards a programmable transmission-based phase plate [7] for use in transmission electron microscopy (TEM), although upscaling of the number of addressable pixels, as well as increasing the transmissivity of the phase plate, may prove challenging.

3.1.1. Electron wave front shaping

Electron wave front modulation is realized by passing the electron through an inhomogeneous optical medium, such as a spatially modulated electric field, or a topographically shaped phase plate. In the basis, electron beam shaping requires a medium that acts spatially on the phase of the electron wave front. The build-up of electrical charge at the surface of this medium will influence the resulting wave front modulation, which is avoided by making use of electrically conducting materials only. Spatial coherence of the electron across the phase modulator can be realized by a combination of a high brightness source and a small beam current [8]. These requirements can be fulfilled in a number of ways.

Most commonly, electric and magnetic fields are used for charged particle beam deflection and focusing, which can be described as electron wave front manipulations. The fields are then generated external to the optical axis of the microscope and the use of electrically conductive elements prevents charging of the electrodes. Series of magnetic and electric multipole elements are seen in transmission electron microscopes and have been demonstrated to correct imaging system aberrations [9]. The combination of a multipole electrode with an annular aperture for vortex beam creation is reported as well [10].

Alternatively, patterned thin film amorphous carbon or silicon nitride membranes that cross the beam path can modulate the phase of the beam [11]. On the one hand this enables contrast enhancement [12], such as Zernike phase contrast [13, 14], while on the other hand beam mode conversion of plane waves into vortex beams [15–18], non-diffracting Bessel beams [19], and probability preserving Airy beams [20] are realized. Although transmission phase plates offer an increased flexibility for beam shaping with respect to externally generated fields, the limited operational life time and sensitivity to contamination [12, 21] are still factors that limit the long-time application of these methods.

In contrast to the former methods that rely on transmission of the electron, electron mirrors slow down and reflect the incident beam prior to reaching the mirror electrode. This facilitates an alternative method to electron beam shaping that avoids electron beam-matter interaction. In the past, the use of tetrode electron mirrors for aberration correction [22] has been experimentally demonstrated [23]. Furthermore, mirror electron microscopy [24] has been successfully employed to measure the roughness of supersmooth surfaces, by electrically biasing the specimen just

below the cathode potential of the source [25]. Also, it is suggested that a pixelwise deformable electron mirror could be used for adaptive phase contrast enhancement [26], and can as well be applied for electron beam lithography [27]. Electron mirrors are usually combined with a beam separator [28] in order to separate the trajectory of the incident and reflected electrons.

The drawbacks of transmission optics, such as phase plate contamination, operational life-time, electrical charge built up at surfaces and reduced optical transmissivity do not present themselves to mirrors. In comparison to transmission based techniques, the use of reflection based optics becomes increasingly advantageous when more than one reflective element is present in the beam line. The use of multiple beam reflective elements is seen with the recent development of an aberration corrected low energy electron microscopy/photo-emission electron microscopy (LEEM/PEEM) [29, 30] instrument. The mirror assemblies are mounted here onto the microscope column under a 90 degree angle, which is a necessity due to the large volume claim of conventional beam separators.

More recent instrumentation developments allow for miniaturization of beam separators [31]. This enables for instance the realization of a proposal for aberration correction in scanning electron microscopy (SEM) based on two miniature electron mirrors [32]. The latter paper describes a miniature column with two parallel optical axes. The use of parallel optical axes enables one to reduce the deflection angles in the beam separator to below 100 mrad. In turn, this limits the deflection dispersion in the corrector, that may ordinarily limit the performance of such instrument [28].

The miniature mirrors in the above mentioned proposal for aberration correction may be replaced by mirrors that contain freely chosen patterns. For the resulting optical setup, we coin the term *virtual phase plate*. In this work, we describe the influence that the mirror pattern topography has on the phase modulation of the reflected electron, and then turn it around to find the surface topography or voltage distribution for a required wave front shape. The results are demonstrated by means of numerical examples.

3.2. Phase modulation with an electron mirror

Electrons are decelerated by an electrode with a negative electric potential that spans across the propagation axis. At a sufficiently negative electrode potential, the incident electron is completely stopped and will be reflected back towards the direction of origin. This requires an equipotential value that equals that of the extraction voltage at the electron source. As the electric field in front of the mirror electrode must satisfy the Laplace equation, the velocity of the electron gradually changes as it approaches the mirror electrode. Hence electron mirrors are characterized by soft reflection fields that act as inhomogeneous refractive medium [33]. This is different from mirrors in light optics, for which a hard reflection of the photon at the mirror surface takes place.

The electric field in front of the mirror electrode satisfies the Laplace equation, and thus any spatial topographic or charge pattern at the mirror electrode will result in the spatial modulation of the electric field in front of the electrode as well. As the electric field of the mirror extends from the mirror electrode into the

3

path of the incident electron beam, a continues modulation of the wave front takes place as the wave front approaches the mirror. Non-flat, structured electron mirrors have the property to locally alter the phase of the wave front of a spatially spread out incident electron, and the quantum mechanical effect of a mirror perturbation [34], and periodic structures [35, 36] have been studied in the past analytically and numerically. It was suggested that the use of controlled wave front modulation with arbitrarily patternable mirrors could be used for structural hypothesis testing [26], but this has to our knowledge not been demonstrated experimentally yet.

Here we will focus our attention to generalized mirror patterns and their resulting effect on the wave front of the reflected electron wave front. For this, we will first provide a relationship between the electric potential and the accumulated phase modulation of the reflected electron wave front. Next, we will derive the electric field in front of the mirror, as a function of the topographic or pixel wise excited mirror pattern. With this, we can then relate the effect of a mirror pattern onto the near-field phase, or far field intensity distribution and use this to provide a first optical insight into the functioning of the patterned mirror. We will conclude this section with a discussion on chromatic effects.

3.2.1. Electron phase as a function of electric potential

In transmission electron microscopy, the acceleration of the electron beam by the (mean inner) potential of a phase plate is usually small in comparison to the nominal beam energy. This justifies the use of the projection assumption, which describes the exit wave ψ_{out} after passing a plane wave electron through a phase plate as [37]

$$\psi_{out} = \exp(i\sigma V_z). \tag{3.1}$$

The term inside the exponent in [Eq. 3.1] may be considered as a phase transfer function, as it describes in the essence the effect that the electric potential has on the phase of the transmitted electron. In this equation, σ is an interaction constant that is proportional to the electron wave length, and $V_z = V_z(x, y)$ is the projected potential along the propagation axis,

$$V_z(x, y) = \int_{-\infty}^{\infty} V(x, y, z)dz. \tag{3.2}$$

This approach does not work for electron mirrors, for a number of reasons. Foremost, the projection assumption is invalid as the mirror potential equals that of the beam energy. In addition, we note that the upper boundary of the integral is ill-defined, as the wave function of the electron will actually penetrate the mirror field to some extend behind the classical turning point. The situation complicates even further when the mirror electrode is not flat, but instead contains a spatial pattern.

Convolution model

Earlier work related to mirror electron interference microscopy has resulted in a relationship between the mirror profile $h(x, y)$ and the phase modulation $\phi(x, y)$ of

the reflected beam [25, 38]. Although the work in [38] is not available to us, it is reproduced by Lichte in [35] and we make use of that here. It was demonstrated that under the assumption $h \ll z_R \ll z_1$, with the mirror electrode at $z = 0$ and the field limiting aperture electrode at z_1, and with z_R the coordinate plane of reflection, or turning point, in front of the mirror surface, that the phase difference between the reflected object and reference beam in a mirror electron interference microscope can be obtained through [35],

$$\phi(x, y) = \frac{2\pi}{\lambda_e} \cdot [h(x, y) * G(x, y, z_R)] \,. \tag{3.3}$$

In the equation, $G(x, y, z_R)$ is called the blurring function, and λ_e is the field free electron wave length. The blurring function as a function of one transverse spatial dimension is plotted in [Fig. 3.1(a)] for a range of turning point coordinates. From the plot it is observed that the blurring function becomes steeper when the turning point of the beam is positioned closer to the mirror substrate. The increased steepness of the curve renders the convolution more sensitive to high spatial frequency components residing in the mirror pattern, as the beam is reflected closer to the mirror electrode.

The blurring function is the Fourier transform of the ‘spectral transfer function’ $P(k, z_R)$, which is given by [25]

$$P(k, z_R) = \sqrt{\frac{\pi}{k z_1}} \times \exp(-k z_R) \times \mathrm{erf}\left(\sqrt{k z_R}\right) . \tag{3.4}$$

This function provides a direct relation between the attenuation of different spatial components at a fixed mirror bias potential. The spectral transfer function is plotted in [Fig. 3.1(b)], for a linear electric field strength of 10 kV/mm that we assume throughout our work.

WKB approximation

The validity of the convolution model is connected to the requirement $h \ll z_R \ll z_1$, and thus potentially reduces when micromachined electron mirrors are considered for which $h \lesssim z_R$. As the original work in which the spectral transfer function was derived [38] is not available to us, we pursue a second line of analysis in which we study the effect of the pattern profile and applied potentials through the WKB approximation. This approximation method assumes the separability of the amplitude $a(\vec{r})$ and phase $\phi(\vec{r})$ of the wave function in the form $\psi(\vec{r}) = a \exp(i\phi)$, for which it is then demonstrated that the phase distribution is related to the scalar electric field through [39],

$$\phi(x, y) = \hbar^{-1} \int_{z_1}^{z_R(x,y)} p(x, y, z) dz = \hbar^{-1} \int_{z_1}^{z_R} \sqrt{2m_e \left(\mathcal{E} - V(x, y, z)\right)}. \tag{3.5}$$

The classical momentum $p(x, y, z)$ of the electron with field-free energy $\mathcal{E}$ is integrated along paths that run in parallel with the optical axis. For an incident plane

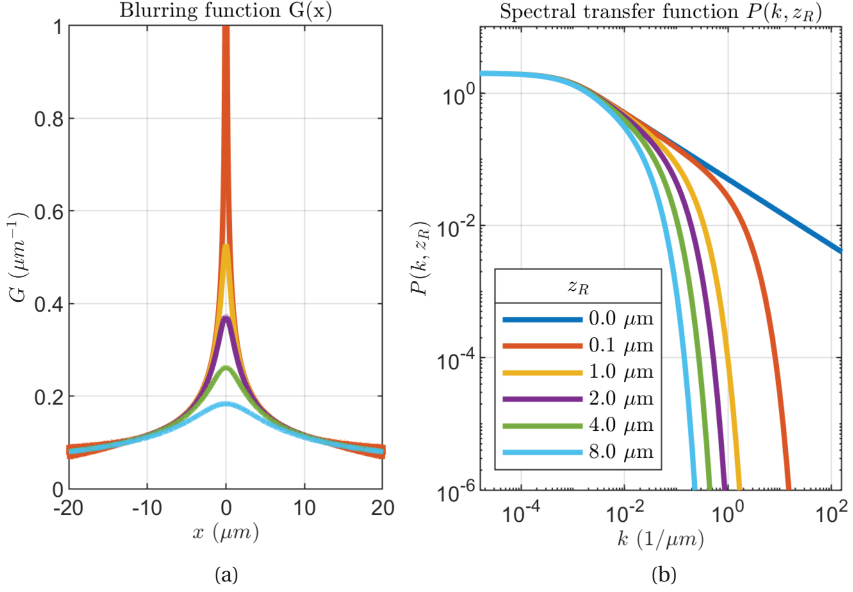

Figure 3.1: (a) Blurring function $G(x, z_R)$, and (b) Spectral transfer function $P(k, z_R)$, for different values of turning point coordinates z_R. Plot and calculations based on methods described in [38] that we reproduced here from [25].

wave, the electron trajectory is defined to coincide with the z-axis here. The classical momentum is related to the scalar electric field (U) through the potential energy function, $V = eU(x, y, z)$. The integration is performed between the coordinates of the field limiting aperture z_1 and the classical turning point $z_R(x, y)$. The classical turning point coincides with the lateral coordinate, at which the electric potential equals that of the extraction voltage of the electron source $(\mathcal{E} = V)$, and this is influenced by the electric perturbations due to the pattern at the mirror electrode.

In order to assess the effect that the pattern at the mirror electrode has on the phase of the reflected electron, we suggest to treat the contributions from the mirror pattern in terms of its Fourier components. This approach is similar to what we have used in previous work, where we demonstrated the agreement between the obtained phase modulation amplitudes through the WKB method and direct solutions to the Schrödinger equation [36], and note that solutions through the WKB method are less computational expense. Then the spatial phase modulation may be obtained for every component of the field separately. For a modulus of spatial frequency $k = |\vec{k}|$ at the pattern, this surmounts to finding the integrated phase difference A_k of the two electron trajectories that coincide with the crest and trough of the component of the field, given as

$$A_k = \phi(0) - \phi(1/(2k)). \tag{3.6}$$

In this expression, A_k denotes the amplitude of the phase modulation associated with spatial frequency k, and essentially corresponds to the maximum of phase difference that would result from application of the convolution model in [Eq. 3.3]. The integration boundary z_R in [Eq. 3.5] is different for both terms in [Eq. 3.6] as the electron approaches the mirror electrode closer at the trough of the modulated electric field. The values of z_R corresponding to the trough and crest of the field can be obtained analytically through the Lambert-W function [see Appendix B], or numerically by solving for $U(z) = E$. The complex wave function after reflection associated with this solution is reconstructed by,

3

$$\psi(k) = \exp\left(iA_k \cos(2\pi kr + \theta_k)\right). \tag{3.7}$$

This expression may be compared to Eq. (31) in [35], where the effect of a single harmonic perturbation at a mirror surface was studied. The full wave function of the incident initial plane wave when exiting the reflection field is then described by the sum of all harmonic components that are present in the pattern at the mirror electrode, and generalizes to

$$\psi_M(r) = \exp\left(i\sum_{n=0}^{\infty} A_{k_n} \cos(2\pi k_n r + \theta_{k_n})\right). \tag{3.8}$$

The angle θ_k fixes the relative position of each term with respect to other spatial contributions in the pattern.

Validity of the convolution model

We can now directly compare the phase modulation that is obtained through the convolution model to that of the WKB approximation. This comparison may offer a more quantitative bound on the restriction $h \ll z_R \ll z_1$ that is placed on the validity of the convolution based model. For this, we obtain the phase modulation through the WKB method for a number of pattern heights, and normalize the obtained data to the lowest spatial frequency that we analyze. Note that the spectral transfer function [Eq. 3.4] in the convolution model is not dependent on the pattern height, and can thus be obtained at once.

In [Fig. 3.2] we have plotted the spectral transfer function that is obtained from the convolution model (dashed lines) and the WKB approximation (solid lines), at a linear electric field strength of 10 kV/mm. In the comparison, we assumed $z_1 = 200$ μm and a pattern height of (a) 100 nm, and (b) 500 nm. The distance of closest approach towards the mirror electrode (z_R) is varied between 0 and 500 nm in this analysis.

In both data sets we observe that the two models are in good agreement in general. However, when $z_R \leq 2h$ we start to observe a deviation. It is thus in principle possible to use the convolution model, as long as the former strict inequality is satisfied. We choose to use the WKB method instead in the remainder of this work.

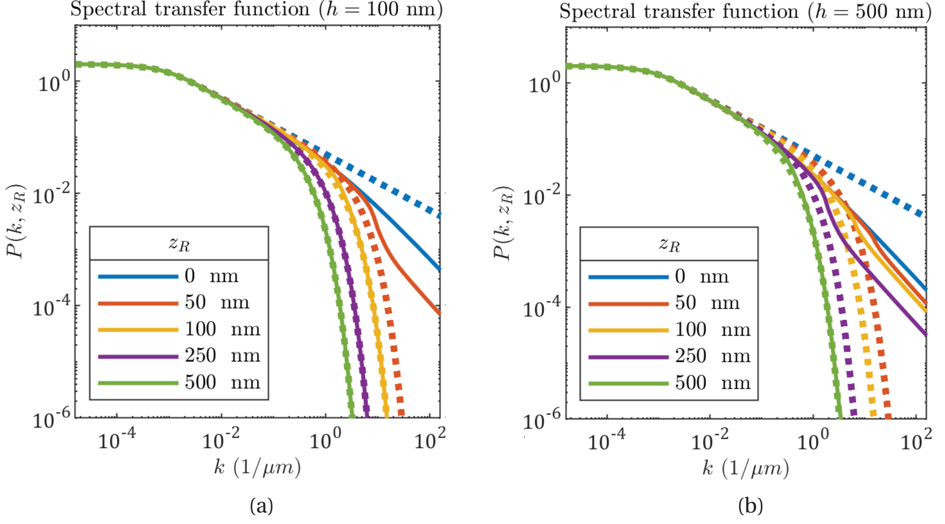

Figure 3.2: Spectral transfer function obtained through the convolution model (dashed lines) and WKB approximation (solid lines), at a profile height of (a) 100 nm, and (b) 500 nm, as a function of spatial frequency k and closest approach z_R.

Far field intensity at one spatial frequency

In the following we relate the near field phase modulation to the resulting intensity in the far field. The far field intensity can be obtained through Fresnel propagation of ψ_M. We can also place a lens in front of the mirror, and use a Fourier transform to obtain the intensity distribution at the image plane that coincides with the focal plane of this lens. The resulting far field diffraction intensity of a WKB phase modulation amplitude A_k can be obtained directly through the Jacobi-Anger relationship, that expands a modulated complex exponential on the left hand side into an infinite sum that contains Bessel functions $J_n(\xi)$ of order n on the right hand side [40],

$$\exp(i\xi\cos(\chi)) = \sum_{n=-\infty}^{\infty} i^n J_n(\xi)\exp(in\chi). \tag{3.9}$$

The infinite sum may be interpreted as a Fourier series, which results in that the intensity of diffraction spots at the far field due to the single spatial frequency k is given explicitly by $|J_n(A_k)|^2$ where n labels for the harmonic tones of k. In [Fig. 3.3(a)] we show the intensity of the unscattered ($n = 0$) and the first (green triangles), second (blue squares), and third (gray stars) order scattered beam intensities, as a function of phase modulation amplitude A_k. From this figure it is apparent that a single spatial frequency in the mirror pattern results in a set of diffraction spots, with intensities that cannot be chosen independently.

A practical limit of phase modulation amplitude emerges from the Jacobi-Anger expansion, above which it becomes no longer possible to modulate the intensity of a

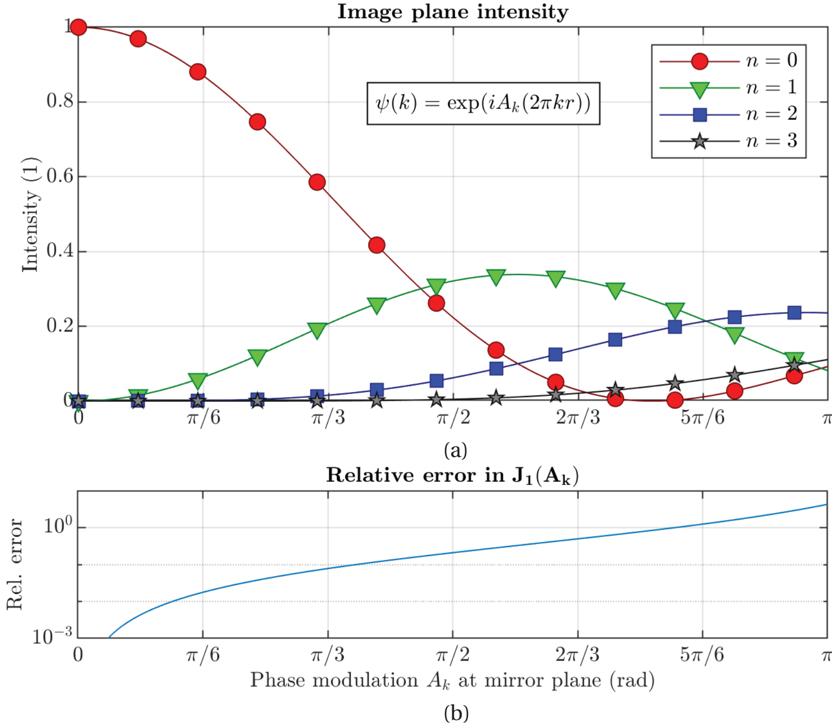

Figure 3.3: (a) Intensity distribution at the image plane, as a function of phase modulation amplitude (A_k) for a single and fundamental spatial frequency k. Plotted orders n correspond to harmonic frequencies nk, with $n = 0$ representing the unscattered component of the beam. (b) Relative error of the intensity of the diffraction intensity due to the generation of higher order spots.

diffraction spot with only a single spatial frequency in the mirror pattern, without generating higher order spots as well. If we allow for 1% of the intensity to be directed into a higher order diffraction spot at the image plane, the amount of phase modulation that can be achieved with a single spatial frequency is upper bound to $\pi/6 \approx 0.5$ rad [Fig. 3.3(b)]. Higher values of phase modulation are then only attainable, when the development of the higher harmonics is suppressed by adding to the fundamental pattern a $\theta = \pi$ rad out of phase contribution of the respective higher harmonic spatial frequencies.

Addition of multiple spatial frequencies

In the following we analyze the extend of the validity of using the results from [Eq. 3.9] and [Fig. 3.3(a)] when multiple spatial frequency components are present in the mirror pattern. The result as shown in [Fig. 3.3(a)] is invariant for a change in spatial frequency k. Hence, we consider for instance the effect of combining two spatial frequencies that are both characterized by a phase modulation amplitude A_k

of say $A_k = \pi/3$. From the data shown in [Fig. 3.3(a)] we observe that the intensity of the unscattered beam is reduced from 1 to approximately 0.58, thus an intensity reduction of $1 - 0.58 = 0.42$. Meanwhile, the intensity in the first order diffraction spots related to both pattern components increases to approximately 0.20, yielding an apparent total intensity increase in the scattered beam of $2 \times 2 \times 0.20 = 0.80$. This suggests that intensity is created in the scattered beam, as a result of adding an additional pattern component. Where did this intensity come from?

It appears that linear addition of the effect of multiple pattern components yields physically incompatible results. We can understand this, by carefully analyzing the effect of multiple spatial frequencies when inserted into [Eq. 3.8], and expanding into the far field intensities using [Eq. 3.9]. For two given spatial frequency k_1 and k_2 (and $k_1 \neq k_2$) the near field wave front is described as

$$\begin{aligned} \psi_M(r) &= \exp(iA_k[\cos(2\pi k_1 x) + \cos(2\pi k_2 x)]) \\ &= \exp(iA_k \cos(2\pi k_1 x)) \times \exp(iA_k \cos(2\pi k_2 x)). \end{aligned} \tag{3.10}$$

In the far field, the intensities are then described by the product of the Jacobi-Anger expansion of both terms, given as

$$\begin{aligned} I &= \left\{ \sum_{n=-\infty}^{\infty} i^n J_n(A_k) \exp(in2\pi k_1) \right\} \times \left\{ \sum_{n=-\infty}^{\infty} i^n J_n(A_k) \exp(in2\pi k_2) \right\} \\ &= \left\{ \sum_{n=-\infty}^{\infty} c_{n,1} \exp(in2\pi k_1) \right\} \times \left\{ \sum_{n=-\infty}^{\infty} c_{n,2} \exp(in2\pi k_2) \right\}. \end{aligned} \tag{3.11}$$

Effectively, the result in [Eq. 3.11] describes a product of two Fourier sums, which can generally be expressed as a convolution of its coefficients $c_{n,1}$ and $c_{n,2}$. From this it is concluded that the linear addition of the effect of multiple spatial frequency components in the pattern is not allowed in general. However, if only values of $A_k \ll 1$ are considered, the effect of the cross terms in the product in [Eq. 3.11] become negligible, since then $J_0(A_k) \approx 1$. This can be made more explicit by considering two pattern components, that satisfy $k_2 = 2k_1$ and contribute a phase modulation amplitude A_{k_1} and A_{k_2} to the reflected electron. Then, the product in [Eq. 3.11] can be evaluated explicitly for the lower order terms and yields the following intensities,

$$I_{\text{far field}} \propto \begin{cases} [J_0(A_{k_1})J_0(A_{k_2})]^2 \sim 1 & \text{Unscattered beam} \\ [J_1(A_{k_1})J_0(A_{k_2})]^2 \sim J_1^2(A_{k_1}) & \text{First order of } k_1 \\ [J_0(A_{k_1})J_1(A_{k_2}) - J_2(A_{k_1})J_0(A_{k_2})]^2 \sim J_1^2(A_{k_2}) & \text{First order of } k_2 \end{cases}. \tag{3.12}$$

In this result, the similarity conditions are satisfied if and only if $J_0(A_{k_2}) \approx 1$ and $J_1(A_{k_1}) \approx 0$, thus in general when $A_{k_n} \ll 1$. We use this result as a justification for

linear addition of the effect that multiple pattern contributions have on the phase of the reflected electron, and we believe that this result is in line with the weak phase object approximation [41] that is conventionally adhered to in the context of thin phase plates.

3.2.2. Electric field as a function of mirror pattern

In the following, a description for the electric scalar potential is derived as a function of topographic and pixel wise patterning. This requires a solution for the Laplace equation of the scalar potential $U(x, y, z)$ in transverse coordinates x and y, and beam propagation direction z. It is assumed [also see Fig. 3.4] that the mirror electrode is positioned at $z = 0$ and the beam incidence and reflection takes place in the region for which $z < 0$. A field limiting aperture electrode is positioned at $z = z_1 < 0$, that connects the mirror electric field to a region of constant potential $U(x, y, z < z_1) = u_1$.

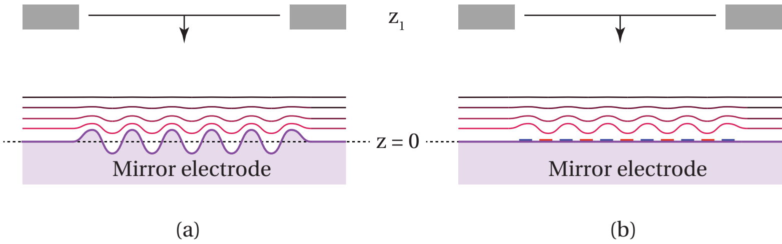

Figure 3.4: Schematic geometry of the mirror electrode, in the case of (a) topographically patterned electron mirror and (b) pixel wise patterned electron mirror. The field limiting aperture at $z = z_1$ connects the mirror electric field to a region of constant potential u_1.

Solutions to the Laplace equation in Cartesian coordinates can be obtained through the method of separation of variables. The method ordinarily invites to look for solutions in the form $U(x, y, z) = X(x)Y(y)Z(z)$, but this will limit the shape of the pattern potential to products of $XY \simeq \cos(f(x)) \times \cos((g(y))$ that introduce a fixed grid of zero crossings. Instead, we will obtain solutions that describe the pattern with cross-terms, $U(x, y, z) = P(x, y)Z(z)$ in which $P(x, y)$ is the mirror pattern function, and $Z(z)$ describes the electric field attenuation above the mirror surface. We must then obtain a solution for

$$\frac{\partial^2 P(x,y)Z(z)}{\partial x^2} + \frac{\partial^2 P(x,y)Z(z)}{\partial y^2} + \frac{\partial^2 P(x,y)Z(z)}{\partial z^2} = 0. \tag{3.13}$$

This can be cast in the separated form given as,

$$\frac{1}{P(x,y)}\left[\frac{\partial^2 P(x,y)}{\partial x^2} + \frac{\partial^2 P(x,y)}{\partial y^2}\right] + \frac{1}{Z(z)}\frac{\partial^2 Z(z)}{\partial z^2} = 0 \Rightarrow C_p^2 + C_z^2 = 0. \tag{3.14}$$

The separation constants, $(C_p,\ C_z) \in \mathbb{C}$ must be allowed complex valued in order to satisfy the sum of separated squared coefficients. There are two boundary conditions that the above equation must satisfy:

1. At $z = z_0$ the potential distribution at the mirror electrode is described by $U_0(x, y, z) = u_0 + \Delta u_0(x, y, z_0)$ in the case of pixel wise patterning. Here, u_0 is the bias potential and $\Delta u_0(x, y)$ describes the (harmonic) potential variation across the mirror surface. In the case of topographic patterning, only a bias u_0 is present, and we approximate Δu_0 based on the pattern amplitude δ and the linear field strength $E_z = u_0/(z_1 - z_0)$, such that $\Delta u_0 = E_z\delta$. We choose $z_0 = 0$ is positioned at the origin of the coordinate system.

2. At $z = z_1 < 0$, a field limiting aperture electrode is positioned and it is assumed that at this point the scalar potential is uniform in the transverse direction, $U_1(x, y, z \leq z_1) = u_1$.

Solutions at the mirror electrode

The first boundary condition relates to the potential variation at the mirror electrode that is due to the pattern. A general solution for $P(x, y)$ is given (for constants p_0 and p_1) by

$$P_0(x, y) = p_0 \exp(i2\pi[k_x x + k_y y + \theta]) + p_1 \exp(-i2\pi[k_x x + k_y y + \theta]). \tag{3.15}$$

The coefficients k_x and k_y are spatial frequencies of the mirror pattern and θ is a constant phase offset. From [Eq. 3.14], this provides the relationship

$$(2\pi i k_x)^2 + (2\pi i k_y)^2 = C_p^2. \tag{3.16}$$

From this it is seen that $C_p^2 < 0$ (since $k > 0$, and $i^2 = -1$) and consequently $C_z^2 > 0$. In the current form, [Eq. 3.15] would allow for only one spatial frequency in the mirror pattern. Solutions to the Laplace equation are linearly independent, which enables us to include multiple spatial components by linear addition,

$$P_0(x, y) = \sum_{(n,m)} F_{n,m} \cos\left(2\pi[k_{n,x}x + k_{m,y}y] + \theta_{n,m}\right). \tag{3.17}$$

Here we implicitly assume $p_0 = p_1 = 1/2$, such that the resulting sum of components represents a discrete Fourier sum of amplitudes $F_{n,m}$ and corresponding angles $\theta_{n,m}$. The amplitude term $F_{n,m}$ relates to the electric potential (in volt, Δu_0 in boundary condition 1) that the corresponding spatial frequency adds to the mirror potential, and its expression depends on the method of mirror excitation.

For topographic patterned mirrors, there is only the bias potential u_0 that is applied to the mirror electrode. The profile amplitude of the topographical features at the electrode surface $(\delta_{n,m})$ and the linear electric field strength $E_z = (u_1 -$

$u_0)/(z_1 - z_0)$ is then used to approximate the effective potential at $z = z_0$. The local potential at $z = z_0 = 0$ is then approximated through the amplitude $\delta_{n,m}$ of the harmonic contribution and the linear field strength,

$$F_{n,m} = E_z \delta_{n,m}. \tag{3.18}$$

In the case of pixel wise applied potentials, the relationship between $F_{n,m}$ and the individual pixel potential is somewhat more complicated due to the finite size of the pixels. The set of potentials $\{u_p\}$ that is used to realize a harmonic variation across the entire mirror electrode then consists of discrete increments, rather than the smooth transition that is the case for topographic patterning. The high spectral frequency components that are associated with the harmonics of the individual pixels are neglected here, as we will demonstrate that such high spectral components (that is, smaller than the width of a single pixel) are not likely to significantly influence the phase of the reflected electron.

Next, a solution for $Z(z)$ must be obtained. Earlier we derived the requirement $C_z^2 > 0$ and this in turn yields the general solution,

$$Z_0(z) = \xi_1 \exp(2\pi k_z z) + \xi_2 \exp(-2\pi k_z z). \tag{3.19}$$

This leads to the relationship $C_z^2 = (2\pi)^2 k_z^2$ and we require $\xi_2 \to 0$ in order to prevent the potential from diverging in the region of reflection. In addition, the constant ξ_1 corresponds to the local potential value, $\xi_1 \equiv F_{n,m}$ for $z = z_0$. Finally, as $C_p^2 + C_z^2 = 0$, we obtain the common wave optical relationship $k_x^2 + k_y^2 = k_z^2$, from which we can construct the solutions for the Laplace equation that satisfy boundary condition 1) as,

$$\begin{aligned} U_0(x,y,z) &= P_0(x,y)Z(z) \\ &= \sum_{(n,m)} \Big\{ F_{n,m} \cos\left(2\pi[k_{n,x}x + k_{m,y}y] + \theta_{n,m}\right) \\ &\qquad \times \exp\left(-2\pi|z|\sqrt{k_{n,x}^2 + k_{m,y}^2}\right)\Big\}. \end{aligned} \tag{3.20}$$

Solutions at the field limiting aperture

A solution that satisfies the second boundary condition is less involved than that at the mirror electrode. It is assumed that the electric field is terminated at an equipotential surface that is flat in the plane perpendicular to the propagation (z) axis, such that the function $P_1(x,y) =$ constant. In a practical situation, an aperture is needed at this plane that allows the electron beam to enter and exit the mirror field. The effect of this aperture is not treated here and may best be treated separately as part of a lens system in front of the mirror. The constant is absorbed into $Z_1(z)$, and we are thus only concerned with finding a solution for $Z_1(z)$, that has to satisfy

$$\frac{1}{Z_1(z)}\frac{d^2Z_1(z)}{dz^2} = 0 \Rightarrow \frac{d^2Z_1(z)}{dz^2} = 0. \quad (3.21)$$

The general solution is a first order polynomial, $Z_1(z) = az + b$. From the boundary conditions $Z(z_1) = u_1$ and $Z(z_0) = u_0$, a solution is readily obtained in the form of,

3

$$Z_1(z) = u_0\left[1 - \frac{z}{z_1}\right] - \frac{u_1 z}{z_1}. \quad (3.22)$$

In this equation, the second term drops out under the assumption of a field-free region of constant potential at or beyond z_1, for which $u_1 = 0$.

Analytical expression for the mirror electric scalar potential

A full solution for the electric potential that is created by a topographic or pixel wise patterned mirror is provided by addition of the separate solutions that were obtained, and is given in full as

$$\begin{aligned} U(x,y,z) &= P_0(x,y)Z(z) + Z_1(z) \\ &= \sum_{(n,m)>0}\Big\{F_{n,m}\cos\left(2\pi[k_{n,x}x + k_{m,y}y] + \theta_{n,m}\right) \\ &\qquad \times\exp\left(-2\pi|z|\sqrt{k_{n,x}^2 + k_{m,y}^2}\right)\Big\} \\ &\qquad +u_0\left[1 - \frac{z}{z_1}\right] - u_1\frac{z}{z_1}. \end{aligned} \quad (3.23)$$

In this expression, we have shifted the contribution of the DC component of the mirror pattern outside of the sum, and it is now explicitly accounted for by the linear potential ramp provided by u_0. The equation is applicable to both pixel wise and topographically patterned mirrors, and the elements in the sum only account for the spatial variations that resemble the surface topography.

The derived expression for the electric potential will be used in the calculation of the spatial phase modulation of a spread out beam that is reflected by this potential. The expression essentially describes a Fourier sum over all spatial frequencies that are contained in the mirror topography. The DC contribution outside the sum contains the linear potential ramp.

Qualitative influence of the pattern components on the phase modulation

We can now combine the obtained description of the mirror electric field [Eq. 3.23] and the WKB approximation [Eq. 3.5] and use this to obtain an initial qualitative understanding of the influence that the spatial frequency components of the mirror

pattern have on the phase of the reflected electron. According to the WKB approximation the phase $\phi(\vec{r}) \propto \int \sqrt{U(\vec{r})}dz$. Because of the square root dependence, a direct solution that yields the phase modulation amplitude [as defined in Eq. 3.6] as a function of the electric field modulation amplitude is not trivial. Instead, we will derive here an approximate analytical relationship between the mirror scalar potential and the resulting phase modulation and use this to obtain an initial understanding of the effect that the pattern frequency component has on the phase modulation amplitude. At a later stage a numerical implementation of [Eq. 3.6] will be provided which serves as the basis of our pattern calculations.

3

Starting from the WKB approximation, we cast [Eq. 3.5] into an alternative form:

$$\phi(x, y, z) = \hbar^{-1}\sqrt{2m_e eE} \int \sqrt{1 - U(x, y, z)/E}dz. \tag{3.24}$$

The square root inside the integral can be approximated by a power series for which the first terms are given below,

$$\sqrt{1-x} \approx 1 - \frac{1}{2}x - \frac{1}{8}x^2 - \frac{1}{16}x^3 - \mathcal{O}(x^4). \tag{3.25}$$

This approximation is valid and converges, provided that $|x| \leq 1$. Here, $x \equiv U/E$ satisfies the convergence condition, exactly up to the turning point of the beam where $U = E$ and thus the use of the approximation is justified.

The full evaluation of [Eq. 3.24] requires to obtain the integral of the polynomial terms x^n, for which we use the electric scalar potential that from [Eq. 3.23],

$$x^n = E^{-n}\left[F\cos(2\pi kr)\exp(-2\pi kz) + u_0\left(1 - \frac{z}{z_1}\right)\right]^n. \tag{3.26}$$

As the integral over the terms in [Eq. 3.26] is bounded by z_1 and z_R, it is noted that for terms $n > 1$ the exponential contribution quickly diminishes the cross terms, since

$$[\exp(-2\pi kz_R)]^n = \exp(-2\pi nkz_R) \rightarrow 0 \text{ for } 1/k \approx z_R, n > 1. \tag{3.27}$$

To understand at least qualitatively the effect that the single spatial frequency k has on the phase modulation, we can drop all but the first term in the expansion, even though this hinders us to quantitatively compare this initial result with any earlier work. The procedure yields the following result for the approximate integrated phase $\hat{\phi}$ along one axis,

$$\begin{aligned}\hat{\phi}(x_0,y_0,k) &= -\hbar^{-1}\sqrt{\frac{m_e e}{2E}}\int_{z_1}^{z_R}\Big\{F\cos\left(2\pi k r(x_0,y_0)\right)\exp(-2\pi k z)\\ &\qquad +u_0\left(1-\frac{z}{z_1}\right)\Big\}dz\\ &= -\hbar^{-1}\sqrt{\frac{m_e e}{2E}}\Bigg[\frac{F\cos(2\pi k r(x_0,y_0))\exp(-2\pi k z)}{-2\pi k}\\ &\qquad +u_0 z\left(1-\frac{z}{2z_1}\right)\Bigg]_{z=z_1}^{z=z_R}. \qquad (3.28)\end{aligned}$$

The net phase modulation amplitude for a single spatial frequency A_k [as defined in Eq. 3.6], is obtained by evaluating the result in [Eq. 3.28] at the crest and trough of the modulated electric potential, at which points $F\cos\ (2\pi kr) = \pm F$,

$$\begin{aligned}A_k &= \hat{\phi}(0,0,k)-\hat{\phi}(1/(2k),0,k)\\ &= -\hbar^{-1}\sqrt{\frac{m_e e}{2E}}\Bigg(\frac{F}{2\pi k}[\exp(-2\pi k z_R^{+})-\exp(-2\pi k z_R^{-})]\\ &\qquad +u_0\left[z_R^{+}-z_R^{-}-\frac{z_R^{2(+)}-z_R^{2(-)}}{2z_1}\right]\Bigg). \qquad (3.29)\end{aligned}$$

The contribution of the exponential terms at the lower boundary $z = z_1$ is set to zero explicitly here, since $1/k \ll z_1$, and $z_R^{\pm}$ labels the turning point for the crest and trough of the field. An analytical form of the turning point coordinates is given in Appendix B, and can be obtained by solving $U(z) = E$ by means of the Lambert-W function [42].

From the obtained expression it is confirmed that, at equal excitation parameter F, higher spatial frequency components in the mirror electrode attenuate faster and consequently can modulate the reflected beam less than low spatial frequencies. This behavior could also be understood from the increased sharpening of the blurring function in [Fig. 3.1] as the electron reflects closer to the mirror electrode. Conversely, one may state that the turning point coordinate $z_R \to z_0$ must be positioned closer to the mirror pattern in order to have high spatial frequencies in the pattern influence the modulation of the phase of the reflected beam. The linear dependence $A_k \propto F$ demonstrates that alternative to the former, the phase modulation in the reflected beam can also be increased by increasing the amplitude of the mirror profile, or the excitation potential in the case of pixelwise programmable mirrors.

3.2.3. Phase modulation as a function of pattern pitch and bias voltage

We have obtained a description of the scalar potential as a function of mirror topography [Eq. 3.29], as well as a relationship between the scalar potential and the phase

modulation [Eq. 3.5] as a function of spatial frequency [Eq. 3.6]. With that, we can now study the effect that the spatial frequency k, and the bias potential ΔU (with respect to the electron beam energy) has on the phase modulation amplitude of the reflected electron. For this, we are limiting ourselves to a maximum allowed electric field strength of 10 kV/mm, which is considered as a feasible value that should not result in electrical break down or arcing. In a setup that we are currently building [43], we aim at using a beam energy of 2 keV and hence the following results are also based on this value.

We have already found [Fig. 3.3] that the phase modulation amplitude must be kept small, and based on this we searched for a parameter space that fits this requirement. We consider that for a mirror pattern, spatial frequencies in the range of $k_0 \in [0.5 \cdots 10]\ \mu\text{m}^{-1}$ can be manufactured for instance with ion beam lithography. In [Fig. 3.5] we show the phase modulation amplitudes that can be realized in this range of spatial frequencies, as a function of profile height amplitude and bias potential (in volt) with respect to the beam energy. This data has been obtained for a 2 keV electron beam energy and a linear field strength of 10 kV/mm. As a general trend, we observe an increase in phase modulation amplitude, as a function of both decreasing spatial frequency (increasing pattern pitch), as well as decreasing bias potential. An increase of the profile height amplitude is seen to lead to an increase of the phase modulation amplitude, and consequently to phase rollovers of 2π at increasing height values.

The obtained data indicates the sensitivity to phase modulation that may arise for instance due to non-flatness of the electrode wafer source material. This non-flatness may be introduced as a result of mechanical stress inside the material, and from the data shown in [Fig. 3.5] we see that this may especially pose a limitation for very low spatial frequency surface height modulation.

3.2.4. Mirror pattern as a function of target phase distribution

In a practical application of patterned electron mirrors, it is likely that the mirror pattern will be based on a desired or 'target' phase distribution $\phi_{\text{target}}(x, y)$ in the near field (diffraction plane). By obtaining the Fourier transform $\Phi_{\text{target}}(k)$ of this target distribution, the phase modulation amplitude $A_k = |\Phi_{\text{target}}(k)|$ of the target distribution is directly obtained in terms of the spatial frequencies that form the mirror pattern.

We make use of the proportionality $A_{k_0} \propto F \equiv \delta_k$, such that the reference pattern amplitude δ_0 [for instance, $\delta_0 = 1$ nm is shown in Fig. 3.5(b)] can be scaled directly to match the phase modulation amplitude A_k, by solving for δ_k in

$$\Phi_k = \frac{\delta_k}{\delta_0} \phi_{\text{WKB}}^{[\delta_0]}. \tag{3.30}$$

In this equation, $\phi_{\text{WKB}}^{[\delta_0]}$ is the data set that contains the phase modulation amplitude as a function of bias voltage and spatial frequency of the mirror pattern, at a fixed reference profile amplitude δ_0 as shown before in [Fig. 3.5].

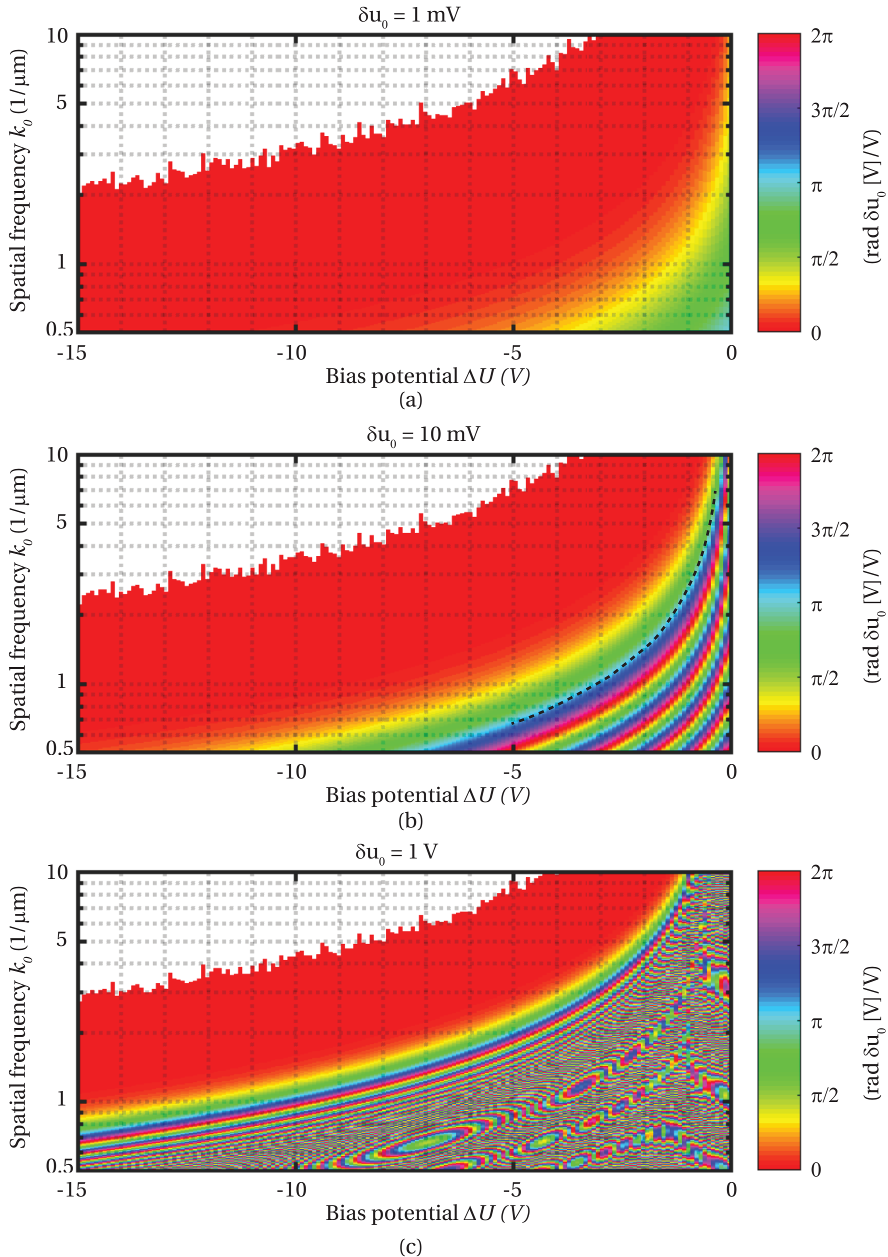

Figure 3.5: Phase sensitivity of a reflected plane wave as a function of the bias potential (with respect to the beam energy) and spatial frequency component of the pattern, for a reference profile pixel voltage amplitude δu_0 of (a) 1 mV (correspondents to 1 Åheight variation), (b) 10 mV (correspondents to 1 nm height variation), and (c) 1 V (correspondents to 100 nm height variation). A free electron energy of $E = 2$ keV and a linear field strength of 10 kV/mm is used in the calculation. The dashed black line in (b) indicates the line of constant phase that is used for the study of sensitivity to energy spread. Phase wrapping is performed on data that corresponds to a phase modulation greater than 2π.

When the scaling is performed for each spatial frequency of the target phase distribution, the obtained pairs $\{\Phi_k, \delta_k\}$ return the complete description of the mirror pattern in Fourier space. The pattern is then constructed in real space through a Fourier sum

$$P(x,y) = \sum_{(n,m)} \delta_{(n,m)} \cos\left(2\pi[k_{n,x}x + k_{m,y}y] + \angle\Phi_{k,(n,m)}\right). \tag{3.31}$$

The electric potential in front of the mirror substrate can be reconstructed in a similar approach.

3

3.2.5. Chromatic effects as a function of pattern parameters

Practical electron beams contain an inherent energy spread (about 0.6 eV for Schottky sources), and the value of this spread can be reduced by means of beam monochromatizating at the expense of beam current. The energy spread in the incident electron beam results in a deviation from the nominal turning point coordinate (z_R). As the modulation of the electric field decays exponentially as a function of this coordinate [Eq. 3.23], the resulting phase modulation will deviate from the nominal target value.

We computed the effect of the beam energy spread through the WKB approximation. The calculation is performed on the basis of the data that was shown in [Fig. 3.5(b)] for a reference profile height of 1 nm. From this data, coordinate pairs of bias potential and spatial frequency $\{U_{\text{bias}}, k_0\}$ were collected that provide π phase shift at the nominal beam energy (the dashed black line in the plot). Next, the WKB approximation is performed numerically for the obtained parameter pairs, at varying beam energies in a range $E = E_0 \pm \Delta E_0$.

The obtained phase modulation as a function of the energy deviation ΔE_0 with respect to the nominal beam energy E and spatial frequency k that was obtained this way is shown in [Fig. 3.6]. This data indicates an increased sensitivity for phase dispersion towards higher spatial frequencies of the mirror pattern, and at increased energy deviation. Notably at spatial frequencies above 2 μm^{-1} a complete phase rollover of 2π already occurs within the 1 V analysis domain. This result suggests that it is necessary to monochromatize the beam. In addition, the data shown motivates the use of a high linear electric field strength as this leads to a reduced spacing between the equipotential surfaces that reflect the slower and faster parts of the beam. A linear field strength of 10 kV/mm that we used in the above analysis is generally considered as feasible in an electron optical setup.

3.3. Amplitude and phase modulation with electron mirrors

The electron mirror is the reflective counterpart of the transmission phase plate that is used in transmission electron microscopy. As the electron mirror fully reflects the incident wave front, the amplitude of the reflected wave front cannot be modulated

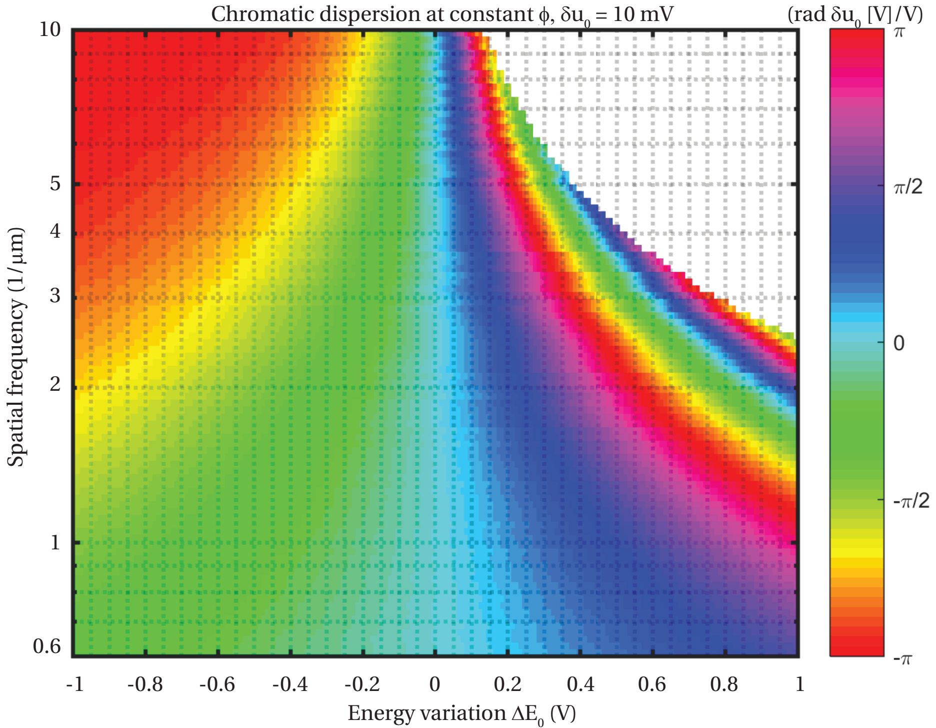

Figure 3.6: Phase sensitivity of the reflected electron as a function of energy variation in the incident beam, for a range of spatial frequency components. Computations are performed for an equal target phase value of π rad, for data points that are indicated by the dashed black line in [Fig. 3.5(b)]. The color map labels the deviation of the phase as a function of energy variation ΔE_0 in the incident beam. Data obtained for a fixed profile amplitude of 1 nm, 2 keV nominal beam energy and linear field strength $E_z = 10$ kV/mm.

at the mirror plane. A single electron mirror can thus be used for phase modulation only, and the effect of this phase modulation appears as an amplitude contrast at a diffraction plane of the mirror. This is good enough for many applications, however, in order to fully control the wave front, not only phase but also amplitude modulation must be realized.

Amplitude modulation in transmission optics is realized by using a comparatively thick amplitude mask that partially blocks the beam. This approach is not viable in the context of mirrors, as no absorption processes take place in front of the mirror. It is however possible to express the modulated phase of a wave front as amplitude contrast at a plane that is conjugated to that of the mirror, by means of defocusing the electron at this conjugate plane. The effect of a defocus of the beam at the conjugated plane is given by the phase contrast transfer function $\mathrm{CTF} = \sin(\chi(u))$, in which [44],

$$\chi(u) = \frac{2\pi}{\lambda}\left(\frac{\Delta f \lambda^2 u^2}{2} + \frac{C_s \lambda^4 u^4}{4}\right). \tag{3.32}$$

Here, λ is the wave length of the electron, u the spatial frequency component of the modulated wave front, and Δf the amount of defocus. The second term inside the brackets accounts for spherical aberration (C_s) of the imaging system in between the two conjugate planes.

3

When we position a second mirror at the plane conjugate to that of the first mirror, the wave front at a later image plane of the microscope is related to the sum of the individual spatial phase contributions ϕ_{M1} and ϕ_{M2} due to mirror M1 and mirror M2,

$$\psi_{out} = \mathcal{F}\left\{\psi_{in} \exp(i[\phi_{\mathrm{M1}} + \phi_{\mathrm{M2}}])\right\}. \tag{3.33}$$

Here, $\mathcal{F}\{\cdot\}$ denotes a Fourier transform. From this expression it is apparent that only one mirror is in principle sufficient to perform phase only modulation, since the contributions of ϕ_{M1} and ϕ_{M2} to the output wave front are interchangeable and add linearly.

If we now provide a defocus Δf at M2, then the phase modulation due to reflection at mirror M1 expresses as an amplitude contrast at mirror M2. Mirror M1 is then used to modulate the amplitude of the wave front at mirror M2, and mirror M2 is used to perform the phase modulation. It then becomes possible to arbitrarily modulate both the phase and the amplitude of the electron beam at a later image plane of the microscope. An alternative mode of operation would require to place mirror M2 in the Fourier plane of mirror M1. One can then adjust the turning point of the distinct diffraction spots in front of mirror M2, that are formed as a result of the phase modulation at mirror M1.

3.3.1. Virtual phase plate based on two electron mirrors

A practical realization of the virtual phase plate requires the positioning of two electron mirrors and additional lenses inside the electron microscope column. An extensive discussion of integrating multiple electron mirrors in a microscope is provided recently by Dohi and Kruit [32]. From that work, it is concluded that through the use of miniature electron optical components it is possible to position the two mirrors at an axis parallel to the optical axis of the microscope. The coupling of the microscope and mirror axis trajectories can be performed by an electrostatic deflector, and two miniature Wien filter type deflectors. By making use of miniaturized optical components, the deflection angles can be kept small, such that deteriorating effects from deflection dispersions can be avoided.

In [Fig. 3.7] we show a schematic design for a virtual phase plate. In this schematic, the two mirrors are positioned opposite of each other on a common axis and the mirror patterns face each other. The mirror axis is parallel with the optical axis of the microscope. The coupling of the beam trajectory between the

microscope axis and mirror axis can be performed with an electrostatic deflector that is positioned at the optical axis on the halfway plane in between the two mirrors, referenced to as the common cross-over plane (C.C.P.). The beam trajectory on the mirror axis demands a deflection towards and away from the mirrors that depends on the sign of the velocity vector ($\vec{v}$) of the beam. This sign dependent deflection could be realized by deflectors with crossed electric ($\vec{E}$) and magnetic ($\vec{B}$) fields if these fields are both perpendicular to each other and the beam path. When the electric and magnetic fields in such deflector satisfy the Wien condition ($\vec{E} = \vec{v} \times \vec{B}$), the resulting force on the electron beam enables either a straight passage or a deflection path for the beam, depending on the direction of incidence. The recent development of a miniature electron beam separator with two parallel axes can explicitly allow for the close proximity of both axes in the described scheme [31].

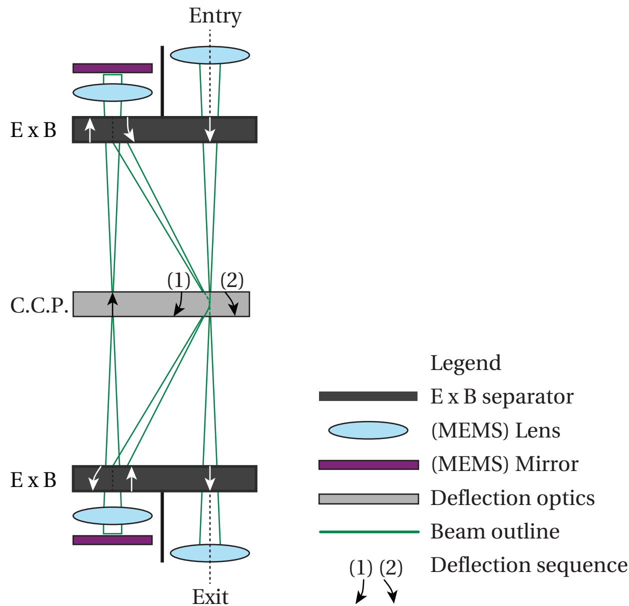

Figure 3.7: Design of a double mirror system for integration inside (the column of) electron microscopes. The beam enters the setup on the microscope axis from the top. Coupling to the mirror axis is performed at the common crossover plane (C.C.P.) by means of an electrostatic deflector. Two Wien filter type beam separators ($E \times B$) are used to perform the direction-of-incidence dependent deflection at the mirror axis. After reflection at both mirror planes, the beam is coupled back to the optical axis and exits the setup on the microscope axis downwards, now with phase and amplitude modulation. Schematic reproduced from [31].

Remarkably, when the Wien condition for straight passage is also enforced onto the straight passages on the optical axis near the entry and exit, a full trip of a beam through the double mirror system does not suffer from deflection dispersion in first order at the common cross-over plane. The system can be miniaturized by making use of MEMS technology, such that the deflection angles can be kept small (below 50

mrad) and thus suppressing deflection dispersions [32]. An in-depth electron optical and mechanical description of the system is provided in [43].

3.4. Numerical methods

We use MATLAB for all numerical calculations. The numerical work consists of the following subroutines:

- WKB approximation solver.
- WKB lookup table interpreter.
- Fresnel propagator.
- Target phase and amplitude solver.
- Scalar potential constructor.

3

In the following sections we discuss the specifics for implementing the above listed routines into MATLAB.

3.4.1. WKB approximation solver

The WKB approximation [Eq. 3.5] is numerically evaluated for a single parameter set consisting of spatial frequency (k_0), pattern amplitude (δ_0), cap electrode spacing (z_1) and excitation parameters beam energy (E), and pattern potential (U_{pattern}). The WKB approximation is calculated along two trajectories that run parallel to the propagation (z) axis and coincide with a crest and through of the considered spatial frequency, in accordance with [Eq. 3.6].

The WKB approximation integral is computed over the full length of the two axss, and is terminated at points z_0 and z_1. To this end, we first calculate the integrated momentum along the both trajectories. This procedure generates complex valued results, as the argument to the square root becomes negative as $|z| < |z_R|$. We only keep the real valued part, as this represents the data in front of the turning point.

Listing 3.1: Definition of axial momentum for crest and trough field.

```
1 % Zero pitch potential
2 U_zero = @(z) Up*(1+1/d*(+delta*exp(2*pi*kp*z)-z));
3 % Half pitch potential
4 U_half = @(z) Up*(1+1/d*(-delta*exp(2*pi*kp*z)-z));
5
6 % Electron momentum per axis
7 p_zero = @(z) real( sqrt(2*me*ee*(E-U_zero(z))) );
8 p_half = @(z) real( sqrt(2*me*ee*(E-U_half(z))) );
```

As the non-linear behavior of the electric potential is confined in the region close to the turning point $z_R \approx z_0$, the numerical integration is performed on logarithmically spaced waypoints, with increased waypoint density near z_R.

Listing 3.2: Definition of axial momentum for crest and trough field.

```
1 % Definition of waypoints for integration.
2 waypoints = -logspace( log10(-z1), -9,
     number_of_waypoints);
3 % Numerical integration and phase extraction.
4 int_zero = 2/hbar*integral(p_zero, z1, z0, 'WayPoints',
     points);
5 int_half = 2/hbar*integral(p_half, z1, z0, 'WayPoints',
     points);
6 % Phase in correspondence with [Eq. (3.5)]
7 phi = int_zero - int_half;
```

3.4.2. WKB lookup table generator

The WKB lookup table data, as shown for three reference amplitudes in [Fig. 3.5] is generated by repetitive calls to the WKB approximation routine. The lookup tables that are used for this work are obtained for parameter space $\mathcal{E} = 2$ keV, linear field strength $E_z = 10$ kV/mm ($z_1 = -200$ μm) and 10^5 waypoints in the WKB approximation integral. The construction of the lookup table data is a relatively time consuming task, but has to be performed in principle only one time. We note that the use of a lookup table reduces the calculation time at a later stage, when the data is used to construct mirror topographies.

Listing 3.3: WKB lookup table generator.

```
1 for k0 = list_k0
2     for Up = list_Upattern
3          WKB_data(i_k, i_U) = WKB_approximation( k0,
             delta0, 'PatternPotential', Up, 'BeamEnergy',
              E0, 'ApertureSpacing', z1, '
             NumberOfWaypoints', 1e5);
4     end
5 end
```

The generated data matrix `WKB_data` and the associated list of spatial frequencies and bias potentials are stored and used as lookup table during the pattern reconstruction. We make use of linear interpolation in the spatial frequency data points in order to compute a pattern frequency component that is not part of the original lookup data.

Listing 3.4: Obtaining the profile scaling parameter for a target phase.

```
1 % Find interpolated reference amplitudes (for 1 AA).
2 phase_per_reference_amplitude = interp1(k0, WKB_data,
     pattern_k0_values);
3 % Scale with respect to the required angle.
4 amplitudes = delta0 ./ phase_per_reference_amplitude .* (
     myPhaseTerms);
```

3.4.3. Fresnel propagator

The relationship between image plane (ψ_1) and diffraction plane (ψ_M) distributions is described by a Fresnel propagation and intermediate lens action [41],

$$\psi_M = \underbrace{\left(\psi_1 * \exp\left[-i2\pi k_e \frac{R^2}{2f}\right]\right)}_{\text{Propagation}} \times \underbrace{\exp\left[i2\pi k_e \frac{R^2}{2f}\right]}_{\text{Focusing}}. \tag{3.34}$$

In the equation, the wave front ψ_1 at the common cross-over plane is convoluted ($*$) with a propagation function that depends on the modulus of the beam wave number (k_e), transverse radial coordinate perpendicular to the optical axis (R) and focal length (f) of the lens, and next focused by the focusing term.

Listing 3.5: Fresnel propagation from image to diffraction plane.

```
1 % Based on Cowley (1975) Ch. 3, Fresnel propagator.
2 prop = exp( -1i*2*pi*k*(X.^2+Y.^2)/(2*f));
3 lens = exp(  1i*2*pi*k*(X.^2+Y.^2)/(2*f));
4 % Obtain the complex wave function at the diffraction
    plane
5 % This calculation may take a while, depending on the
    image size.
6 diffraction_plane = conv2(psi1, prop, 'same') .* lens /
    sqrt(numel(lens));
```

3.4.4. Target phase and pattern solver

The Fourier transform of the phase distribution at the mirror plane is obtained and the complex valued terms provide the basis for the pattern reconstruction. For each phase value of the Fourier term and associated spatial frequency, the WKB lookup is performed on the magnitude of the Fourier term. This provides the amplitude for this mirror topography contribution. The complex angle of the Fourier term is used in the reconstruction of the mirror pattern in order to provide proper relative positioning of the wave components. The number of Fourier terms that is considered is limited by a threshold value that can be set arbitrarily close to zero. The threshold allows to limit computation time by skipping very high frequency components that add virtually no phase to the reflected beam, or that would otherwise result in an excessive pattern profile height.

Listing 3.6: Relating phase to pattern topography.

```
1 reduced_diffraction_plane = angle(diffraction_plane);
2 
3 % Obtain spectral components of the angle distribution.
```

```
spectral_components = fft2(reduced_diffraction_plane) /
    numel(reduced_diffraction_plane);
spectrum = fftshift(spectral_components);

% Loop over all spectral components
for row = 1:length(ky)
    for col = 1:length(kx)
        thisPhi = abs(spectrum(row,col));
        thisK   = sqrt( kx^2 + ky^2 );
        % WKB lookup
        amplitude = WKB_lookup(WKBdata, thisPhi, thisK,
            Up);
        % Add the geometrical pattern angle to this value
        GeoAngle = angle(spectrum(row,col));
        % Save for pattern reconstruction
        reconstruct(end+1,:) = [ky kx amplitude*exp(1i*
            GeoAngle)];
    end
end
```

The mirror topography is reconstructed based on the coefficients that were obtained in the previous step. For each spatial component, the contribution to the topography is determined as a Fourier term.

Listing 3.7: Reconstructing the mirror topography.

```
%  reconstruct = (3x1) double complex [ky kx amp*exp(1i*
    phi)]
full_field = zeros(size(X));
for index = 1:size(reconstruct,1)
    el = reconstruct(index,:);
    ky = real(el(1));
    kx = real(el(2));
    % Verified reconstruction sum.
    component = abs(el(3)) .* ( cos( 2*pi*(kx.*X + ky.*Y)
        + angle(el(3)) ) );
    full_field = full_field + component;
end
% Scale the field to units of nanometer.
full_field = 1e9 * fftshift(full_field);
```

3.4.5. Scalar potential constructor

The shape of the scalar electric potential, as a function of pattern topography is calculated in accordance with [Eq. 3.23]. We make use of anonymous function declarations in MATLAB for this calculation.

Listing 3.8: Scalar potential reconstruction.

```
% Bias at analysis point (zz), assuming U1 = 0.
U0 = Up*(1-(zz/z1));
% Modulated potential as Anonymous function.
UU = @(X,Y,zz, kx, ky, amp, theta)          b@x          ...
        amp .* cos( 2*pi*(kx.*X + ky.*Y) + theta ) *    ...
        exp(-abs(zz)*2*pi*sqrt(kx^2+ky^2) );

for index = 1:size(reconstruct,1)
   % Row elements of reconstruction array.
    el = reconstruct(index,:);
    ky = real(el(1));
    kx = real(el(2));
    amp = abs(el(3));
    theta = angle(el(3));
    % Calculate contribution for this term.
    component = UU(X, Y, zz, kx, ky, amp, theta);
    potential = potential + component;
end
```

3.5. Application examples for electron mirrors

We demonstrate possible applications for patterned electron mirrors. Throughout this section we assume a beam energy of 2 keV and a linear electric field strength of 10 kV/mm in the mirror region. These numbers are based on a proof of principle experiment that we are currently designing.

3.5.1. Zernike phase mirror

The use of a Zernike phase plate in TEM results in a change to the contrast transfer function provided in [Eq. 3.32] as given by [44],

$$\mathrm{CTF} = \sin\left(\chi\left(u\right)\right) \rightarrow -\cos\left(\chi\left(u\right)\right) \;\text{ for } u > u_h. \tag{3.35}$$

In words, the equation states that the contrast is enhanced from near-zero to near unity for spatial frequencies u that exceed the modulus of the spatial frequency u_h of the central hole in the phase plate. The mirror equivalent of such Zernike phase plate would require an alteration in the reflected beam such that the unscattered (on-axis) component is shifted $-\pi/2$ rad with respect to the scattered wave components.

In the past it is already suggested that this could be achieved with a pixel wise programmable mirror simply by applying a bias in the order of 70 mV (assuming a linear field strength of 10 kV/mm) to the central pixel [26], and here we apply the method that we derived above to the same model system. As we only aim to shift the phase of the unscattered beam, the desired phase profile shows resemblance with a top hat function and it should thus be expected that a large number of spatial frequencies is involved in the resulting mirror topography.

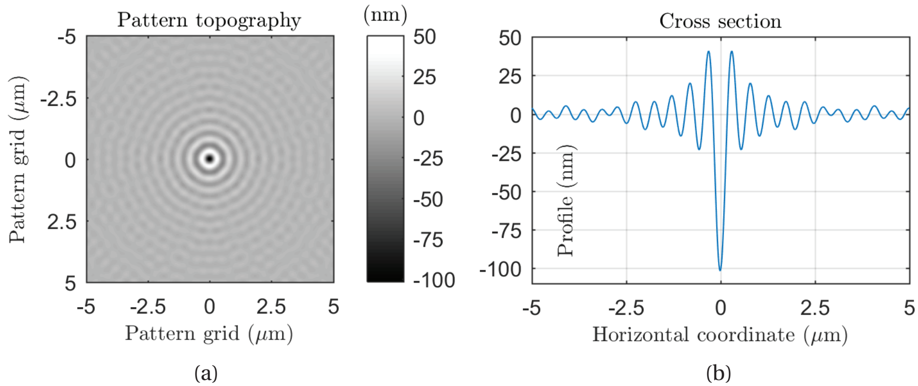

Figure 3.8: Mirror topography for Zernike phase manipulation. (a) Full field reconstruction of the pattern, for a bias potential of 7 V with respect to the beam energy. (b) Cross section of the reconstructed pattern, through the center of the topography.

The result of the analysis is shown in [Fig. 3.8] for an assumed 200 nm hole size in the Zernike phase plate. We observe a peak in excitation close to the optical axis that is representative of this hole size, followed by a damped oscillation of higher harmonic contributions. It should be noted that the effective value for u_h is determined in the case of an electron mirror by the focal distance of the mirror-lens system towards the image plane. For instance, one could increase the spread out the wave front over the mirror surface, thereby effectively increasing the magnification. If the mirror topography is not scaled laterally by an equal factor, this effectively changes the range of spatial frequencies in the reflected wave front that are phase shifted by the Zernike mirror pattern.

3.5.2. Tuning diffraction efficiency

The origin of this work stems from the question if interaction-free measurements [45] can be performed with electrons [46] in a practical manner, in order to reduce electron beam induced radiation damage [47] in electron microscopy [48]. Subsequent proposals for designs of a quantum electron microscopes [49, 50] that could perform this type of experiment introduces the need for a two-port diffractive element for electron beams [51]. The electron grating mirror is one means to this end, but in its current form suffers from the disadvantage of generating a two-sided diffracted beam, instead of the targeted one-sided first order diffracted beam [36].

Here we study how the diffraction efficiency of the intensity that is directed into the first order spot can be maximized, while at the same time keeping the intensity in the higher order spots to a minimum. We already discussed the effect of a single spatial frequency at the mirror pattern that would result from a sinusoidal pattern, and concluded that the intensity of the resulting diffraction spots are provided by the squared Bessel function of the respective diffraction order as a function of phase modulation amplitude (A_k) [ref. Eq. 3.9, and dashed line in Fig. 3.9].

The generation of the higher order diffraction spots could be in principle sup-

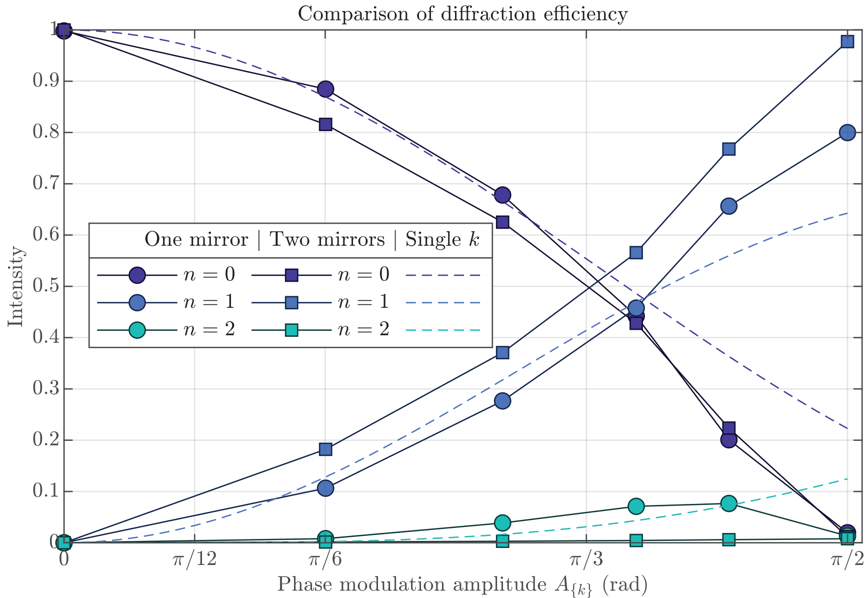

Figure 3.9: First order diffraction spot intensity dependence on the mirror patterning approach. The first order diffraction spot intensity at the image plane that results from the use of one spatial frequency in the mirror pattern (dashed line) can be increased by inclusion of higher order spatial frequencies into the pattern. We demonstrate the efficiency that can be reached when performing phase-only modulation with one patterned mirror (circles), and when performing phase and amplitude modulation by using two mirrors (squares). Shown intensities are the sum of positive and negative contribution per order.

pressed, by adding higher order spatial frequency components to the mirror pattern. These pattern components must cancel the out-of-phase contribution to their respective diffraction spot at the image plane, with respect to the higher harmonic spot that is due to the fundamental pattern frequency.

Numerically the pattern that is required for this is found by providing a target image plane distribution consisting of only a central spot and the two first order diffraction spots. The target phase of the central spot relative to the two first order diffraction spots is set to $-\pi/2$, which is a physical requirement for a first order diffracted beam when only a single mirror reflection takes place [also see sct. 3.2.1, and sct. 3.3]. The image plane distribution is then Fresnel propagated to the diffraction plane, in order to obtain the amplitude and phase modulation that must be provided for by the mirror pattern.

We have performed this computation using two different approaches. First, we considered the use of only one mirror, thus limiting ourselves to phase-only modulation. The obtained diffraction spot intensities that could be realized this way are plotted in [Fig. 3.9] with circle markers. The range of phase modulation amplitude values that are shown in the plot are realized by adjusting the ratio of the targeted

central and diffracted spot amplitudes at the image plane. The target image plane distribution is propagated towards the mirror plane, at which we obtain the plotted phase modulation amplitude as the largest absolute phase difference at this plane. Note that this definition for $A_{\{k\}}$ is somewhat broader than what we used before in [Eq. 3.6], where A_k was used to label for the phase modulation amplitude related to a specific spatial frequency k, instead of that of the entire spectrum $\{k\}$.

From the shown data it is observed, that by making use of an image plane target distribution (circle markers) instead of a single spatial frequency mirror topography (dashed lines), the first order diffraction efficiency is increased. However, we do observe that 20% intensity is still diffracted to higher order spots when the central beam becomes fully attenuated, although this may also be due to a limitation in the current numerical methods that we use. A possible explanation for this effect is given by the fact that at increasing attenuation of the central spot, the phase modulation amplitude that is responsible for the two first order diffraction spots increases. Consequently, this also leads to an increase of the higher order diffraction spot intensities at the image plane. In principle, the amount of phase that must be compensated to cancel the generation of the higher order beams is numerically known, and accounted for by the mirror pattern reconstruction. However, what is currently not accounted for in the reconstruction routine is the special case, in which the phase modulation amplitude correction of these higher orders exceeds the threshold phase of $\sim \pi/6$ rad [also see Eq. 3.9, and Fig. 3.3]. In that case, an iterative scheme must be used that also accounts for the resulting higher harmonics. This correction is not yet performed in the current work that is presented here.

Another effect that leads to the generation of the higher orders is the neglection of the amplitude contrast at the mirror plane. When we propagate the targeted image plane distribution towards the mirror plane, the resulting wave front distribution shows both an amplitude and a phase modulation. In the foregoing analysis, we were required to neglect the amplitude information and instead assume a uniform amplitude distribution at the mirror plane, as with a single mirror we can only realize phase modulation.

We can include the effect of amplitude modulation to our calculations, by making use of two mirror reflections. In the image plane reconstruction routines, we then assume that first mirror reflection enables the required amplitude modulation at the second mirror plane. With this modification in place, we can show that the diffraction efficiency is increased. This is indicated by the square markers in [Fig. 3.9]. From this, it is observed that all intensity of the central beam can be directed into the first order positive and negative diffraction spot.

For use as a beam splitter in Quantum Electron Microscopy, it is necessary that the intensity of the central beam is directed into only either the positive, or negative first order diffraction spot. Optically this would be performed by a blazed grating, which adds a linear phase ramp into the reflected wave front. Blazed grating diffraction has already been demonstrated in TEM with phase plates [52]. We have studied the feasibility of doing this with one electron mirror by providing a phase-only distribution at the mirror plane, and gradually increased the phase modulation amplitude of this phase ramp. We note that such computation can in principle

also be performed by starting out with a target wave front at the image plane and propagate this wave front towards the mirror plane. However, this would require a significant increase of the numerical grid at the image plane without any expected advantages in terms of accuracy of the wave front description at the image plane.

In [Fig. 3.10] the obtained intensity of the central spot (circles), blazed spot (rectangles), and other spots combined (triangles) is plotted as a function of the maximum phase modulation amplitude $A_{\{k\}}$ across the entire spectrum of the linear phase ramp at the diffraction plane. From this it is seen that a high diffraction efficiency can be obtained especially for weak or strong exchange of spot intensity between the central and blazed spot. The maximum intensity loss towards other orders is limited to 19% and is found when the intensities of the central and blazed spots are equal.

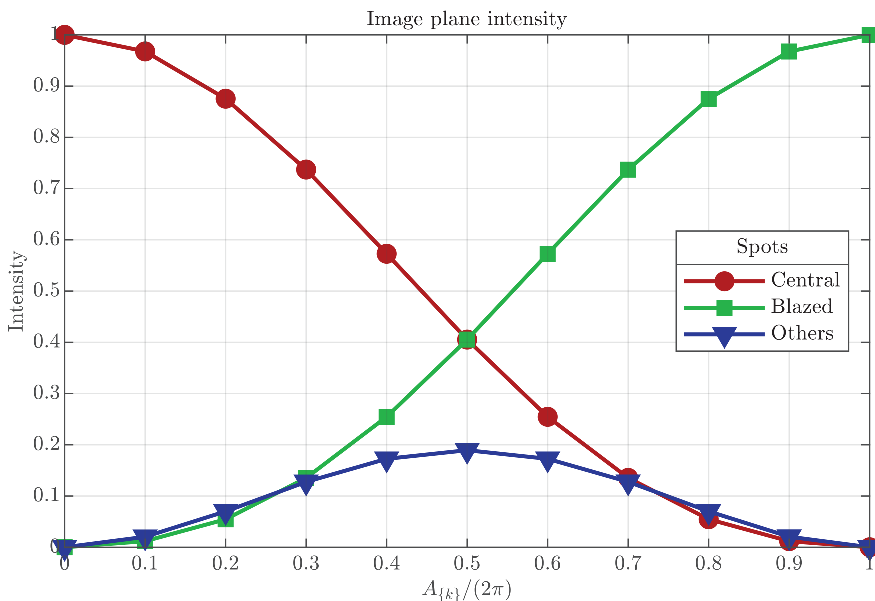

Figure 3.10: Blazed grating diffraction efficiency with one electron mirror, as a function of phase modulation amplitude $A_{\{k\}}$ of the linear phase ramp at the diffraction plane. The values of $A_{\{k\}}$ are realized by adjusting the ratio of the targeted central and blazed diffraction spot intensities at the image plane. The blazed spot intensity (squares) indicates the intensity of the first order positive diffraction spot.

A direct comparison of the potential variation near the turning point of the beam, in the case of (a) regular and (b) blazed diffraction is provided in [Fig. 3.11]. In the figure, the bold lines indicate the shape of the equipotential at the classical turning point of the beam. Each next equipotential is obtained in steps of 0.5 V, and these are included in the plot to demonstrate how the higher spatial frequency components in the field attenuate faster away from the mirror electrode than the slower spatial components. Also, from the shown equipotential lines the importance

of working with a beam with low energy spread can be directly understood, as the spatial components that create the characteristic shape of the equipotential lines attenuate within the range of energy spread of a conventional Schottky source that is not monochromatized.

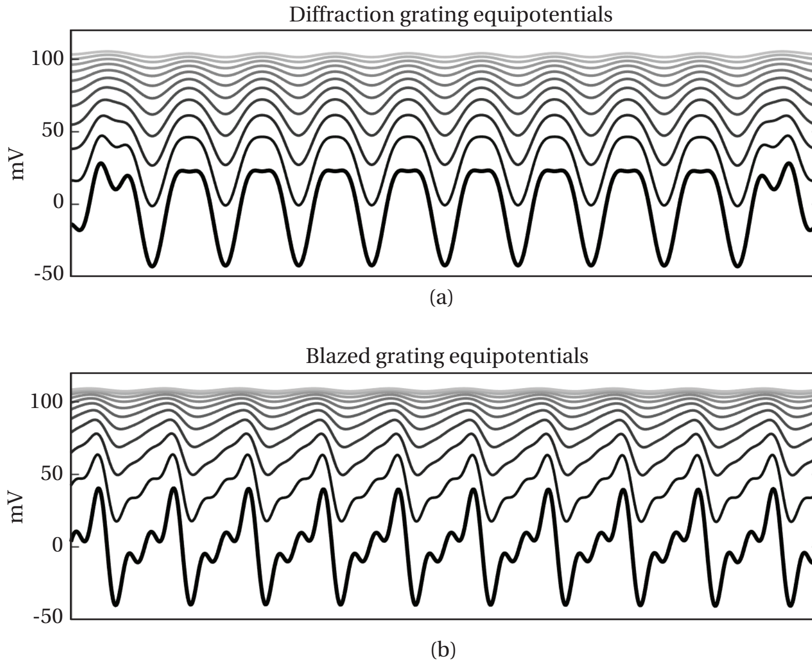

Figure 3.11: Comparison of the potential landscapes corresponding to (a) a regular diffraction pattern and (b) a blazed diffraction mirror pattern near the classical turning point z_R. The bold line plots the potential at the classical turning point (-2000 V), and each consecutive line is obtained in steps of 0.5 V.

For the regular diffraction we observe the fundamental spatial frequency that is associated with the first order diffraction, and near the classical turning point an additional higher spatial component is visible as well. It is the higher spatial component that provides attenuation of the undesired higher order beams that result from the fundamental frequency.

The equipotential lines that are associated to the blazed diffraction pattern exhibit a distinct (near)-linear slope. This is to be expected for blazed diffraction, as a linear phase ramp must be added to the reflected beam and the phase scales proportional to the square root of the potential. From the equipotential lines above the classical turning point the fast attenuation of higher spatial frequencies in the field is observed, and at approximately 5 V above the classical turning point only the fundamental frequency is distinctly visible.

3.5.3. Beam mode conversion

The conversion of plane waves into vortex beams has gained increasing interest in the recent decade. Vortex beams are solutions to the Schrödinger equation in cylindrical coordinates and are characterized by carrying an Orbital Angular Momentum (OAM, ℓ), which expresses itself through an azimuthal component in the wave front [15, 16].

Vortex beam generation in TEM can be realized both by using a phase plate, or an amplitude mask. On a phase plate, a spiral ramp is applied [15], where as in the case of an amplitude mask a diffraction grating pattern with a dislocation at the optical axis is used [16]. The number of dislocations N then dictates the Orbital Angular Momentum (ℓ) that is added into the diffracted beam.

With the use of one mirror, we can only adjust the phase of the reflected electron and thus the proper mirror pattern can be obtained by modeling a spiral phase pattern at the mirror plane. Such phase pattern is shown in [Fig. 3.12(d)] and corresponds to $\ell = 3$ here. In [Fig. 3.12(a)] we show the equivalent phase pattern that corresponds to a diffracted beam with $\ell = \pm 2$ in the first order.

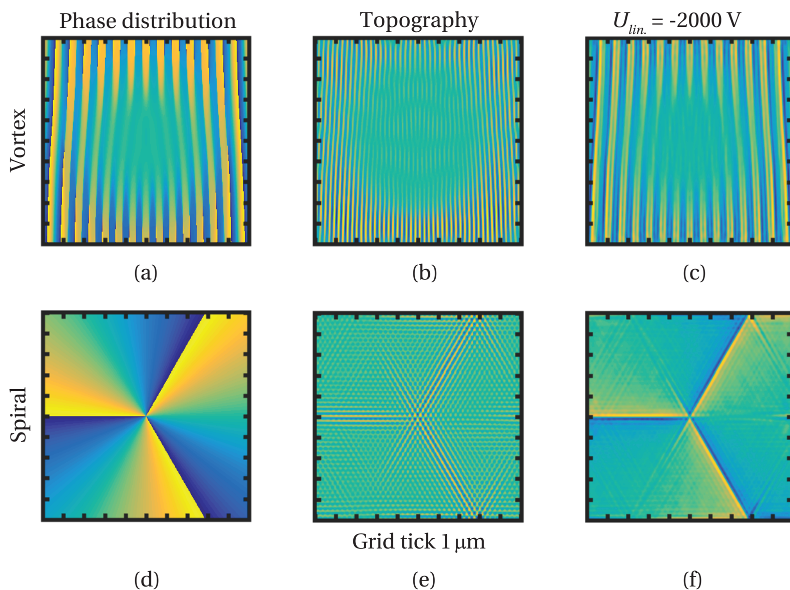

Figure 3.12: Two methods for beam mode conversion from plane wave illumination to an orbital angular momentum carrying beam. Reflection on the vortex pattern (a-c) generates a diffraction pattern, in which the diffracted beams carry orbital angular momentum. Two dislocations are applied in this pattern, leading to a lowest value $\ell = \pm 2$ in the reflected beam. Reflection on the spiral pattern (d-f) generates an on-axis spot with orbital angular momentum, with $\ell = 3$ in the presented case. (Last column) For both patterns, the potential at the classical turning point is shown and these display resemblance to the phase or amplitude masks that would produce a similar effect in TEM. Colormap ranges: phase distribution $[-\pi, \pi]$, topography ± 400 nm (vortex) and ± 200 nm (spiral) and ± 2 mV at the classical turning point. Results obtained for pattern bias potential of 3 V.

The reconstructed mirror pattern topographies are shown in [Fig. 3.12(b, e)] and

consist of high spatial frequency components with an amplitude of up to ±400 nm (b) and ±200 nm (e) at the edges. Near the center of the vortex pattern, the profile height amplitudes are smaller and range around ±20 nm. We note that overall, the spatial frequencies in the mirror pattern appear higher than those observed at either the phase pattern at the diffraction plane, or the potential variation near the classical turning point. This is explained by the attenuation of high frequency components, which occur faster away from the mirror electrode compared to the lower frequency components. Hence, the profile amplitude of these higher spatial frequencies at the mirror electrode are relatively high in comparison to the lower spatial frequencies, in line with the observations made in [sct. 3.2.3]. The effect of the high spatial frequency components in the pattern quickly attenuates in the electric field, as can be observed from the potential variation around the averaged coordinate of the turning plane [Fig. 3.12(c, f)]. At this plane, a potential modulation of ±2 mV remains, and the shape of the potential variation mimics closely to that of the targeted phase distribution at this plane.

3.5.4. Arbitrary phase and amplitude modulation

We conclude this section with a demonstration of the generality of electron beam modulation with patterned mirrors. For this, we attempt to create a probe at the image plane after a double mirror reflection that shows resemblance to the institute logo of Delft University of Technology. The logo contains a flame, and our goal here is to obtain the mirror patterns that are required to realize the amplitude and phase modulation as shown in [Fig. 3.13(a)]. As a first step, the targeted image plane distribution is Fresnel propagated to the first mirror plane. This provides us with the amplitude and phase distribution that we must imprint into the beam. However, note that a mirror cannot be used for near field amplitude modulation. Hence, we consider here the situation where mirror 2 is positioned in the Fourier plane of mirror 1. We can then realize the required amplitude distribution in front of mirror 2, by means of phase modulation at mirror 1. We then use the reflection at mirror 2 to add the phase modulation, such that at a Fourier plane of mirror 2 the target wave front is realized.

In [Fig. 3.13(b)] we show the Fourier spectrum of the phase components that must be added by mirror 2. From this data it is seen that a large number of spatial frequencies are required in the mirror pattern. Note, however, that all of the required phase modulation amplitudes satisfy $A_k \leq 0.2$ rad, which in turn is well below the limit for addition of multiple spatial frequencies of $\pi/6$ rad as set forth in [sct. 3.2.1]. Based on this spectrum, the mirror topography is constructed and the result of this is shown in [Fig. 3.13(c)]. The resulting modulation of the electric potential in the vicinity of the classical turning point, corresponding to the plane at which the linear electric potential equals -2 kV, is shown in [Fig. 3.13(d)].

Admittedly, this result is not very intuitive as it does not clearly resemble any feature of our targeted image plane distribution. In order to verify the effect on the beam at the image plane after the double mirror reflection, we reconstruct the wave front directly after the reflection at mirror 2 through [Eq. 3.8], and by multiplying this result with the amplitude distribution that resulted from the reflection at mirror

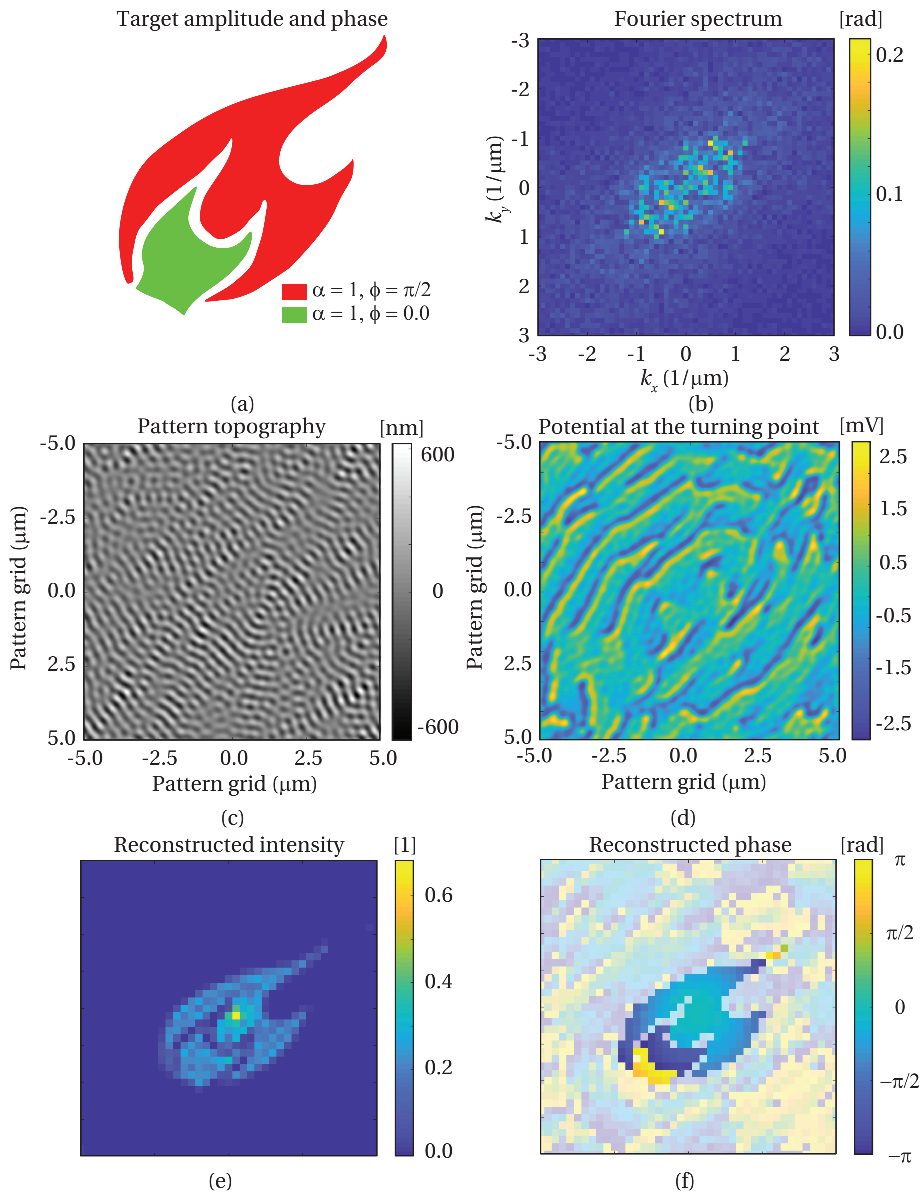

Figure 3.13: Demonstration of controlled amplitude and phase modulation with two patterned mirrors. (a) Target amplitude and phase at the image plane. (b) Fourier spectrum of target phase modulation amplitude in front of mirror 2. (c) Pattern topography of mirror 2. (d) Electric potential variation in the vicinity of the classical turning point plane of mirror 2. (e) Reconstructed intensity at the image plane after double mirror reflection. (f) Reconstructed phase distribution at the image plane after double mirror reflection, with partial transparency at pixels for which the reconstructed intensity is less than 0.05 for visual clarity.

1, as we currently do not yet have a proper model for propagating the reflected beam from mirror 1 onto mirror 2. The obtained intensity and phase distribution at the image plane are shown in [Fig. 3.13(e-f)] and here we can identify what shows a resemblance with the targeted image plane distribution. The recovery of the targeted image plane distribution as demonstrated here provides to us an initial evidence for the feasibility of controlled wave front shaping with two patterned electron mirrors.

3.6. Discussion and conclusion

We outlined above that in principle it is possible to gain control over the electron beam wave front through the application of two patterned electron mirrors. This may be referenced to methods in light optics, where the use of two spatial light modulators (SLMs) and polarizers [53], or the use of multiple deformable mirrors [54] enable full spatial beam control.

The effect that a mirror pattern has on the phase of the reflected wave front can in principle be obtained through an existing convolution model, that we discussed in [sct. 3.2.1]. Lichte made use of this model when he successfully demonstrated its use for the measurement of the roughness of 'supersmooth' electrodes by using electron mirror interference microscopy [25]. The validity of this method is however limited to situations where the mirror roughness is much smaller than the distance of closest approach of the electron beam towards the mirror electrode. This is generally not the case for electron mirrors that are intentionally being patterned, especially for the micromirror setup that we are currently designing [43].

For this reason, we have generalized the method by numerically obtaining the phase difference through application of the WKB method. In fact, our method of integrating the electric field along the crest and through of the modulated field to obtain the phase modulation shows some form of analogy to the experimental work of Lichte, when one considers the integral along the crest and trough as the object and reference beam in an interference microscope. Regardless, for this we must rely on the validity of the WKB approximation in the vicinity of the turning point of the electron beam. The validity of this has been suggested by our earlier calculations [36] on grating mirrors that are characterized with a single pitch value. We have compared our WKB method to the example data of figure 5 in [25]. For this comparison, we estimated from the cited work a mirror field length of $z_1 = 6$ mm and found a good agreement, indicating that our method converges to the convolution model at large values of pitch. At the same time, we have demonstrated empirically that the validity of the convolution model breaks down whenever $z_R \leq 2h$, i.e., when the beam approaches the mirror pattern to within the height variations inside that pattern.

Further, we have assumed the generality of the method and have motivated that linear addition of the effect of multiple spatial frequencies in the mirror topography is at least valid when the individual components do not add more than $\pi/6$ rad phase modulation to the reflected wave front. If we prefer to include stronger phase modulation terms, this would require some form of iterative scheme that removes the unwanted higher order spots that form during the first step of the topography construction.

The use of replaceable, or otherwise dynamically programmable mirror patterns would significantly increase experimental flexibility. Although we recognize that this is technologically challenging, we also stipulate the advantage that the backplane of the mirror does not obscure the beam path, thus leaving plenty of access for any control logic or circuitry. A good deal of progress with programmable mirrors is made in the past with the development of Reflective Electron Beam Lithography (REBL) [27]. Albeit that the geometry of the mirrors in the REBL deviate from our implementation, since the REBL mirror contains an individual Einzel lens in front of each pixel, it has demonstrated the use of CMOS technology for (individual) addressing of mirror pixels through the back plane of the device. If a practical linear mirror field strength of $E_z = 10$ kV/mm is assumed, this yields a correspondence between pattern profile amplitude and pixel potential of $U = E_z\delta/\delta_0 \approx 10$ mV/nm. The use of pixelwise programmable mirrors instead of relying on a topographic pattern would require a smoothness that is less strict than that of an etched pattern, under the assumption that each pixel can be addressed individually.

The advantage of a pixelwise programmable mirror instead of a topographic patterned mirror is also apparent from the ability to correct for mechanical tolerances. Tilt is the simplest form of a mechanical error that can arise in a mirror setup. The effect of tilt is a linear field strength gradient perpendicular to the optical axis. This resembles a dipole field that acts perpendicular to the electron beam propagation and results in a sideways beam deflection.

The effect of this dipole field on the beam deflection can be approximated. For an assumed mirror tilt angle θ, and beam width w, the dipole strength along the propagation axis becomes $E_2 = U\theta w/(z_1(z_1 + \theta w))$. Here, z_1 is the length of the mirror field, and U the mirror electrode bias potential. In most practical cases, $\theta w \ll z_1$. For an average beam energy in the mirror field equal to half the electrode potential, the deflection angle in the field may then become approximately given as $\alpha \approx 2\theta w/z_1$ if we assume a top hat field distribution. In a setup that we are currently developing, we have $w = 10$ μm, and $z_1 = 200$ μm, which leads to $\alpha \approx 0.1\theta$, i.e., the deflection due to a tilt error equals roughly 10% of that tilt error. With the use of silicon based mirror electrodes and flat glass spacers, the tilt error is easily limited below $\theta \leq 1$ mrad.

Other optical effects may arise from the non-flatness of the mirror electrode that extends the mirror pattern topography. Non-flatness can arise for instance from mechanical stress in the mirror electrode. Stress in one direction may lead to astigmatism in the reflected beam, and the effect of this on the reflected beam can actually be modeled by adding a spatial frequency with the assumed curvature into the mirror calculations. In reference to [Fig. 3.5] we note that a beam width of 10 μm (i.e., a spatial frequency of 0.1 μm^{-1}) already adds phase modulation amplitude to the reflected beam when the curvature of the electrode is in the order of single or double digit nanometers, depending on the bias potential. While we recognize the non-flatness of the mirror electrode as a possible technology barrier during the initial development of a double mirror system based on topographic patterned mirrors, the development of pixelwise programmable mirrors will offer a solution to this limitation.

We conclude the discussion on optical effects by noting that the high coefficient of spherical aberration that is usually associated with flat electron mirrors can to a large extend be compensated for by the geometry of the imaging lens in between the mirror electrode and the image plane [55]. For use of the virtual phase plate with high energy electron beams, such as those found inside a transmission electron microscope, we recognize the risk of electrical breakdown as one of the main limitations. As we rely on mirrors, this implies slowing down of the incident beam to zero kinetic energy and thus the mirror potential must always be slightly more negative than that of the electron source cathode. However, we believe that this issue can be circumvented for instance by placing the double mirror system in front of the beam accelerator, close to the source module of the microscope.

Controlled wave front shaping requires a coherent electron beam. As the degree of coherence is directly related to the reduced brightness B_r of the source, a high-quality source is required. For a coherent beam, the beam current must be limited to less than $I_{\text{beam}} \leq 10^{-18} B_r$ [8]. In practice this leads to a beam current in the order of 1–100 pA for a Schottky source. The throughput of the microscope then becomes limited as a trade of for beam coherence, as is similar to other phase plate techniques.

Finally, we discuss various opportunities that present themselves even when only fixed mirror patterns are used. In the integrated double mirror setup as it is shown in [Fig. 3.7], there is room for the placement of a specimen in between the two mirrors at the mirror axis, at the cross-over plane of the beam next to the electrostatic deflector. If one would apply a grating pattern on both the top and bottom mirror, the diffractive action of both mirrors constitutes an amplitude splitter (first mirror) and amplitude combiner (second mirror). Placement of a specimen in the common cross over plane of the mirror axis that may or may not block the surroundings of the mirror axis, while leaving the on-axis region free, creates a Mach-Zehnder interferometer and thus enables an experimental demonstration of interaction-free measurement for electrons [45, 46].

As a next step, we now imagine further possibilities when pulsed operation of the electrostatic deflector on the optical axis becomes possible. When given the possibility to double the low-voltage deflection field strength of this deflector within the time spent by the electron at the mirror axis, the electron will be cycled back to the mirror axis upon passing the deflector for the second time, since the deflection angle doubles as well. This would enable multi-pass interaction free measurements with electrons [56]. When a grating pattern is used as beam splitter and combiner, the setup also offers a feasible method for experimentally performing quantum electron microscopy [49], although additional alignment difficulties must be considered for this [50]. Of course, this would only demonstrate the principles of quantum electron microscopy, because a real application on beam sensitive materials would require at least 60 keV beam energy instead of the 2 keV that was used in our calculations.

In conclusion, we have described a novel microscopy scheme that could potentially enable the manipulation of both phase and amplitude of an electron beam. This is realized by using two patterned electron mirrors inside a microscope. The scheme makes use of reflective electron optical components to modulate the phase

of the reflected wave front, and in this way we expect to avoid typical issues that are encountered in transmission based approaches to beam shaping.

Acknowledgements. The authors would like to acknowledge discussions within the Quantum Electron Microscopy collaboration. This work is funded in part by the Dutch Research Council (NWO), and in part by the Gordon and Betty Moore Foundation (GBMF) as part of the QEM collaboration.

References

[1] C. Maurer, A. Jesacher, S. Bernet, and M. Ritsch-Marte, *What spatial light modulators can do for optical microscopy,* Laser & Photonics Reviews **5**, 81 (2010).

[2] D. Dudley, W. M. Duncan, and J. Slaughter, *Emerging digital micromirror device (DMD) applications,* in *MOEMS Display and Imaging Systems*, edited by H. Urey (SPIE, 2003).

[3] J. B. Sampsell, *Digital micromirror device and its application to projection displays,* Journal of Vacuum Science & Technology B: Microelectronics and Nanometer Structures **12**, 3242 (1994).

[4] G. Guzzinati, L. Clark, A. Béché, R. Juchtmans, R. V. Boxem, M. Mazilu, and J. Verbeeck, *Prospects for versatile phase manipulation in the TEM: Beyond aberration correction,* Ultramicroscopy **151**, 85 (2015).

[5] H. Okamoto, T. Latychevskaia, and H.-W. Fink, *A quantum mechanical scheme to reduce radiation damage in electron microscopy,* Applied Physics Letters **88**, 164103 (2006).

[6] H. Okamoto, *Noise suppression by active optics in low-dose electron microscopy,* Applied Physics Letters **92**, 063901 (2008).

[7] J. Verbeeck, A. Béché, K. Müller-Caspary, G. Guzzinati, M. A. Luong, and M. D. Hertog, *Demonstration of a 2×2 programmable phase plate for electrons,* Ultramicroscopy **190**, 58 (2018).

[8] P. Kruit, *Electron sources,* in *Transmission Electron Microscopy*, edited by C. B. Carter and D. B. Williams (Springer International Publishing, 2016) pp. 1–15.

[9] P. W. Hawkes, *Aberration correction past and present,* Philosophical Transactions of the Royal Society A: Mathematical, Physical and Engineering Sciences **367**, 3637 (2009).

[10] L. Clark, A. Béché, G. Guzzinati, A. Lubk, M. Mazilu, R. V. Boxem, and J. Verbeeck, *Exploiting lens aberrations to create electron-vortex beams,* Physical Review Letters **111** (2013), 10.1103/physrevlett.111.064801.

[11] D. Willasch, *High resolution electron microscopy with profiled phase plates,* Optik **44** (1975).

[12] R. Danev and K. Nagayama, *Phase plates for transmission electron microscopy,* in *Methods in Enzymology* (Elsevier, 2010) pp. 343–369.

[13] F. Zernike, *Phase contrast, a new method for the microscopic observation of transparent objects,* Physica **9**, 686 (1942).

[14] R. Danev and K. Nagayama, *Transmission electron microscopy with zernike phase plate,* Ultramicroscopy **88**, 243 (2001).

[15] M. Uchida and A. Tonomura, *Generation of electron beams carrying orbital angular momentum,* Nature **464**, 737 (2010).

[16] J. Verbeeck, H. Tian, and P. Schattschneider, *Production and application of electron vortex beams,* Nature **467**, 301 (2010).

[17] B. J. McMorran, A. Agrawal, I. M. Anderson, A. A. Herzing, H. J. Lezec, J. J. McClelland, and J. Unguris, *Electron vortex beams with high quanta of orbital angular momentum,* Science **331**, 192 (2011).

[18] S. Lloyd, M. Babiker, G. Thirunavukkarasu, and J. Yuan, *Electron vortices: Beams with orbital angular momentum,* Reviews of Modern Physics **89** (2017), 10.1103/revmodphys.89.035004.

[19] V. Grillo, E. Karimi, G. C. Gazzadi, S. Frabboni, M. R. Dennis, and R. W. Boyd, *Generation of nondiffracting electron bessel beams,* Physical Review X **4** (2014), 10.1103/physrevx.4.011013.

[20] N. Voloch-Bloch, Y. Lereah, Y. Lilach, A. Gover, and A. Arie, *Generation of electron airy beams,* Nature **494**, 331 (2013).

[21] R. M. Glaeser, *Invited review article: Methods for imaging weak-phase objects in electron microscopy,* Review of Scientific Instruments **84**, 111101 (2013).

[22] D. Preikszas and H. Rose, *Correction properties of electron mirrors,* Journal of Electron Microscopy **46**, 1 (1997).

[23] G. F. Rempfer, D. M. Desloge, W. P. Skoczylas, and O. H. Griffith, *Simultaneous correction of spherical and chromatic aberrations with an electron mirror: An electron optical achromat,* Microscopy and Microanalysis **3**, 14 (1997).

[24] A. Bok, J. le Poole, J. Roos, and H. de Lang, *Mirror electron microscopy,* in *Advances in Imaging and Electron Physics* (Elsevier, 2017) pp. 99–192.

[25] H. Lichte and G. Mollenstedt, *Measurement of the roughness of supersmooth surfaces using an electron mirror interference microscope,* Journal of Physics E: Scientific Instruments **12**, 941 (1979).

[26] H. Okamoto, *Adaptive quantum measurement for low-dose electron microscopy,* Physical Review A **81** (2010), 10.1103/physreva.81.043807.

[27] A. M. Carroll, *Pattern generators for reflective electron-beam lithography (REBL),* in *Advances in Imaging and Electron Physics* (Elsevier, 2015) pp. 1–23.

[28] H. Muller, D. Preikszas, and H. Rose, *A beam separator with small aberrations,* Journal of Electron Microscopy **48**, 191 (1999).

[29] R. Tromp, J. Hannon, A. Ellis, W. Wan, A. Berghaus, and O. Schaff, *A new aberration-corrected, energy-filtered LEEM/PEEM instrument. I. Principles and design,* Ultramicroscopy **110**, 852 (2010).

[30] R. Tromp, J. Hannon, W. Wan, A. Berghaus, and O. Schaff, *A new aberration-corrected, energy-filtered LEEM/PEEM instrument II. Operation and results,* Ultramicroscopy **127**, 25 (2013).

[31] M. A. R. Krielaart, D. J. Maas, S. V. Loginov, and P. Kruit, *Miniature electron beam separator based on three stacked dipoles,* Journal of Applied Physics **127**, 234904 (2020).

[32] H. Dohi and P. Kruit, *Design for an aberration corrected scanning electron microscope using miniature electron mirrors,* Ultramicroscopy **189**, 1 (2018).

[33] H. Rose and W. Wan, *Aberration correction in electron microscopy,* in *Proceedings of the 2005 Particle Accelerator Conference* (IEEE).

[34] S. M. Kennedy, D. E. Jesson, M. J. Morgan, A. E. Smith, and P. F. Barker, *Phase sensitivity of slow electrons to interactions with weak potentials,* Physical Review A **74** (2006), 10.1103/physreva.74.044701.

[35] A. J. Hermans and J. A. Petterson, *A quantum mechanical treatment of the mirror electron microscope,* Journal of Engineering Mathematics **4**, 141 (1970).

[36] M. A. R. Krielaart and P. Kruit, *Grating mirror for diffraction of electrons,* Physical Review A **98** (2018), 10.1103/physreva.98.063806.

[37] M. Vulović, L. M. Voortman, L. J. van Vliet, and B. Rieger, *When to use the projection assumption and the weak-phase object approximation in phase contrast cryo-EM,* Ultramicroscopy **136**, 61 (2014).

[38] R. S. Gvosdover and B. Y. Zel'dovich, *The quantum theory of image contrast formation of electric and magnetic microfields in mirror electron microscopy,* J. Microscopie **17** (1973).

[39] P. W. Hawkes and E. Kasper, *Principles of electron optics*, Vol. 3 (Academic press, 1996).

[40] *Handbook of Continued Fractions for Special Functions* (Springer Netherlands, 2008).

[41] J. M. Cowley, *Diffraction physics* (Elsevier, 1995).

[42] R. M. Corless, G. H. Gonnet, D. E. G. Hare, D. J. Jeffrey, and D. E. Knuth, *On the LambertW function,* Advances in Computational Mathematics **5**, 329 (1996).

[43] Chapter 4 in this thesis.

[44] J. M. Zuo and J. C. Spence, *Advanced Transmission Electron Microscopy* (Springer New York, 2017).

[45] A. C. Elitzur and L. Vaidman, *Quantum mechanical interaction-free measurements,* Foundations of Physics **23**, 987 (1993).

[46] W. P. Putnam and M. F. Yanik, *Noninvasive electron microscopy with interaction-free quantum measurements,* Physical Review A **80** (2009), 10.1103/physreva.80.040902.

[47] R. Egerton, P. Li, and M. Malac, *Radiation damage in the TEM and SEM,* Micron **35**, 399 (2004).

[48] S. Thomas, C. Kohstall, P. Kruit, and P. Hommelhoff, *Semitransparency in interaction-free measurements,* Physical Review A **90** (2014), 10.1103/physreva.90.053840.

[49] P. Kruit, R. Hobbs, C.-S. Kim, Y. Yang, V. Manfrinato, J. Hammer, S. Thomas, P. Weber, B. Klopfer, C. Kohstall, T. Juffmann, M. Kasevich, P. Hommelhoff, and K. Berggren, *Designs for a quantum electron microscope,* Ultramicroscopy **164**, 31 (2016).

[50] M. Turchetti, C.-S. Kim, R. Hobbs, Y. Yang, P. Kruit, and K. K. Berggren, *Design and simulation of a linear electron cavity for quantum electron microscopy,* Ultramicroscopy **199**, 50 (2019).

[51] Y. Yang, C.-S. Kim, R. G. Hobbs, P. Kruit, and K. K. Berggren, *Efficient two-port electron beam splitter via a quantum interaction-free measurement,* Physical Review A **98** (2018), 10.1103/physreva.98.043621.

[52] C. W. Johnson, D. H. Bauer, and B. J. McMorran, *Improved control of electron computer-generated holographic grating groove profiles using ion beam gas-assisted etching,* Applied Optics **59**, 1594 (2020).

[53] L. Zhu and J. Wang, *Arbitrary manipulation of spatial amplitude and phase using phase-only spatial light modulators,* Scientific Reports **4** (2014), 10.1038/srep07441.

[54] C. Wu, J. Ko, J. R. Rzasa, D. A. Paulson, and C. C. Davis, *Phase and amplitude beam shaping with two deformable mirrors implementing input plane and fourier plane phase modifications,* Applied Optics **57**, 2337 (2018).

[55] M. A. R. Krielaart and P. Kruit, *Flat electron mirror,* Ultramicroscopy **220**, 113157 (2021).

[56] P. Kwiat, H. Weinfurter, T. Herzog, A. Zeilinger, and M. A. Kasevich, *Interaction-free measurement,* Physical Review Letters **74**, 4763 (1995).

4

Design of a miniature double mirror setup for electron wave front shaping

---

Abstract.

Wave front shaping is the controlled manipulation of the amplitude or phase distribution of for instance a photon or electron. It significantly increases the experimental degrees of freedom, and is routinely applied in light optics. The electron microscopy society would as well benefit from the development of a programmable phase modulator, an effort that only recently gained traction. Here, we present the experimental design of an electron wave front modulator that relies on two patterned electron mirrors. The mirrors face each other and are placed on an axis parallel to the optical axis of the microscope column. Miniature electron optical components, including lenses, deflectors and liner tubes are designed, and allow for the integration of the setup into the column of an electron microscope. In addition, the use of miniature optics enables to keep deflection angles inside the setup small, therewith reducing dispersive effects inside the beam. In addition to the use of the setup for wave front shaping, we will discuss the potential application of the setup as an electron cavity or resonator for use in quantum electron microscopy (QEM).

4.1. Introduction

The controlled shaping of the amplitude and phase of an electron beam is not yet as versatile as that what is seen in light optics. There, the use of digital micromirror devices, and spatial light modulators, has enabled full and dynamic control over the wave front of the light beam. In contrast, electron beam shaping is mainly achieved by transmission of the electron wave front through an amplitude mask or phase plate. And, although their use has been successfully applied to cases like beam mode conversion [1], off-axis holography [2], and Zernike phase contrast [3], the inability of dynamically changing the transmission mask pattern puts a serious constraint on the experimental freedom, as a new mask must be designed depending on the experimental needs.

4

Recent developments to overcome the static limitation of transmission mask techniques show great promise towards programmable transmission phase plates. Verbeeck et al. [4] demonstrated that vortex beam generation can be achieved with as little as a 2×2 array of miniature electron lenses. However, practical limitations remain, in terms of addressing more than four pixels, increasing transmissivity of the phase plate, and avoiding electrical charge from building up in the device.

Contrary to relying on transmission optics, it is possible to modulate the phase of an electron beam with electron mirrors. Programmable electron mirrors, with individual Einzel lenses on top of each pixel, have been used in the Reflective Electron Beam Lithography (REBL) project in the past [5]. This mirror configuration may be regarded as the electron optical counterpart of the digital micromirror device from light optics, and would allow for amplitude shaping of the beam.

4.1.1. Electron microscopy with two mirrors

Okamoto has suggested that a programmable, pixelated electron mirror can act as a programmable phase shifter [6], which would allow to alter the phase of the electron wave front when it is spread out over the mirror surface. We are expanding this idea by adding a second electron mirror that may in principle allow for both amplitude and phase shaping [7]. That way, an alternative method to electron beam shaping is provided that does not require the transmission of the beam through amplitude masks or phase plates, therewith avoiding the typical difficulties such as charge build up and reduced transmissivity.

A wide variety of electron optical techniques could potentially benefit from a setup that contains two electron mirrors. In the most basic configuration, the combination of two aperture mirrors can be used to enable aberration correction in (critical dimension) scanning electron microscopy (CD-SEM) [8]. This concept revolves around the placement of two electron mirrors on an axis parallel to the optical axis of a conventional SEM, and could be implemented as an extension module to existing microscope column designs.

The more generic application of two electron mirrors concerns the use of closed surface, flat mirror electrodes, that contain a topographical or pixel wise applied pattern. The electric field in front of the mirror will then adhere to the shape of the pattern. When the electron wave front is spread-out over the mirror surface, the phase of the reflected beam becomes modulated accordingly [7], similar to what is

seen in mirror electron microscopy [9], and low energy electron microscopy (LEEM).

Quantum electron microscopy (QEM) is potentially a low-dose imaging technique [10, 11] that would benefit from the development of electron mirror-based optics. In QEM, a two-beam condition that consists of a sample and a reference beam inside a cavity or resonator is needed. The sample beam is used to repeatedly probe a specimen, and after each pass through the sample plane the two beams are recombined at a coherent beam splitter, at which point the two beams exchange intensity.

A coherent beam splitter for electrons can be realized with an electron mirror that contains a weak phase grating [12]. A practical realization consists of a grating pattern at the mirror electrode. A grating pattern that consists of parallel grooves will modulate the electric field in front of the mirror electrode. When the electron wave front is spread out over this modulated potential, the phase of the reflected wave front becomes modulated accordingly. At the sample plane, this phase modulation expresses as a diffraction pattern [13]. The intensity of the central order and diffracted beams can be tuned by adjusting the bias potential of the mirror electrode.

If two electron grating mirrors are positioned symmetrically opposite around a shared image plane, the beam splitting effect of the first mirror can in principle be amplified by reflection at the second mirror. QEM relies on the stepwise exchange of beam intensity to complete a full Rabi cycle [14] and in this way reduces the radiation that is received by the specimen when compared to conventional microscopy techniques [15].

Essentially, the approach to QEM that is just described is based on a cascade of Mach-Zehnder interferometers with non-50/50 ratio beam splitters [16]. At the same time, it must then be noted that two electron mirrors, in the absence of more than one reflection per mirror inside a cavity provide a realization for a Mach-Zehnder interferometer for electrons.

Two electron mirrors can also be used to realize multi-pass TEM (MP-TEM), a low-dose imaging technique in which phase contrast is enhanced by passing a spread-out electron wave through the sample multiple times, therewith removing the necessity of averaging over many separate images [17]. Practical implementations of this technique make use of temporally gated aperture mirrors that fulfill the dual role of providing a beam entrance and exit to the resonator cavity in the open state, as well as providing aberration correction in the closed state of the mirror [18].

Instead of letting the electron enter the resonator through the aperture electron mirror, we suggest to position the resonator at a separate axis parallel to that of the microscope column. In this arrangement, the electron mirrors are positioned sideways of the optical axis of the microscope, and instead of using temporally gated electron mirrors, the use of an ultrafast deflector at the microscope axis enables the transition of the beam between the microscope axis and the resonator (or mirror) axis. A schematic implementation of this concept as an extension module to an existing TEM column is shown in [Fig. 4.1(a)]. Admittedly, this suggestion calls for an involved timing sequence for the deflectors, and we do not deem it practical to commence the development of a full TEM prototype based on this principle just

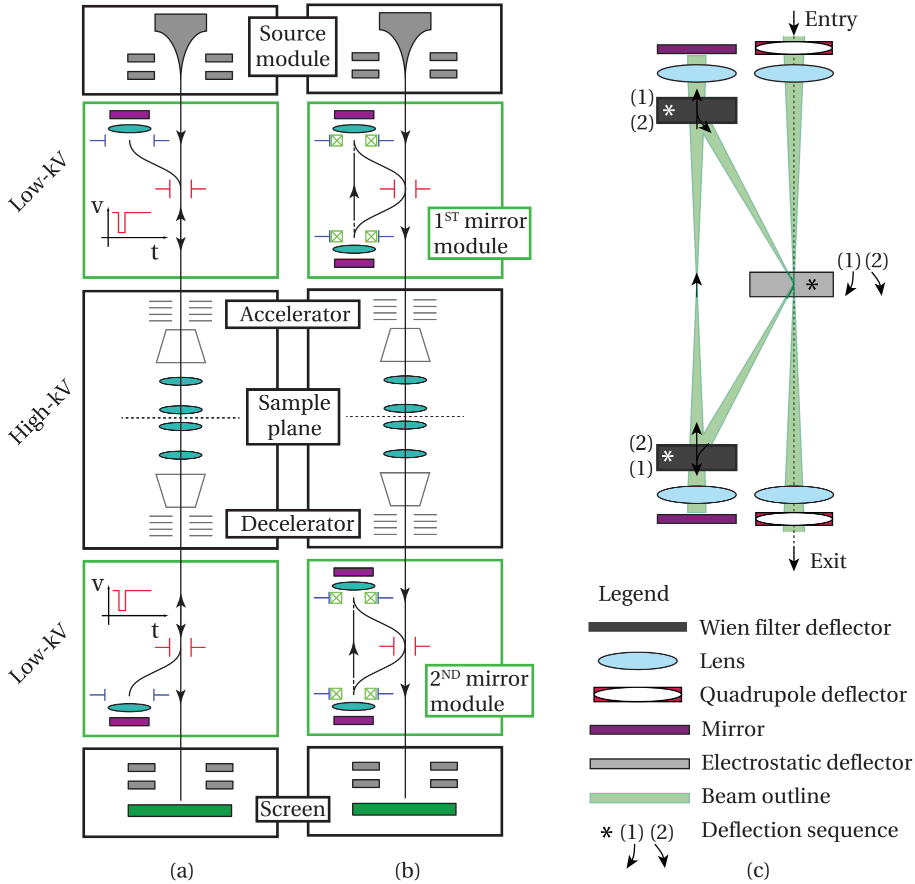

Figure 4.1: Proposal for integration of two mirror modules that contain ultrafast deflectors into a TEM column. (a) MP-TEM and QEM implementation. (b) Pre- and post-specimen wave front shaping. (c) Prototype optical setup for experiments with two electron mirrors that can be mounted on the stage platform of a scanning electron microscope.

yet.

A more feasible approach is based on the positioning of two electron mirrors inside a mirror module, as is shown in [Fig. 4.1(b)]. In this design, the temporally gated deflectors are replaced by static field deflectors. In front of the mirror, the use of a miniature beam separator that makes use of combined electric and magnetic deflection fields enables an electron trajectory that continues downwards the TEM column after a double reflection. An overview of the optical design of this double mirror approach is shown in [Fig. 4.1(c)].

Here, we present the optical and mechanical design for this 'double mirror' setup. The design will be suitable for the placement of a double mirror unit at the stage platform of a scanning electron microscope (SEM). This enables a feasible method of

access to the optical and mechanical components and in general offers more flexibility in terms of modifying the setup, when compared to the immediate integration of the setup inside a TEM column.

4.1.2. Experimental modalities

The presented experimental designs could in principle be used as a prototype for QEM and MP-TEM [Fig. 4.1(a)], and structural hypothesis testing and wave front shaping in general [Fig. 4.1(b)]. Unique to the double mirror prototype proposal is that it does not require (sub) nanosecond switching of the mirror electric potentials. Instead, we make use of an electrostatic deflector that is positioned next to the sample plane of the resonator to insert and remove the electron from the resonator. The use of static field operated Wien filters in front of the electron mirrors enables the direction dependent deflection angles at the resonator axis.

This approach offers a number of advantages compared to designs with temporally gated mirrors. We already mentioned the relaxed requirement on switching of high voltage potentials. In addition, the proposed setup can be used in a constant-current mode that does not require switching of any field, when no more than one reflection per mirror is required. This is for instance the case for the realization of a Mach-Zehnder interferometer for electrons, and more generally the demonstration of phase and amplitude modulation of the electron wave front with patterned mirrors.

4.2. Optical design

The schematic optical design of the SEM based prototype is shown in [Fig. 4.1(c)]. In the setup, the incident beam is focused onto the deflector that is in the middle layer of the setup. This deflector can be operated with a static potential to enable a constant-current mode in which one round trip in the resonator is performed, or at a gated potential that allows for multiple round trips through the resonator. Inside the resonator, crossed electric and magnetic fields ($E \times B$) are oriented in the Wien configuration in front of both mirrors. This configuration results in a deflection path that depends on the direction of incidence of the beam, and realizes the shown trajectory inside the resonator. A collimator lens is placed in front of both mirrors, and these are used to spread out the beam over the mirror pattern, as well as providing a focus at the common crossover plane that coincides with the middle layer.

At the optical axis that coincides with the microscope column objective lens (right hand side in the figure), an additional lens and quadrupole deflector pair is placed both above and below the sample plane. The entrance lens and quadrupole deflector above the sample plane are used for alignment and projection of the last virtual source of the probe onto the electrostatic (E) deflector. The lens and quadrupole pair below the sample plane are used to coordinate the image formation of the sample plane onto the detection optics that are positioned below the setup.

4.2.1. Miniature electron mirrors

The use of an electron mirror as part of a microscope column always introduces the need to separate the incident and reflected beam trajectories, in order to avoid the electron from propagating back to the source module [19]. For this reason, electron mirrors are usually integrated into a microscope column in a separate module that is mounted under an angle with respect to the source and detection axes of the microscope. At the intersection of these axes, a beam separator provides the necessary deflection fields that transits the beam between the various optical axes.

The volume claim of a mirror and beam separator unit is typically large due to the use of conventionally machined mechanical parts and the high voltages that are present in such setups. And, while aberration corrected low energy/photoemission electron microscopy (LEEM/PEEM) machines even feature multiple beam separators and mirror units [20], one for the specimen and one for performing the aberration correction, the dispersion of the large angle deflections in the beam separators may limit the use of such setup for controlled beam shaping.

In a recent proposal for low-voltage aberration correction in SEM by Dohi and Kruit, an extensive overview on using multiple miniature electron mirrors in a microscope column has been provided [8]. The advantage of miniaturizing a multi-mirror setup is found in the reduction of the inherent deflection induced dispersion and deflection aberrations of the beam separator. By keeping the deflection angle of the beam between the axes small, deflection dispersions can be avoided. However, the necessity of small deflection angles introduces the need for miniaturized electron optics, in order to keep the total system within a reasonable length.

4.2.2. Electron ray trajectory

We based our experimental design on that for aberration correction in SEM from Dohi and Kruit [8] and to some extend modified the beam path, as shown in [Fig. 4.1(c)]. In our current proposal, we suggest that the electron beam is deflected away from the optical axis at the common crossover plane at the middle layer, where the beam is focused. After a double reflection at the electron mirrors the beam returns to this same position and is being deflected back onto the microscope axis. This is in contrast to the original K-path corrector proposal, in which this deflection is performed at the top and bottom layers of the setup. We refer to this beam deflector as a 'barn door', due to its role of inserting and removing the electron beam from the resonator.

This modification is at first sight not a necessary one. However, we note here already that this modification allows us to place an ultrafast deflector at the common crossover plane at a later stage of development. Consequently, that would allow to trap the electron in a loop, enabling multi-pass electron microscopy [11, 18] with this setup. This requires that the deflection field strength of the fast deflector can be doubled in the order of nanoseconds, and we don't consider this feasible with the original K-path corrector design, where a magnetic field must be switched in the same time period as well. The disadvantage of this approach is that we need two Wien deflectors instead of the one in the original K-path corrector. Conventional Wien deflectors usually place a large volume claim, and the presence of two parallel

optical axes must be explicitly taken into account in the design of the Wien deflector.

4.2.3. Round trip dispersion

When the electron beam is deflected in an electric (E) or magnetic (B) field, the inherent energy spread of the beam results in a spread in deflection angle as well. This is an effect known as deflection dispersion. When the electron is deflected by an angle α, the resulting error in deflection angle ($\delta\alpha$) depends on the type of deflection field. For a magnetic and electric field that yield an equal deflection angle for the nominal beam energy, it can be shown that the electric field introduces twice the dispersion error when compared to the magnetic field, such that

$$\frac{\delta\alpha_B}{\alpha_B} = \frac{1}{2}\frac{\delta\alpha_E}{\alpha_E}. \tag{4.1}$$

4

When the deflection takes place outside of an image plane of the probe, the resulting blurring of the probe at the image plane depends on the distance (u) between the image plane and the principal plane of the deflection field, such that $d_{spot} \sim \delta\alpha \times u$. From this first order relationship it is also directly observed that no additional dispersion effects at the image plane can take place, when the deflected electron beam is focused onto the principal plane of the deflection field.

In our setup, the incident beam is focused onto the principal deflection plane of the barn door. Hence, no dispersion effects at the cross-over plane are induced when the electron beam is deflected initially away from the microscope axis, and at a later stage back onto the microscope axis. This is however not the case for deflections that take place in the Wien filter fields in front of the electron mirrors. These fields are positioned in the top and bottom layers of the setup, at which location the beam is spread out.

For a systematic study of the net dispersion effects at the common crossover plane of a full round trip of the electron through the setup [based on the trajectories shown in Fig. 4.1(c)], it is convenient to define a unit Δ as the probe shift at the common crossover plane due to deflection dispersion. This is possible here, since the deflection angles at each deflector are fixed. For a given full angle α at the barn door, the Wien filter fields are adjusted such that $\alpha_B = \alpha_E = \alpha/2$. The smallest amount of dispersion is then provided by the deflection action of the magnetic field inside the Wien filter, which yields $\Delta \equiv \delta\alpha_B \times u$. Reasoning along similar lines then shows that the electric field contributes 2Δ at the Wien filter. Depending on the direction of incidence towards the Wien filter, the beam (at nominal beam energy) either passes straight through the Wien filter when $\alpha_E = -\alpha_B$, or the beam is deflected in the case where $\alpha_E = \alpha_B$.

An estimate for the unit quantity Δ is provided by the relation between the deflection angle due to the magnetic field at deflector (α_B), and the energy ($\mathcal{E}$) and energy spread ($\delta\mathcal{E}$) of the beam through

$$\frac{\delta\alpha_B}{\alpha_B} = \frac{1}{2}\frac{d\mathcal{E}}{\mathcal{E}} \Rightarrow \Delta = \delta\alpha_B u = \frac{1}{2}\frac{d\mathcal{E}}{\mathcal{E}}\alpha_B u. \tag{4.2}$$

In our initial experiments we aim at a beam energy of 2 keV, and we can reduce the energy spread to 0.3 eV. In combination with the requirement of small deflection angles, say $\alpha_B \sim 25$ mrad, and $u = 15$ mm (see sct. 4.4 for a justification of these values), this leads to $\Delta \approx 30$ nm.

With the above definitions in place, the effect of a straight passage of the beam through the Wien turns out to be $+2\Delta^{(E)} - 1\Delta^{(B)} = \Delta$, where the first contribution comes from the electric field, and the second contribution comes from the magnetic field as indicated by the superscript. From a similar reasoning, for a net deflection angle α in the beam separator, the resulting dispersion induced probe shift at the image plane becomes $2\Delta^{(E)} + \Delta^{(B)} = 3\Delta$. Finally, it should be noted that a reflection on either mirror at the mirror axis places the resulting image at the opposite side of the optical axis at the common crossover plane.

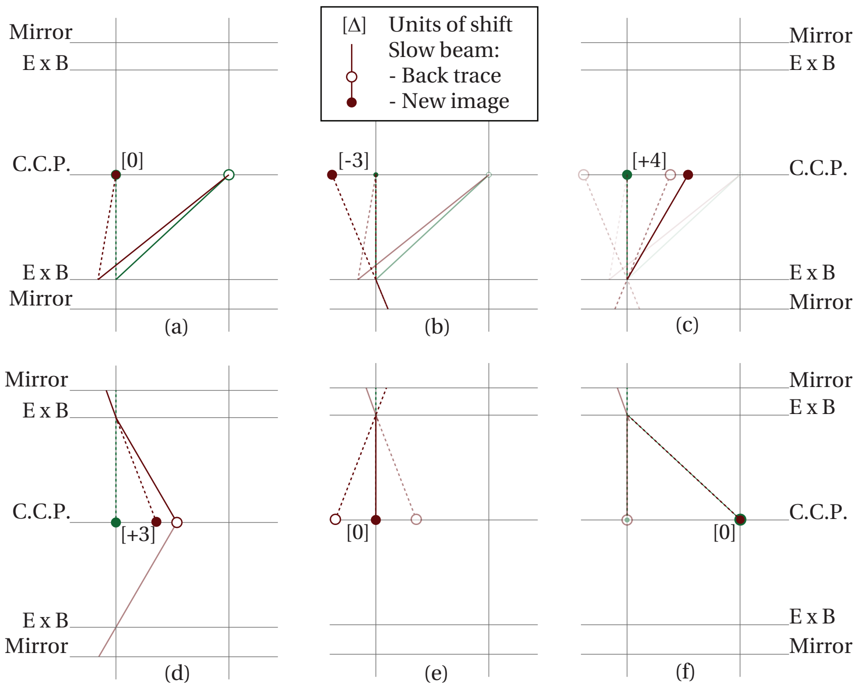

Figure 4.2: Systematic dispersion analysis for a single round trip started and terminated at the barn door deflector. (a) Deflection towards the mirror axis does not disperse the beam as the barn door plane coincides with an common crossover plane (C.C.P.) of the beam. (b-c) Passage towards and away from the bottom mirror, through the mixed electric and magnetic ($E \times B$) fields of the bottom Wien filter. (d-e) Passage towards and away from the top mirror, through the mixed electric and magnetic fields of the top Wien filter. (f) Net effect of the top Wien filter, deflecting the beam back onto the barn door deflector. A full round trip does not add dispersion to the beam in first order at the common crossover plane.

With the above, we can trace out the deflection dispersion of the setup in first

order. In this analysis, we assume that the incident beam is initially not-dispersed at the common crossover plane when it is imaged onto the barn door plane, that coincides with an image plane at the common crossover plane of the setup. The steps in the analysis are shown in [Fig. 4.2], where the position of the virtual probe with nominal (green) and reduced (red) energy are traced through the resonator. At each step, open circles label the position of the last image point, and closed circles label the position of the new image point after passing through the respective deflection fields.

At the barn door, the beam is deflected by an angle α towards the mirror axis, as shown in [Fig. 4.2(a)]. As the deflection takes place at an image plane, the virtual image of the probe at the mirror axis does not show any effect of dispersion at the common crossover plane. Next, we consider the effect of the first passage (downward) through the Wien filter. This passage deflects the beam (at nominal beam energy) by an angle α, and the slower part of the beam experiences an additional deflection, which places the probe image at 3Δ units of dispersion at the image plane to the left of the optical axis [Fig. 4.2(b)].

After the first reflection of the beam at the bottom mirror, the image of the probe at the image plane is shifted to the opposite side of the optical axis. In addition, the upward passage through the Wien filter field adds an addition Δ unit to the dispersion effect at this image plane. Consequently, after a full first reflection the beam arrives at the image plane with a dispersion of 4Δ units [Fig. 4.2(c)].

The second halve of the round trip through the resonator is opposite of the first halve, consisting now of first a straight upwards pass through the Wien filter at the top layer, followed by a reflection and a downward deflection pass through the same Wien filter. Following a reasoning similar to that above, it can be shown that after a double passing through the Wien filter, and a single reflection at the top mirror, the beam is imaged back at the barn door without suffering from first order dispersion effects [Fig. 4.2(d-f)] at this plane. From this it can be concluded that one round trip through the resonator does not add dispersion to the beam at the image plane that coincides with the barn door deflector.

4.3. Optical components

We aim for designs of optical components that will fit inside a TEM column extension after we have finished our initial experiments with the SEM stage platform based setup. For this reason, the length of the optical system is limited to approximately 50 to 100 mm. By keeping the deflection angles below $50 - 100$ mrad, the second order deflection aberrations can be kept small [8]. The combination of these requirements leads to a close proximity of the two parallel axes in the system. In [sct. 4.4], we will elaborate more on the exact dimensions that are involved in the experimental design. Here, we already note that the axial separation that our design is based on is only 1 mm, and the mirror electrodes are positioned at approximately 25 mm distance away from the common crossover plane. This motivates the use of miniature electron optical components.

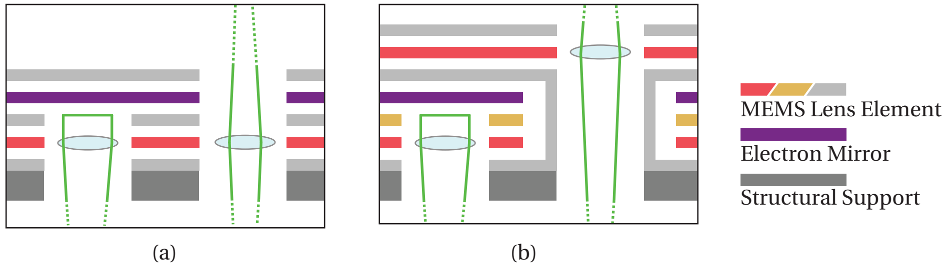

Figure 4.3: (a) Naïve implementation of lenses at the microscope and mirror axis at the same level. This results in severe design and experimental limitations as the focal strength of the lenses cannot be tuned independently, unless the electrode is split somehow. (b) Stacked approach, in which the lens action at both axes can be tuned independently. The (yellow) cap electrode can now be used to tune the electric field in front of the mirror.

4.3.1. Miniature electron optics

Various lenses in the setup provide means to focus the beam onto the common crossover plane, and spread-out the beam over the mirrors. The refractive action of an electron lens is usually realized through either a magnetic or electric field that acts on the beam. The use of magnetic lenses in a miniature system would require to embed coils in close proximity of the lens aperture, and magnetic shielding material must be used to limit the extend of fringe fields. Small magnetic lenses and deflectors with embedded coils have been successfully manufactured with microfabrication techniques in the past [21–23], however the dimensionality of these methods does not suit our needs and does not easily scale. For the miniature system that we are building, the use of magnetic lenses is thus not considered a feasible approach.

Electrostatic lenses on the other hand consist of a stack of electrodes that contain an aperture through which the beam can pass. By applying an electric potential onto the electrodes, the focal length is readily adjusted and no additional embedded circuitry is required. Very round apertures can be fabricated from Silicon wafers by means of Bosch-etching or Reactive Ion Etching [24] and the mutual alignment of the apertures can be accurately performed with a dedicated 6-degree of freedom (6-DOF) aligner [25]. Electrostatic lenses thus potentially offer a feasible method for application in multi-axes miniature systems when compared to magnetic lenses. The combination of lithographic processes for manufacturing very round apertures, and the sub-micron alignment precision that can be achieved with the 6-DOF aligner prevents sources of astigmatism in the optics, and thus avoid the need for additional stigmators in the setup.

At the top and bottom layers, a total of two lenses (one at each axis), one mirror, one cap electrode, and one beam deflector are required. Naïvely, a single electrode with two apertures could be used to provide the lens action at both axis [Fig. 4.3(a)]. One could then choose the radius of the apertures in such ratio as to provide the required focal strength at each axis, at equal and fixed value of excitation. However, this would severely impact the degrees of freedom for tuning the focal strength on

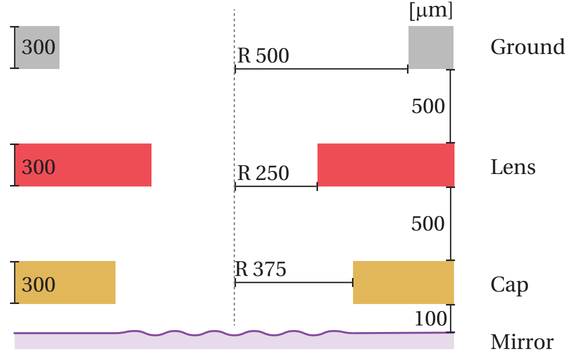

Figure 4.4: Schematic design of a flat electrode patterned electron mirror, with small aberrations at the image plane. Electrodes and pattern not to scale, dimensions based on results from [26].

both axes independently as well as put a severe design tolerance on the setup.

Instead, we suggest to separate the two lenses spatially from each other, and shield the beam at the microscope axis from the mirror axis [Fig. 4.3(b)]. This way, the cap electrode (yellow in the figure) that is in between the lens and mirror electrode can also be used to further tune to electric field in front of the mirror, independently of the beam propagation at the microscope axis. A method for shielding the electric field of both axes by means of miniature liner tubes is discussed in the next section.

The combination of three aperture electrode lens elements and an electron mirror is commonly referred to as a tetrode mirror and is historically found in mirror based setups for aberration correction [20, 27]. The aberration correcting properties then usually stems from the hyperbolic shape of the mirror surface, which is realized through an indentation at the mirror electrode. In the absence of the hyperbolic shaped mirror field, large aberrations may result upon reflection from the flat mirror surface. In recent work, we found a mechanical configuration for the tetrode mirror system that exhibits only very small aberrations [26], which is shown in [Fig. 4.4]. As a result of this, topographic mirror patterns may now be applied onto the otherwise flat mirror electrode.

Based on the results obtained in [26], at a 2 keV beam energy that we initially aim to use the setup at, the spot size at the common crossover plane can be kept diffraction limited up to a beam semi-angle of 2.3 mrad. This results in a possible beam width at the mirror plane of approximately 40 μm. For this, respectively a ground, lens, and cap radius of $R_{ground} = 500$ μm, $R_{lens} = 250$ μm, and $R_{cap} = 375$ μm, valid under the assumption of a thickness of 300 μm for all electrodes, and 500 μm spacing of the apertured electrodes are required. The spacing between the cap and mirror electrode is much smaller than this and equals 100 μm. The resulting design is shown in [Fig. 4.4].

4.3.2. Miniature liner tubes

Following the dual axis lens electrode design shown in [Fig. 4.3(a)], the close proximity of the two parallel electron optical axes towards one another, results in a shared electric potential of some electrodes among both axes. The one aperture aligns with the mirror axis, whereas the other aperture provides a passage for the beam at the microscope axis. This approach inherently introduces severe cross talk between the two axes, since the potential at the electrode cannot be set independently for one of both axes.

In what follows, we suggest to make use of electrically grounded miniature liner tubes to resemble to situation shown in [Fig. 4.3(b)]. This liner tube is to be inserted through the aperture in the electrode for which the electrode potential should not be applied. In the example shown in [Fig. 4.3], the miniature liner tube is inserted through the right hand side aperture. In this way, the optical configuration as shown in [Fig. 4.1(c)] can be realized. This is achieved by placing the lens electrodes for lenses on the mirror and microscope axis, at different vertical positions. The lenses in front of the electron mirrors at the top and bottom layers of the mirror axis can be tuned independently this way from the entry and exit lenses at the microscope axis.

A consequence of placing the (electrically grounded) miniature liner tube is that it disturbs the shape of the electric field at the neighboring axis, at which the lens action takes place. The effect of this disturbance could be understood from [Fig. 4.5(a)] that shows a cross section of a three-electrode (Einzel) lens at the mirror axis, and a miniature liner tube positioned at the microscope axis. The presence of the grounded liner tube results in a dipole disturbance of the electric field at the mirror axis, that increases as a function of increased spacing between the electrodes.

As a result of this dipole disturbance, a beam passing through the lens field will experience an undesired deflection component. In principle, this effect could be compensated for by adding a second, 'dummy', miniature liner tube at the opposite side of the mirror axis. This would result in an equal but oppositely oriented dipole disturbance at the mirror axis, and this consequently eliminates the dipole disturbance. This situation is shown in [Fig. 4.5(b)].

With the addition of the 'dummy' liner tube, the dipole distortion is cancelled out. However, a quadrupole distortion will develop since the perpendicularly oriented out-of-plane fields are not influenced by the presence of grounded liner tubes. We suggest to place another set of two liner tubes, as shown (top view) in the schematic of [Fig. 4.5(c)]. This configuration will lead to a suppression of the quadrupole distortion at the lens plane as well, and the lowest distortion that could develop is an eight-pole. A photograph of a manufactured holder plate with four miniature liner tubes that are positioned around the aperture of the mirror axis is shown in [Fig. 4.5(d)].

In [Appendix C] the quantitative effects that placement of one or multiple miniature liner tubes have on field distortions is numerically analyzed. The findings that are presented there support the qualitative analysis that is provided in the above text. The numerical findings indicate an expected spot size blurring at the image plane after reflection in the range of 10-100 nm.

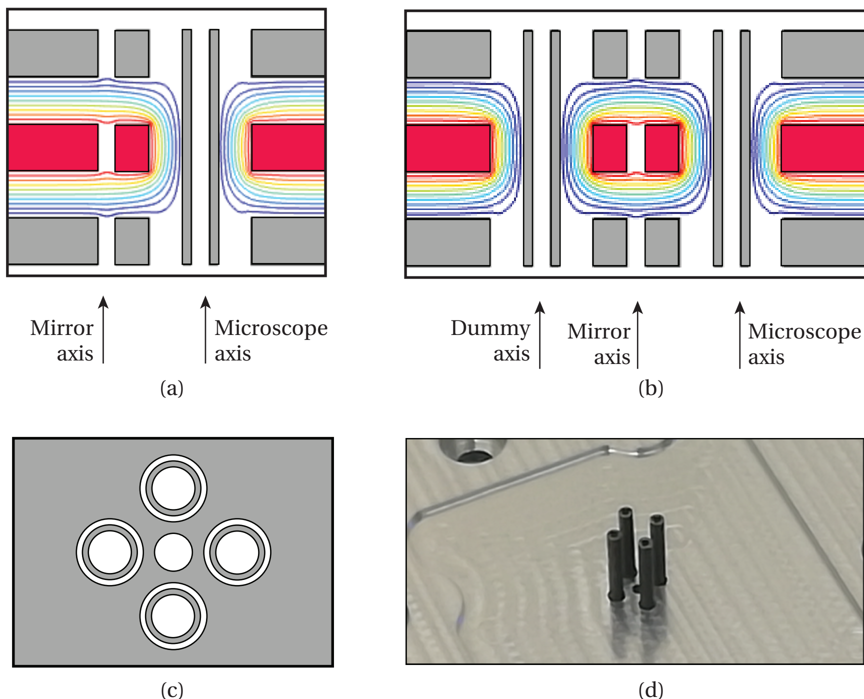

Figure 4.5: The effect of positioning miniature liner tubes on the generation of electric field (contours) disturbances. (a) (Cross section) The use of a single miniature liner tube results in a dipole distortion of the electric field at the mirror axis. (b) The addition of a 'dummy' miniature liner tube opposite to the lens plane prevents the development of the dipole distortion. Instead, a quadrupole distortion will be generated at the mirror axis. (c) Four-fold liner tube symmetry (seen from above) suppresses the quadrupole distortion. (d) Photograph of a holder plate showing four miniature liner tubes positioned around the (in the photograph partially obscured) mirror axis aperture.

4.3.3. Slit deflector ('Barn door')

At the central layer of the system, a beam deflector is required that performs the deflection of the incident beam at the microscope axis towards the mirror axis, and vice versa for the returning beam after double reflection. This deflector acts as entrance and exit deflector for the mirror axis, hence it is also referred to as 'barn door', in analogy to its role in a QEM design [10]. In order to operate this deflector with time-independent (static) fields, the deflector must be positioned in the symmetry plane with respect to the top and bottom layer of the setup, such that the principal plane of the deflector coincides with the common crossover plane of the setup.

Basic electrostatic deflectors consist of multiple poles and are operated with an antisymmetric potential. As the deflection takes place in one direction only, it is in principle sufficient to make use of two elongated deflector plates. The parallelism

4

of the plates is of importance, as harmonic field distortions are introduced into the deflection field in the form of astigmatism when the electrodes are not parallel to each other. An additional deflector electrode pair must be positioned perpendicular to the elongated plates in order to enable alignment correction in the direction perpendicular to the main deflection path. A mechanical configuration that enables both the main and correction deflection is included in [sct. 4.4.2].

The deflection angle θ from a parallel plate deflector is obtained in first order by relating the electrode thickness t, spacing w, and electric bias potential U and beam acceleration voltage Φ, through

$$\theta = \frac{Ut}{\Phi w}. \tag{4.3}$$

4

It is thus seen that a high aspect ratio $AR \equiv t/w$ leads to a lower electrode potential, and vice versa. In our current design we use Silicon wafers of thickness $t = 300\ \mu$m, and a gap width of $w = 200\ \mu$m. This yields an electrode excitation of $U = \pm 67$ V. The actual value will be smaller due to the fringe fields that are not accounted for in the above expression. Initial experiments have pointed towards an actual excitation of $U_{exp.} = \pm 48$ V.

4.3.4. Quadrupole deflector

The quadrupole deflector enables the optical alignment with respect to the optics in between which the double electron mirror setup is positioned. In our prototype setup, the quadrupole deflector that is positioned at the top layer enables alignment between the microscope objective lens and the barn door deflector. The quadrupole deflector that is positioned at the bottom layer of the setup enables the alignment between the barn door and the YAG scintillator screen. Additionally, a raster scan signal can be applied onto the quadrupole electrodes which aids in the optical alignment of the setup.

4.4. Mechanical design

In this section we discuss the mechanical design of the SEM prototype setup. We start by identifying the dimensional constraints that follow from the available space inside the SEM specimen chamber that holds the setup. Based on these constraints, we develop and present practical designs for the barn door deflector, beam separators in front of the electron mirrors, and means of combining the various components into a setup. We conclude this section with a discussion on alignment tolerance.

4.4.1. Dimensional constraints

The initial dimensions for the setup [Fig. 4.6(a)] are constraint by the space that is available in the specimen chamber of the electron microscope that we will use for our experiments. A commercially available FEI Verios 460 Nanolab SEM that is equipped with a monochromator will be used for our future experiments, which offers a usable system length $L = 80$ mm in between the pole piece and the stage platform. The use of a miniature tetrode mirror design as presented in [sct. 4.3.1]

places the electron mirror close to the principal plane of the intermediate lens that is used to spread out the beam over the mirror, and focus the beam back onto the common crossover plane after reflection. This leads to a focal length of the intermediate lenses that approximately equals the semi-height of the resonator that is formed by the mirrors, i.e., $u_1 \approx f$. The full length of the system then becomes $L = 2u_1 + v_1$ and a magnification of the common crossover plane towards the YAG detection screen of $M = v_1/u_1 = [L - 2u_1]/u_1$ is obtained.

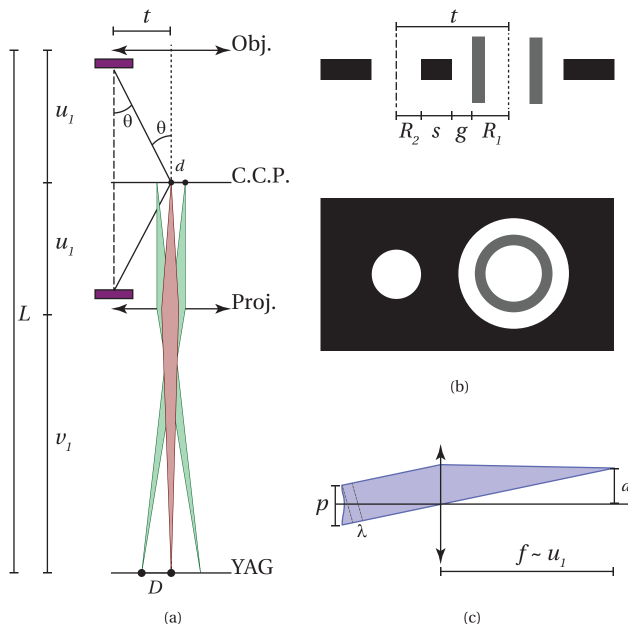

Figure 4.6: (a) Dimensional design constraints in order to fit the setup into the specimen chamber of a commercial electron microscope. For our system, the overall length $L = 80$ mm determines the focal length of the double mirror lens system, and the magnification (M) from the common crossover plane (C.C.P.) towards the YAG detection screen. (b) Inter-axial design constraints are dictated by the radius of the apertures and the miniature liner tube that provides optical separation between the two axes. (c) Relationship between grating pitch (p), free electron wave length λ, the focal length ($f \approx u_1$) of the double mirror lens system, and first order diffraction spot spacing (d).

In order to choose u_1, we first examine its effect on electric breakdown. For this, we consider the aperture configuration in [Fig. 4.6(b)]. This shows a cross section and top view of a single electrode with two apertures, that coincide with the mirror and microscope optical axes and are separated by a distance t. Cross talk between the axes is eliminated by inserting an electrically grounded miniature liner tube around one of the optical axes, resulting in a strong in-plane electric field

between the electrode and the (grounded) liner tube. The strength of this field is determined by the gap (g) between the miniature liner tube and the aperture wall, as well as the electric potential difference.

The lens potential ranges in between $1 - 5$ kV, which leads to a minimum gap $g \sim 250$ μm when a breakdown field through vacuum of 15 kV/mm is allowed for. Minimum practical liner tube diameters range around 500 μm and the radius for the non-filled aperture may be expected in the same range. This leads to an axial separation of the microscope and mirror axis that is given by

$$\begin{aligned} t &= R_2 + s + g + R_1 \\ &= 750\ \mu\text{m} + s. \end{aligned} \tag{4.4}$$

The variable (s) accounts for electrode body material in between the two apertures and must not be chosen too small, in order to guarantee the mechanical strength of the system. We choose $s = 250$ μm, leading to an axial separation of $t = 1$ mm.

The separation distance (t) between the two parallel optical axes relates to the semi-height of the cavity by $\theta = t/u_1$. On the one hand, maximum magnification of the probe onto the detector is achieved at minimum u_1 and thus a high deflection angle θ. On the other hand, large angles introduce deflection dispersions and deflection aberrations to the system. From the earlier work of Dohi and Kruit [8] it is known that a deflection angle of $\theta = 50$ mrad is sufficiently small to avoid deflection aberrations, and in [sct. 4.2.3] we have demonstrated that no additional deflection dispersion is created at the common crossover plane after a round trip in the setup. At this angle, $u_1 = t/\theta = 2$ cm, leading to a magnification of $M = 2$ from the common crossover plane to the YAG scintillator screen.

The effect that the mirror pattern has on the reflected beam can be studied with the setup by imaging the common crossover plane onto the YAG screen. That way, we are effectively imaging the electron diffraction pattern that results from the reflection at the mirror. From the obtained magnification, the minimum detectable diffraction spot separation at the common crossover plane can be estimated. At 2 keV beam energy, the approximate diffraction limited spot size at the YAG screen is in the order of $\lambda_{YAG}/2NA \sim 200$ nm for a numerical aperture (NA) that equals one (1). In order to comfortably distinguish diffraction spots on the screen, we require a spacing of $D \geq 2$ μm at the YAG screen. For the given magnification between the common crossover plane and the YAG detector screen, this results in a diffraction spot separation at the common crossover plane of $d \geq 1$ μm.

A spot size separation of 1 μm is related to the spatial frequencies ($k = p^{-1}$) at the mirror pattern [Fig. 4.6(c)] and the free electron wavelength (λ) through the optical Young's double slit equation,

$$d = \frac{\lambda u_1}{p} = \lambda u_1 k. \tag{4.5}$$

From this, a maximum pitch (p) [or minimum spatial frequency (k)] at the mirror pattern is found to be $p_{max} = 27$ pm $\times$ 20 mm/1 μm $= 540$ nm. From earlier work,

Table 4.1: Overview of dimensional design constraints for a proof-of-concept double electron mirror setup that is positioned inside the specimen chamber of a commercial scanning electron microscope.

Parameter	Label	Value	Unit
System length	L	80	mm
Mirror system focal length	f	25	mm
Max. mirror structure pitch	p	540	nm
Magnification C.C.P. to YAG	M	2	–
Axial separation	t	1	mm
Distance C.C.P. to beam separator	–	18	mm
Deflection angle at the barn door	θ	55	mrad

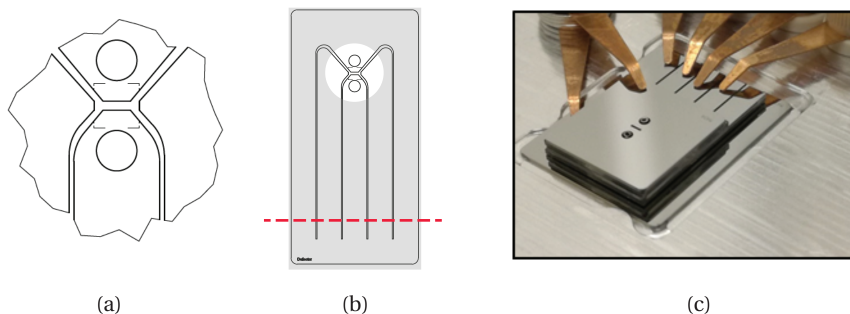

(a) (b) (c)

Figure 4.7: Barn door manufacturing. (a) The deflector geometry of the barn door consists of two elongated deflector electrodes (top and bottom electrode). Small angle deflections in the perpendicular plane are accomplished through the side deflectors (left and right electrode). (b) The barn door electrode as a whole is glued to a glass insulator that also acts as a spacer. After curing of the glue, the electrode poles are electrically separated by dicing across the red dashed line. (c) Manufactured barn door deflector (external optical shields removed). The phosphor bronze contacts are used to apply an electric potential at the deflector electrodes, and at a later stage the electric contact may be provided with wire bond contacts onto a dedicated custom printed circuit board.

we concluded that the electron beam is increasingly more sensitive to energy spread as a function of reduced pitch [13]. However, at a monochromatized beam energy spread of 0.3 eV that is attainable with the used electron microscope, we expect that a mirror pattern with a 500 nm pitch structure will provide sufficient contrast for the diffracted spots at the common crossover plane.

An overview of the obtained dimensional design constraints is provided in [Table 4.1].

4.4.2. Deflector manufacturing

In order to achieve parallelism between deflector pole electrodes of the barn door [Fig. 4.7(a)], we suggest a manufacturing protocol in which the deflector plates are machined from a single silicon wafer. The etching pattern is shown in [Fig. 4.7(b)]

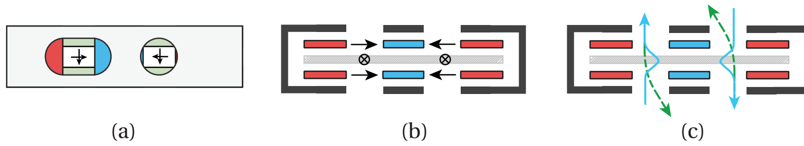

Figure 4.8: (a) Top view and (b) cross sectional view of an EBE beam separator of the main deflection plane. The direction of the electric fields in the top and bottom layer are indicated by arrows and the magnetic field in the central layer is orientated perpendicular to these fields. (c) The effective beam path through the EBE beam separator, dependent on the axis and direction of incidence. By configuration of the fields, all deflection paths are point-symmetric with respect to the hearth of the device. Figures and schematic styles are reproduced from [28].

and is created such that during the etching process the individual deflector poles do not become detached from to each other. After development, the etched wafer is glued onto a glass insulator that also acts as a spacer for the deflector towards field limiting apertures above and below the deflector electrode. After curing the glue, the wafer is diced across the dashed line that is indicated in the figure, and this process electrically separates the various poles. A similar process is used to manufacture the quadrupole electrodes.

A photograph of the completed barn door assembly, including field limiting apertures and electrical contacts, is shown in [Fig. 4.7(c)]. In order to optically shield the returning beam (at the mirror axis) from the deflection dipole field on the microscope axis, miniature liner tubes are applied on this layer at the mirror axis as well as on the opposite side of the microscope axis.

4.4.3. Beam separator

The required deflection angles in front of the mirrors are dependent on the direction of incidence of the electron beam. To realize this, one must resort to combining electric and magnetic fields. The close proximity of the two optical axis ($t = 1$ mm) hinders the use of conventional beam separators, as miniature beam separators that we know of usually do not accommodate multiple parallel axis [23]. An exception to this is the miniature electric-magnetic-electric field (EBE) beam separator [28] that we recently developed.

The EBE beam separator consists of three stacked dipole electrode pairs that are positioned around both axes of the setup, with the middle dipole pair positioned perpendicular to the remaining pairs. The acronym EBE refers to the sequence of field excitation inside the beam separator, which is sequentially electric, magnetic, and again electric. A top-down view [Fig. 4.8(a)] and a cross sectional view [Fig. 4.8(b)] are shown, with the orientation of the main deflection fields indicated by the arrows and crosses in the figure. The direction of the fields in the top and bottom layer of the beam separator are anti-parallel between both axes, whereas the field generated at the middle layer is shared and thus in parallel among both axes. The resulting deflection paths for an electron entering on either axis, for either top or bottom incidence is shown in [Fig. 4.8(c)].

4.4.4. Integrated design

A schematic mechanical representation of a fully integrated setup is shown in [Fig. 4.9(a)]. The schematic shows the three distinct layers that compose the full setup. At the top and bottom layer, a holder plate is positioned that supports on the one side the stack of MEMS electrode elements, and on the other side the EBE beam separator. Note from the schematic that the MEMS electrodes are stacked in a stair case fashion. This way, a part of each electrode is left uncovered and an electrical wire bond connection can be made between the electrode and a flexible printed circuit board that is positioned at the support plate, as shown in [Fig. 4.9(c)].

4.4.5. Layer alignment tolerance

By design of the EBE beam separator, the deflection field that is generated in the middle layer of the separator is shared among both axes and thus forms an explicit source of cross talk between the beam propagation at both axes. That is, the deflection action of an EBE beam separator is anti-symmetric for its two axes around the center of the device. This would possess no problem to a mechanically perfect aligned system. In a practical system misalignment is to be expected and consequently the electron beam trajectory at the microscope axis becomes altered as soon as the EBE beam separator is intentionally mistuned in order to correct for mechanical misalignment at the mirror axis, and vice versa. This may cause a problem that may occur at two explicit positions in the beam trajectory through the system:

- **At the top layer.** The beam deflection correction angle when passing through the top layer EBE beam separator, prior to reflection on the top layer mirror is explicitly coupled to the beam trajectory of the incident beam on the microscope axis [angles τ, τ' in Fig. 4.10(a)].
- **At the bottom layer.** The beam deflection correction angle after reflecting from the first mirror and passing through the EBE beam separator is explicitly coupled to the beam trajectory prior to leaving the system on the microscope axis [angles β, β' in Fig. 4.10(b)].

At the top layer, the misalignment is compensated for by placing an additional (electrostatic) quadrupole deflector at the beam entrance of the setup. Such deflector can be fabricated by means of MEMS techniques similar to the method that we outlined above for the barn door.

At the bottom layer, there is no sufficient space available to position an additional quadrupole deflector in between the beam separator and the exit lens, and thus the cross talk cannot be compensated for at this stage. Consequently, this part of the beam trajectory dictates the mechanical precision of layer alignment that must be accomplished.

We set out to approximate the effect of this on the resulting beam trajectory [Fig. 4.10(c)]. Considering that the lateral misalignment of the mirror axis in the top and bottom layer is given by Δt and these layers are separated in the miniature setup by $L \approx 50$ mm, a correction angle $\beta \equiv \Delta t/L$ at the bottom layer EBE beam separator

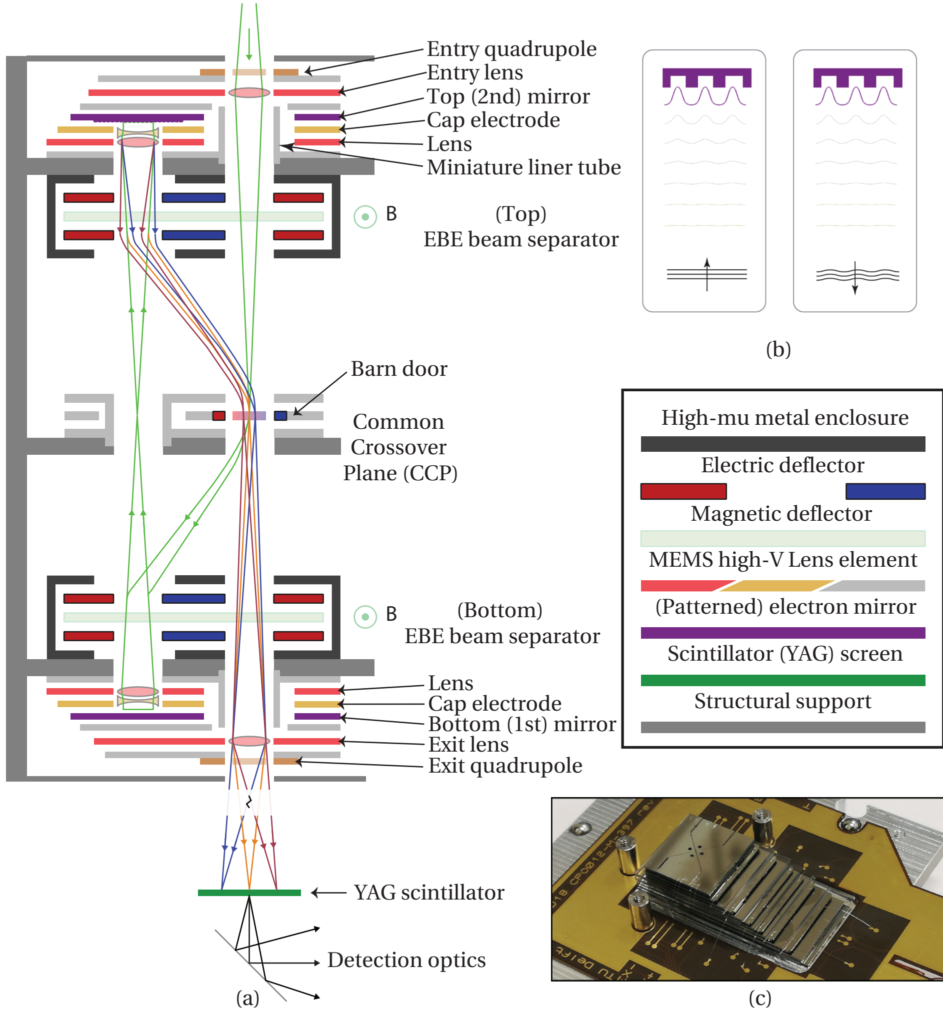

Figure 4.9: (a) Schematic cross section of the setup, containing all electron optical components. Ray trajectories are indicated for a beam entering the setup at the microscope axis from the top, and for a flat mirror at the bottom and a grating mirror at the top level layer. (b) Principle of electron wave front modulation at a patterned electron mirror. (c) Stair case stacking of MEMS electrodes, allowing for room to perform wire bonding between the electrodes and the flexible printed circuit board. Schematics are not to scale.

would be needed. This angle will offset the beam at the exit lens (on the microscope axis) by an approximate distance of $B'' = \beta\ell$ where ℓ is the spacing between the bottom EBE separator and the exit lens. A tolerable offset of ϵ_{tol} then yields a manufacturing precision of $\Delta t \leq \epsilon_{tol} L/\ell$. With conventional mechanical machining techniques, a reasonable precision of $\Delta t = 10$ μm would yield a beam offset in the exit lens of approximately 1 μm, which is small compared to the expected width of

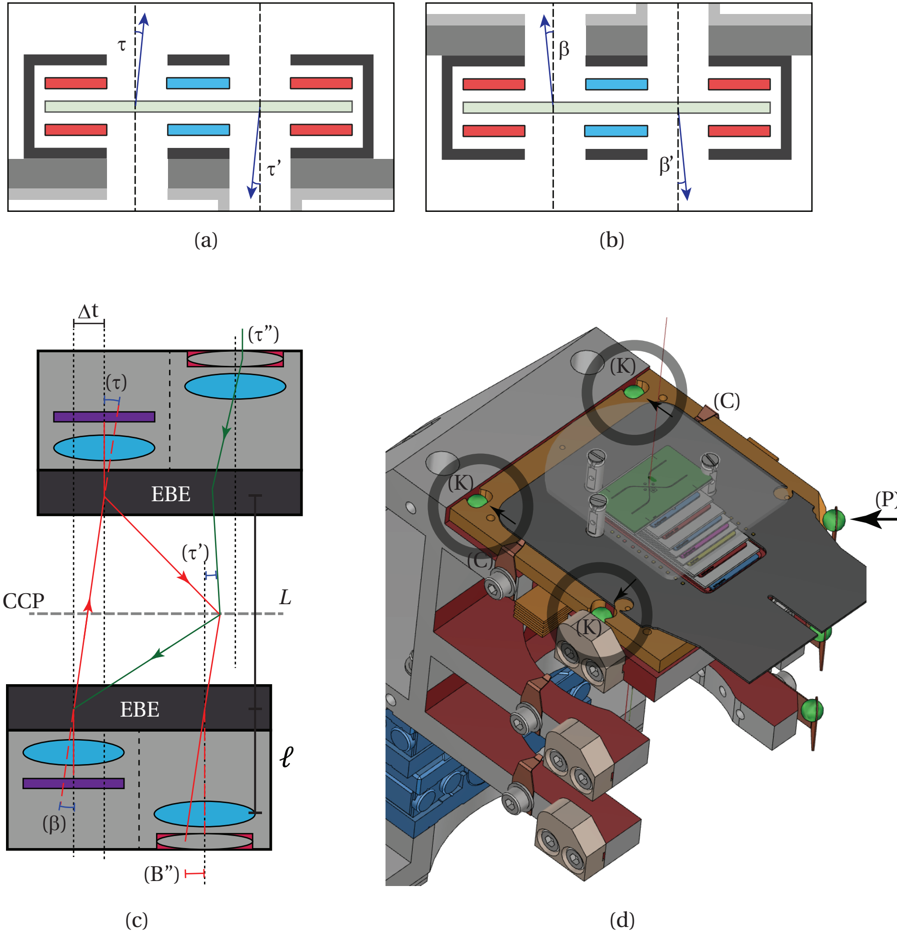

Figure 4.10: Requirements on mechanical alignment based on cross talk between the axes of the beam separator. (a, b) Compensation steering of the beam towards the coma free point on the mirror induces a cross talk deflection angle on the adjacent axis. (c) Axial misalignment Δt leading to an additional deflection angle in the top and bottom beam separators. At the top layer, the effect in the incident beam (green) is corrected for by the entry quadrupole. This correction cannot be performed at the bottom layer, leading to an off-axis propagation of the beam through the exiting lens (B''). (d) Kinematic precision ball positioning of the (top) layer, using a compression spring (P) that provides point contact positioning at (K). Two clamps (C) prevent out-of-plane movement. The holder is mounted on a two-direction piezo stage (blue elements).

the beam at this plane (order of magnitude larger).

The alignment of the three layers of the setup within the above mentioned accuracy is mechanically achieved by machining a support bracket by means of spark erosion. This bracket supports the base plates that hold the optical components at each of the three functional layers. Placement of these base plates with respect

to each other and onto the bracket can be performed through kinematic coupling design [29] with precision balls [Fig. 4.10(d)].

4.5. Integration of parts

We have commenced the manufacturing and integration of various components into a setup that fits on a custom made specimen stage of a scanning electron microscope. In this section, we share photographs of the completed mechanical parts.

4.5.1. Top and bottom layer

The top and bottom layer consist each of a mechanical support plate, that on the one side provides support for the beam separator, and on the other side provides support for the MEMS optics. The MEMS electrodes are stacked on one side of the support plate by making use of a 6 degree of freedom (6-DOF) aligner that is described in [25]. After the stacking is completed, a (flexible) printed circuit board is glued onto the support plate, and wire bond connections are used to provide the electrical contact between the MEMS electrodes and the contact pads at the circuit board.

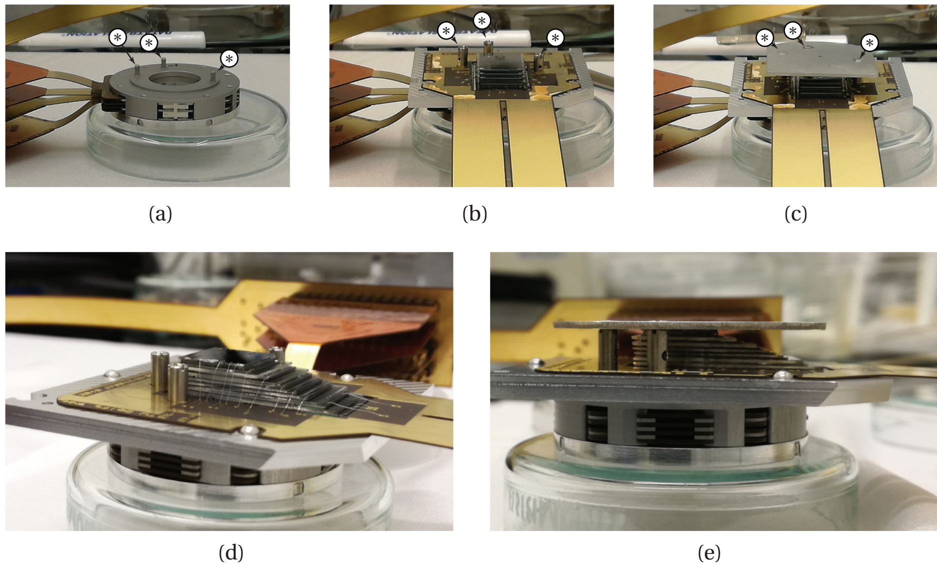

Figure 4.11: Integration of the beam separator and MEMS optics on a support plate. (a) Beam separator with wire threaded poles (indicated by asterisk). (b) Positioning of the support plate that already contains the stack of MEMS electrodes and (flexible) printed circuit board. The support plate and beam separator are clamped together with stand-of poles (indicated by asterisk). (c) Protective cover that provides mechanical protection and shielding from stray electric fields. The cover is supported on the stand-of poles. (d) Perspective view photograph of the assembled unit, with the cover removed to visualize the wire bonds. (e) Side view of the assembled unit.

Next, the beam separator is positioned at the opposite side of the support plate. The enclosure of the beam separator contains wire threaded poles [indicated by asterisk in Fig. 4.11(a)] that protrude through the support plate. This allows to fasten the beam separator against the support plate. For this, we make use of stand-of tubes with an inner wire thread. The resulting composition is shown in [Fig. 4.11(b)].

As a last step, a metal cover is positioned above the stack of MEMS electrodes, as shown in [Fig. 4.11(c)]. This cover both serves the purpose of providing a mechanical protection for the MEMS, as well as to provide additional shielding from stray electric fields that may be present in the specimen chamber of the scanning electron microscope. A perspective and side view photograph of the assembled unit is shown in [Fig. 4.11(d, e)].

4.5.2. Middle layer

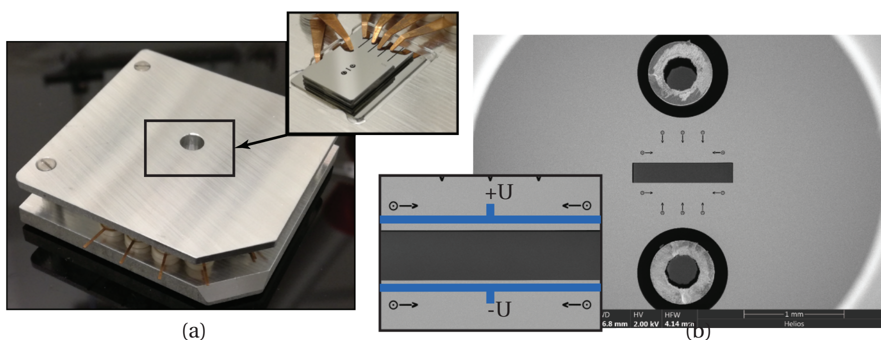

Figure 4.12: Barn door layer assembly. (a) Photograph of a completed middle layer. The barn door is shielded from stray fields with a metal cover that contains a large aperture near the optical axis. The inset shows the barn door electrodes that are positioned below the metal cover. (b) Micrograph (top-down view) of the barn door, showing the miniature liner tubes that coincide with the mirror axis and the opposite 'dummy' axis, and showing the field limiting electrode and alignment markers of the barn door. The inset shows a magnified view around the slit, including the alignment markers that are used for stacking, and a schematic indication of the orientation of the main deflector poles.

The middle layer consists of a support plate that holds the barn door deflector on one side, and is void of components at the other side. A photograph of the assembled layer is shown in [Fig. 4.12(a)], and shows the presence of a metal cover that provides mechanical protection to the barn door electrodes, as well as shielding from stray electric fields. The metal cover contains a large aperture near the optical axis. In the current design, we make use of phosphor bronze electrical contacts that at a later stage may be replaced with a custom printed circuit board.

The barn door electrodes are stacked using the 6-DOF aligner in a similar way as to how the MEMS electrodes in the top and bottom layers are stacked. A top-down micrograph of the barn door [Fig. 4.12(b)] shows the field limiting aperture

and the alignment markers around the entrance slit that are used to accomplish sub-micrometer alignment precision. Also, the presence of the miniature liner tube around the mirror axis, as well as the 'dummy' liner tube at the opposite side of the slit deflector are visible in the photograph.

4.5.3. Combination of layers

The top and bottom layers that contain the beam separator and MEMS optics, as well as the middle layer that contains the barn door deflector, are each placed at the respective stage of the E-bracket that was already shown schematically as the gray element in [Fig. 4.10(d)]. A photograph of the assembled unit is shown in [Fig. 4.13(a)]. After placing each layer in the E-bracket, the assembly is mounted onto the specimen stage of the scanning electron microscope [Fig. 4.13(b)]. The flexible circuits boards are connected to an electrical patch panel that is positioned at the vacuum side of the microscope stage. In [Fig. 4.13(c)] a detail photograph shows the compression spring, clamps, and kinematic precision balls that were earlier discussed in [sct. 4.4.5].

4.6. Discussion and conclusion

The double mirror setup that we proposed here can in principle be integrated as a column extension into a transmission electron microscope (TEM). This would potentially enable novel imaging schemes, including multi-pass electron microscopy, quantum electron microscopy, structural hypothesis testing, and wave front shaping in general. At the current stage of progress, we have designed a prototype setup that is currently being tested inside the specimen chamber of a scanning electron microscope.

The initial tests have indicated that the titanium miniature liner tubes that we used are prone to the built up of electrical charge inside the cylinder walls. This has so far prohibited us from obtaining a full round trip through the setup. Attempts of suppressing this problem by means of increasing the electron beam energy are limited due to the sensitivity of the MEMS electrodes for electrical break down. Additional research is needed into materials and processing methods that reduce or eliminate the charge built-up inside the miniature liner tube. Early attempts at this indicate Molybdenum-based tubes as a relatively cost-effective method, although these have only been tested in an isolated test setup and are currently not yet integrated in the assembled setup.

The current optical design of the setup is shown theoretically to be free of dispersions at the sample plane after a round trip through the resonator. This is however not the case for the dispersion at the mirror planes. We do not expect that this is a problem, as long as only a single round trip is considered and only one mirror is used for beam shaping. Thus, the setup in its present form can be used to validate design principles and to obtain initial experience with double mirror based miniature optics. However, a problem may arise when the setup is used for multi-pass microscopy, or when both mirrors are patterned for controlled wave front shaping. In that case a field lens at the common crossover plane in between the mirrors may

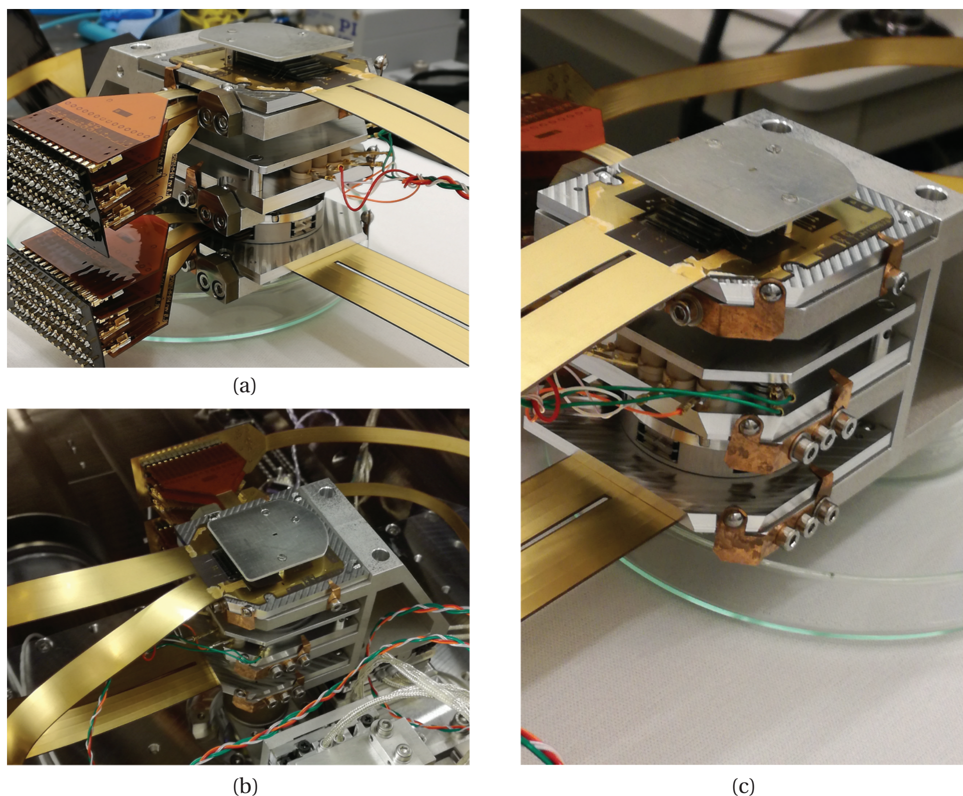

Figure 4.13: Assembly of top, middle, and bottom layer onto the E-bracket. (a) Photograph of the assembly with all layers placed. (b) Photograph of the assembled unit positioned at the specimen stage inside the scanning electron microscope. (c) Detail of the top layer placement, showing the compression spring, clamps, and kinematic precision ball parts.

be needed, but we do not have a detailed design available for that at this moment.

With an improved optical design in place that provides a dispersion free plane in front of the mirrors, a further extension to the setup would be to replace the static barn door by an ultrafast deflector. At a 2 keV beam energy, the time it takes to complete a round trip in the resonator is approximately $4-5$ ns. In order to trap the electron inside the resonator loop, this requires to double the deflection potential within that time frame. It is then preferable to work with a small deflection potential, which should be possible by reducing the width of the gap between the deflector poles.

An alternative approach to the design of this ultrafast deflector would be to distribute the deflector potential among two stacked electrodes, as shown in [Fig. 4.14]. Two independent power supplies can then be used to provide the deflection potentials. The phase difference between the outputs of these supplies can be tuned with relative ease, and this enables one to vary the number of round trips inside the

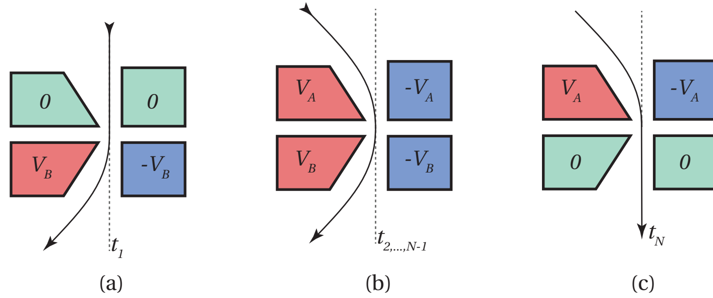

Figure 4.14: Design for an ultrafast barn door deflector that consists of two deflection layers. The tapered design enables a reduced gap width between the electrode pairs and helps to reduce the needed deflection potential. (a) Excitation of only the lower electrode pair enables the entrance to the resonator. (b) Excitation of both electrode pairs traps the electron inside the resonator. (c) Excitation of only the upper electrode pair enables the exit from the resonator.

resonator.

The excitation of only the bottom electrode pair in this configuration provides the entrance field for the electron to enter the resonator, as is shown in [Fig. 4.14(a)]. The electron is next trapped inside the resonator by excitation of both the upper and lower electrode pair [Fig. 4.14(b)]. After an integer amount of round trip times t_N the electron is removed from the resonator by only exciting the upper electrode pair [Fig. 4.14(c)]. The tapered design of the electrodes as shown in the schematic enables one to reduce the gap width between the electrode pairs and therewith help to further reduce the switching potential $V = V_A = V_B$, and additionally also increases the clearance of the electron with respect to the side wall of the electrodes.

In conclusion, we have described an experimental setup that provides a way of using two patterned electron mirrors inside the specimen chamber of a scanning electron microscope. Initial numerical and experimental results show the potential of using miniature electron optics to realize the proposed experimental design. We are currently performing initial experimental tests with the double mirror unit.

References

[1] G. Guzzinati, L. Clark, A. Béché, R. Juchtmans, R. V. Boxem, M. Mazilu, and J. Verbeeck, *Prospects for versatile phase manipulation in the TEM: Beyond aberration correction,* Ultramicroscopy **151**, 85 (2015).

[2] C. W. Johnson, J. S. Pierce, R. C. Moraski, A. E. Turner, A. T. Greenberg, W. S. Parker, and B. J. McMorran, *Exact design of complex amplitude holograms for producing arbitrary scalar fields,* Optics Express **28**, 17334 (2020).

[3] R. Danev and K. Nagayama, *Transmission electron microscopy with Zernike phase plate,* Ultramicroscopy **88**, 243 (2001).

[4] J. Verbeeck, A. Béché, K. Müller-Caspary, G. Guzzinati, M. A. Luong, and M. D. Hertog, *Demonstration of a 2×2 programmable phase plate for electrons,* Ultramicroscopy **190**, 58 (2018).

[5] A. M. Carroll, *Pattern generators for reflective electron-beam lithography (REBL),*

in *Advances in Imaging and Electron Physics* (Elsevier, 2015) pp. 1–23.

[6] H. Okamoto, *Adaptive quantum measurement for low-dose electron microscopy,* Physical Review A **81** (2010), 10.1103/physreva.81.043807.

[7] Chapter 3 in this thesis.

[8] H. Dohi and P. Kruit, *Design for an aberration corrected scanning electron microscope using miniature electron mirrors,* Ultramicroscopy **189**, 1 (2018).

[9] A. B. Bok, J. B. le Poole, J. Roos, and H. de Lang, *Mirror electron microscopy,* in *Advances in Imaging and Electron Physics* (Elsevier, 2017) pp. 99–192.

[10] P. Kruit, R. Hobbs, C.-S. Kim, Y. Yang, V. Manfrinato, J. Hammer, S. Thomas, P. Weber, B. Klopfer, C. Kohstall, T. Juffmann, M. A. Kasevich, P. Hommelhoff, and K. K. Berggren, *Designs for a quantum electron microscope,* Ultramicroscopy **164**, 31 (2016).

[11] M. Turchetti, C.-S. Kim, R. Hobbs, Y. Yang, P. Kruit, and K. K. Berggren, *Design and simulation of a linear electron cavity for quantum electron microscopy,* Ultramicroscopy **199**, 50 (2019).

[12] Y. Yang, C.-S. Kim, R. G. Hobbs, P. Kruit, and K. K. Berggren, *Efficient two-port electron beam splitter via a quantum interaction-free measurement,* Physical Review A **98** (2018), 10.1103/physreva.98.043621.

[13] M. A. R. Krielaart and P. Kruit, *Grating mirror for diffraction of electrons,* Physical Review A **98** (2018), 10.1103/physreva.98.063806.

[14] W. P. Putnam and M. F. Yanik, *Noninvasive electron microscopy with interaction-free quantum measurements,* Physical Review A **80** (2009), 10.1103/physreva.80.040902.

[15] S. V. Loginov, M. A. R. Krielaart, and P. Kruit, *Shot noise limited phase contrast in quantum electron microscopy,* In preparation (2020).

[16] P. Kwiat, H. Weinfurter, T. Herzog, A. Zeilinger, and M. A. Kasevich, *Interaction-free measurement,* Physical Review Letters **74**, 4763 (1995).

[17] T. Juffmann, S. A. Koppell, B. B. Klopfer, C. Ophus, R. M. Glaeser, and M. A. Kasevich, *Multi-pass transmission electron microscopy,* Scientific Reports **7** (2017), 10.1038/s41598-017-01841-x.

[18] S. A. Koppell, M. Mankos, A. J. Bowman, Y. Israel, T. Juffmann, B. B. Klopfer, and M. A. Kasevich, *Design for a 10 keV multi-pass transmission electron microscope,* Ultramicroscopy **207**, 112834 (2019).

[19] H. Müller, D. Preikszas, and H. Rose, *A beam separator with small aberrations,* Journal of Electron Microscopy **48**, 191 (1999).

[20] R. M. Tromp, J. B. Hannon, A. W. Ellis, W. Wan, A. Berghaus, and O. Schaff, *A new aberration-corrected, energy-filtered LEEM/PEEM instrument. I. Principles and design,* Ultramicroscopy **110**, 852 (2010).

[21] R. Rong, H. S. Kim, S. S. Park, N. W. Hwang, B. J. Kim, and C. H. Ahn, *A novel magnetic microdeflector for electron beam control in electron beam microcolumn systems,* IEEE Transactions on Magnetics **42**, 3237 (2006).

[22] J. Harrison, O. Paydar, Y. Hwang, J. Wu, E. Threlkeld, P. Musumeci, and R. N. Candler, *Fabrication process for thick-film micromachined multi-pole electromagnets,* Journal of Microelectromechanical Systems **23**, 505 (2014).

[23] J. Harrison, Y. Hwang, O. Paydar, J. Wu, E. Threlkeld, J. Rosenzweig, P. Musumeci, and R. Candler, *High-gradient microelectromechanical system quadrupole electromagnets for particle beam focusing and steering,* Physical Review Special Topics - Accelerators and Beams **18** (2015), 10.1103/physrevstab.18.023501.

[24] P. Kruit, *The role of MEMS in maskless lithography,* Microelectronic Engineering **84**, 1027 (2007).

[25] A. Zonnevylle, *Individual beam control in multi electron beam systems*, Ph.D. thesis, Delft University of Technology (2017), ch. 5.

[26] M. A. R. Krielaart and P. Kruit, *Flat electron mirror,* Ultramicroscopy **220**, 113157 (2021).

[27] D. Preikszas and H. Rose, *Correction properties of electron mirrors,* Journal of Electron Microscopy **46**, 1 (1997).

[28] M. A. R. Krielaart, D. J. Maas, S. V. Loginov, and P. Kruit, *Miniature electron beam separator based on three stacked dipoles,* Journal of Applied Physics **127**, 234904 (2020).

[29] A. H. Slocum, *Precision machine design; ISBN: 0-13-690918-3, Ch. 7, Sct. 7,* Society of Manufacturing Engineers: Dearborn, MI, USA (1992).

5

Miniature electron beam separator based on three stacked dipoles

M. A. R. Krielaart, D. J. Maas, S. V. Loginov, P. Kruit

Abstract.
We designed and built a compact bi-axial electron beam separator. This separator is an indispensable electron optical element in the development of MEMS-mirror-based miniaturized concepts for quantum electron microscopy (QEM) and aberration-corrected low-voltage scanning electron microscopy (AC-SEM). The separator provides the essential cycling of the electron beam between the two parallel optical axes that are part of these systems. This requires crossed electric and magnetic fields perpendicular to the beam path, as can be found in Wien-filter type beam separators. In our miniaturized QEM or AC-SEM concepts, the parallel axes are separated by only one millimeter. Conventional Wien-filter-based beam separator concepts rely on in-plane electric and magnetic multipole electrode configurations that are larger than the restricted available volume in these miniaturized QEM/AC-SEM systems. Our compact beam separator design introduces three stacked dipole electrode layers which enables simultaneous beam separation at two parallel axes that are in close proximity. The outer layer electrodes maintain an electric field for which the direction on the one axis is opposed to that on the other axis. The middle layer generates a perpendicularly oriented magnetic field that spans both axes. The total field configuration enables deflection of the beam on one axis and simultaneously provides a straight passage on the other axis. The deflection strength and distortion fields of the beam separator are experimentally obtained with a 2 keV electron beam energy. The results validate the use of the beam separator for electron energies up to 5 keV and deflection angles up to 100 mrad.

This chapter has been published as M. A. R. Krielaart, D. J. Maas, S. V. Loginov, and P. Kruit, *Miniature electron beam separator based on three stacked dipoles*, Journal of Applied Physics **127**, 234904 (2020).

5.1. Introduction

Advanced inspection and analysis equipment such as electron microscopes, mass spectrometers and focused ion beam systems contain sophisticated optical elements. These elements control both the charged particles in the primary beam, and in the secondary electron or ion signals. In most of these instruments, a beam separator is an important element in which the primary beam and the secondary beams are separated with a negligible impact on both the qualities of the primary beam and the secondary beam strength [1], thus enabling efficient high quality imaging and analysis.

Charged particle beams can be manipulated with electric and magnetic fields through the Lorentz force. While propagating through a dipole field, a charged particle beam is accelerated and/or deflected. In the special case of a spread out beam that traverses a cleverly arranged series of multipole fields, also aberration correction is achieved [2]. As the Lorentz force is dependent on both beam energy and direction, crossed electric (E) and magnetic (B) dipole fields provide zero deflection for exactly one beam energy only, for which the Wien condition $E = vB$ is satisfied. Consequently, a polychromatic beam that propagates a crossed E and B field is dispersed. The amount of dispersion is controlled by the magnitude of the fields. Beam energy analyzers such as a Wien filter [3] make use of the latter effect to measure the energy spectrum of a beam [4], and to restore longitudinal coherence in interferometers [5]. When a Wien filter is combined with a narrow aperture slit positioned behind the exit port, a monochromator is realized [6, 7]. Furthermore, overlapping perpendicular electric and magnetic fields find application in beam separators, for which the deflection angle upon propagation depends on the sign of the velocity vector.

When combining a beam separator with a beam-reflecting element, for instance an aperture mirror as in (aberration corrected) low energy electron microscopy [8], and/or a specimen at cathode potential as seen in low energy/photo emission electron microscope (LEEM/PEEM) [9–11] and mirror electron microscopy [12], again the need arises to separate the trajectories of the incident and reflected particles. For these cases there are even more challenging constraints on e.g. the separator size and its optical properties [1], since the uncorrectable aberrations cannot easily be de-magnified to have a negligible impact on the (improved) primary beam probe size.

Especially for recent suggestions for aberration correction [8] and beam patterning [13], both setups [Fig. 5.1] are enabled by the use of sub-mm-sized accurate electrodes which are manufactured using MEMS production technology [14]. As a consequence of the miniaturization, the lateral separation between the microscope axis and the mirror axis is only one or two mm, leaving a too restricted space for both conventional and state of the art miniature [15, 16] beam separators.

In this paper, we present the design, construction and evaluation of a compact electron optical beam separator that facilitates most of the above mentioned configurations. In our novel beam separator design, crossed E- and B-dipole fields are applied after each other, rather than at the same axial position as in conventional Wien filter designs. Our prototype consists of three layers of perpendicularly ar-

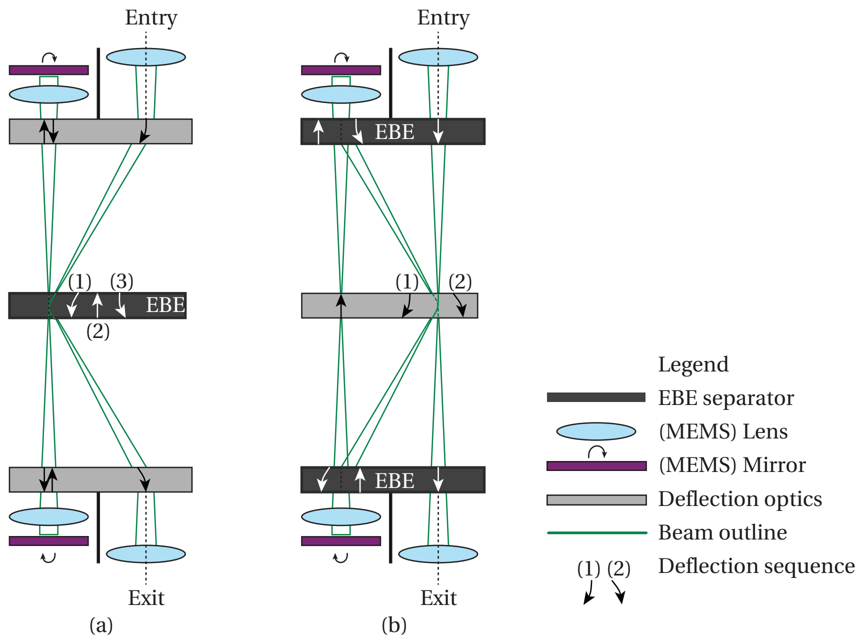

Figure 5.1: MEMS based multi-axes electron optical setups, based on proposals for (a) miniaturized double electron mirror based aberration correction for scanning electron microscopy, and (b) mirror based beam patterning. The beam enters from the top on the right hand side axis, and propagates through the setup as indicated by the beam outline (green) and deflection sequence (numbered arrow). The use of MEMS electron optics enables small deflection angles (below 100 mrad), such as to limit deflection dispersion errors. The EBE separator units indicate optical planes that require a directional dependent deflection. Other deflection optics relies on electrostatic deflection fields only.

ranged dipoles. Similar to what is seen in Mook's monochromator [6], the magnetic poles can also be used as electrostatic poles, which has the practical benefit of well-matching fringe fields. The beam is deflected in one plane by passing a sequence of E-B-E dipole fields, and in the perpendicular plane by a sequence of B-E-B dipole fields. We coin the term EBE separator for this device.

Because of the initial application of the beam separator in Low-Voltage SEM, and for miniature setups as we described above, the design that we present here is aimed at single digit keV beam energies, and deflection angles up to 100 mrad. The axes are laterally separated by 1 mm. We will obtain multipole distortion coefficients that enable to determine the limit of the beam spread in the device that is tolerable in the case of integration with setups in which the crossover plane of the beam does not coincide with the device, such as shown in [Fig. 5.1(b)].

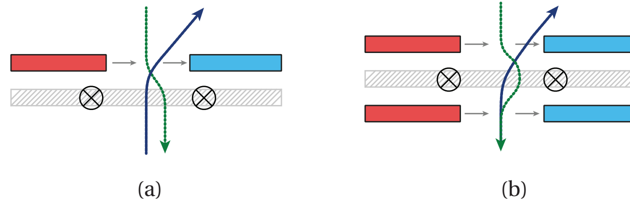

Figure 5.2: (a) Schematic beam path through two consecutive dipole fields (one electric, one magnetic) and (b) the schematic beam path through three consecutive dipole fields (two electric, one magnetic). The electric field is distributed equally among the top and bottom layer and balances the deflection through the middle magnetic field. Notice that the role of magnetic and electric fields can be interchanged.

5.2. EBE Electron optics

5.2.1. Beam separator

5

The function of a beam separator is to provide either a deflection trajectory or straight path for the incident beam [1], depending on the sign of the velocity vector. Simple beam separators exhibit (shared) in-plane magnetic and electric fields, and require a single electric and a single magnetic field that are rotated 90° in-plane with respect to each other in order to facilitate both trajectories. Consequently, the electrode geometry will not only result in a dipole (deflection) field but also a higher order hexapole field is generated.

For this reason, we separate the electric and magnetic fields spatially behind one another. This enables the use of flat dipole electrodes. However, the use of only two dipole layers would not suffice as the net effect for the supposed straight path would result in a beam shift as the dipole fields don't overlap in space [Fig. 5.2(a)]. Hence, it is required to add a third dipole layer and distribute either the electric or magnetic field contribution equally over the top and bottom layers [Fig. 5.2(b)]. This way, the straight path through the beam separator will not suffer from a beam shift, while the deflection trajectory angle can still be set independently.

Two configurations of fields comply with the above:

1. E-B-E, the electric dipole is equally distributed among the first and third level dipole and the magnetic field is generated on the second layer [Fig. 5.3(b)].

2. B-E-B, the magnetic field is equally distributed among the first and third level dipole and the electric field is generated on the second layer [Fig. 5.3(c)].

Both configurations can be set independently of each other, and the two resulting deflection planes are perpendicular to one another.

The first order effect of an excitation in one of the dipole layers can be obtained by calculating the velocity change in the direction of the resulting force upon traversing the field. For an electric dipole, the deflection angle (α_E) is dependent on the beam energy Φ (in V) and the strength of the electric field (E_x) as well as the effective length ℓ_{eff}, via

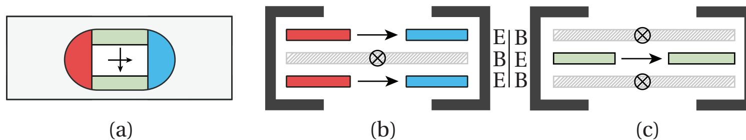

Figure 5.3: Schematic representation of the electrodes and field orientation inside the beam separator. (a) Top view, with the elongated entrance slit (grey), primary electric (red and blue) and magnetic (green) poles visible. (b) Horizontal cross section view of the beam separator, with the in-plane electric field and out-of-plane magnetic field arrows. (c) Vertical cross section view, perpendicular to the view of (b), showing the direction of the generated fields. The signs of the fields are all interchangeable.

$$\alpha_E = \frac{E_x \ell_{\text{eff}}}{2\Phi}. \tag{5.1}$$

The effective length relates to the thickness ℓ of the electrode that generates the field through the constant $k \equiv \ell_{\text{eff}}/\ell$ and accounts for the fringe fields in the first order top hat model. A value for the effective length can be obtained either through numerical modeling or matching of the deflection term to experimental data. For a magnetic induction field (B_y) dipole the deflection angle is by

$$\alpha_B = \sqrt{\frac{e}{m}} \frac{B_y \ell_{\text{eff}}}{\sqrt{2\Phi}}. \tag{5.2}$$

In both equations a top hat field is assumed in order to account for the fringe fields. The net deflection angle α that the beam obtains upon passage through the device is given by the sum of the contribution from each of the three layers.

From a numerical COMSOL model the on-axis magnetic and electric field strength is obtained for the E-B-E configuration (in plane deflection) as well as the B-E-B configuration (out of plane deflection) [Fig. 5.4]. In the model, an excitation current of 1 A, and electric potential of ± 1 V across the optical axis is used. From this data, the effective length is determined by equating the integrated on-axis fields to the top hat model, given by

$$\int F(z)\, dz = F_0 \ell_{\text{eff}}. \tag{5.3}$$

Here, $F(z)$ represents the numerical solution data for the electric or magnetic field and F_0 is the nominal field strength that is used in the top hat model. Application of [Eq. 5.3] on the numerical data yields a value of $k_{\text{t+b}} = 1.88$ for a combined excitation of the field at the top and bottom layer and $k_{\text{m}} = 1.75$ for a field excitation at the middle layer.

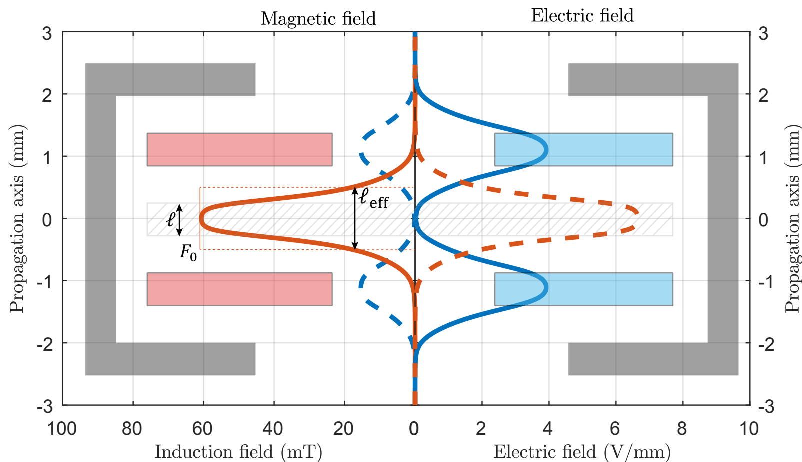

Figure 5.4: Axial (left) magnetic induction, and (right) electric field strength components, for fields that provide a net force on the beam in the in-plane (solid) and out-of-plane (dashed) direction. An excitation current of 1 A, and potential of ±1 V were used for this calculation. The definitions for the electrode thickness (ℓ) and effective field length (ℓ_{eff}) are indicated for the middle layer.

5.2.2. Beam separator for two parallel axes

We discussed in the introduction two microscope schemes [Fig. 5.1] that would benefit from the presence of a second axis. This axis should run in parallel and be separated with the optical axis over a lateral distance of order of magnitude one millimeter. The concept of the beam separator with one optical axis can be extended to include this second axis that is placed in parallel with the first axis. The resulting E-B-E and B-E-B field configurations [Fig. 5.5] then explicitly take into account the presence of the entry or exit trajectories for MEMS based setups that contain reflective elements.

The geometry of the beam separator for two parallel axes differs from the single axis design only in the top and bottom dipole layer. In these layers, an anti-parallel electric or magnetic field is added with respect to the single-axis design, whereas the geometry of the middle layer is unchanged from the single axis design. Hence, the effect of the middle layer field is the same for a both axes, whereas the effect of the top and lower layer is opposite for both axes.

For this two-axes design the E-B-E field configuration will deflect the beam in the direction of the parallel axis and thus realize the electron trajectories as shown earlier [Fig. 5.1]. Simultaneously, the B-E-B field configuration enables the deflection of the beam perpendicular to the plane that is spanned by the two axes. The latter offers a practical means of correcting for small (mechanical) alignment errors.

5.2.3. Energy filter

The dispersion relationships for the electric and magnetic fields are derived by obtaining the derivative of the deflection angle formulas with respect to the beam energy. This yields two simple equations that relate the deviation in deflection an-

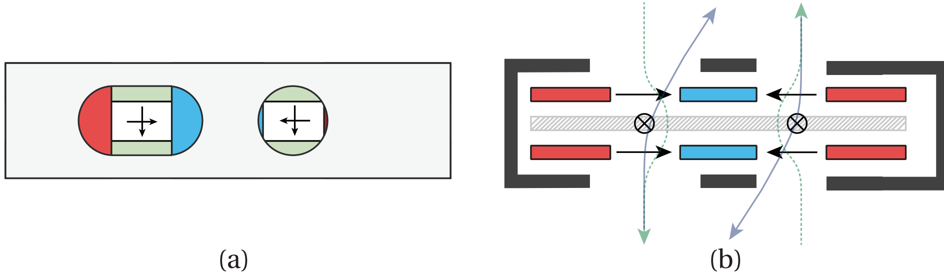

Figure 5.5: Schematic representation of the electrodes and field orientation inside the beam separator for two parallel axes. (a) Top view showing the entrance apertures (grey) and inside electrodes. (b) Direction of the fields inside the device, with respect to the various electrodes. The field in the top and bottom layer always points in opposite direction for both axes. The central field is shared across both axes and thus performs an axis-independent action on the beam. Resulting beam trajectories for electrode excitations that satisfy the Wien condition are shown. The perpendicular cross section is unchanged from the single-axis design and not shown here again.

gle ($\Delta\alpha$) as a function of the deviation of the beam energy ($\Delta\Phi$) from the nominal energy (Φ), given by

$$\Delta\alpha_E = \frac{\Delta\Phi}{\Phi}\alpha, \tag{5.4}$$

and,

$$\Delta\alpha_B = \frac{1}{2}\frac{\Delta\Phi}{\Phi}\alpha, \tag{5.5}$$

for respectively the electric and magnetic deflection dispersion. Ordinary energy filters rely on the factor two difference between the magnetic and electric dispersion relation since the fields that provide the net zero deflection, $\alpha_E = -\alpha_B$ overlap,

$$\frac{\Delta\Phi}{\Phi} = \frac{\Delta\alpha_E}{\alpha_E} = 2\frac{\Delta\alpha_B}{\alpha_B}. \tag{5.6}$$

In our device, the three dipole fields are separated in space, which does not change the outcome of the above analysis to first order.

5.2.4. Higher order effects

Our main motivation for splitting the electric and magnetic deflection layers results from the attempt of reducing the generation of higher order distortion fields. By choosing the sideways extend of the electrodes much larger than the longitudinal spacing between the dipole electrodes, we aim to eliminate the higher harmonic field distortions that are associated with more complex shaped electrodes.

The geometry that we described for the beam separator with either one axis or two axes allows for the generation of dipole fields. In the presence of a single dipole

layer, no higher order distortion can develop, neither in between the electrodes nor as a result of the fringe fields at the edge of the electrode pair.

However, the addition of multiple crossed layers of dipole electrodes may cause a 3-dimensional influence, such that the fringe fields of the separate electrode pairs become deformed under the presence of the neighboring electrode pair. Due to the symmetry of the stacked electrode geometry, and due to the asymmetry of the electric and magnetic excitations of the electrode pairs per layer, no quadrupole distortion can be generated. Instead, the first harmonic distortion field that is associated with the device geometry and field configuration is a hexapole.

The deflection and distortion field strength are described quantitatively by a projected potential along the optical axis. This is obtained as the solution of the Laplace equation for non-rotationally symmetric fields [17] with excitation amplitude U_0, given by

$$U(r,\phi) = -U_0 \sum_{n=1}^{N} c_n n r^{n-1} \cos(2\pi n[\phi + \theta_n]). \tag{5.7}$$

5

The magnitude (c_n) and orientation angle (θ_n) correspond to the optical dipole field ($n = 1$), astigmatism or quadrupole field ($n = 2$) and higher order fields. Since the deflection angle $\alpha \propto U$ is proportional to the above expression for the potential, the effect of beam propagation through the above field results in a spatial position dependent beam deflection. It must be observed that, except for the dipole field itself, all higher harmonic fields contain an off-axis radial dependence.

Consequently, the first higher order field causes astigmatism to a spread out beam due to the quadrupole field which degrades the size of the (virtual) probe size, and the second higher harmonic causes a hexapole distortion in the (virtual) probe. The resulting blur is then obtained by calculating the additional beam deflection α_n for each order, and tracing the distinct contributions back to the last image plane at distance u away from the EBE separator. For a beam of radius R_0 inside the separator, the contribution to the probe size degradation is then given by

$$d_n^{\text{spot}} = u c_n n U_0 R_0^{n-1}. \tag{5.8}$$

It depends on the final application what degree of blurring is tolerated. For the special case where the crossover of the beam coincides with the EBE separator [for instance, in Fig. 5.1(a)], the effects of higher orders can usually be neglected.

5.3. Electromechanical design

In this section we discuss the construction of the beam separator for two parallel axes. The two-axes implementation covers the functionality that is required for both one-axis and two-axes beam separation, as well as the other applications that we discussed before. We will discuss the outline, placement and machining of the electrode poles and device enclosure, the mechanical requirements on alignment, and the integration of the electrical signals into the device.

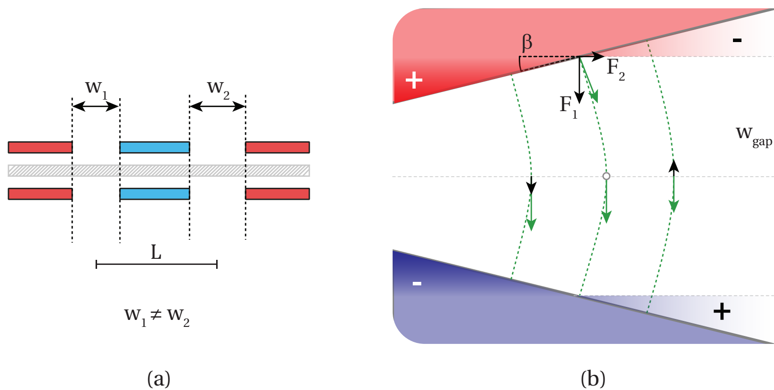

Figure 5.6: (a) Gap width mismatch as seen from the side between both axes results in a net deflection error that is proportional to the deflection angle and variation in gap width. (b) A wedge geometry as seen from above leads to a quadrupole contribution to the deflection field, that would ordinarily be absent when $\beta \to 0$.

5.3.1. Machining tolerances

The tolerances on machining accuracy and mechanical alignment of the electrodes are dictated by the application of the device. As the device is built up from different layers of dipole geometry, any longitudinal stacking error will affect both axes equally and is of limited concern. In contrast, it is expected machining tolerances will result in variations of dipole gap spacing within the individual layers.

For both magnetic and electric dipole fields, the resulting deflection angle $\alpha \propto w_{\mathrm{gap}}^{-1}$ is inversely proportional to the separation gap width (w_{gap}) of the dipole [Fig. 5.6(a)]. Hence, a width variation $\mathrm{d}w = w_2 - w_1$ between the dipole pair on the one and on the other axis will introduce a deflection angle error ($\mathrm{d}\alpha$) that is approximated by

$$\mathrm{d}\alpha = -\frac{\alpha}{w_{\mathrm{gap}}}\mathrm{d}w. \tag{5.9}$$

In turn, for the mentioned deflection angles for use as a beam separator of up to 100 mrad, the electron trajectory through the effective straight path gets erroneously deflected by approximately 0.1 mrad/μm gap width variation. The above result is mainly applicable to the top and bottom layer of the device, as the dipole fields on these layers are not shared across both axes.

A rotation misalignment of a dipole electrode pair leads to multiple optical distortions. The dipole field at the central layer of the device is shared by both axes. Hence, an in-plane rotational placement error between the two electrodes leads to the wedged geometry when seen from the top. The gap width variation $\mathrm{d}w_{\mathrm{gap}} = L\tan(\beta)$ then provides the variation in deflection strength across both axes for a given wedge angle (β).

Additionally, the wedge angle leads to a symmetric non-uniformity in the dipole field. This is understood by comparing the dipole field strength, leading to a force

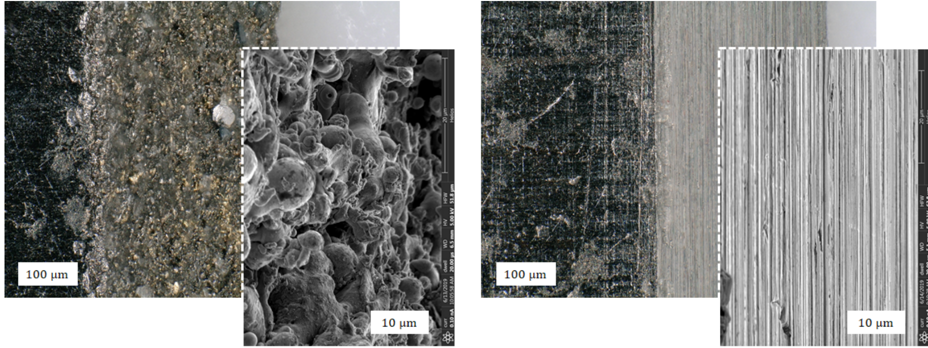

Figure 5.7: Optical and SEM inspection photo- and micrograph (tilted) of a spark eroded electrode pole before (left) and after (right) polishing with a fine grain abrasive paper. Notice the yellowish colored sediment in the photograph of the unpolished electrode, which suggests that the spark wire deposits material onto the electrode. No traces of this deposited material were found after surface treatment.

F_1 on the beam for a parallel plate geometry ($\beta = 0$), to the additional force F_2 that develops for an increasing wedge angle [see Fig. 5.6(b)]. The wedge angle β can then be obtained by comparing the (experimentally obtained) dipole (c_1) and quadrupole (c_2) coefficients, which are related through

$$\beta = \tan\left(\frac{c_2}{c_1} w_{\mathrm{gap}}\right). \tag{5.10}$$

A method for obtaining these coefficients in an experiment are discussed in the Experimental Methods section of this work.

5.3.2. Electrodes and enclosure

All electrodes are fabricated from metal that exhibits high magnetic permeability. We used μ-metal to this end, an alloy consistent of 77% Ni, 16% Fe and traces of Cu and Cr. The combination of high magnetic relative permeability of up to 3×10^5 and limited susceptibility to oxidization of the NiFe makes that magnetic and electric fields can be injected away from the optical axis of the device. In addition, μ-metal is known for its limited sensitivity to magnetic hysteresis [18].

Mechanical stress is known to deteriorate the magnetic properties of μ-metal. For this reason, all electrodes are manufactured through the use of spark erosion. The absolute machining accuracy for this technique is limited to approximately 10 μm and thus by following the earlier reasoning we may expect deflection errors up to 0.1 mrad. During manufacturing we also noticed that the spark wire deposits material onto the electrode surface, which causes surface roughness of up to 30 μm that is afterwards reduced to bulk roughness by a surface polish [Fig. 5.7].

The mechanical enclosure of the device is milled out of aluminum alloy Al 7075-T6 (AlZnMgCu1,5). Tangent surfaces are milled into the enclosure to enable the

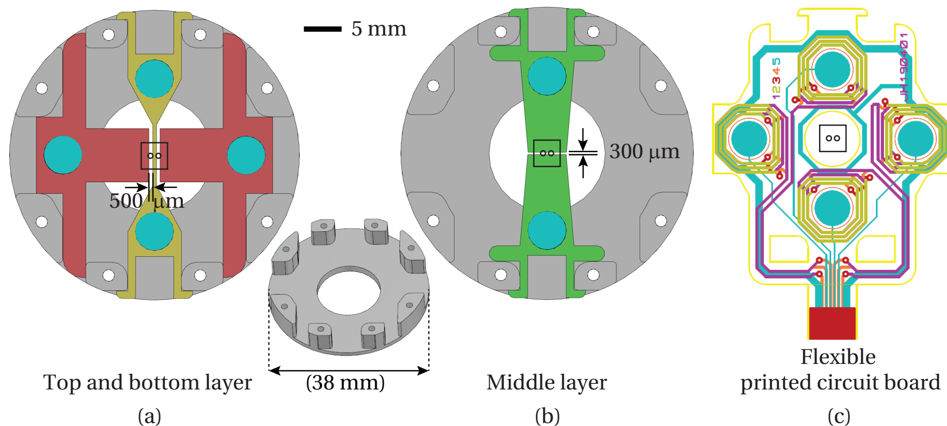

Figure 5.8: Mechanical outline of the device enclosure (inset for perspective view) and shape and orientation for (a) the top and bottom layer electrodes and (b) the central layer electrodes. All electrodes are manufactured by spark erosion from mu-metal. The alignment of the elements relies on the tangent surfaces and grips at the circumference of the device enclosure. Electrical contact and magnetic flux injection are achieved through (c) the flexible printed circuit boards (fPCBs). The turquoise islands provide electrical contact for the electrodes and these are surrounded by 12 turn coils (distributed over four layers, 3 turns per layer). The circles inside the black square indicate the position of both optical axes.

mechanical alignment of the electrodes [Fig. 5.8(a) and Fig. 5.8(b)]. After milling, the enclosure is dimensionally stable anodized in order to provide electrical insulation of the enclosure towards the electrodes.

The demonstration of principle experiments that we carried out for this work were performed inside an SEM at a beam energy of 2 keV. Because of possible application areas of the EBE beam separator that we showed before [Fig. 5.1], the two axes in the manufactured device are separated by 1 mm and a deflection angle of approximately 50 mrad must be realized during operation. In the design, care must be taken that the deflected beam path does not collides with the entrance or exit apertures of the device. The use of 0.5 mm thick electrode material, and a comparable spacing between the layers results in sufficient clearance between the beam path and the apertures.

5.3.3. Electromechanical integration

The electric potentials and the magnetic fluxes are injected into the device through flexible printed circuit boards (fPCBs) [Fig. 5.8(c)] that are positioned in between the various dipole layers. A total of four identical fPCBs is used for this. The fPCBs each contain four electrical contact pads that are exposed on one side of the fPCBs. The contact pads are rotationally separated by an angle of 90°.

Around each contact pad a multi-layer coil is integrated in the fPCBs, that is electrically independent of the included contact pad. Each mu-metal electrode is sandwiched in between two of these coils. Consequently, an opposite direction of

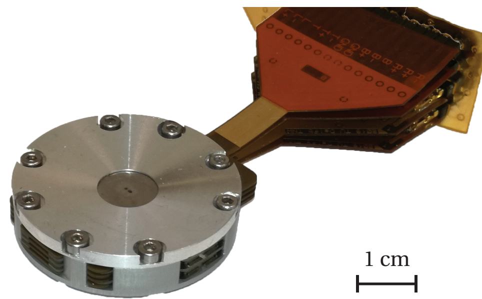

Figure 5.9: Photograph of the assembled EBE separator that was used during the experiments. The outer diameter of the holder measures 38 mm and the total thickness of the device (including the cover) measures 9.4 mm.

current through the coil pair that is formed this way allows to either source or sink magnetic flux from the in-between sandwiched mu-metal electrode. This way, the magnetic dipole fields at the optical axis are generated independently for the top and bottom layers, or middle layer. The magnetic field lines are closed through the lid of the EBE separator.

Because of the thickness that the multi-layer coils add to the fPCBs, a μ-metal disc is inserted in each of the coils and acts as a magnetic bore. The inserted disc performs a dual role by also providing the electrical interface between the embedded contact pad from the one side, and the metal electrode on the other side. The reliability of the electrical contact of the disc towards the electrode may be further improved by gold plating of the disc, although our current results were obtained without performing this step and no indications of poor electrical contact were observed.

5.4. Experimental methods

We have manufactured and assembled the two-axis beam separator [Fig. 5.9] and assess the performance through beam deflection measurements. These measurements are performed by positioning the EBE separator on an xy-translation stage inside the specimen chamber of a scanning electron microscope. A series of micrographs is obtained of a specimen that is positioned behind the separator, at increasing excitation field strength and at a beam energy of 2 keV. The resulting deflection strength and higher order multipole coefficients are obtained through numerical analysis of the micrographs.

5.4.1. Experimental setup

The experiments are performed inside the specimen chamber of a FEI Verios 640 scanning electron microscope (SEM) by mounting the device onto a custom stage. The mounting structure consists of two vertically separated levels such that the device can be positioned at a fixed distance above the sample plane. By means of two piezo actuators (Physik Instrumente, PI Q-545), we can translate the mounting

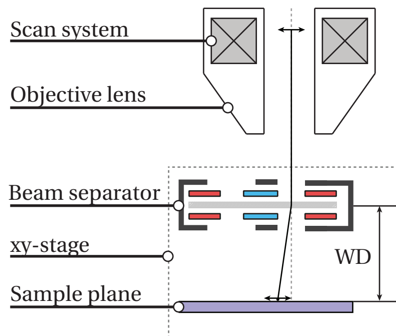

Figure 5.10: Schematic of the experimental setup. The beam separator and specimen are placed together on an xy-translation stage inside the specimen chamber of the microscope. The scan system of the microscope provides the scanning and detector logic, and the beam is focused onto the specimen by the normal-mode objective lens of the microscope.

structure in a plane perpendicular to the optical axis of the microscope for alignment purposes [Fig. 5.10].

The voltage and current supplies that are used for excitation of the deflection fields are designed and built in-house. The voltage supplies are bipolar with an output range of ±300 V and are built around a PA91 Apex Microtechnology amplifier chip. The current supply has an output current of ±500 mA and is centered around a Texas Instruments LM675T amplifier. We make use of a LabVIEW application to control the DT9854 digital-analog converters that are used to program the amplifier output signals. Micrographs are recorded by collecting secondary electrons with the ETD positioned inside the SEM chamber.

5.4.2. Deflection and distortion fields

Series of micrographs are obtained by scanning the electron beam with the microscope scanning system through one of the axes of the device, while focusing the beam onto a specimen that is positioned behind the separator. The field excitation of the EBE separator is stepwise increased in between the acquisition of each micrograph, which results in a change of beam angle [Fig. 5.10]. After the acquisition, image registration is performed on consecutively recorded micrographs and in this way we obtain displacement maps that relate corresponding regions in both micrographs. The image registration is performed numerically through an implementation of Speeded-Up Robust Features (SURF) based feature recognition [19] in MATLAB [20]. We found that the unpolished side of a single side polished (SSP) Si wafer provides us with sufficient and detailed unique features for the SURF method to work.

From the proportionality [see Eq. 5.7] between the projected electric field $U(r,\phi)$ and the distortion field coefficients c_n, the spatial displacement map $\vec{v}(r,\phi)$ of a narrow beam that passes through this field upon small changes (ΔU) in excitation of the field is given by

$$\vec{v}(r,\phi) = -W\Delta U \sum_{n=1}^{N} c_n n r^{n-1} \cos(2\pi n[\phi + \theta_n]). \tag{5.11}$$

W is the work distance between the EBE separator and the image plane. The coefficients are extracted from the displacement maps by placement of an analysis circle that is centered on the optical axis [Fig. 5.11(a)]. The dot product of the tangential vectors that describe the circle ($\vec{\kappa}$) and local displacement vector ($\vec{v}$) offer a quantitative scalar description of local distortion $f(\phi)$, where ϕ is the angle with the positive horizontal axis [Fig. 5.11(b)]. Analysis of the spectrum of $f(\phi)$ by means of a Fourier transform yields the complex valued coefficients F_n at the circle radius R. These coefficients are related to the multipole coefficients of [Eq. 5.11] through

5

$$c_n = \frac{|F_n|}{nWR^{n-1}}. \tag{5.12}$$

The field orientation angle is obtained from the angle of the complex valued coefficient F_n. For $n > 1$, phase wrapping occurs at field orientation angles of $2\pi/n$, which is accounted for in the numerical implementation of the method.

5.4.3. Detection limit and errors

The deflection caused by order n is dependent on the radial distance from the optical axis, as given by [Eq. 5.1]. Hence, the minimum detectable field magnitude varies for each multipole order as the effect only shows up in the displacement map when the effect is at least equal to the distance that corresponds to (a multiple of) one pixel in the recorded micrographs. Hence, weak distortion coefficients can only be discerned from the data when both a large field of view and a small pixel and probe size is used.

In the results that we obtained, the Fourier analysis is performed on a circle radius of 100 μm and this radius is limited by the field of view of the micrograph. The micrographs are recorded at a resolution of 162.8 nm per pixel. Evaluation of [Eq. 5.12] then directly provides the detection threshold for the various distortion coefficients, for a given excitation step ΔU of the field. In the data that we present next, the electrode potential is increased by 0.5 V between each measurement, thus resulting in a detection threshold of $c_{2,E_0} = 174$ mrad m^{-1} V^{-1} and $c_{3,E_0} = 1.7 \times 10^6$ mrad V^{-1} m^{-2}. Likewise, for a step wise increase of the coil current by 4 mA, the detection threshold for magnetic deflection measurements is given by $c_{2,B_0} = 21$ mrad m^{-1} mA^{-1} and $c_{3,B_0} = 2.2 \times 10^5$ mrad mA^{-1} m^{-2}.

5.5. Results and discussion

5.5.1. Dipole strength

The electric and magnetic deflection field strengths are independently measured, for both the E-B-E configuration that provides a deflection in the direction of both

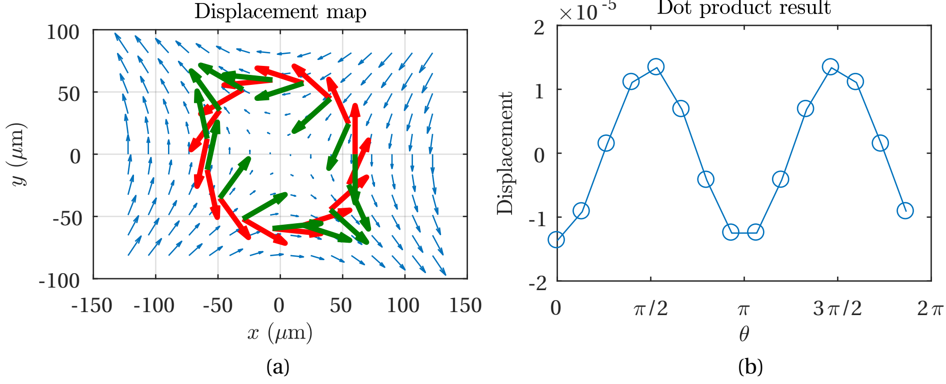

Figure 5.11: Outline of the detection method. (a) The displacement map data is interpolated onto a regular spaced grid and the displacement map vectors are shown (blue arrows). The dot product is calculated for the analysis circle tangent vectors $\vec{\kappa}$ (red arrow) and interpolated displacement vectors $\vec{v}$ (green arrows). (b) Result of the dot product calculation for the displacement map shown, a sparse data set shown for clarity.

axes, as well as for the B-E-B configuration that deflects the beam in the perpendicular plane. The deflection field strength is measured for both axes separately (distinctively labeled Axis 1 and Axis 2), and we could obtain dipole and quadrupole contributions that exceed the detection limit.

The obtained electrostatic dipole contribution for both axes [Fig. 5.12(a) and Fig. 5.12(b)] yield $c_{1,E} = 1.95$ mrad/V and the data for both axes overlaps within the uncertainty of the measurement. This value is in agreement with the theoretical expectation [Eq. 5.1], which yields an expectation of $\tilde{c}_{1,E} = 1.9$ mrad/V for an effective length factor of $k_{\mathrm{t+b}} = 1.88$. For the range of data that is shown here, an electrostatic excitation of $U = \pm 20$ V corresponds to a net deflection angle of 40 mrad.

The origin of the seemingly structured noise that is observed in the electric dipole measurement results is most likely caused by the digital to analog converter (DAC). We use a 16 bit DAC that outputs over a voltage span of ± 10 V. This signal is fed to an instrumentation amplifier with a gain of 50, thus leading to a least significant bit resolution of 15 mV. As the electrode potential is increased by 0.5 V in between each measurement, the output steps are confined around ($0.5/0.015 = 32 = 2^5$) the fifth bit of the DAC.

The magnetic dipole contributions for both axes do not fully overlap within the uncertainty of the measurement. In addition, the dipole magnitude first increases with approximately 1% of the initial value and afterwards reduces back to the initial value. The average magnetic dipole magnitude reads $c_{1,B} = 0.27$ mrad/mA for Axis 1, and $c_{1,B} = 0.28$ mrad/mA for Axis 2. We make use of the numerically determined $k_{\mathrm{m}} = 1.75$ for deflection in the middle layer in order to estimate the effective value μ of the magnetic material [through Eq. 5.2, and $B = \mu\mu_0 NI$, with N the number of coil turns and I the current through the coils], and this yields a value of $\mu = 800$

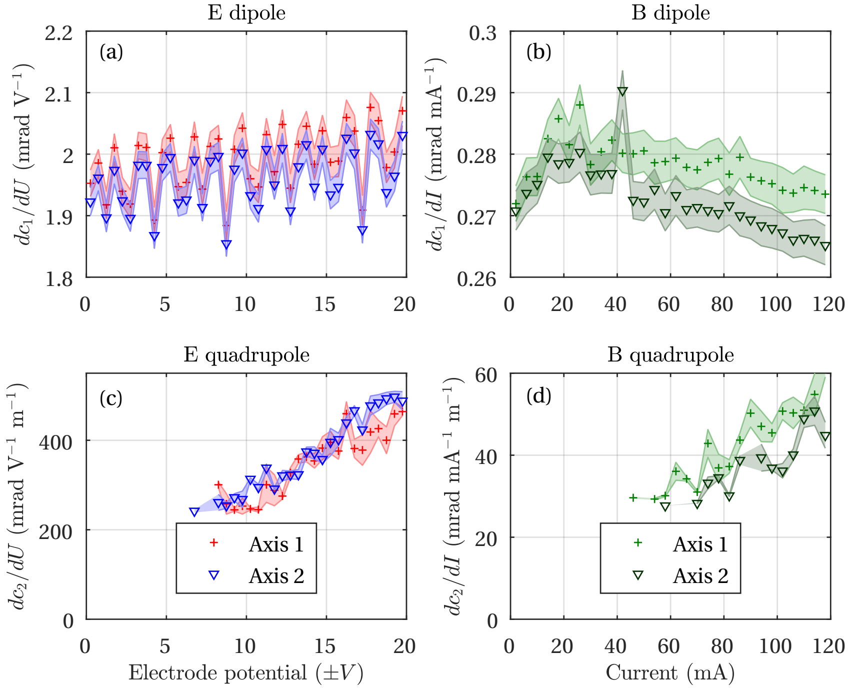

Figure 5.12: (a) Electric and (b) magnetic dipole magnitudes, and quadrupole (c) electric and (d) magnetic magnitudes obtained for both axes in the E-B-E configuration. Results obtained at 2 keV beam energy.

for the magnetic circuit.

5.5.2. Multipole strength

The obtained quadrupole contributions display a linear increase as function of excitation parameter [Fig. 5.12(c) and Fig. 5.12(d)]. This is a nontrivial result, since the coefficients are supposed to be independent of excitation. However, the former is strictly true only when an increasing excitation would not modify the position of the beam inside the field. This is not the case here, since the dipole fields, that act simultaneously with the distortion field on the beam, move the beam off-axis [Fig. 5.13(a)].

From the geometry that is shown [Fig. 5.13(a)], the off-axis effect is most apparent for the characterization of the electric field. Then, the beam propagation through the top layer is responsible for an initial deflection angle of $Uc_{1,E}/2$. This results in an off-axis position for the beam on the third layer that is given by $\delta = U\lambda c_{1,E}/2$.

For a fixed azimuth angle $\phi = \phi_0$, the multipole description [Eq. 5.8] can be simplified to

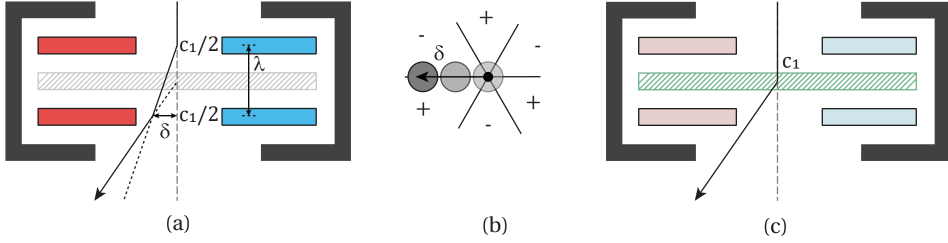

Figure 5.13: The effect of a hexapole distortion shows up as a quadrupole contribution that is dependent on the off-axis distance δ. The effect is most pronounced for (a) simultaneous deflection in the top and bottom layer, either electrically or magnetically. (b) A narrow beam that propagates off-axis through a hexapole field initially suffers a quadrupole field, which gradually is taken over by an apparent dipole field. (c) When the deflection is performed by the middle layer only, a definition of δ that is consistent with the former is nontrivial.

$$U(r,\phi_0) \propto c_1 + 2c_2 r + 3c_3 r^2 + \mathcal{O}(r^3). \tag{5.13}$$

The field that is generated by an on-axis hexapole can be described by two quadrupole fields that are positioned opposite of one another, and rotated with respect to each other by 90° [Fig. 5.13(b)]. Since a hexapole increases radially quadratic in strength, the incremental change for a fixed azimuthal angle at off-axis position $r = \delta$ is given by

$$\left.\frac{\mathrm{d}U_3}{\mathrm{d}r}\right|_{r=\delta} = 6c_3\delta. \tag{5.14}$$

This term increases linearly off-axis and we recognize it as the local quadrupole contribution, through $6c_3\delta \equiv 2c_2$. By plotting the obtained c_2 terms as a function of δ [Fig. 5.14(a)], the hexapole strength is approximated from the slope of the linear curve that fits the data, and we find $c_3 = 3.3 \times 10^5$ mrad V^{-1} m^{-2}. When the offset of the linear fit is interpreted as the residual quadrupole distortion, a value of $c_{2,E} = 7.5 \times 10^1$ mrad V^{-1} m^{-1} is obtained.

A similar analysis that would yield the hexapole magnitude of the central magnetic layer is less trivial, since an expression for the off-axis position δ would be less intuitive [Fig. 5.13(c)]. For this, we assumed a value of δ that corresponds to the off-axis position of the beam as it is propagated half way through the field. A linear fit through the data points is obtained with this assumption [Fig. 5.14 (b)], and a hexapole magnitude of $c_{3,B} = 9.27 \times 10^5$ mrad mA^{-1} m^{-2} was found.

The obtained quadrupole coefficients now enable an estimate of wedge angle β_2 inside the various layers of the structure. For the main electric deflection field (top and bottom layer), in accordance with [Eq. 5.10] we find a wedge angle $\beta_{\text{top+bottom}} =$ 19 mrad. The wedge angle in the middle layer is determined through the magnetic dipole and quadrupole coefficients and results in $\beta_{\text{middle}} = 7$ mrad.

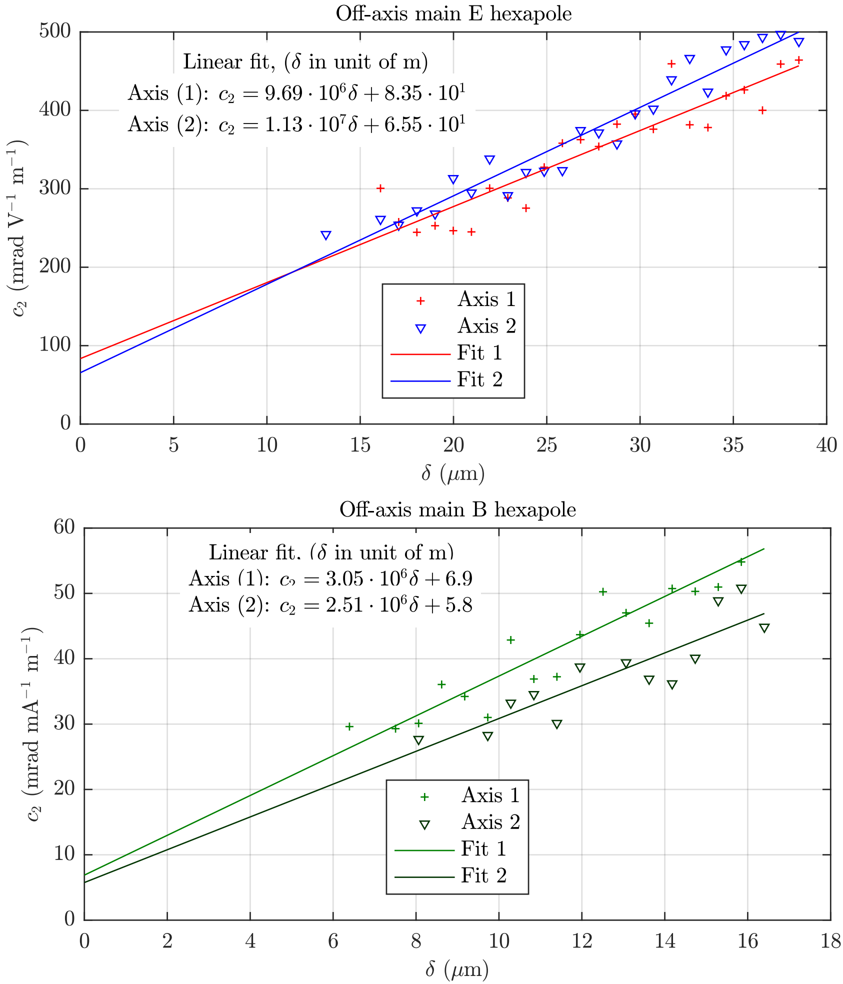

Figure 5.14: (a) The obtained electric quadrupole magnitude c_2 as a function of the off-axis position in the bottom layer, for both axis and obtained for a 2 keV beam energy. From the slope, the hexapole field strength is approximated, $c_{3,E} = 3.3 \times 10^5$ mrad V^{-1} m^{-2}. (b) The obtained magnetic quadrupole magnitude, as a function of the estimated average off-axis position in the middle layer magnetic field. From the slope, $c_{3,B} = 9.27 \times 10^5$ mrad mA^{-1} m^{-2} is obtained.

Table 5.1: Overview of the obtained electric and magnetic field multipole strengths, depending on the level of field excitation and at 2 keV beam energy. Q represents the excitation method ($Q \equiv$ mA for magnetic excitation, and $Q \equiv$ V for electric excitation). Entries are blank when no sufficient data points for sampling are obtained.

	Electrostatic ($Q \equiv$ V)		Magnetic ($Q \equiv$ mA)	
	Top & Bottom	Middle layer	Top & Bottom	Middle layer
c_1/Q [mrad/Q]	1.98	1.22	1.68×10^{-1}	2.75×10^{-1}
c_2/Q [mrad/(Q · m)]	7.5×10^{1}	–	–	6.35
c_3/Q [mrad/(Q · m^2)]	3.50×10^{6}	–	–	9.27×10^{5}

5.5.3. Overview of obtained fields

An overview of the measured and numerically approximated deflection coefficients is given in Table 5.1. The data for deflection in the direction perpendicular to the two axes (B-E-B configuration) are obtained in line with the above outlined methods as well. The integration of the EBE separator in a setup in which the crossover plane of the beam coincides with the device, such as in [Fig. 5.1(a)] results in feasible excitation values for low-keV beam energies. In contrast, for applications where the beam is spread out, the application is currently limited by the astigmatism caused by c_2, which at a working distance of 25 mm and for a beam waist of 10 μm results in conservative numbers $d_2^{\text{spot}} \sim 500$ nm, and $d_3^{\text{spot}} \sim 150$ nm in accordance to [Eq. 5.8]. We expect that improved machining accuracy for the wedge angles may improve the off-axis performance of the device for the latter application.

Finally, we observe that the electric dipole contribution from the top and bottom excitation is larger than that of the middle layer, while the opposite behavior is observed for the magnetic dipole contributions. This observation is ascribed to the difference in gap width, which is 500 μm for the outer layers, and 300 μm for the middle layer in the device that we tested. Hence, the magnetic resistance in the middle layer is smaller than that of the outside layers and this leads to an increase in magnetic deflection per mA excitation, since an equal number of coil windings and thus magnetic flux is used in the central layer as well as for the outer layers combined. Contrarily, the electric dipole coefficient for the outer layers is larger than the central layer despite the higher field strength in the central layer at equal excitation. This is explained by the double passage of a deflection field in the outer layers [ref. Fig. 5.4], and thus an effective increase in deflector area.

5.6. Conclusions

We have built a versatile miniature electron optical device [Fig. 5.9] that is demonstrated for use as an electron beam separator, and that can principally also be deployed as an energy analyzer and monochromator. The incorporation of two parallel axes in the device allow for integration with multi-axes MEMS based electron optical setups. The device departs from conventional beam separator designs by

spatially separating the electric and magnetic fields in different layers. In this way, three deflection dipole layers are realized that can accommodate either an electric or magnetic field.

The obtained magnitudes for deflection of the beam in the direction of the other axis are obtained as an electric dipole, $c_{1,E} = 1.98$ mrad/V, and a magnetic dipole with a strength given by $c_{1,B} = 0.275$ mrad/mA. The method that we used was not sensitive enough for direct measurement of the hexapole distortion coefficient, but these coefficients were obtained from the slope in the quadrupole data points.

Acknowledgments. EBE separator concept by P. Kruit, M. A. R. Krielaart, and D. J. Maas, image registration and processing by S. V. Loginov and M. A. R. Krielaart. The authors acknowledge technical support for mechanical design by Ruud van Tol and Youp van Goozen, flexible PCB design by Han van der Linden, and electrical supplies design by Paul Keijzer. Author M. A. R. Krielaart also acknowledges experimental support from J. te West during initial evaluation experiments. We acknowledge financial support for this work by the Dutch Research Council (NWO) and the Gordon and Betty Moore Foundation. D. J. Maas gratefully acknowledges support by Hitachi High Technologies for his contribution to this work.

Data availability statement. The data that support the findings of this study are available from the corresponding author upon reasonable request.

References

[1] H. Müller, D. Preikszas, and H. Rose, *A beam separator with small aberrations,* Journal of Electron Microscopy **48**, 191 (1999).

[2] P. W. Hawkes, *Aberration correction past and present,* Philosophical Transactions of the Royal Society A: Mathematical, Physical and Engineering Sciences **367**, 3637 (2009).

[3] E. Plies, K. Marianowski, and T. Ohnweiler, *The Wien filter: History, fundamentals and modern applications,* Nuclear Instruments and Methods in Physics Research Section A: Accelerators, Spectrometers, Detectors and Associated Equipment **645**, 7 (2011).

[4] N. Sillon and R. Baptist, *Micromachined mass spectrometer,* Sensors and Actuators B: Chemical **83**, 129 (2002).

[5] M. Nicklaus and F. Hasselbach, *Wien filter: A wave-packet-shifting device for restoring longitudinal coherence in charged-matter-wave interferometers,* Physical Review A **48**, 152 (1993).

[6] H. W. Mook and P. Kruit, *Optics and design of the fringe field monochromator for a Schottky field emission gun,* Nuclear Instruments and Methods in Physics Research Section A: Accelerators, Spectrometers, Detectors and Associated Equipment **427**, 109 (1999).

[7] H. W. Mook and P. Kruit, *Construction and characterization of the fringe field monochromator for a field emission gun,* Ultramicroscopy **81**, 129 (2000).

[8] H. Dohi and P. Kruit, *Design for an aberration corrected scanning electron microscope using miniature electron mirrors,* Ultramicroscopy **189**, 1 (2018).

[9] R. M. Tromp, J. B. Hannon, A. W. Ellis, W. Wan, A. Berghaus, and O. Schaff, *A new aberration-corrected, energy-filtered LEEM/PEEM instrument. I. Principles and design,* Ultramicroscopy **110**, 852 (2010).

[10] E. Bauer, *LEEM and UHV-PEEM: A retrospective,* Ultramicroscopy **119**, 18 (2012).

[11] R. M. Tromp, J. B. Hannon, W. Wan, A. Berghaus, and O. Schaff, *A new aberration-corrected, energy-filtered LEEM/PEEM instrument II. Operation and results,* Ultramicroscopy **127**, 25 (2013).

[12] A. B. Bok, J. B. le Poole, J. Roos, and H. de Lang, *Mirror electron microscopy,* in *Advances in Imaging and Electron Physics* (Elsevier, 2017) pp. 99–192.

[13] M. A. R. Krielaart and P. Kruit, *Potentially programmable virtual phase plate for electron beams,* Microscopy and Microanalysis **25**, 92 (2019).

[14] P. Kruit, *The role of MEMS in maskless lithography,* Microelectronic Engineering **84**, 1027 (2007).

[15] J. Harrison, O. Paydar, Y. Hwang, J. Wu, E. Threlkeld, P. Musumeci, and R. N. Candler, *Fabrication process for thick-film micromachined multi-pole electromagnets,* Journal of Microelectromechanical Systems **23**, 505 (2014).

[16] J. Harrison, Y. Hwang, O. Paydar, J. Wu, E. Threlkeld, J. Rosenzweig, P. Musumeci, and R. Candler, *High-gradient microelectromechanical system quadrupole electromagnets for particle beam focusing and steering,* Physical Review Special Topics - Accelerators and Beams **18** (2015), 10.1103/physrevstab.18.023501.

[17] P. Kruit, *Introduction to Charged Particle Optics,* Lecture notes, Delft University of Technology (2015).

[18] S. Tumanski, *Handbook of Magnetic Measurements* (Taylor & Francis Ltd., 2016).

[19] H. Bay, A. Ess, T. Tuytelaars, and L. V. Gool, *Speeded-up robust features (SURF),* Computer Vision and Image Understanding **110**, 346 (2008).

[20] MATLAB, *Detect SURF features and return SURFPoints object* (accessed August, 2019).

5

6

Flat electron mirror

Abstract.

Electron beams can be reflected by an electrode that is at a more negative potential than the cathode from which the beam is emitted. We want to design a mirror with a flat mirror electrode where the electrons are reflected at a plane very close to the electrode. The wave front of an electron can then be shaped when the mirror contains a surface topography or modulated potential. However, electron beams reflected by flat electron mirrors are usually characterized by high coefficients of chromatic and spherical aberration. When the mirror is combined with an electrostatic lens to form a tetrode mirror system, the situation deteriorates even further. This places a restrictive limit on the maximum aperture angle of the beam, and consequently also limits the attainable resolution at the image plane. We have numerically studied the dependence of these aberrations as a function of design parameters of the tetrode mirror consisting of a ground, lens, cap, and mirror electrode, and limited ourselves to only using flat electrodes with round apertures, at fixed electrode spacing. It turns out that the third order spherical aberration can be made negative. The negative third order aberration is then used to partially compensate the positive fifth order aberration. This way, a system configuration is obtained that, at 2 keV beam energy, provides a diffraction limited resolution of 7.6 nm at an image plane 25 mm from the mirror at beam semi-angles of 2.3 mrad, enabling an illumination radius of 40 mum at the mirror. The presented tetrode mirror design could spark innovative use of patterned electron mirrors as phase plates for electron microscopy in general, and for use as coherent beam splitters in Quantum Electron Microscopy in particular. An appendix presents a method to calculate the spot size of a focused beam in the presence of both third and fifth order spherical aberration coefficients, which is also applicable to Scanning (Transmission) Electron Microscopes with aberration correctors.

This chapter has been published as M. A. R. Krielaart, and P. Kruit, *Flat electron mirror*, Ultramicroscopy **220** (2021), 10.1016/j.ultramic.2020.113157.

6.1. Introduction

An electron beam is reflected at an equipotential surface, under the condition that the electric potential matches that of the electron beam acceleration voltage. Mirror electron microscopy (MEM) [1, 2] schemes revolve around this principle, and derived techniques are mainly applied in the field of surface physics [3–5]. In one mode of operation, the specimen is kept at a bias potential that is slightly more negative than the beam acceleration voltage, so that the equipotential surface of reflection closely resembles the surface topography or structure of the specimen. It is the modulation of the reflection field that imprints a spatial phase distribution in the reflected beam. By imaging the reflected beam onto a detector, the imprinted phase distribution offers information about the specimen.

The former principle can also be reversed. By carefully sculpting a topographic pattern into a mirror substrate, the modulation of the electric field can be controlled [6]. Current research focuses on using topographically patterned grating mirrors [7] that can act as beam splitters and recombiners in quantum electron microscopy (QEM) [8]. QEM constitutes an interaction-free measurement scheme that is based on multiple passes through a Mach-Zehnder type interferometer [9]. The grating mirror is then part of an electron resonator [Fig. 6.1] in which repetitive reflection of the beam at the mirror allows for the gradual transition of amplitude between the sample and reference beam of the interferometer [10].

Electron mirrors are more typically used for the correction of axial chromatic and spherical aberrations [12]. This can be achieved with a concave shaped electric field, which can be created for instance by using an aperture with a radius much larger than the beam envelop as a mirror electrode. Another approach, for which an analytical solution to the shape of the electric field can be provided, is realized by making a cone-shaped indentation in the mirror electrode [13]. The latter is however more mechanically challenging, when compared to machining a round aperture.

Unfortunately, (nearly) flat mirror surfaces as found in the linear QEM resonator are usually characterized by large coefficients of spherical and chromatic aberration. When the mirror is positioned in the diffraction plane of an imaging system, as is the case for grating mirrors for QEM, the high aberration coefficients will result in loss of resolution at the image plane. In an electron resonator system, a second electron mirror that provides a concave reflection field can correct for these aberrations [13–16] when positioned in the conjugate plane of the flat mirror. A schematic design of such system [8, 17] is shown in [Fig. 6.1].

In principle, the required field shape of the aberration correcting mirror can be provided by the patterned (first) mirror as well. This would eliminate the need for the second mirror or the second mirror could be used for a different purpose. For this, one has to obtain the shape of the concave equipotential surface of the aberration correcting mirror at the potential of the patterned mirror. The shape of this equipotential surface can then be added to any topography that is already present on the first mirror. Alternatively, when using a mirror with a modulated potential, the aberration correction can be added as a radial potential distribution. However, especially when the desired pattern on the electrons phase front contains small features, such as the line pattern for the grating, it seems better to start with

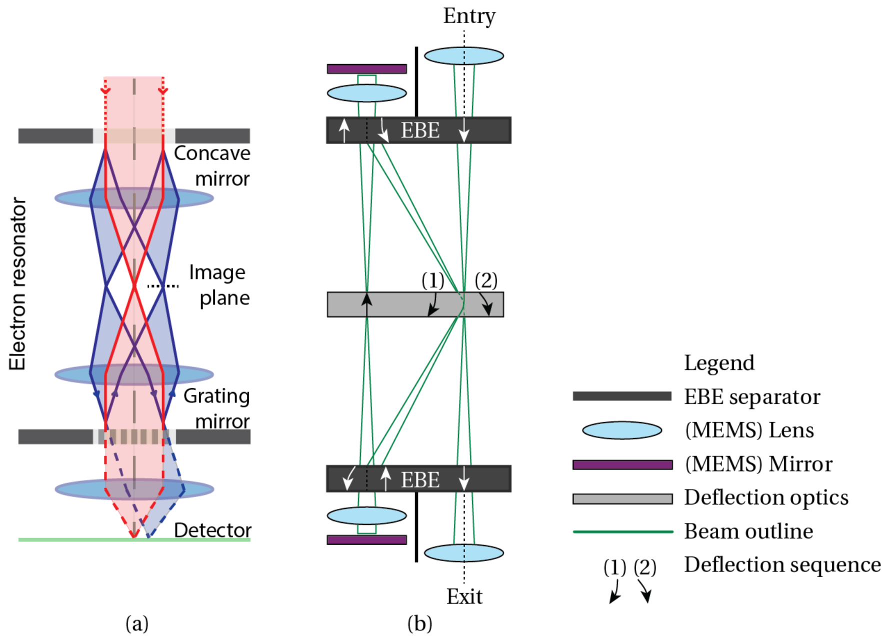

Figure 6.1: Principle and schematic design of a linear QEM resonator. (a) The electron beam enters the cavity through a temporally gated electron mirror. The central beam is diffracted at the lower mirror element, and the diffracted beam is repeatedly imaged onto the image plane. Based on the system in [8]. (b) Practical design of a linear QEM cavity that requires no temporal gating of the mirror potential. Instead, a low-voltage electrostatic deflector to the right side of the image plane enables the in-coupling, cycling, and out-coupling of the beam. Based on a system in [11].

an atomically flat surface at a single potential.

The difficulty of combining spatial frequencies that range over multiple decades stems from the drop in field modulation in the longitudinal direction, perpendicular to the mirror substrate [6]. In the above example, the grating pattern for creating diffraction would require a line profile amplitude in the order of 100 nm, while the profile amplitude for the aberration correction would be in the order of single-digit nanometers, making it very difficult to fabricate.

Thus, it would be much preferable to have a mirror design with a flat mirror electrode that has no axial aberrations. Earlier, van Aken et al. suggested that aberrations can be corrected for when a slow electron beam is transmitted elastically through a flat thin foil [18, 19], at energies well below 1 eV. This requires that the foil is maintained at a potential that is close to the acceleration voltage of the beam. The corrective properties are then obtained by a careful choice of the foil and lens geometry. The geometry of such low-voltage foil corrector must satisfy the critical condition $s \ll R_C$, with s the longitudinal spacing between the foil and the field limiting cap aperture, and R_C the radius of this aperture.

The low-voltage foil corrector provides for axial aberration correction and the basic geometry shows close resemblance to a tetrode electron mirror [Fig. 6.2(a)]

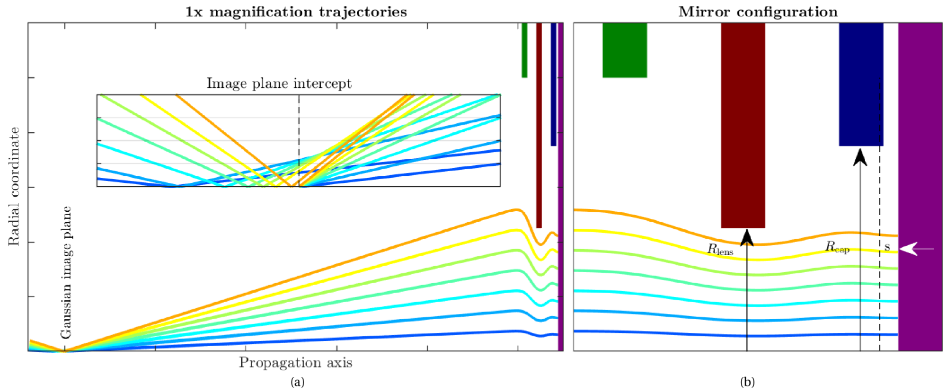

Figure 6.2: (a) Ray trajectories at 1x magnification and for coinciding object and image (sample) plane. The front focal plane of the lens coincides with these planes. The inset contains details of the ray trajectories near the Gaussian image plane. (b) Schematic overview of the mechanical configuration of a tetrode electron mirror (rotational symmetric around the propagation axis), with labels for aperture electrode radii R and spacing between the mirror and cap electrode s. Elements are identified as (green) ground, (red) lens, (blue) cap, and (purple) mirror electrode. The radial coordinate of the trajectories is magnified by factor 3. Horizontal and vertical axes are not to equal scale.

that is found in a QEM resonator. For this reason, we believe that it is possible to correct for the combined axial aberrations of tetrode mirror systems by means of the mechanical configuration.

In the past, exotic shapes for the lens element apertures were considered in order to tune the axial aberrations of the tetrode mirror [20, 21]. Here, we consider only plane through-hole apertures [Fig. 6.2(b)], and at fixed electrode spacing for the lens elements. Modern day lithographic processes have found their way into the manufacturing of very round miniature apertures [22], which allows for an easy means of tuning the aperture radius in a production process. Meanwhile, the axial separation of the distinct miniature apertures is limited by the available dimensions of flat spacer elements. For this reason, we only study the axial aberration properties of tetrode mirror systems for a range of aperture radii and potentials, at fixed aperture spacing.

We performed a numerical study with the model system that is shown in [Fig. 6.2(b)]. It consists of the flat mirror electrode and three thin plates with apertures. We have a lot of experience with making electron lens electrodes from silicon wafers using lithography and etch processes. We are able to etch apertures of typically 0.1 to 1 mm diameter with a roundness better than 1 μm which we can also align to within 1 μm.

6.2. Basic concepts

For the electron resonator design, and for repetitive imaging in QEM, we require that the image plane coincides with the front focal plane of the focusing lens of the

mirror system. This enables symmetric ray trajectories that provide the re-imaging of the reflected beam back onto the sample plane, with 1x magnification [Fig. 6.2(a)]. As we assume that the specimen is positioned in a field free region, we need at least three lens electrodes for the lens design.

The first electrode (that is positioned closest to the sample plane) provides the boundary to the field free region on the left. Without at least this one electrode, a symmetric ray trajectory can never be obtained. The second element performs the lens action. In principle, the third lens element may be omitted. However, the inclusion of the third element (positioned closest to the mirror) provides a second degree of freedom in the electric excitation of the lens that will allow to simultaneously alter the strength of the mirror electric field to the right, while also maintaining the 1x magnification re-imaging onto the sample plane. We call this third element the “cap electrode”.

The ability to tune the linear electric field strength in between the cap and mirror electrode allows for adjusting the longitudinal spacing between equipotential planes in front of the mirror [20]. Consequently, this influences the turning points and ray trajectories for a polychromatic beam and offers a degree of freedom for tuning the chromatic aberrations of the electron mirror. The object and image planes coincide with the front focal plane of the lens, thus placing the mirror electrode in the Fourier plane of the lens. For a 1x magnification, this necessarily results in a collimated beam at the mirror plane, hence we refer to the lens as a collimator.

The spot size at the image plane is determined by the semi-angle of the beam. A spot size contribution due to diffraction is unavoidable, but is reduced by increasing the beam semi-angle. While a larger beam semi-angle reduces the diffraction limited spot size, at the same time the chromatic and spherical spot size contributions will increase. In the design method that we use in this work, the mechanical configuration of the tetrode mirror is optimized to allow for a maximum beam semi-angle, that is still mainly diffraction limited.

6.3. Numerical methods

Traditionally, aberration coefficients are calculated using aberration integrals, in the case of mirrors using time dependent perturbation algorithms instead of position dependent algorithms [23, 24]. We shall rely here on the precision of modern ray trace simulations, as is also done for instance for the design of modern low-energy and photo-emission (LEEM/PEEM) microscopes [25], and additionally motivated by the given, that only axial aberrations and small beam semi-angles are considered. We performed electron ray trace simulations using the EOD software package [26–29] and extract aberration coefficients from the obtained radial coordinates of the ray trajectories at the image plane after reflection. The analyzed systems contain spatial degrees of freedom in terms of the radius of the electrode apertures [Fig. 6.2(b)], as well as electrical degrees of freedom in terms of the mirror, cap, and collimator lens potential. In a miniature QEM resonator setup that we are currently building, the distance between the mirror electrode and cross-over at the image plane of the system is 25 mm and the simulation results shown in the following are based on this value.

For the calculation of spherical (C_{s3} and C_{s5}) and chromatic (C_{c1}) aberration coefficients, the range of cap and lens aperture radius is varied from $R = 100 - 500$ μm. For a fixed beam energy of 2 keV, the potential of the cap electrode is varied between -800 V and -1200 V. We expect that the spacing between the cap and mirror electrode must be small compared to the radius of the cap electrode, similar to the condition for low-energy foil corrector geometries [18, 19], and thus fixed the electrode spacing to $s = 100$ μm between the mirror and cap electrode. This implies that a maximum field strength of up to 12 kV/mm is considered, which is slightly above a field strength of 10 kV/mm that is normally considered feasible in an experimental electron optical setup [30, 31]. The spacing between the cap, lens, and ground electrode is fixed as well at $d = 500$ μm and we only vary the radius of the various apertures as the latter offers a feasible parameter to control in (micro)fabrication and lithographic processes.

The calculation of the effect of each geometrical combination (in terms of aperture radius and cap electrode potential) is performed by first finding the lens electrode potential that allows to image the reflected beam back onto the origin. This is achieved through the following two steps:

1. A series of ray traces is performed with a marginal ray that departs from the object plane under a 4 mrad angle. At fixed mirror and cap potential, the collimator lens potential is monotonically increased until the reflected marginal ray is imaged back onto the image plane. This condition is numerically detected when two conditions are met:
   - The sign of the slope of the reflected marginal ray, at the image plane, is equal to the sign of the slope of the initial marginal ray.
   - The sign of the radial coordinate at the image plane is opposite to the former ray trace of lower collimator lens potential, indicating that the optical axis was crossed for a collimator lens potential that is higher than that of the former and smaller than that of the current calculation.
2. A full ray trace simulation is performed with the results of step 1. For determination of the third and fifth order coefficients of spherical aberration, 9 rays are traced at angles α in the range of 0 through 8 mrad. For the calculation of the chromatic aberration coefficient, the energy of the 4 mrad ray is varied in a range of ± 2 V.

6.3.1. Computationally updating the EOD input file

The EOD software package requires an input file that contains the geometry of the system. Each considered geometrical combination requires adjustments to this input file, and in order to perform a numerical study over a large parameter range, this process needs some form of automation. To this end, we use the command line options from EOD and built a MATLAB script that manages the execution of the EOD calculations.

Any input file (*.EODinp) for EOD is human readable and contains the coordinates and properties of optical elements. The coarse mesh lines that define the

contours of the electrode elements are conveniently numbered in horizontal and vertical direction and find their origin in the top-left of the grid. In any calculation routine, we first update the radius of the electrodes computationally. Each electrode is associated with a field setting that is controlled in the EOD trace file (*.EODtrc). The trace file settings are controlled through the MATLAB script by read/write operations on the specific lines of the file. After setting all parameters for the model, the command line options for EOD can start the computation through a MATLAB system-command call;

```
% Call EOD for computation and wait for finish.
system(['"path/to/EOD.exe" -p' EOD_project_name ' -tr -qt
    ']);
```

The call takes care of updating the EOD field data (in case of a change in the input file) and performs the preset ray trace operations. When the computation is finished, EOD quits automatically and returns control to MATLAB for further data processing. The obtained ray trace results are contained in EOD plot files (*.EODplt). These files are human readable, and consist of a list of prior selected properties of each traced particle. When multiple particles are traced, the results are vertically concatenated in the file.

6

6.3.2. Aberration coefficients and spot size calculation

The spot size of the beam at the Gaussian image plane after reflection from the mirror depends on the (aperture) semi-angle (α) of the beam. For small semi-angles, the spot size is diffraction limited, whereas at larger semi-angles the spot size is usually dictated by the chromatic and spherical aberration coefficients of the imaging system. It is common to describe spot size contributions with the Full Width (FW) of the beam that contains only a Fraction of Current (FC) of usually 50%. With this definition, the FW50 of the diffraction limited probe size is given (for an electron wave length λ) by [32],

$$d_{A50}(\alpha) = 0.54\lambda/\alpha. \tag{6.1}$$

The aberration coefficients are obtained from the intersect of the ray traces with the image plane. For the determination of the chromatic aberration coefficient (C_{c1}), we fit a first order linear polynomial,

$$y(\alpha) = \left(C_1 + C_{c1}\frac{\Delta E}{E} \right) \alpha. \tag{6.2}$$

Here, the coefficient C_1 allows for a defocus of the beam with nominal energy (E) at the image plane. The deviation of beam energy is labeled by ΔE. From the chromatic aberration coefficient, the FW50 contribution d_{C50} is obtained through [32],

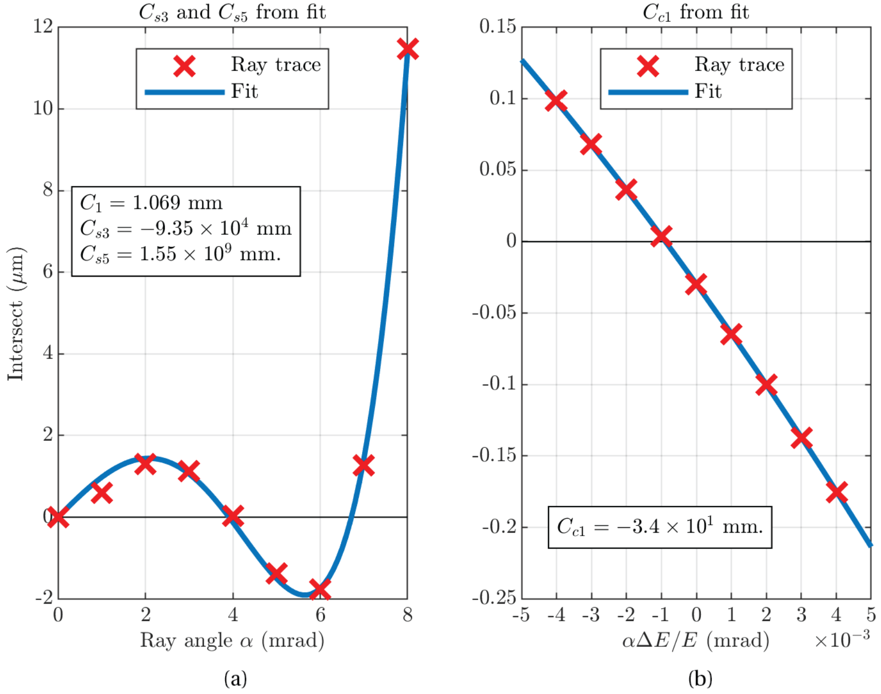

Figure 6.3: Aberration coefficients are obtained by fitting a necessarily odd valued polynomial (a) for spherical aberration coefficients (C_{s3} and C_{s5}), through the intersect of the ray trajectories at the image plane as a function of ray angle [ref. Eq. 6.4], and (b) for the chromatic aberration coefficient through the product of $\alpha\Delta E/E$ [ref. Eq. 6.2]. The absolute error in (a) is approximately 10%, and larger than that for small ($\alpha \leq 1$ mrad) ray angles.

$$d_{C50} = 0.6C_{C1}\frac{\Delta E_{FW50}}{E}\alpha. \tag{6.3}$$

From the numerically obtained ray trajectories, the third (C_{s3}) and fifth (C_{s5}) order coefficients of spherical aberration are obtained by fitting the necessarily odd polynomial,

$$y(\alpha) = C_1\alpha + C_{s3}\alpha^3 + C_{s5}\alpha^5, \tag{6.4}$$

to the resulting data set of beam angle (α) versus image plane intersect coordinate (y). Unless elsewise specified, we refer to both C_{s3} and C_{s5} in any mention of spherical aberration (coefficients). The coefficient C_1 corresponds to the defocus of the reflected beam at the image plane. In [Fig. 6.3] we show an example of fitting the polynomials to the obtained ray coordinates at the image plane.

We have assessed the accuracy of the numerical ray trace calculations by analyzing the third and fifth order spherical aberration coefficients of a diode mirror,

at a comparable grid size and interpolation method that we use for the flat mirror calculations. An exact analytical result for the diode mirror configuration is given by [14]. We found a relative error of 0.5% for the third order, and -3.8% for the fifth order coefficient of spherical aberration.

As we stated before, it is common to obtain the effect of spherical aberration coefficients on the spot size in terms of a FW50 contribution. When the fifth order coefficient is set to zero, the minimum FW50 is obtained at small defocus C_1 in between the Gaussian image plane and the image plane of the marginal ray, and given by [32]

$$d_{S50} = 0.18 C_{s3} \alpha^3 \text{ when } (C_{s5} = 0). \tag{6.5}$$

When the third order coefficient is set to zero, the minimum FW50 is also obtained at a (different) defocus, and is given by [19]

$$d_{S50} = 0.0463 C_{s5} \alpha^5 \text{ when } (C_{s3} = 0). \tag{6.6}$$

As these results are valid at a different defocus, they cannot be added into a single FW50 contribution from spherical aberration. Instead, one has to integrate the normalized weighted current $w(\alpha)$ that is contained within an infinitesimal angle $d\alpha$, in order to find the FW50. This calculation requires the inverse function $\alpha = \alpha(y)$ of [Eq. 6.4] for which no analytical solution is available, and instead must be solved numerically (see Appendix D for details about this procedure).

An interesting case arises when the signs of C_{s3} and C_{s5} are opposite. Then, as a function of increasing semi-angle α, the rays are first found on one side of the optical axis, and at increasing ray angle at the other side of the optical axis as well. This effect reduces the growth of the spherical spot size, and the spot size can be further reduced by setting the proper defocus of the beam through C_1.

The total spot size is determined by a root-power-sum of its components, in which the powers are not trivially 2 [33]. However, the coefficients for the root-power-sum from literature assume only the presence of a C_{s3}, and not the C_{s5} term when weighting the contribution of spherical aberration to the total spot size. Since the addition of C_{s5} shifts the optimum defocus plane as well, we can no longer rely on the conventional summing method. Instead, we fall back here to squared addition of terms, in the absence of a better alternative. The total probe size of the system is then given by

$$d_{FW50} = \sqrt{d_{S50}^2 + d_{C50}^2 + d_{A50}^2}. \tag{6.7}$$

In the case of a spherical aberration limited spot size, the squared addition of the spherical and diffraction limited contribution (instead of the conventional power 4), will then result in an overestimation of the spot size contribution for these two terms.

Table 6.1: Overview of system configurations that were analyzed in the numerical study. Asterisk (*) denote independent variables, the range of other properties denote practical limitations in order to provide reasonable field strengths. The actual used lens potential is interpolated from the data.

Label	Property	Range	Step	unit
R_C	Cap radius (*)	$100 \cdots 500$	50	μm
R_L	Lens radius (*)	$100 \cdots 500$	50	μm
R_G	Ground radius	500	–	μm
U_M	Mirror potential	-2000	–	V
U_C	Cap potential (*)	$-800 \cdots -1200$	100	V
U_L	Lens potential	$1000 \cdots 8000$	200	V
$\mathcal{E}$	Electron beam energy	-1990	–	V
s	Mirror cap spacing	100	–	μm
f	Focal length	25	–	mm
t	Electrode thickness	300	–	μm

6.4. Design of the tetrode mirror

We have numerically obtained electron ray trajectories for a range of cap and collimator radii, while using the cap and lens potentials to obtain 1x magnification. The beam energy is always 1990 V and the mirror electrode is at −2000 V. We only make use of accelerating lens potentials as this results in a larger spread of the beam in front of the mirror electrode, in comparison to when a decelerating lens potential is used. In principle, an optimization routine could be used to find the best values for these parameters [29, 34], but this approach is not pursued at this point. The axial aberration coefficients that were obtained through these calculations are used to determine the FW50 spot size (containing 50% of the current) for each system configuration for a range of semi-angles, after reflection, and for 1x magnification imaging to the image plane. From the resulting data set the system configurations that result in the minimum spot size as a function of semi-angle after reflection are obtained.

6.4.1. Coarse parameter sweep

The first design step consists of a coarse parameter sweep across lens and cap electrode radii, and cap potential. A total of 405 systems [for configurations, see Table 6.1] are analyzed during this step. This results in a large data set that relates the system configuration parameters and the resulting aberration coefficients.

From the obtained data, it is observed that for the third order spherical aberration coefficient both positive and negative values are obtained [Fig. 6.4(a)]. In the figure, the white line indicates the contour at which the coefficient equals zero, and negative values are found in between the two contour lines. We observe that the coefficients mainly vary as a function of the cap radius, and are less sensitive to changes in the lens electrode radius. Note that for some configurations, we could not obtain a 1x magnified reflected beam at the image plane, and these data points are indicated by the white tiles in the plot.

The data for the fifth order spherical aberration coefficient [Fig. 6.4(b)] is mainly

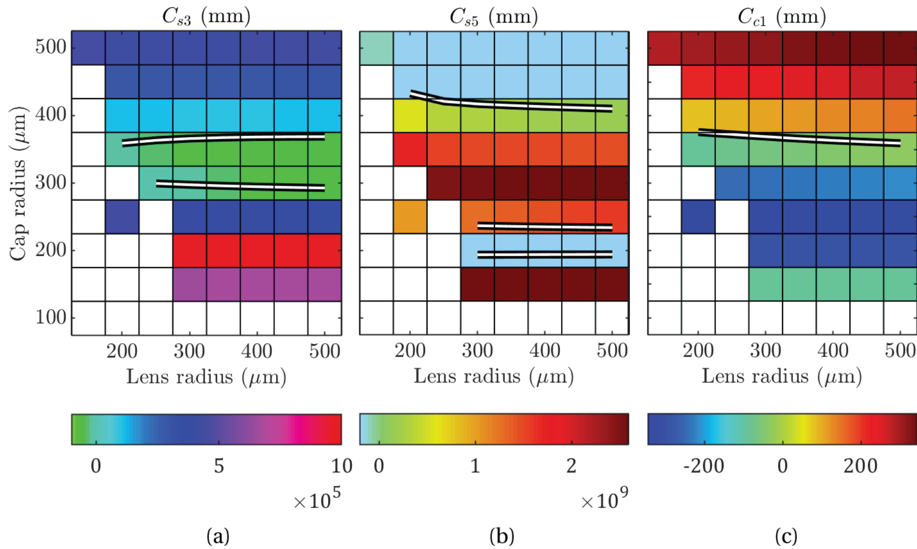

Figure 6.4: Aberration coefficients as a function of the lens and cap electrode radius, at a cap potential of -1000 V. (a) Third order and (b) fifth order spherical aberration coefficient, and (c) first order chromatic aberration coefficient, obtained from the coarse parameter sweep. White lines indicate (interpolated) zero-contours in the respective data set.

6

positive valued in the studied parameter range, and shows a decrease as a function of increasing cap radius, with a local maximum at a cap radius of approximately 300 μm.

For the first order chromatic aberration coefficient we obtained both positive and negative contributions as well [Fig. 6.4(c)]. Similar to what is observed for the spherical aberration coefficients, we notice that also the chromatic coefficient is more sensitive to the value of the cap electrode radius rather than the lens electrode radius.

We are looking for the system configuration that allows us to minimize the spot size at the image plane, after reflection at the flat mirror. The spherical spot size (due to C_{s3} and C_{s5}) is minimized by selecting a region in which the two coefficients have opposite signs. This way, the one coefficient suppresses the influence of the other coefficient on the increase of spot size for a range of semi-angles (also see [Fig. 6.3(a)]), similarly as to how a negative defocus allows one to partially correct for the spot size degradation due to a positive C_{s3} in electron microscopes. From the shown data, it is observed that a large region satisfies the criterion of opposite signs.

6.4.2. Fine parameter sweep

In the second design step, the ray trace calculations are repeated in a reduced region of the parameter space and at a finer grid step size [for details, see Table 2]. The new parameter space for the cap electrode radius is based on the observation that

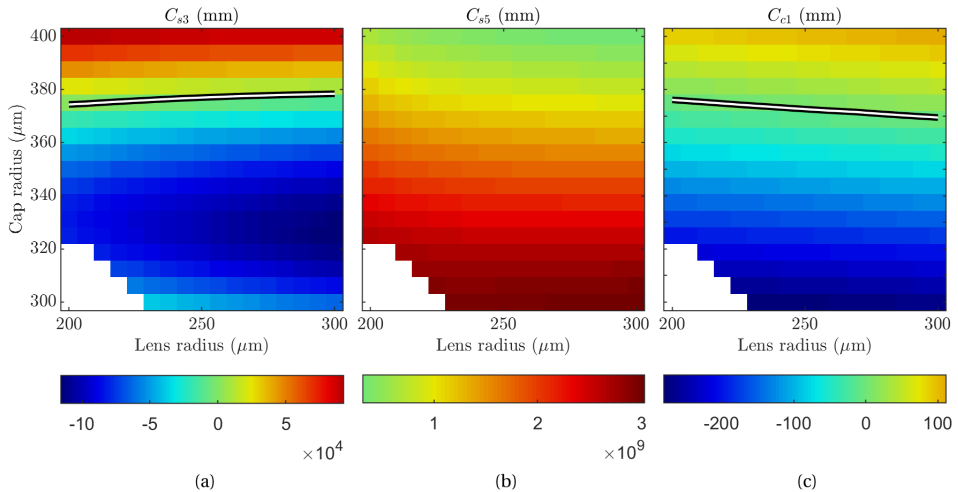

Figure 6.5: Aberration coefficients as a function of the lens and cap electrode radius at −1050 V cap potential. (a) Third order and (b) fifth order spherical aberration coefficient, and (c) first order chromatic aberration coefficient, obtained from the fine parameter sweep. White lines indicate (interpolated) zero-contours in the respective data set.

Table 6.2: Fine parametric sweep limits and grid step sizes.

Label	Property	Range	Step	unit
R_C	Cap radius (*)	$300 \cdots 400$	6.25	μm
R_L	Lens radius (*)	$200 \cdots 300$	6.25	μm
U_C	Cap potential (*)	$-900 \cdots -1100$	50	V

both spherical and chromatic aberrations are near zero in the region, for which $R_{cap} \sim 300 - 400$ μm. For the lens electrode radius, no such distinct selection criterion is apparent. We selected the region, for which $R_{lens} \sim 200 - 300$ μm, based on the observation that the chromatic aberration coefficient increases at higher lens radii. The aberration coefficients that are obtained at this stage are shown in [Fig. 6.5]. A zero-aberration coefficient value contour line is provided for the third order spherical and the first order chromatic aberration coefficient (white lines). Only positive values for the fifth order spherical coefficient are obtained in this reduced parameter space.

The new data set provides more smooth data since the grid resolution is enhanced in comparison to the coarse parameter sweep. It is now clearly observed that a local minimum for which $C_{s3} < 0$ is formed for cap electrode radii of approximately 330 μm. Larger cap electrode radii lead to an increase in C_{s3}, and simultaneously a decrease in C_{s5}. Within the new data set, it is visible that the conditions for $C_{s3} = 0$ and $C_{c1} = 0$ coincide within a narrow band. It is thus to be expected that a minimum spot size will be obtained for $R_{cap} \sim 375$ μm, and relatively independent of the lens electrode radius.

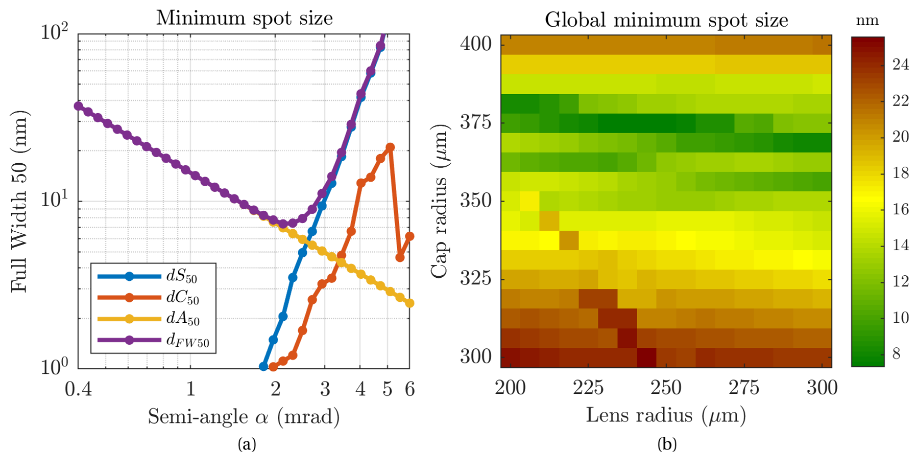

Figure 6.6: (a) (Contributions to) the best resolution out of all systems, as a function of semi-angle. Indicated are the spherical (blue), chromatic (orange), diffraction (yellow), and total (purple) FW50 spot size. (b) Global minimum spot size per mechanical configuration.

6.4.3. Dependence of aberration coefficients on design parameters

The minimum spot size of the tetrode mirror system depends on the beam semi-angle. For small semi-angles, the spot size is usually diffraction limited and at larger semi-angles spherical and chromatic effects will dominate the spot size. We obtained the spot size for all system configurations that are part of the fine parameter sweep, by means outlined in section 6.3.2.

The calculation is performed for various semi-angles in the range $0.4 < \alpha < 6$ mrad, at 35 equally logarithmically spaced values. For each system configuration, the spherical FW50 spot size contribution is obtained by varying the defocus C_1 [ref. Eq. (6.4) and App. D for details]. The chromatic FW50 spot size contribution (d_{C50}) is obtained for a nominal beam energy of 2 keV, and a FW50 energy spread of 0.3 eV that we can achieve in experiments with a monochromatized beam emitted from a Schottky source. This results in a new data set, that contains the (contributions to the) FW50 spot size of each system, at each semi-angle.

For each semi-angle, the system configuration that provides the smallest total FW50 spot size (d_{FW50}) is obtained from this new data set. The resulting subset of data is shown in [Fig. 6.6(a)], and provides the minimum spot size that can be obtained as a function of beam semi-angle. From this data, we note that the spot size can be kept diffraction limited for semi-angles up to $1.5 - 2$ mrad. A global minimum FW50 spot size of $d_{FW50} = 7.6$ nm is found at a semi-angle of 2.3 mrad, and requires a defocus of $C_1 = 3.3$ μm. At increasing semi-angles, the minimum spot size becomes limited by the spherical aberration of the systems.

The obtained minimum spot size for each mechanical configuration in terms of lens and cap electrode radius is plotted in [Fig. 6.6(b)]. From this data, it is noted that the global minimum spot size is obtained for a cap electrode radius of

$R_{cap} = 375$ μm, and a lens electrode radius of $R_{lens} = 250$ μm. For the electrical configuration a cap electrode potential of $U_{cap} = -1050$ V is found. In order to focus the beam with 1x magnification onto the sample plane after reflection, a lens potential of $U_{lens} = 3.5$ kV was obtained from the EOD calculations. Consequently, a maximum field strength of $E = 9.5$ kV/mm is present in the tetrode mirror, which is considered feasible in electron optical setups.

The global minimum spot size that we show in [Fig. 6.6(b)] seems to closely follow the zero contour line of the chromatic aberration coefficient that is plotted in [Fig. 6.5(c)]. This suggests that the chromatic aberration has a strong influence on the spot size of the reflected beam at the image plane, and should be chosen close to zero. After that, the effect of spherical aberration on the spot size at the image plane can be balanced by a proper amount of defocus. It should be noted that the slope of the spherical spot size contribution in [Fig. 6.6(a)] scales proportional with α^5. From this we can conclude that the smallest spot size at the image plane after reflecting on the flat electron mirror is limited either by diffraction, or by the fifth order aberration coefficient.

6.5. Discussion and conclusion

We obtained geometries for tetrode electron mirror systems with a flat surface of reflection, that exhibits only small axial aberrations. As a result, the FW50 spot size at the image after reflection from the flat mirror surface remains mainly diffraction limited for semi-angles up to $1.5-2$ mrad, at a beam energy of 2 keV. The ability to correct for axial aberrations by means of the tetrode mirror mechanical configuration, rather than additional optical components, or superimposed mirror topographies, opens new possibilities for the use of electron mirrors in general, and for repetitive imaging systems and phase plates in particular.

The low beam energy (2 keV) in our study allows for the sub-millimeter dimensions of the aperture radius. The sub-millimeter dimensions that are involved allow for lithographic fabrication processes. The use of lithographic processes allows for the fabrication of very round apertures, that show virtually no astigmatism when properly aligned to one another [22]. The alignment of individual lens electrodes can be routinely performed with our in-house built hexapod aligner [35] to within 500 nm resolution.

In conclusion, a feasible design for a topographically patternable tetrode electron mirror is described. The axial aberrations of the tetrode mirror system are minimized through careful analysis of the role of aperture dimensions of the electrodes. The successful demonstration of the proposed configuration would enable the integration of a mirror based electron beam splitter in miniature QEM setups, or reduce the number of optical components that are needed in existing electron microscopes thus offering means for increased resolving power.

Acknowledgements
We acknowledge funding for this work from the Dutch Research Council (NWO), and the Gordon and Betty Moore Foundation (GBMF).

References

[1] A. B. Bok, J. B. le Poole, J. Roos, and H. de Lang, *Mirror electron microscopy,* in *Advances in Imaging and Electron Physics* (Elsevier, 2017) pp. 99–192.

[2] S. A. Nepijko and N. N. Sedov, *Aspects of mirror electron microscopy,* in *Advances in Imaging and Electron Physics* (Elsevier, 1997) pp. 273–323.

[3] S. M. Kennedy, C. X. Zheng, W. X. Tang, D. M. Paganin, and D. E. Jesson, *Caustic imaging of gallium droplets using mirror electron microscopy,* Ultramicroscopy **111**, 356 (2011).

[4] C. X. Zheng, W. X. Tang, and D. E. Jesson, *Asymmetric coalescence of reactively wetting droplets,* Applied Physics Letters **100**, 071903 (2012).

[5] J. C. Dupuy, A. Sibai, and B. Vilotitch, *Mirror electron microscopy (MEM): Work function and imaging of an electron beam biased junction of silicon (100),* Surface Science **147**, 191 (1984).

[6] Chapter 3 in this thesis.

[7] M. A. R. Krielaart and P. Kruit, *Grating mirror for diffraction of electrons,* Physical Review A **98** (2018), 10.1103/physreva.98.063806.

[8] M. Turchetti, C.-S. Kim, R. Hobbs, Y. Yang, P. Kruit, and K. K. Berggren, *Design and simulation of a linear electron cavity for quantum electron microscopy,* Ultramicroscopy **199**, 50 (2019).

[9] P. Kwiat, H. Weinfurter, T. Herzog, A. Zeilinger, and M. A. Kasevich, *Interaction-free measurement,* Physical Review Letters **74**, 4763 (1995).

[10] P. Kruit, R. G. Hobbs, C.-S. Kim, Y. Yang, V. R. Manfrinato, J. Hammer, S. Thomas, P. Weber, B. Klopfer, C. Kohstall, T. Juffmann, M. A. Kasevich, P. Hommelhoff, and K. K. Berggren, *Designs for a quantum electron microscope,* Ultramicroscopy **164**, 31 (2016).

[11] M. A. R. Krielaart, D. J. Maas, S. V. Loginov, and P. Kruit, *Miniature electron beam separator based on three stacked dipoles,* Journal of Applied Physics **127**, 234904 (2020).

[12] E. G. Ramberg, *Aberration correction with electron mirrors,* Journal of Applied Physics **20**, 183 (1949).

[13] G. F. Rempfer, *A theoretical study of the hyperbolic electron mirror as a correcting element for spherical and chromatic aberration in electron optics,* Journal of Applied Physics **67**, 6027 (1990).

[14] D. Preikszas and H. Rose, *Correction properties of electron mirrors,* Journal of Electron Microscopy **46**, 1 (1997).

[15] Z. Shao and X. D. Wu, *Properties of a four-electrode adjustable electron mirror as an aberration corrector,* Review of Scientific Instruments **61**, 1230 (1990).

[16] P. W. Hawkes, *Examples of electrostatic electron optics: The farrand and elektros microscopes and electron mirrors,* Ultramicroscopy **119**, 9 (2012).

[17] S. A. Koppell, M. Mankos, A. J. Bowman, Y. Israel, T. Juffmann, B. B. Klopfer, and M. A. Kasevich, *Design for a 10 keV multi-pass transmission electron microscope,* Ultramicroscopy **207**, 112834 (2019).

[18] R. H. van Aken, C. W. Hagen, J. E. Barth, and P. Kruit, *Low-energy foil aberration corrector,* Ultramicroscopy **93**, 321 (2002).

[19] R. H. van Aken, D. J. Maas, C. W. Hagen, J. E. Barth, and P. Kruit, *Design of an aberration corrected low-voltage SEM,* Ultramicroscopy **110**, 1411 (2010).

[20] Z. Shao and X. D. Wu, *Adjustable four-electrode electron mirror as an aberration corrector,* Applied Physics Letters **55**, 2696 (1989).

[21] R. T. Hamarat, J. Witzani, and E. M. Hörl, *Electron optical characteristics of a concave electrostatic electron mirror for a scanning electron microscope,* Scanning **6**, 75 (1984).

[22] P. Kruit, *The role of MEMS in maskless lithography,* Microelectronic Engineering **84**, 1027 (2007).

[23] H. Rose and D. Preikszas, *Time-dependent perturbation formalism for calculating the aberrations of systems with large ray gradients,* Nuclear Instruments and Methods in Physics Research Section A: Accelerators, Spectrometers, Detectors and Associated Equipment **363**, 301 (1995).

[24] H. Dohi and P. Kruit, *Design for an aberration corrected scanning electron microscope using miniature electron mirrors,* Ultramicroscopy **189**, 1 (2018).

[25] R. M. Tromp, J. B. Hannon, A. W. Ellis, W. Wan, A. Berghaus, and O. Schaff, *A new aberration-corrected, energy-filtered LEEM/PEEM instrument. I. Principles and design,* Ultramicroscopy **110**, 852 (2010).

[26] B. Lencová and J. Zlámal, *A new program for the design of electron microscopes,* Physics Procedia **1**, 315 (2008).

[27] J. Zlámal and B. Lencová, *Development of the program EOD for design in electron and ion microscopy,* Nuclear Instruments and Methods in Physics Research Section A: Accelerators, Spectrometers, Detectors and Associated Equipment **645**, 278 (2011).

[28] J. E. Barth, B. Lencová, and G. Wisselink, *Field evaluation from potentials calculated by the finite element method for ray tracing: the slice method,* Nuclear Instruments and Methods in Physics Research Section A: Accelerators, Spectrometers, Detectors and Associated Equipment **298**, 263 (1990).

[29] H. W. G. van der Steen, J. E. Barth, and J. P. Adriaanse, *Engineering constraints and computer-aided optimization of electrostatic lens systems,* Nuclear Instruments and Methods in Physics Research Section A: Accelerators, Spectrometers, Detectors and Associated Equipment **298**, 377 (1990).

[30] H. Okamoto, *Adaptive quantum measurement for low-dose electron microscopy,* Physical Review A **81** (2010), 10.1103/physreva.81.043807.

[31] A. M. Carroll, *Pattern generators for reflective electron-beam lithography (REBL),* in *Advances in Imaging and Electron Physics* (Elsevier, 2015) pp. 1–23.

[32] P. Kruit, *Electron sources,* in *Transmission Electron Microscopy*, edited by C. B. Carter and D. B. Williams (Springer International Publishing, 2016) pp. 1–15.

[33] J. E. Barth and P. Kruit, *Addition of different contributions to the charged particle probe size,* Optik (Stuttgart) **101**, 101 (1996).

[34] N. H. M. Nezhad, M. G. Niasar, C. W. Hagen, and P. Kruit, *Local versus global optimization of electron lens system design,* in *2020 IEEE 6th International Conference on Optimization and Applications (ICOA)* (IEEE, 2020).

[35] A. C. Zonnevylle, *Individual beam control in multi electron beam systems*, Ph.D. thesis, Delft University of Technology (2017), Ch. 5.

6

7

Conclusion

Commercial electron microscopes are vastly expansive tools, and that is for good reason. A lot of development work and effort must be spent to improve the performance and to obtain interpretable micrographs. When introducing new imaging schemes, it is then wise to start out small, and built up towards a prototype machine, that may eventually turn into a commercial device. The necessary optical developments for designing a (prototype) quantum electron microscope include at least a design for an electron resonator, a coherent beam splitter and combiner, and a method for inserting and extracting electrons from the resonator. In this thesis, a prototype design for a quantum electron microscope has been described.

Initially, the work was focused onto experimentally demonstrating that electron mirrors that are patterned with a grating structure can be used to diffract the reflected electron beam. For this, a grating mirror was placed below the sample plane in the specimen chamber of the scanning electron microscope. In the experiment, the beam was used to scan a specimen that contained holes that allowed the beam to reach the grating mirror. We collected micrographs of the reflected beam while scanning a specimen with that beam, and expected the effect of beam diffraction to show up in the micrograph as a convolution of the specimen with the point spread function of a diffracted beam. It turned out that this demonstration experiment is not as trivial as reflecting electron beams may sound, for a variety of reasons. Foremost, optical aberrations in front of the electron mirror quickly built up and we reasoned that this prevents us from observing diffraction effects. In addition to that, it proved difficult to image the pivot point of the scanning beam onto the mirror surface, leading to a non-stationary beam position at the mirror plane. Furthermore, the experimental procedure would not allow for the direct detection of the diffraction effect. Instead, the effect of scanning a diffracted beam across a specimen would be visible in the micrographs, requiring additional post processing steps to deconvolve the diffraction spots from the obtained micrograph.

As a response to not finding diffraction in an experiment that was mainly based on back of the envelop calculations, a more in depth analysis of the problem at hand was performed. For this, a numerical method was constructed, that solves the time independent Schrödinger equation for an electron that is reflected in a modulated mirror potential. A new insight that we gained from these calculations and their

results is that the use of the WKB approximation to predict the phase modulation of an electron that is reflected in a modulated potential is valid and accurate, given that the phase modulation is described as a function of the amplitude of the classical turning point of the electron, rather than as a function of the mirror bias potential.

Based on the initial experimental and numerical findings, we deemed a number of changes necessary for the follow up experiments. In order to reduce the effect of aberrations, we required a stationary beam at the mirror plane. The absence of beam scanning requires to image the reflected beam onto a scintillator screen such that the diffraction pattern of the reflected beam could be directly observed with a light microscope. However, the position of the scintillator screen could not coincide with the original sample plane of the microscope, as this would leave insufficient room for the light optical detection path.

The double electron mirror setup that is presented in chapter 4 is designed in response to these requirements. The use of two electron mirrors that both terminate one of the ends of an optical axis parallel to that of the microscope, and the use of a number of deflectors to coordinate the beam trajectory in between the mirrors is suggested here. With this setup, a static current beam without need of scanning could in principle be used to study the effect that a mirror pattern has on the reflected beam. Moreover, the addition of a second mirror to the setup offers a new degree of freedom in arbitrarily shaping the wave front of the electron beam, as is discussed in chapter 3. Next to this, it is recognized that the addition of the second mirror in principle provides a viable method for realizing the electron resonator that is necessary in a prototype quantum electron microscope.

As part of the design of the double mirror experimental setup, the necessity for a miniature beam separator that explicitly coincides with both parallel axes in the setup has led to the design of a novel EBE beam separator. The acronym EBE refers to the sequence of electric, magnetic, and again electric deflection fields, that are laterally combined each in a separate layer in a Wien configuration in this device. The full characterization was presented in chapter 5. This novel type of beam separator does not only find application in the prototype design of the quantum electron microscope in this thesis, it is also already being integrated in a prototype machine for aberration correction in a (critical dimensional) scanning electron microscope.

The last optical development that followed from the design process is a geometrical optimization of the electron mirror and lens stack. By means of electron ray trace calculations and optical aberration calculations that are presented in chapter 6 we were able to minimize the paraxial spherical and chromatic aberrations of a tetrode electron mirror. The optimization is constraint by assuming flat aperture electrode elements for the lens, such that lithographic processes for the electrode manufacturing are not further complicated by the optimized design. The resulting design promises an increase in semi-angle of the beam, such that larger mirror patterns can be illuminated while at the same time remaining single digit nanometer resolution at the image plane.

In conclusion, an experimental design for a prototype quantum electron microscope that could also be used for arbitrary electron wave front shaping is introduced

in this thesis. The design is supported by numerical electron optical calculations. A first version of the setup has already been built, and now the stage of improving the setup has commenced. At the moment, the main concern in progress is related to avoiding electric charge from building up in the miniature liner tubes that are present in the design. After this issue is resolved, it is expected that a double reflection can take place in the setup, and this may finally demonstrate the diffractive nature of the electron grating mirror. More future paths to follow are also discussed at the end of chapter 4 and include temporal switching of the deflector that regulates the access of the electron towards the resonator.

Appendices

A

Numerical solutions of the Schrödinger equation

A.1. Introduction

We seek for a full solution of the (time independent) Schrödinger equation as a means of obtaining an accurate description of the wave function upon reflection of a (modulated) potential surface. The analysis is based on coupling (known) analytical solutions to Schrödinger's equation for linearly sloped potential fields (region II) to a modulated potential field with unknown solution (region I) as defined in [Fig. 2.1] of chapter 2. First, the analytical solution in region II is described. Then, the coupling of this solution to region I is demonstrated and finally the numerical implementation is discussed.

A.2. Solutions for a linear sloped potential

The analytical solution to the Schrödinger equation for a linear sloped potential is obtained by solving the time independent Schrödinger equation,

$$\left[-\frac{\hbar^2}{2m}\nabla^2 + V(x)\right]\psi(x,y) = \mathcal{E}\psi(x,y). \tag{A.1}$$

The potential energy function $V(x)$ is dependent on the aperture-mirror separation d and potential difference ΔU. In the absence of a pattern, i.e. a flat mirror, and assuming a grounded aperture, the potential is described as $U(x) = \bar{E}x + U_p$ with $\bar{E}$ the linear field strength (V/m) and $V(x) = eU(x)$. Here, $e = -1.6 \times 10^{-19}$ C represents the electron charge. The general solution to the resulting differential equation is given by Airy functions of first and second kind [1]. As the solution has to vanish for $x > 0$, the Airy function of first kind (from now on referred to as 'the Airy function') is the only valid solution of the Schrödinger equation here.

This appendix has been published as supplementary material of M. A. R. Krielaart, and P. Kruit, *Grating mirror for diffraction of electrons*, Physical Review A **98** (2018), 10.1103/physreva.98.063806.

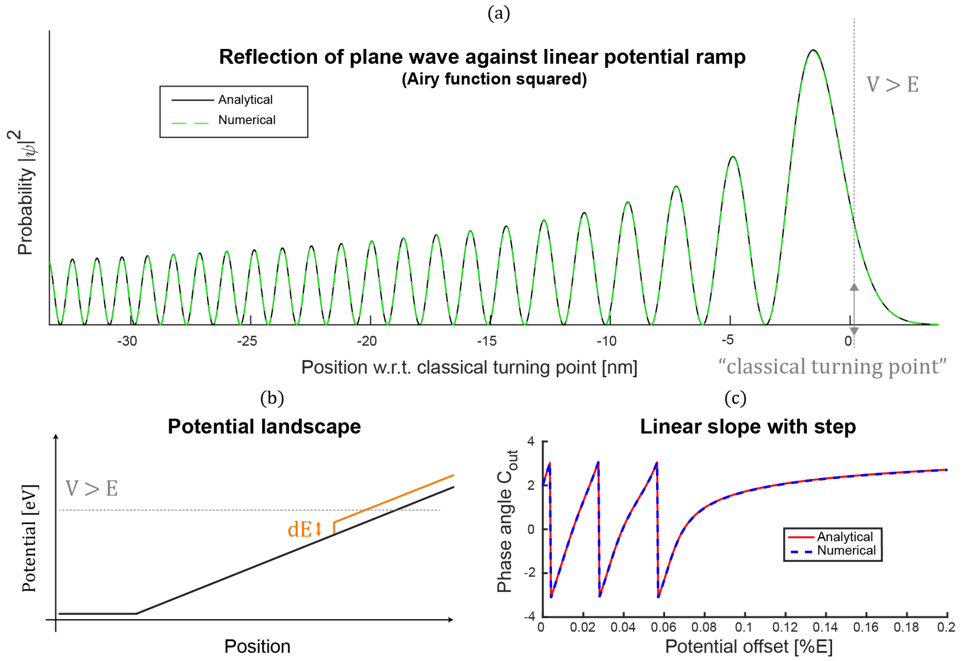

Figure A.1: (a) The Airy function of first kind squared is plotted. The classical turning point coordinate is indicated. Notice that the reflected electron has finite probability of reaching behind this point. (b) 1-Dimensional potential ramp starting in free-space. The grey line indicates the energy that corresponds to the classical turning point of the electron. (c) Comparison between analytical and numerically obtained phase angles for the potential bump at x_0, obtained at x_s.

For two spatial dimensions, the solution is given by the product of the Airy function in the direction of the linear sloped potential and plane waves in the direction perpendicular to the ramp, thus

$$\psi(x, y) = X(x)Y(y) = \text{Ai}(u_n(x)) \exp(ik_{y,n}y). \tag{A.2}$$

The Airy function $\text{Ai}(u_n(x))$ is a standing wave-type, which is described by

$$\text{Ai}\left(u_n\right) \equiv \frac{1}{\pi} \int_0^\infty \cos\left(\frac{s^3}{3} + su_n\right) \text{d}s. \tag{A.3}$$

The term $u_n(x)$ is a scaling factor that depends on the parameters of the pattern. The derivation of this term is provided inside [App. A.7], and given here by

$$u_n(x) = \alpha \left[x - \frac{\mathcal{E} - V_p}{E} + \frac{\hbar^2 k_{y,n}^2}{2mE}\right]. \tag{A.4}$$

This expression is obtained by solving the Schrödinger equation analytically in two spatial dimensions by the method of separation of variables. In this equation, $\alpha \equiv (2mE/\hbar^2)^{1/3}$ is a constant that depends only on the linear field strength E in region II. The second term in brackets is recognized as the 'classical turning point'. This is the coordinate plane where classically the electron would be reflected. However, quantum mechanically there is a finite probability for the electron to penetrate this barrier. Moreover, the electron spends most time just in front of the classical turning point [2]. This is also visible in [Fig. A.1(a)], where the square of the Airy function is plotted as a function of position in front of the mirror plane. The last term in brackets is considered a correction due to the transverse component $k_{y,n}$ of the wave and $m = 9.1 \times 10^{-31}$ kg is the electron rest mass.

A.3. Coupling the linear and modulated potential region

The numerical solution of the Schrödinger equation in region I is obtained by a finite element method and described as boundary value problem. By virtue of the periodicity of the pattern in transverse direction, we only require a single pitch and may apply periodic boundary conditions to both sides. A zero-boundary condition is applied sufficiently far below the classical turning point resulting in full reflection.

The boundary values at each point of the interface of regions I and II are described by the incident and reflected part of the wave function at this boundary,

$$\psi_b = \psi_{\text{incident}} + \psi_{\text{reflected}}. \tag{A.5}$$

For this, the standing wave-type Airy function must be split in counter traveling components. The asymptotic approximation of the Airy function, valid for $u_n > \pi$ allows for this [3], since

$$\text{Ai}(-u_n) \approx \frac{\sin(\gamma)}{\sqrt{\pi}u_n^{1/4}} = \underbrace{\frac{\exp(i\gamma)}{2i\sqrt{\pi}u_n^{1/4}}}_{\text{Ai}^+(u_n)} - \underbrace{\frac{\exp(-i\gamma)}{2i\sqrt{\pi}u_n^{1/4}}}_{\text{Ai}^-(u_n)}. \tag{A.6}$$

The result after the equality sign follows from applying Euler's identity, using $\gamma \equiv \frac{2}{3}u_n^{3/2} + \pi/4$ as short hand notation. This allows us to describe the wave function at the interface in general by

$$\begin{aligned} \psi_b(x_b, y) &= \sum_n A_n \text{Ai}^-(u_n(x_b)) \exp(ik_{y,n}y) \\ &+ \sum_n B_n \text{Ai}^+(u_n(x_b)) \exp(ik_{y,n}y). \end{aligned} \tag{A.7}$$

The complex coefficients A_n and B_n provide the probability amplitudes for various wave numbers k_n.

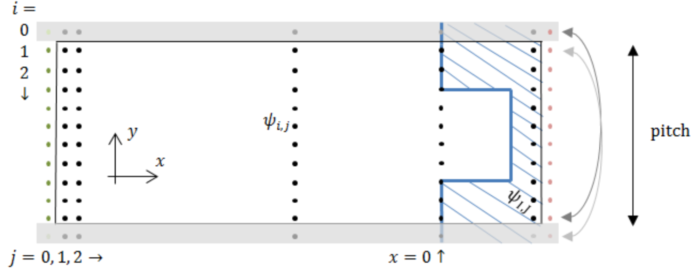

Figure A.2: Schematic representation of the grid, showing the single pitch, boundary conditions and the labeling of index points.

A.4. Numerical implementation

The solution at the interface [Eqn. A.5] is a linear combination of the wave(s) incident towards and reflected by the patterned mirror. The allowed values for the transverse wave component $k_{y,n}$ are determined by the pitch of the mirror pattern and must yield wave numbers that exactly fit an integer number of times within the pitch. As a result, the interface between regions I and II must consist of N_y (necessarily odd) number of points, resulting in allowed values of $k_{y,n} = \pm 2\pi n$, with $n = 0, 1, \cdots, (N_y - 1)/2$, in order to prevent numerical aliasing.

The solution to the Schrödinger equation within the proximity of the pattern can now be obtained by a finite difference scheme. Grid points are labelled $\psi_{i,j}$, with $i = 1 \cdots N_x$ (rows), $j = 1 \cdots N_y$ (columns) and the grid size is given by h_x and h_y. The full domain consists of $N_x \times N_y$ grid points. Elements $\psi_{1,j}$ represent the first row of grid points of region I, directly below the interface. The grid is shown in [Fig. A.2].

The Laplacian operator in the kinetic part of the Hamiltonian $\mathbf{H}$ is described by

$$\begin{aligned} \nabla^2_{i,j}\psi_{i,j} &= \frac{\psi_{i+1,j} + \psi_{i-1,j} - 2\psi_{i,j}}{h_x^2} \\ &+ \frac{\psi_{i,j+1} + \psi_{i,j-1} - 2\psi_{i,j}}{h_y^2}. \end{aligned} \tag{A.8}$$

This introduces a nearest-neighbor dependence. When the grid points $\psi_{i,j}$ are represented by a column vector $\bar{\psi} = \left(\psi_{1,1}, \cdots, \psi_{1,N_y}, \psi_{2,1}, \cdots, \cdots, \psi_{N_x,N_y}\right)^T$ the Hamiltonian can be described as a sparse square matrix.

The above definition for the Laplace operator introduces the interface grid points ψ_b into the system of equations, since the interface coincides with $\psi_{0,j}$. In turn, this introduces the unknown coefficients A_n and B_n into the set of equations and the resulting system becomes underdetermined, since we now have $N_x \times N_y$ equations and (when we choose the incident wave form coefficients A_n) $N_x \times (N_y + 1)$ unknowns, due to the unknown coefficients $B_1, \cdots, B_{N_y}$.

To overcome this problem, one more step is required. By describing the first row of grid points inside the numerical domain (grid elements $\psi_{1,j}$) in terms of a Taylor expansion of the interface grid points, the first row entries inside the solution column vector $\bar{\psi}$ can be replaced by coefficients B_n, such that $\bar{\psi} \to (B_1, B_2, \cdots, B_{N_y}, \psi_{2,1}, \cdots, \cdots, \psi_{N_x,N_y})^T$. The Taylor expansion of the interface elements is given by

$$\psi_{1,j} \approx \psi_{0,j} + \left.\frac{\mathrm{d}\psi_{0,j}}{\mathrm{d}x}\right|_{\overline{x_0}} h_x, \tag{A.9}$$

where the derivative is taken at the half-way point in between $i = 0$ and $i = 1$. The Schrödinger equation can now be written as a matrix equation by $(\mathbf{H} - \mathbf{I}\mathcal{E})\bar{\psi} = \vec{X}$ and $\vec{X}$ is determined by the choice of the incident wave condition. If we define $\mathbf{M} \equiv (\mathbf{H} - \mathbf{I}\mathcal{E})$, we will first explicitly state the form of $\mathbf{M}\bar{\psi} = \vec{X}$ in the set of expressions in [Eq. A.10]. Here, the terms a_q relate to the step size in the respective direction (x, y). The analytical expression (also see [Eq. A.7]) at the interface is given by

$$\psi_b \equiv \psi_{0,j} = \sum_n \left[A_n \psi_{\mathrm{in}}[j,n] + B_n \psi_{\mathrm{out}}[j,n]\right], \tag{A.11}$$

that is, for every point on the interface, the contributions of all modes n are summed for the specific position j. For an incident plane wave parallel to the optical axis, only $A_m = 1$ for $n = m$, the mode corresponding to $k_{y,m} = 0$, i.e. the mode that has no transverse wave number component. Further, the derivative of $\psi_{\mathrm{in/out}}[j,n]$ is defined as given by the Taylor expansion evaluated at the x-coordinate related to column j and mode n. Also, definition of $\psi_{i\pm1,j} \equiv \psi_{i-1,j} + \psi_{i+1,j}$ and $\psi[j \pm 1, n] \equiv \psi[j+1,n] + \psi[j-1,n]$ allow for short hand notations.

The right hand side for $i = 1$ and $i = 2$ in [Eq. A.10] provide the source terms for $\vec{X}$. From this scheme it is also clear that only the first $2J$ positions of $\vec{X}$ are filled with non-zero entries.

A.5. Obtaining a solution

Next, the system $\boldsymbol{M}\vec{\psi} = \vec{X}$ must be solved for $\vec{\psi}$. This is done by left-multiplication of both sides of the equation by the inverse of matrix $\boldsymbol{M}$,

$$\boldsymbol{M}^{-1}\boldsymbol{M}\vec{\psi} = \boldsymbol{M}^{-1}\vec{X} \Rightarrow \vec{\psi} = \boldsymbol{M}^{-1}\vec{X}. \tag{A.12}$$

By definition of $\vec{\psi}$ the first J elements contain the coefficients of the reflected waves, $B_1, B_2, \cdots, B_J$. Moreover, for transverse waves of the form $Y_n(y) = B_n \exp(ik_{y,n}y)$ the coefficients B_n are equivalent to the spectrum of outgoing wave vectors with (field free) small angle approximation angle $\theta_n = k_{y,n}/k_{x,n}$ with respect to the optical axis. The corresponding values for $k_{x,n}$ are readily obtained via the field-free solution of the Schrödinger equation, $k_{x,n} = 2m\mathcal{E}/\hbar^2 - k_{y_n}^2$ and allow, for

$$
\begin{aligned}
i = 1: \quad & \sum_n B_n \Big[\psi_{\text{out}}[j,n] \left(-a_x - 2a_y + V_{1,j} - \mathcal{E}\right) + \psi^{'}_{\text{out}} \left(-2a_x - 2a_y + V_{1,j} - \mathcal{E}\right) \\
& \qquad + a_y \left(\psi_{\text{out}}[j \pm 1, n] + \psi^{'}_{\text{out}}[j \pm 1, n] \right) \Big] + \psi_{2,j}(a_x) \\
& = - \sum_n A_n \Big[\psi_{\text{in}}[j,n] \left(-a_x - 2a_y + V_{1,j} - \mathcal{E}\right) + \psi^{'}_{\text{in}}[j,n] \left(-2a_x - 2a_y + V_{1,j} - \mathcal{E}\right) \\
& \qquad + a_y \left(\psi_{\text{in}}[j \pm 1, n] + \psi^{'}_{\text{in}}[j \pm 1, n] \right) \Big], \\
i = 2: \quad & \sum_n B_n \left[a_x \left(\psi_{\text{out}}[j,n] + \psi^{'}_{\text{out}}[j,n] \right) \right] + \psi_{2,j} \left(-2a_x - 2a_y + V_{2,j} - \mathcal{E}\right) \\
& \qquad + \psi_{3,j}(a_x) + \psi_{j \pm 1, 2}(a_y) \\
& = - \sum_n A_n \left[a_x \left(\psi_{\text{in}}[j,n] + \psi^{'}_{\text{in}}[j,n] \right) \right], \\
i \geq 3: \quad & \psi_{i \pm 1, j}(a_x) + \psi_{i,j} \left(-2a_x - 2a_y + V_{i,j} - \mathcal{E}\right) + \psi_{i, j \pm 1}(a_y) = 0.
\end{aligned}
\tag{A.10}
$$

instance, to directly obtain the intensity of the various diffraction orders induced by placing a grating mirror.

We use MATLAB to solve the inversion problem, $\bar{\psi} = (\mathbf{H} - \mathbf{I}\mathcal{E})^{-1}\vec{X}$, where the first N_y entries of $\bar{\psi}$ directly yield the probability coefficients B_n of various reflected wave components.

A.6. Stability and convergence

In region I, the time-independent Schrödinger equation is solved on a uniform grid with step size h_x and h_y for the longitudinal and transverse direction. The maximum step value of h_x is limited by the shortest wave length that occurs in the numerical domain. This wave length occurs at the interface (with potential $V_{0,j}$), since the electron is decelerated towards the mirror plane. In order to sample q steps within one wave length λ the value of h_x is upper bound by

$$h_x \leq \frac{\lambda_e}{q} \qquad \Rightarrow \qquad h_x \leq \frac{1}{q}\frac{\sqrt{2m[\mathcal{E} - V_{0,j}]}}{\hbar}. \tag{A.13}$$

The step size h_y on the other hand is unconditionally stable as long as the aliasing requirement ($n = 0, 1, \cdots, \frac{N_y - 1}{2}$) is met. Then, the second spatial derivative is obtained by two central difference operations,

$$\begin{aligned}\nabla^2_{i,j}\psi_{i,j} &= \frac{\psi_{i+1,j} + \psi_{i-1,j} - 2\psi_{i,j}}{h_x^2} \\ &+ \frac{\psi_{i,j+1} + \psi_{i,j-1} - 2\psi_{i,j}}{h_y^2}.\end{aligned} \tag{A.14}$$

Here, the wave function on coordinate (x, y) is represented by $\psi_{i,j}$, where $i = 1 \cdots I$ (and $I \equiv N_x$) labels the row coordinate and $j = 1 \cdots J$ (and $J \equiv N_y$) the column coordinate. Periodic conditions imply that $\psi_{i,J+1} = \psi_{i,1}$ and $\psi_{i,0} = \psi_{i,J}$. The zero boundary condition opposite to the interface imply that $\psi_{i,J+1} \equiv 0$.

A.7. Linear sloped potential solution for two dimensional wave $\psi(x, y)$

The solution for a linear sloped potential in the x-direction, that extends infinitely in the (transverse) y-direction is derived here. The potential with slope E (unit eV/m) and mirror pattern potential V_p (unit eV) is given by

$$V(x, y) = \begin{cases} 0 & \text{for } x \leq b \text{ with } b < 0 \\ Ex + V_p & \text{for } b < x < 0 \end{cases}. \tag{A.15}$$

By using separation of variables $\psi_{\mathrm{III}}(x, y) = X(x)Y(y)$, the solution in the field-free region (III) follows from the solution of

$$\frac{1}{X}\frac{\mathrm{d}^2X}{\mathrm{d}x^2}+\frac{1}{Y}\frac{\mathrm{d}^2Y}{\mathrm{d}y^2}=-\frac{2m\mathcal{E}}{\hbar^2}. \tag{A.16}$$

The right hand side is the separation constant and the corresponding solutions are

$$X(x)=A_{\mathrm{in}}\exp(ik_xx)+A_{\mathrm{out}}\exp(-ik_xx), \tag{A.17}$$
$$Y(y)=B_{\mathrm{in}}\exp(ik_yy)+B_{\mathrm{out}}\exp(-ik_yy), \tag{A.18}$$

with $k_x^2+k_y^2=2m\mathcal{E}/\hbar^2$. Next, the solution for the sloped region (II) follows from solving

$$\underbrace{-\frac{\hbar^2}{2m}\frac{1}{X}\frac{\mathrm{d}^2X}{\mathrm{d}x^2}+V(x)}_{C}\underbrace{-\frac{\hbar^2}{2m}\frac{1}{Y}\frac{\mathrm{d}^2Y}{\mathrm{d}y^2}}_{D}=\mathcal{E}$$
$$\Rightarrow C+D=\mathcal{E}. \tag{A.19}$$

Since the potential $V=V(x)$ is only varying in the x-direction, it is absorbed in the separation constant C, and the solution for $Y(y)$ is equated to a related separation constant D such that $C+D=\mathcal{E}$. The solution for $Y(y)$ is readily obtained,

$$\begin{aligned}\frac{\mathrm{d}^2Y}{\mathrm{d}y^2} &= -\frac{2mD}{\hbar^2}Y\\ &\Rightarrow \; Y(y)=D_1\exp(ik_yy)+D_2\exp(-ik_yy)\end{aligned} \tag{A.20}$$

for given k_y. Note that k_y remains initially a free variable, unless periodic boundary conditions are applied. Then, the values of k_y are limited (numerically, for N_y is odd) to values $k_{y,n}=\pm 2\pi n/p$ (with p the pattern pitch) for $n=0,1,\cdots,\frac{N_y-1}{2}$, and either $D_1=0$ or $D_2=0$ to avoid double solutions.

The differential equation describing the x-direction is given by

$$\begin{aligned}\frac{\mathrm{d}^2X}{\mathrm{d}x^2} &= -\frac{2m}{\hbar^2}\left[C-V(x)\right]X(x)\\ &= -\frac{2m}{\hbar^2}\left[C-Ex-V_p\right]X(x)\\ &= \frac{2mE}{\hbar^2}\left[x-\frac{C-V_p}{E}\right]X(x).\end{aligned} \tag{A.21}$$

This differential equation can be solved by change of variable. First, define

$$u = \alpha\,[x - C_1] \text{ with } \begin{cases} C_1 & \equiv \frac{C - V_p}{E} \\ \alpha & \equiv \left(\frac{2mE}{\hbar^2}\right)^{1/3} \end{cases} . \tag{A.22}$$

Then[1], $\mathrm{d}u/\mathrm{d}x = \alpha \Rightarrow \mathrm{d}^2X/\mathrm{d}x^2 = \alpha^2\mathrm{d}^2X/\mathrm{d}u^2$ and thus the differential equation for $X(x)$ may also be written as

$$\frac{\mathrm{d}^2X}{\mathrm{d}u^2} = uX, \text{ with } X = X(u(x)). \tag{A.23}$$

This is a well-known type of differential equation and the solution is given by the Airy functions of first and second kind, respectively $\mathrm{Ai}(u)$ and $\mathrm{Bi}(u)$. Note that the latter grows to infinity for $x > 0$ and is no valid solution here. On the other hand, the Airy function of first kind $\mathrm{Ai}(u(x))$ is a valid solution since it vanishes for $x > 0$. The function $\mathrm{Ai}(u)$ is real and defined as

$$\mathrm{Ai}(u(x)) = \frac{1}{\pi}\int_0^\infty \cos\left(\frac{s^3}{3} + su\right)\,\mathrm{d}s. \tag{A.24}$$

The scaling factor $u = u_(x)$ is explicitly given by

$$\begin{aligned} u_n(x) &= \alpha\,[x - C_1] \\ &= \alpha\left[x - \frac{C}{E} + \frac{V_p}{E}\right] \\ &= \alpha\left[x - \frac{2m\mathcal{E} - \hbar^2k_{y,n}^2}{2mE} + \frac{V_p}{E}\right] \\ &= \alpha\left[x - \frac{\mathcal{E} - V_p}{E} + \frac{\hbar^2k_{y,n}^2}{2mE}\right]. \end{aligned} \tag{A.25}$$

In this equation, the term $(\mathcal{E} - V_p)/E$ may be recognized as the 'classical turning point' for 1D, that is the position of zero momentum (kinetic energy) of a classical particle. The second term (involving $k_{y,n}^2$) can be regarded then as a 2-dimensional energy conservation correction term. Effectively, this term shifts the point where the Airy function is evaluated in a way that can be regarded as if reflection took place a little earlier (since some of the kinetic energy is in the transverse component now).

When desired, the solutions in region II and III can be connected by equating the normal and first derivative of the wave function at $x = b$ for a selected incident coefficient A_{in} and B_{in} for comparison of numerical and analytical results.

[1]It should not be confused that $\mathrm{d}^2/\mathrm{d}u^2 = (\mathrm{d}/\mathrm{d}u)^2$ in general! This is only coincidental the case here, since u is only linearly dependent on x. This result follows from applying the chain rule for derivation twice.

A

A.8. Phase angle of an electron reflected from a sloped potential with a bump

The presented method is verified against known analytical solutions of the 1- and 2-dimensional Schrödinger equation. The verification is performed using (i) field free, (ii) constant potential, (iii) linear sloped potential and (iv) sloped potential with a step-edge at the back [2] (and also see [Fig. A.1(b, c)]).

The following example involves two parts, both in which an incident electron wave is reflected against a linear sloped potential with maximum $V_{\mathrm{max}} > \mathcal{E}$. First, it is shown that the phase angle of the returning wave is obtained, again when this returning wave propagates in a field-free region ($V = 0$) in front of the slope. Next, it is shown that the effect of a perturbation at the top of the slope (near the turning point) can be obtained both analytically and numerical, the latter using the method presented here. A good agreement is obtained for this method.

For a plane incident wave (in field-free region) that is reflected by a linear sloped potential, it can be shown that the analytical solution (for the potential landscape as shown in [Fig. A.1(b)] to the time-independent Schrödinger equation reads

$$\psi(x) = \begin{cases} A\exp(ikx) + B\exp(-ikx) & \text{for } V(x) = 0 \\ C\mathrm{Ai}(u(x)) & \text{for } V(x) = Ex + \mathcal{E}. \end{cases} \tag{A.26}$$

The numerical solution is obtained and compared to the analytical solution (for which the value of B and C are uniquely determined for given coefficient A) and this is shown in [Fig. A.1(c)]. Note that the analytical expressions for B and C are obtained by equating the expression for the wave function (and the spatial derivative) just to the left and right of the onset for the sloped potential.

In the second part of this example, the validity of the Airy-splitting method is demonstrated (as suggested in [Eq. A.6]). The goal is to obtain the additional phase shift that is due to a potential step (or perturbation) on the top of the linear slope (the orange line in [Fig. A.1(b)]. An analytical solution for this type of potential (field free, sloped, sloped with additional offset) exists and is given by

$$\psi(x) = \begin{cases} A\exp(ikx) + B\exp(-ikx) & \text{for } V(x) = 0 \\ C\mathrm{Ai}(u_{\mathrm{I}}(x)) & \text{for } V(x) = Ex + \mathcal{E} \\ D\mathrm{Ai}(u_{\mathrm{II}}(x)) & \text{for } V(x) = Ex + \mathcal{E}(1+\delta) \end{cases}. \tag{A.27}$$

Notice that the argument to the Airy function differs for the two parts of the sloped potential. The scaling is given by

$$u(x) = \begin{cases} \left(\frac{2mE}{\hbar^2}\right)^{1/3}(x) & \text{for } u(x) = u_{\mathrm{I}}(x) \\ \left(\frac{2mE}{\hbar^2}\right)^{1/3}\left(x + \frac{\delta\mathcal{E}}{E}\right) & \text{for } u(x) = u_{\mathrm{II}}(x) \end{cases}. \tag{A.28}$$

When the value of C_{in} is known (or selected) it is possible to calculate the effect of the offset potential on C_{out} by starting the calculation just in front of

the boundary between the two sloped potentials. The boundary condition ψ_0 must then discriminate between the incident and reflected component of the Airy function $\mathrm{Ai}(u_\mathrm{I}(x_0))$, since the Airy function in itself is a real function. This discrimination is made by selecting

$$\begin{aligned} \psi_0 &= C_\mathrm{in}\psi_\mathrm{in} + C_\mathrm{out}\psi_\mathrm{out} \\ &= C_\mathrm{in}\mathrm{Ai}^+(u_0) + C_\mathrm{out}\mathrm{Ai}^-(u_0), \end{aligned} \tag{A.29}$$

which *are* left and right traveling waves. Note that the *analytical* result for C_out is obtained by solving the following system of linear equations

$$\begin{pmatrix} \mathrm{Ai}^-(u_\mathrm{I}(x_s)) & -\mathrm{Ai}(u_\mathrm{II}(x_s)) \\ \frac{\mathrm{d}}{\mathrm{d}x}\left(\mathrm{Ai}^-(u_\mathrm{I}(x_s))\right) & -\frac{\mathrm{d}}{\mathrm{d}x}\left(\mathrm{Ai}(u_\mathrm{II}(x_s))\right) \end{pmatrix} \begin{pmatrix} C_\mathrm{out} \\ D \end{pmatrix} = \begin{pmatrix} -C_\mathrm{in}\mathrm{Ai}^+\left(u_\mathrm{I}(x_s)\right) \\ -C_\mathrm{in}\mathrm{Ai}^+\left(u_\mathrm{I}(x_s)\right) \end{pmatrix}. \tag{A.30}$$

The property of interest now is the phase angle $\phi_{C_\mathrm{out}} = \mathrm{im}(C_\mathrm{out})/\mathrm{re}(C_\mathrm{out})$ and this is shown in [Fig. A.1(c)]. Note that the (wrapped) phase angle will not linearly increase with $\delta\mathcal{E}$ when the step size creates a barrier that extends above $V = \mathcal{E}$. This is the case here for $\delta\mathcal{E} = 10\%$ of $\mathcal{E}$.

References

[1] D.J. Griffiths, *Introduction to Quantum Mechanics* (Pearson Prentice Hall, 2005).

[2] S. M. Kennedy, D. E. Jesson, M. J. Morgan, A. E. Smith, and P. F. Barker, *Phase sensitivity of slow electrons to interactions with weak potentials,* Physical Review A **74** (2006), 10.1103/physreva.74.044701.

[3] E. T. Copson, *On the asymptotic expansion of airy's integral,* Proceedings of the Glasgow Mathematical Association **6**, 113 (1963).

B

Turning point coordinates through the Lambert-W function

The classical turning point $z_R^{\pm}$ for the most and least nearest approach of the beam towards the mirror with a modulated potential are found by equating the scalar electric field to the cathode potential E at the source,

$$U(x_{\pm}, y_{\pm}, z_R^{\pm}) = u_0 \left[1 - \frac{z_R^{\pm}}{z_1}\right] \pm F_{n,m} \exp(-2\pi k_0 |z_R^{\pm}|). \tag{B.1}$$

Solutions to these equations are provided by the Lambert-W function, in the form of [1],

$$z_R^{\pm} = \frac{1}{2\pi k_0} \times \frac{-AW_0\left(-A^{-1}\exp\left[-\frac{B}{A}\right]\right) - B}{A}. \tag{B.2}$$

In this equation,

$$A = \pm\frac{u_0}{2\pi F_{n,m} k_0 z_1}, \qquad B = \pm\frac{E - u_0}{F_{n,m}}, \qquad k_0 \equiv k_z = 2\pi\sqrt{k_{n,x}^2 + k_{m,y}^2}. \tag{B.3}$$

In MATLAB, use of the function `lambertw(k, x)` enables the calculation of k-th branch of the Lambert function, evaluated at x [2]. Solutions for $z_R^{\pm}$ are obtained from the zero-th (principal) branch.

References

[1] R. M. Corless, G. H. Gonnet, D. E. G. Hare, D. J. Jeffrey, and D. E. Knuth, *On the LambertW function,* Advances in Computational Mathematics **5**, 329 (1996).

[2] MathWorks, *Lambert W function* (Before 2006, (accessed April 2020)), https://nl.mathworks.com/help/symbolic/lambertw.html.

C

Quantitative effects of miniature liner tubes on field distortions

The effectiveness of including one or multiple dummy miniature liner tubes [also see chapter 4.3.2] is assessed numerically. Traditionally, one would obtain distortion coefficients by releasing electrons at different heights in the optical system, and relating the intersection coordinate of the electrons at the common crossover plane to the various distortion coefficients. In the following analysis, we think this extensive procedure can be simplified to working with the projected potentials of the electrodes only, as we are interested in the relative increase of distortion coefficients when compared to a situation at which no liner tubes would be present at all.

Thus, the analysis is performed here by analyzing the multipole coefficients of the electric potential of a lens electrode, when projected along the optical axis of the electrode. A 3-dimensional (3D) COMSOL model is created for calculating the projected potential, and further processing is done in MATLAB. In COMSOL, we apply a fixed excitation of 1 kV at either the lens, cap, or (flat) mirror electrode, and set the remaining electrodes at ground potential. The projected potential then offers a measure of effective action per kV electrode excitation.

The distortion coefficients of the projected potential are obtained through Fourier analysis. For this, concentric circles of increasing radius R are positioned in the dataset, around the optical axis. A Fourier analysis of the potential at these circles yields complex valued Fourier coefficients F_n ($n = 1$ for dipole, $n = 2$ for quadrupole, $n = 3$ for hexapole, $n = 4$ for octupole, etc.), from which the distortion coefficients c_n (in units of $\mathrm{V/(kV\ n\ m^{n-1})}$) are determined, via [1]

$$c_n = \frac{|F_n|}{nR^n}. \tag{C.1}$$

We obtained the distortion coefficients up to $n = 4$ (octupole) in this manner, and the resulting coefficients are included in [Table C.1]. Results are shown for zero (reference case), one (minimally required), two, and four miniature liner tubes present in the setup, corresponding to the layouts as shown in [Fig. 4.5(a-c)].

From the c_0 (DC, monopole) data, a small (0-3%) decrease is observed as a function of adding more liner tubes. Thus, the addition of liner tubes requires only

Table C.1: Distortion coefficients in the presence of zero (numerical reference), one (minimally required tube count), two, and four liner tubes. Orange cells signify severe distortions with respect to the reference case.

Tubes	c_0	c_1	c_2	c_3	c_4
Lens electrode at 1 kV					
0	0.95	2.75×10^{-2}	$5.53 \times 10^{+1}$	$6.51 \times 10^{+4}$	$7.21 \times 10^{+8}$
1	0.94	$2.64 \times 10^{+1}$	$2.03 \times 10^{+4}$	$1.61 \times 10^{+7}$	$9.88 \times 10^{+9}$
2	0.93	3.45×10^{-1}	$4.16 \times 10^{+4}$	$3.00 \times 10^{+6}$	$2.85 \times 10^{+10}$
4	0.92	3.70×10^{-2}	$6.89 \times 10^{+1}$	$5.00 \times 10^{+5}$	$6.80 \times 10^{+10}$
Cap electrode at 1 kV					
0	0.42	1.90×10^{-2}	$3.59 \times 10^{+1}$	$1.95 \times 10^{+5}$	$6.18 \times 10^{+8}$
1	0.42	$1.16 \times 10^{+1}$	$9.45 \times 10^{+3}$	$7.74 \times 10^{+6}$	$4.94 \times 10^{+9}$
2	0.41	1.50×10^{-1}	$1.92 \times 10^{+4}$	$1.26 \times 10^{+6}$	$1.39 \times 10^{+10}$
4	0.41	1.89×10^{-2}	$8.51 \times 10^{+1}$	$4.34 \times 10^{+5}$	$3.30 \times 10^{+10}$
Mirror electrode at 1 kV					
0	0.49	1.30×10^{-2}	$4.21 \times 10^{+1}$	$2.07 \times 10^{+5}$	$7.35 \times 10^{+8}$
1	0.49	2.02×10^{-2}	$4.00 \times 10^{+1}$	$2.05 \times 10^{+5}$	$7.37 \times 10^{+8}$
2	0.49	1.33×10^{-2}	$3.72 \times 10^{+1}$	$2.07 \times 10^{+5}$	$7.22 \times 10^{+8}$
4	0.49	1.33×10^{-2}	$4.73 \times 10^{+1}$	$2.07 \times 10^{+5}$	$7.17 \times 10^{+8}$

a small increase in lens excitation in order to maintain an equal focal strength for the system.

From the c_1 (dipole) data, it is observed that indeed a strong dipole field is formed when only the first (required) liner tube is positioned at the microscope axis. Placement of this liner tube results an increase of 3 decades in dipole distortion and will thus result in a significant deflection field inside the lens. We also notice from the c_1 data that the field that is generated by the flat mirror electrode is hardly influenced by the placement of a liner tube. This is explained by the limited spacing (100 μm) between the mirror and the neighboring cap electrode, which is small compared to the distance towards the nearest liner tube ($\sim$ 500 μm).

Addition of the second tube does away with the dipole field distortions, while creating a strong quadrupole distortion for the lens and cap electrodes. Based on the data shown in [Table C.1] it appears that at least four liner tube symmetry is required in order to suppress the primary distortions. At this stage, the dipole and quadrupole distortion coefficients are no longer easily discerned from the noise of the calculation, that is obtained from the reference calculation of 0 tubes.

The approximate effect that these coefficients have on the blurring of the spot size at the common crossover plane is estimated for a 2 keV beam energy. The blurring may be, in a coarse approximation, be obtained by finding the erroneous focusing that is the result of a multipole distortion. This is given by the additional deflection that is imparted onto the outside of the spread-out beam, and is approximately given by

$$d_{n,\ blur} \approx \frac{U_{el} c_n n R^{n-1} u_1}{\Phi}. \quad \text{(C.2)}$$

In the equation, R is the beam width inside the tetrode mirror, u_1 the distance between the mirror and the common crossover plane, and Φ the beam energy. Since the coefficients are obtained at a 1 kV excitation of the electrode, a scaling term U_{el} is used to provide correspondence to the actual electrode potential.

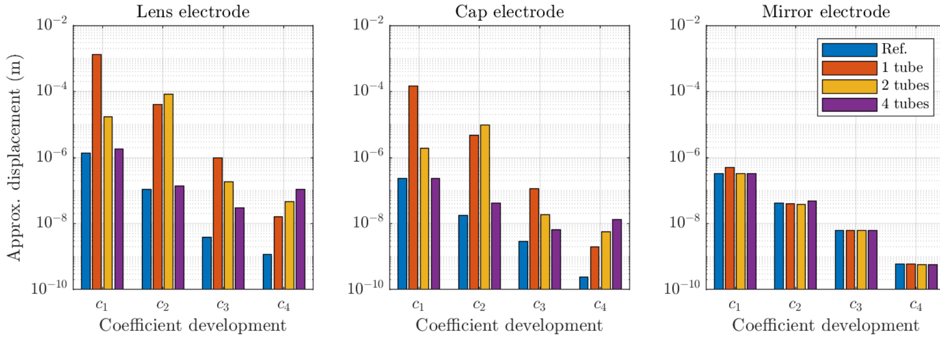

Figure C.1: Multipole distortion coefficient development, as a function of number of symmetry tubes. 'Ref.' labels for the reference case with no tubes present, and serves as indicator for the numerical detection threshold of the method. The approximate displacement indicates the estimated Full Width (FW) 100 beam blur at the common crossover plane, and is obtained for a beam width of 40 μm inside the tetrode mirror.

The above coarse model is applied onto the tetrode mirror, and the obtained beam blurring values are shown in [Fig. C.1]. The blue bars indicate blurring values that are based on the numerical data obtained in the absence of any tubes, and serve as a measure for the numerical accuracy. The data shown in based on the coefficients in [Table C.1] and thus follow similar behavior as to what is described before. It is evident from the data that spot size blurring in the order of $10 - 100$ nm is to be expected at the common crossover plane.

References

[1] M. A. R. Krielaart, D. J. Maas, S. V. Loginov, and P. Kruit, *Miniature electron beam separator based on three stacked dipoles,* Journal of Applied Physics **127**, 234904 (2020).

D

Spot size as a function of defocus, in the presence of both third and fifth order spherical aberration coefficients.

D.1. Introduction

In this appendix we describe how to obtain the contribution to the FW50 spot size from spherical aberration in the general case, for which C_{s3}, and C_{s5} are both non-zero, and may have opposite sign. The method can be directly extended to include higher orders as well. This method is not only applicable to our case in which the beam is reflected by a mirror, but also for the calculation of the probe size in an aberration corrected SEM or STEM.

We assume a uniform current distribution in the imaging system. When the image plane coincides with the focal plane of a lens, the beam (aperture) semi-angle (α) with the optical axis at the image plane, the distance between the principle optical plane of the lens and the image plane (f), and the radial distance from the optical axis at the principle optical plane of the lens system (h), are related under the small angle approximation by

$$h = \alpha f. \tag{D.1}$$

The full current (I) at the principal plane of the lens, as a function of the beam semi-angle and under the assumption of a uniform (angular) current distribution Ω is given by

$$I_{100}(\alpha) = \pi(\alpha f)^2 \Omega. \tag{D.2}$$

We can transform this into a normalized current ($\hat{I}$), which provides the current within the reduced semi-angle $[0, \tilde{\alpha}]$, which lies in the range $0 \leq \alpha \leq \tilde{\alpha}$, given by

This appendix has published as supplementary material of M. A. R. Krielaart, and P. Kruit, *Flat electron mirror*, Ultramicroscopy **220** (2021), 10.1016/j.ultramic.2020.113157.

$$\hat{I}(\tilde{\alpha}) = \left(\frac{\tilde{\alpha}}{\alpha}\right)^2. \tag{D.3}$$

Within an infinitesimal emission ring $d\alpha$ corresponding to ray angle $\tilde{\alpha}$, the contained normalized current is then given by

$$w(\tilde{\alpha}) \equiv \frac{d\hat{I}}{d\tilde{\alpha}} = \frac{2\tilde{\alpha}}{\alpha^2}. \tag{D.4}$$

D

Here, $w(\tilde{\alpha})$ may be regarded as a normalized weight factor, or as the fraction of current that is emitted from an infinitesimal ring.

The intersection coordinate y_S of a ray at angle $\tilde{\alpha}$ (with $0 \leq \tilde{\alpha} \leq \alpha$) at the image plane, due to defocus, and third and fifth order coefficients of spherical aberration is given by

$$y_S(\tilde{\alpha}) = \left|C_1\tilde{\alpha} + C_{s3}\tilde{\alpha}^3 + C_{s5}\tilde{\alpha}^5\right|. \tag{D.5}$$

When the product $C_{s3}C_{s5} > 0$, i.e., the aberration coefficients are of equal sign, and with C_1 equal to zero or having the same sign, then the spherical spot size diameter FW50, containing 50% of the current, is found by solving for α_1 in

$$\int_0^{\alpha_1} w(\tilde{\alpha})d\tilde{\alpha} = 0.5 \Rightarrow FW50 = 2y_S(\alpha_1). \tag{D.6}$$

The upper limit of integration α_1 is related to y_S by inverting the latter for $\tilde{\alpha} = y_S(\tilde{\alpha})^{-1}$, and increasing $\tilde{\alpha}$ until the equality in [Eq. (D.6)] is satisfied. Inserting the obtained α_1 back into [Eq. (D.5)] then directly yields the FW50, also see [Fig. D.1(a)].

When either C_1, C_{s3}, or C_{s5} is of opposite sign of the other coefficients, and for sufficiently large coefficients, or at sufficiently large semi-angle α, the situation arises at which for increasing ray angle $\tilde{\alpha}$ the ray first crosses the optical axis at one side of the image plane, and for increasing ray angle at the other side of the image plane. Thus, for a given C_{s3} and C_{s5} of opposite sign, and C_{s5} usually but not necessarily positive, a sufficiently large semi-angle will result in a region of $\tilde{\alpha}$ for which the spot size will not increase radially outward. This situation is depicted in [Fig. D.1(b)]. A proper calculation of the spherical spot size would then require to take into account that the current that is incident from the higher ray angles $\tilde{\alpha}$ contribute a large amount of the total current, at a limited increase of spot size. To take this effect into account in the calculation of the FW50 spot size, an extension of [Eq. (D.6)] is required that allows for the additional zero-crossings of $y_S(\tilde{\alpha})$ [Eq. (D.5)] at the image plane. As we consider spherical aberration up to fifth order, in principle we expect up to five solutions [Fig. D.1(c)]to the inverse problem $\alpha = \alpha(y)$,

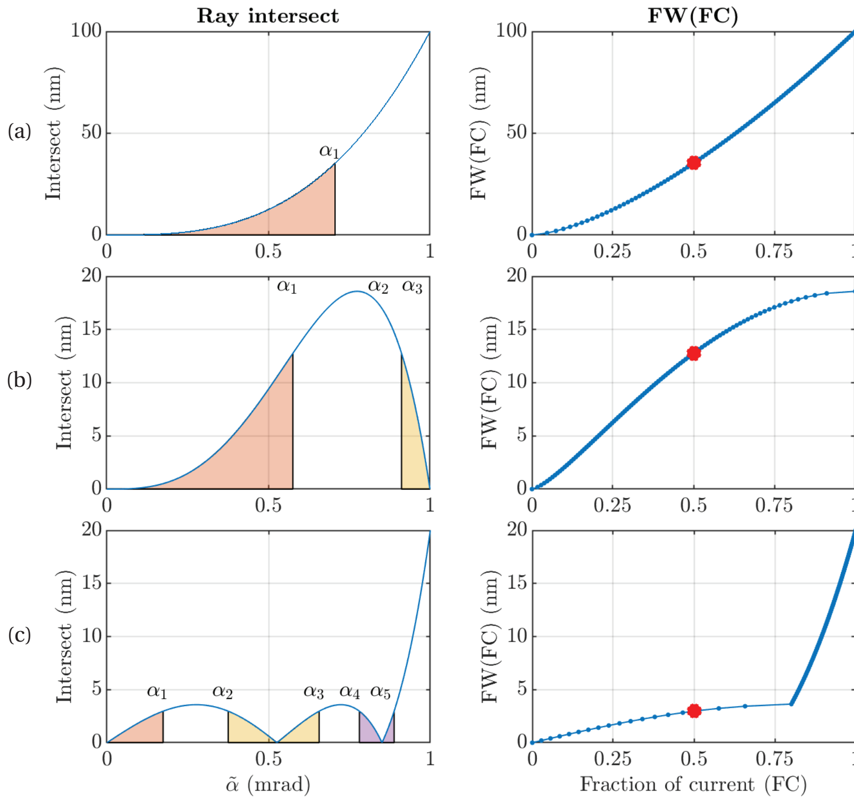

Figure D.1: Ray trajectory intersect at the image plane as a function of ray angle. The integration domain(s) (left panels) related to the Full Width (FW) containing a Fraction of Current (FC) (right panels) is shown for three distinct cases. (a) Third order spherical aberration. (b) Third and fifth order coefficient of spherical aberration with opposite sign. (c) Negative defocus and fifth order spherical aberration coefficient, positive third order coefficient of spherical aberration.

meaning that the FW50 ($FC = 0.5$) is found by solving the following equality for α_n, with $n = 1 \cdots 5$, and for which $y_S(\alpha_1) = \cdots = y_S(\alpha_5)$,

$$\int_0^{\alpha_1} w(\tilde{\alpha})d\tilde{\alpha} + \int_{\alpha_2}^{\alpha_3} w(\tilde{\alpha})d\tilde{\alpha} + \int_{\alpha_4}^{\alpha_5} w(\tilde{\alpha})d\tilde{\alpha} = FC. \tag{D.7}$$

In order to satisfy this equality for all α_n, the inverse to [Eq. (D.5)] must be obtained, which contains 5 roots and for which to our knowledge no (practical) analytical solution exists. In the following we outline a numerical solution method that allows one to find the $FW(FC)$.

D.2. Numerical methods

The problem at hand is two-fold. On the one hand, we require up to five values for ray angles $\tilde{\alpha}$ that yield equal intersect coordinates when inserted into [Eq. (D.5)].

On the other hand, we must solve the integral in [Eq. (D.7)] using these same ray angles as integration boundaries, while satisfying the equality for the given Fraction of Current (FC). As the result of the latter calculation depends on the former, it is difficult to directly obtain the integral boundaries that exactly correspond to the FW50 case. Therefore, we suggest the following solution strategy:

1. Obtain the FW100 of the beam, for chosen beam semi-angle α.
2. Obtain the FW for a number of FW values $0 < FW \leq FW100$.
   - For a given FW, obtain the integration boundaries through the inverse of [Eq. (D.5)].
   - Perform the integral in [Eq. (D.7)], to obtain the FC related to the FW value.
3. Interpolate the obtained data set of FW and FC, in order to obtain the FW50.

D

D.2.1. Obtaining the FW100

The FW100 must be obtained first. This is readily performed when all coefficients are of equal sign. In that case, the FW100 is always determined by the value of the beam semi-angle, such that $FW100 = 2 \times y_S(\alpha)$. In the more general case, in which the signs of the coefficients may be oppositely valued, the FW100 may be found at a smaller ray angle, as can be understood from [Fig. D.1(b)]. From the expression of local disc radius, $y_S(\tilde{\alpha}) = C_1\tilde{\alpha} + C_{s3}\tilde{\alpha}^3 + C_{s5}\tilde{\alpha}^5$, one can find the local maxima through differentiation,

$$\frac{dy_S}{d\tilde{\alpha}} = C_1 + 3C_{s3}\tilde{\alpha}^2 + 5C_{s5}\tilde{\alpha}^4 = 0. \tag{D.8}$$

Substitution of $\beta \equiv \tilde{\alpha}^2$ enables an analytical solution through the abc-formula:

$$\beta = \frac{-3C_{s3} \pm \sqrt{9C_{s3}^2 - 20C_1C_{s5}}}{10C_{s5}}. \tag{D.9}$$

From this, we obtain $\tilde{\alpha} = \sqrt{\beta}$, and only keep the real valued solutions, that satisfy $0 < \tilde{\alpha} \leq \alpha$. The FW100 is then determined by whichever term is bigger, from the set $\{y_S(\tilde{\alpha})\}$ (case in [Fig. D.1(b)])or from the marginal ray $y_S(\alpha)$ (case in [Fig. D.1(c)]).

Note for the special case where $C_{s5} = 0$, the solution provided by [Eq. (D.9)] becomes invalid, and instead $\beta = -C_1/(3C_{s3})$ must be used.

D.2.2. Obtaining the Fraction of Current (FC)

After having obtained the FW100, an array of FW values in the range $0 < FW \leq FW100$ is created. We next step through these values, and obtain the (set of) ray angles α_n that correspond to the FW. This is performed in MATLAB through the use of the symbolic equation solver, as outlined in listing D.1.

Listing D.1: Numerical inversion solution

```
% One-time solution for inverse a = a(y) problem
syms y c1 c3 c5 a;
a_inv_y = solve(y == abs(c1*a + c3*a^3 + c5*a^5), a);

% Update parameters based on s, to the inverse problem a = a(y).
copy_a_inv_y = subs(a_inv_y, [c1 c3 c5 y], [s.Cs1 s.Cs3 s.Cs5 yFC]);

% copy_a_inv_y now contains the solutions to a, in symbolic roots.
```

D

In terms of execution speed, the bottleneck in this process is in finding the solution to the inverse problem numerically, and by creating the necessary symbolic variables in MATLAB for each execution of the subroutine. We noticed that the process can be speed-up significantly through two distinctive methods:

1. Explicit passing along of symbolic variables and the symbolic solution of the inverse problem as an input argument to the subroutine.
2. Parallel execution (using MATLABs `parfor` method) in a high-core count system, of the for-loop in which the system configurations are looped over.

With the obtained solution $(\alpha_1, \cdots, \alpha_5)$ of the inversion problem, the Fraction of Current (FC) is obtained from the integral of [Eq. (D.7)], repeated here:

$$FC = \int_0^{\alpha_1} w(\tilde{\alpha})d\tilde{\alpha} + \int_{\alpha_2}^{\alpha_3} w(\tilde{\alpha})d\tilde{\alpha} + \int_{\alpha_4}^{\alpha_5} w(\tilde{\alpha})d\tilde{\alpha}. \tag{D.10}$$

This returns the fraction of current (FC) as a function of increasing FW. The FW50 ($FC = 0.5$) is then found through interpolation of the obtained data set of FW and FC values.

D.2.3. Defocus leading to minimum FW50

In a practical calculation, we assume the values for C_{s3} and C_{s5} to be given and fixed. However, the defocus value C_1 could be easily changed in an experimental setup, by adjusting the lens potential. In order to obtain the minimum spherical contribution to the spot size at the image plane, the above outlined routines for finding the FW50 must be repeated at many different defocus values C_1.

To this end, we use a number of values as initial guess for the optimum defocus. For each of these defocus values, we obtain the FW50. If it happens that the smallest FW50 is obtained at the first or last defocus element in the array of guesses, the domain of initial guess values is extended into the direction of this element. This process is repeated until a local minimum FW50 is obtained, after which a refinement of the domain around the local minimum is used to further improve the calculation result.

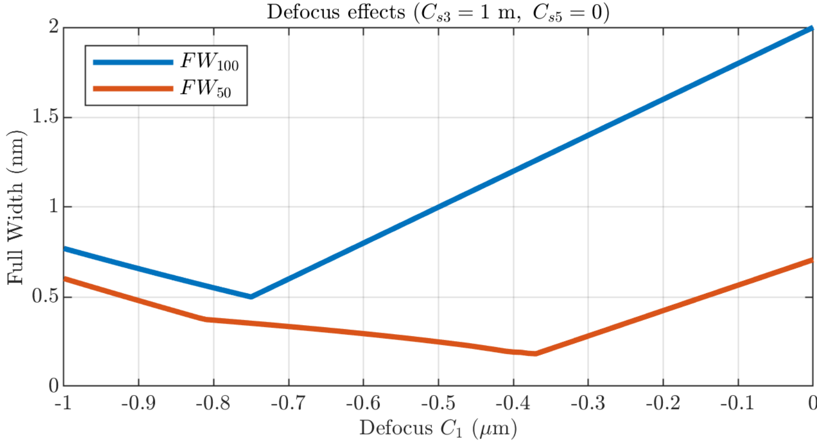

Figure D.2: FW50 as a function of C_1 defocus, at a semi-angle of 1 mrad and C_{s3} of 1 m. At zero defocus, the obtained FW50 equals 0.5 nm. The global minimum is found at 370 nm defocus, and provides a FW50 of 0.18 nm. Both values are in agreement with the theory.

D.3. Applications

We will now demonstrate the application of the numerical method by means of two examples.

D.3.1. Minimize C_{s3} effects through defocus of C_1.

Example 1. In this example, we assume for now $C_{s5} = 0$, and a positive value for C_{s3}, say $C_{s3} = 1$ m, and a beam semi-angle of $\alpha = 1$ mrad. Initially, the system is not defocused, i.e., $C_1 = 0$. Then, the FW100 at the image plane is given by definition by $FW100 = 2 \times y_S(\alpha) = 2$ nm. This could however be reduced to $0.5 C_{s3}\alpha^3 = 0.5$ nm by defocusing the beam. This is demonstrated by the blue curve in [Fig. D.2].

The minimum FW50 is much smaller, and is given by theory [1] as $0.18 C_{s3}\alpha^3$, and also requires a defocus of C_1. We obtained the FW50 as a function of defocus as well (orange curve in [Fig. D.2]). The global minimum is in agreement with the theoretical expectation. From this, it is confirmed that the spot size blurring due to C_{s3} can be compensated for in part by chosen a negative C_1.

D.3.2. Minimize C_{s5} and C_{s3} effects through defocus of C_1

Example 2. The results from Example 1 might also be obtained analytically, and serve as a validation of the method. Analytical difficulties arise as soon as the third- and fifth order coefficient have opposite sign. Then, the integral boundaries in [Eq. (D.7)] can no longer be obtained analytically, and one may be led to the false conclusion that there exists a semi-angle for which the spherical spot size vanishes completely. In the following example we obtain the FW100 and FW50 at zero defocus, and compare these results to the FW50 that may be obtained by obtaining the optimum defocus value, as a function of the beam semi-angle α.

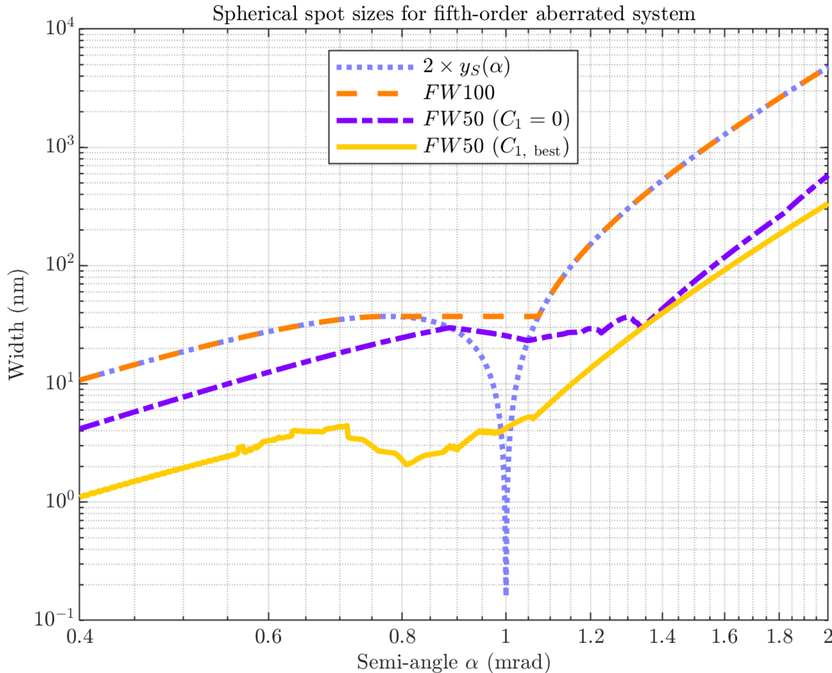

Figure D.3: FW100 and FW50 (with and without optimizing the defocus C_1). Function $2 \times y_{100}(\alpha)$ indicates the full width of a single ray at the given semi-angle value, and is plotted for reference.

For this, we (arbitrarily) choose $C_{s3} = -1 \times 10^2$ m, and $C_{s5} = 1 \times 10^8$ m. These parameters yield the special case for which $y_S(\alpha) = 0$ at $\alpha = 1$ mrad (at zero defocus), while the Full Width containing (a Fraction of) the total Current should not vanish at this point, as for ray angles $\tilde{\alpha} < \alpha$, the ray crosses the image plane of-axis.

With the above parameters, the FW100, and FW50 (at zero and best defocus) are obtained numerically. The results of the calculation are shown in [Fig. D.3]. The blue dotted line indicates the value of $2 \times y_S(\alpha)$, i.e., full width of the transverse coordinate of the marginal (outermost) ray at the image plane, at zero defocus. The orange dashed curve represents the FW100, and should satisfy that it equals the global maximum max $(2 \times y_S(\alpha))$ in the range $[0, \alpha]$. This behavior is indeed observed in the plot.

More of interest is the behavior of the FW50 spot size diameter (purple double dashed line), that indicates the diameter of the beam containing 50% of the current at zero defocus. At increasing semi-angle, it is observed that the FW50 first increases monotonically. However, around $\alpha = 0.9$ mrad a local maximum is observed. This is explained by the decrease of y_S around this semi-angle, which means that a large amount of the total current is hardly contributing to the probe size at this point

(also see [Fig. D.1(b)]). This effect extends for semi-angles of up to approximately 1.35 mrad, after which the fifth order aberration becomes dominant and the spot size increases rapidly again.

Finally, the yellow curve indicates the FW50 that could be achieved when properly defocusing the system through C_1. The result indicates a large reduction in spot size diameter compared to the non-defocused case.

References

[1] P. Kruit, *Electron sources,* in *Transmission Electron Microscopy*, edited by C. B. Carter and D. B. Williams (Springer International Publishing, 2016) pp. 1–15.

D

Acknowledgements

I would like to provide a warm thank you to anybody that has contributed to the completion of this thesis. Your help is most appreciated, and it cannot be understated that to build a 'microscope inside a microscope', as some people came to refer to as my project, is not a one man's job.

In particular and foremost, I would like to extend my deepest gratitude to my promotor, Pieter Kruit, for providing me with excellent, well thought of, and thorough scientific counseling, and in addition to that also for providing an excellent electron microscopy research facility in his group.

I have enjoyed to be part of the international quantum electron microscopy collaboration that we have with Karl Berggren's group at MIT, Mark Kasevich's group at Stanford, and Peter Hommelhoff's group at Erlangen, and which is gracefully funded by the Gordon and Betty Moore Foundation. In particular I would like to thank Navid Abedzadeh from MIT, for the close collaboration on our grating mirror related experiments.

At some point, Diederik Maas joined our group to work on a project that is closely related to the work in this thesis. We found many of our scientific challenges to overlap, which has formed the initial basis for what I experience has become a good friendship that I appreciate. Also, I want to thank him specifically for showing exemplary how project progress can benefit from collaborations with industrial partners.

The support staff has helped me out a lot, and I cannot imagine how to realize all the hardware developments without you. Thanks to you all, Jan, Johan, Ruud, and Youp for the mechanical work, Han, and Paul, for the electronics you built for me, Carel, and Martin, for all your lithography work, and Dustin, for your wide knowledge about the microscopes in our group.

When I started my research in Delft, I think I was the last of six that started in close proximity from each other. I really enjoyed sharing experiences and the many (ir)relevant discussions that we had. In particular I want to thank Kerim for joyfully sharing an office throughout the years, and Wilco for getting me started on using the multibeam-SEM for my initial experiments. At a later stage, Sergey joined the project, and I appreciate all the work that he has done so far, as well as his apparent strong belief that anything can be done with a laser.

Finally, I want to kindly thank all family and friends that have shown their support and interest in my research throughout the years. My wife, Yana, for all of here support, and perfect understanding of all mood swings that come with research work. And to both of our parents, brother and sisters, your support is most appreciated and has not gone by unnoticed.

– *Maurice Krielaart, 2021.*

Curriculum Vitæ

M. A. R. Krielaart

16 May 1991	Born in Kampen, The Netherlands.

Education

2003–2009	Secondary school Almere College, Kampen
2009–2013	Applied Physics bachelor program Twente university, The Netherlands
2013–2016	Applied Physics master program Twente University, The Netherlands
2016–2021	PhD candidate Applied Physics Delft University of Technology, The Netherlands *Thesis:* Electron wave front modulation with patterned mirrors *Promotor:* Prof. dr. ir. P. Kruit

Awards

2019	First prize poster contest M&M Portland, OR, USA.

List of Publications

- **M.A.R. Krielaart**, C.H. Vermeer, S. Vanapalli, *Compact flat-panel gas-gap heat switch operating at 295 K*, Review of Scientific Instruments **86**, 115116 (2015).
- **M.A.R. Krielaart**, P. Kruit, *Grating mirror for diffraction of electrons*, Phys. Rev. A **98**, 063806 (2018).
- **M.A.R. Krielaart**, P. Kruit, *Potentially Programmable Virtual Phase Plate for Electron Beams*, Microscopy and Microanalysis, **25**(S2), 92-93 (2019).
- P. Kruit, **M.A.R. Krielaart**, Y.S. van Staaden, *Phase Contrast in Quantum Electron Microscopy*, Microscopy and Microanalysis, **25**(S2), 1664-1665 (2019).
- **M.A.R. Krielaart**, D.J. Maas, S.V. Loginov, P. Kruit, *Miniature electron beam separator based on three stacked dipoles*, Journal of Applied Physics **127**, 234904 (2020).
- **M.A.R. Krielaart**, P. Kruit, *Flat electron mirror*, Ultramicroscopy **220** (2021).